Earth remote sensing with SMOS,
Aquarius and SMAP missions

Miriam Pablos Hernández

Ph.D. Thesis

Earth remote sensing with SMOS, Aquarius and SMAP missions

Author:

Miriam Pablos Hernández

Department of Signal Theory and Communications (TSC)
Technical University of Catalonia–BarcelonaTech (UPC)
Campus Nord, Building D3 and D4, 08034 Barcelona, Spain
miriam.pablos@tsc.upc.edu

Barcelona Expert Centre (BEC)
Passeig Marítim de la Barceloneta, 37-49, 08003 Barcelona, Spain
mpablos@icm.csic.es

Advisors:

Dr. María Piles Guillem
mpiles@icm.csic.es, maria.piles@tsc.upc.edu

Dr. Mercè Vall-llossera Ferran
merce@tsc.upc.edu

Barcelona, September, 2016

"I was taught that the way of progress is neither swift nor easy."

Marie Sklodowska-Curie

Abstract

The first three of a series of new generation satellites operating at L-band microwave frequencies have been launch in the last decade. L-band is particularly sensitive to the presence of water content in the scene under observation, being considered the optimal bandwidth for measuring the Earth's global surface soil moisture (SM) over land and sea surface salinity (SSS) over oceans. Monitoring these two essential climate variables is needed to further improve our understanding of the Earth's water and energy cycles. Additionally, remote sensing at L-band has been proved useful for monitoring the stability in ice sheets and measuring sea ice thickness.

The ESA's Soil Moisture and Ocean Salinity (SMOS, 2009-2017) is the first mission specifically launched to monitor SM and SSS. It carries on-board a novel synthetic aperture radiometer with multi-angular and full-polarization capabilities. NASA's Aquarius (2011-2015) was the second mission, devoted to SSS monitoring with a combined real aperture radiometer/scatterometer system that allows correcting for sea surface roughness. NASA's Soil Moisture Active Passive (SMAP, 2015-2018) is the second mission dedicated to measuring SM. It carries on-board a real aperture full-polarimetric radiometer and a synthetic aperture radar (SAR) for enhanced spatial resolution and freeze/thaw detection.

This Ph.D. Thesis is focused on analyzing the geophysical information that can be obtained from L-band SMOS, Aquarius and SMAP observations. The research activities are structured as follows:

- *Inter-comparison of radiometer brightness temperatures at selected targets*
  A novel methodology to measure the consistency between SMOS and Aquarius radiometric data over the entire dynamic range of observations (land, ice and ocean) is proposed. It allows detecting spatial/temporal differences or biases without latitudinal limitations neither cross-overs. This is a necessary step to combine observations from different instruments in long term datasets for environmental, meteorological, hydrological or climatological studies.

- *Ice thickness effects on passive remote sensing of Antarctic continental ice*
  The relationship between Antarctic ice thickness spatial variations and changes detected by SMOS and Aquarius measurements is explored. The emissivity of Antarctica is analyzed to disentangle the role of the geophysical contributions (snow layers at different depths and subglacial lakes) to the observed signal. The stability of the L-band signal in the East Antarctic Plateau, a calibration/validation site for microwave satellite missions, is assessed.

- *Microwave/optical synergy for multi-scale soil moisture sensing*
  The relationship of SM and land surface temperature (LST) dynamics is evaluated to better understand the fundamental SM-LST link through evapotranspiration and thermal inertia physical processes. A new approach to measure the critical soil moisture from time-series of spaceborne SM and LST is proposed. The synergistic use of SMOS SM and remotely sensed LST for refining SM disaggregation algorithms is also analyzed.

- *Comparison of passive and active microwave vegetation parameters*
  Recent research has shown that microwave vegetation opacity, sensitive to biomass and water content, and albedo, related to canopy structure, can be retrieved from passive L-band observations. The relationships between these two parameters and radar-derived vegetation descriptors have been explored using airborne observations from the SMAP Validation Experiment 2012 (SMAPVEX12). The obtained relations could allow for improved SM retrievals in active-passive systems, and also to estimate the vegetation properties at high resolution using SAR observations.

The Ph.D. Thesis has been developed within the activities of the Barcelona Expert Centre (BEC). The results presented contribute to the use of L-band remote sensing in different scientific disciplines such as climate, cryosphere, hydrology and ecology.

Contents

List of Figures

List of Tables

List of Acronyms

AF-FOV	**A**lias **F**ree-**F**ield **O**f View
BEC	**B**arcelona **E**xpert **C**entre
BOA	**B**ottom **O**f the **A**tmosphere
CONAE	**CO**misión **N**acional de **A**ctividades **E**spaciales
EAF-FOV	**E**xtended **A**lias **F**ree-**F**ield **O**f View
EASE	**E**qual **A**rea **S**calable **E**arth
ECMWF	**E**uropean **C**entre for **M**edium-Range **W**eather **F**orecast
ESA	**E**uropean **S**pace **A**gency
ESAC	**E**uropean **S**pace **A**stronomy **C**entre
ET	**E**vapo**T**ranspiration
EUMETSAT	**EU**ropean Organization for the Explotation of **MET**eorological **SAT**ellites
FC	**F**ield **C**apacity
FOV	**F**ield **O**f **V**iew
GNSS-R	**G**lobal **N**avigation **S**atellite **S**ystems-**R**eflectometry
GPCC	**G**lobal **P**recipitation **C**limatology **C**entre
H-pol	**H**orizontal **pol**arization
ISEA	**I**cosahedral **S**nyder **E**qual **A**rea
IR	**I**nfra-**R**ed
JPL	**J**et **P**ropulsion **L**aboratory
LAI	**L**eaf **A**rea Index
LEO	**L**ow **E**arth **O**rbit
LP DAAC	**L**and **P**rocesses **D**istributed **A**ctive **A**rchive **C**enter
LST	**L**and **S**urface **T**emperature
MIRAS	**M**icrowave **I**maging **R**adiometer by **A**perture **S**ynthesis
MODIS	**MOD**erate resolution **I**maging **S**pectroradiometer
MPDI	**M**icrowave **P**olarization **D**ifference **I**ndex
NASA	**N**ational **A**eronautics and **S**pace **A**dministration
NCEP	**N**ational **C**enter for **E**nvironmental **P**rediction
NDVI	**N**ormalized **D**ifference **V**egetation **I**ndex
NDWI	**N**ormalized **D**ifference **W**ater **I**ndex
OTT	**O**cean **T**arget **T**ransformation
PO.DDAC	**P**hysical **O**ceanography.**D**istributed **A**ctive **A**rchive **C**enter
REMEDHUS	**R**ed de **E**staciones de **MED**ición de la **HU**medad del **S**uelo
RFI	**R**adio-**F**requency **I**nterferences
RMSD	**R**oot **M**ean **S**quare **D**ifference
SAC	**S**atélite de **A**plicaciones **C**ientíficas

SAR	**S**ynthetic **A**perture **R**adar
SM	**S**oil **M**oisture
SMAP	**S**oil **M**oisture **A**ctive **P**assive
SMOS	**S**oil **M**oisture and **O**cean **S**alinity
SSS	**S**ea **S**urface **S**alinity
SST	**S**ea **S**urface **T**emperature
TEC	**T**otal **E**lectron **C**ontent
TOA	**T**op **O**f the **A**tmosphere
TOI	**T**op **O**f the **I**onosphere
UPC	**U**niversitat **P**olitècnica de **C**atalunya–BarcelonaTech
VIS	**VIS**ible
VOD	**V**egetation **O**ptical **D**epth
VWC	**V**egetation **W**ater **C**ontent
V-pol	**V**ertical **pol**arization
WP	**W**ilting **P**oint
WS	**W**ind **S**peed

List of Symbols

Symbol	Variable
a	Particle radius [m]
b	Constant of proportionality between VOD and VWC ($VOD = b \cdot VWC$)
c	Speed of light in vacuum ($3 \cdot 10^8$ m·s)
d	Distance between radiating source and receiving antenna [m]
e	Emissivity
e_{coh}	Coherent emissivity
e_{inc}	Incoherent emissivity
f	Frequency [Hz]
Δf	Bandwidth [Hz]
f_v	Relative volume of air
h	Planck's constant ($6.63 \cdot 10^{-34}$ J·s)
h_s	Roughness parameter
k_c	Ice thermal conductivity [W·m^{-1}·K^{-1}]
k_d	Ice thermal difussivity [m^2·year^{-1}]
k_e	Extinction rate [Nep·m^{-1}]
k_B	Boltzmannn's constant ($1.38 \cdot 10^{-23}$ J·K^{-1})
m_g	Gravimetric soil moisture
m_v	Volumetric soil moisture
n	Refractive index
s	Slope estimated from a robust linear regression
x_s	Angular dependence of roughness
z	Depth [m]
A_t	Effective radiating area [m^2]
B	Brightness or radiance [W·m^{-2}·sr^{-1}]
B_{av}	Average Earth's magnetic field along the propagation path [Wb·m^{-2}]
B_{bb}	Brightness of a blackbody [W·m^{-2}·sr^{-1}]
B_f	Spectral brightness [W·m^{-2}·Hz^{-1}·sr^{-1}]
C	Clay content [%]
DP	Deep percolation [mm]
E_H	Electric field of a polarized wave at H polarization [V·m^{-1}]
E_V	Electric field of a polarized wave at V polarization [V·m^{-1}]
F_r	Normalized receiving antenna pattern [W·sr^{-1}]
F_t	Normalized radiation antenna pattern [W·sr^{-1}]

G	Geothermal heat flux [W·m^{-2}]
H	Ice thickness [m]
I	First Stokes parameter in terms of brightness temperature [K]
IRR	Irrigation [mm]
K_{cb}	Basal crop coefficient
K_e	Soil evaporation coefficient
K_s	Water stress coefficient
L_a	Attenuation of the atmosphere
M	Snow accumulation rate [m·year^{-1}]
M_{org}	Organic matter content [%]
N_{TEC}	Ionospheric total electron content [electrons·m^{-2}]
P	Effective precipitation [mm]
P_{bb}	Power of a blackbody [W]
P_f	Spectral power [W·Hz^{-1}]
P_r	Received power [W]
P_s	Soil porosity
Q	Second Stokes parameter in terms of brightness temperature [K]
Q_s	Polarization mixing factor
R	Correlation
RO	Surface run-off [mm]
S	Sand content [%]
S_0	First Stokes parameter
S_1	Second Stokes parameter
S_2	Third Stokes parameter
S_3	Fourth Stokes parameter
T_{isurf}	Ice surface temperature [K]
T_{ph}	Physical temperature [K]
T'_A	Antenna temperature [K]
T_B	Brightness temperature [K]
T_{B_H}	Brightness temperature at horizontal polarization [K]
$T_{B_{LHC}}$	Brightness temperature at left-hand circular polarization [K]
$T_{B_{RHC}}$	Brightness temperature at right-hand circular polarization [K]
T_{B_V}	Brightness temperature at vertical polarization [K]
T_{B_X}	Brightness temperature (antenna plane) at X-axis [K]
T_{B_Y}	Brightness temperature (antenna plane) at Y-axis [K]
$T_{B_{+45°}}$	Brightness temperature skewed +45°with respect to normal [K]
$T_{B_{-45°}}$	Brightness temperature skewed -45°with respect to normal [K]
T_{DN}	Brightness temperature reflected by the Earth's surface [K]
T_{SE}	Brightness temperature self-emitted by the Earth's surface [K]
T_{SS}	Downward-emitted atmospheric brightness temperature [K]
T_{UP}	Self-emitted atmospheric upward brigthness temperature [K]
U	Third Stokes parameter in terms of brightness temperature [K]
V	Fourth Stokes parameter in terms of brightness temperature [K]
Vol	Volume [m^3]
W	Weight [kg]
WS	Water storage or soil moisture at root-zone [mm]

α	Attenuation constant of a material [Nep·m^{-1}]
α_w	Areal water fraction
β	Phase constant of a material [rad·m^{-1}]
γ	Propagation constant of a material ($\gamma = \alpha + j\beta$)
δ_p	Penetration depth [m]
ϵ_1	Atomic energy level 1 [J]
ϵ_2	Atomic energy level 2 [J]
η_0	Intrinsic impedance of free space (120π Ω)
θ	Incidence angle referred to nadir [°]
κ	Normalized attenuation coefficient
λ	Wavelength [m]
ϕ	Azimut angle refered to nadir [°]
ρ	Density [kg·m^{-3}]
σ	Stefan-Boltzmann's constant ($5.67 \cdot 10^{-8}$ W·m^{-2}·sr^{-1}·K^{-4})
σ_{eff}	Effective conductivity [S·m^{-1}]
σ_{HH}	Backscatter cross-section at horizontal-horizontal polarizations
σ_{HV}	Backscatter cross-section at horizontal-vertical polarizations
σ_s	Root mean square height of a rough surface [m]
σ_{VV}	Backscatter cross-section at vertical-vertical polarizations
τ	Relaxation time [s]
ω	Single-scattering albedo
ε	Complex dielectric constant of a material ($\varepsilon = \varepsilon' - j\varepsilon''$)
ε'	Permittivity of a material (real part of ε)
ε''	Loss factor of a material (imaginary part of ε)
φ	Sum of geometric and Faraday rotation angles ($\varphi = \varphi_G + \varphi_F$) [rad]
φ_F	Faraday rotation angle [rad]
φ_G	Geometric rotation angle [rad]
ϱ_p	Reflection coefficient at polarization p
Γ_p	Reflectivity at polarization p
Υ	Transmittivity
Ω_r	Solid angle subtended by the receiver [sr]
Ω_t	Solid angle subtende by the transmitter [sr]

Chapter 1

Introduction

1.1 Context

Present evidences of climate change and global warming include, but are not limited to, global temperature increase, ocean warming, sea level increase, decrease of snow cover, shrinking of Greenland ice sheet, declining of Arctic sea ice, retreat of glaciers, intense rainfall events, more frequent floods and droughts [IPCC, 2013, 2014]. In this context, Earth observing satellites are a useful tool to better understand the impact of a changing climate; they allow to collect essential bio-geophysical parameters that the scientific community can use to get a comprehensive view of the Earth's water, energy and carbon cycles, and monitor their global evolution.

Remote sensing consists of extracting information from an object or a phenomenon through measuring its radiation emitted or reflected at a particular frequency band, without physical contact. In the microwave spectrum region (0.3–300 GHz), all bodies at a physical temperature greater than the zero absolute (0 K, $\approx -273°$C) naturally emit energy as an electromagnetic radiation (e.g., [Ulaby & Long, 2014]). This is because all matter above 0 K is composed of particles with kinetic energy, which are continuously in movement, generating electric and magnetic fields and radiating energy away from its body through its surface boundary. An example of this fact is the thermal radiation emitted by the Earth's surface.

The Earth is always receiving electromagnetic radiation, mainly coming from the Sun, but also from the Moon, and the cosmic and celestial background. A fraction of this radiation is scattered and absorbed by the atmosphere, and the remainder is transmitted to the Earth's surface. Part of the radiation that arrives to the surface is scattered outward and another part is absorbed. The energy absorbed by the surface produces an increase of its physical temperature. Consequently, the Earth's surface emits thermal radiation to keep the energy balance, achieving the thermodynamic equilibrium. At this state, all materials exhibit this behaviour, independently of its media (solid, liquid, gas or plasma).

Radiometry is the field of science and engineering concerned with the measurement of the thermal electromagnetic radiation. This energy can be detected by a radiometer, a passive sensor capable of accurately measuring the so-called brightness temperature (T_B), a magnitude which is proportional to the amount of radiated power (e.g., [Ulaby & Long, 2014]). There are numerous applications of microwave radiometry; most of them can be grouped in three disciplines: i) astronomical studies, in which radiometers are used to measure the electromagnetic radiation of celestial bodies in our galaxy or other galaxies; ii) security, for detecting the presence of metal or explosives targets; and iii) enviromental monitoring, including several scientifc fields, such as meteorology, climatology, oceanography, hydrology, and ecology.

At L-band (1–2 GHz), there is a protected band from 1.4 GHz to 1.427 GHz, reserved for radio-astronomy and passive microwave remote sensing [CNAF, 2013]. At these frequencies, the amount of thermal radiation naturally emitted by the Earth's surface decreases with increasing soil moisture (SM) over land [Schmugge *et al.*, 1974, 1986], and with increasing sea surface salinity (SSS) over oceans [Swift, 1980, Blume & Kendall, 1982]. This is illustrated in Fig. 1.1 (left) and 1.1 (right), respectively.
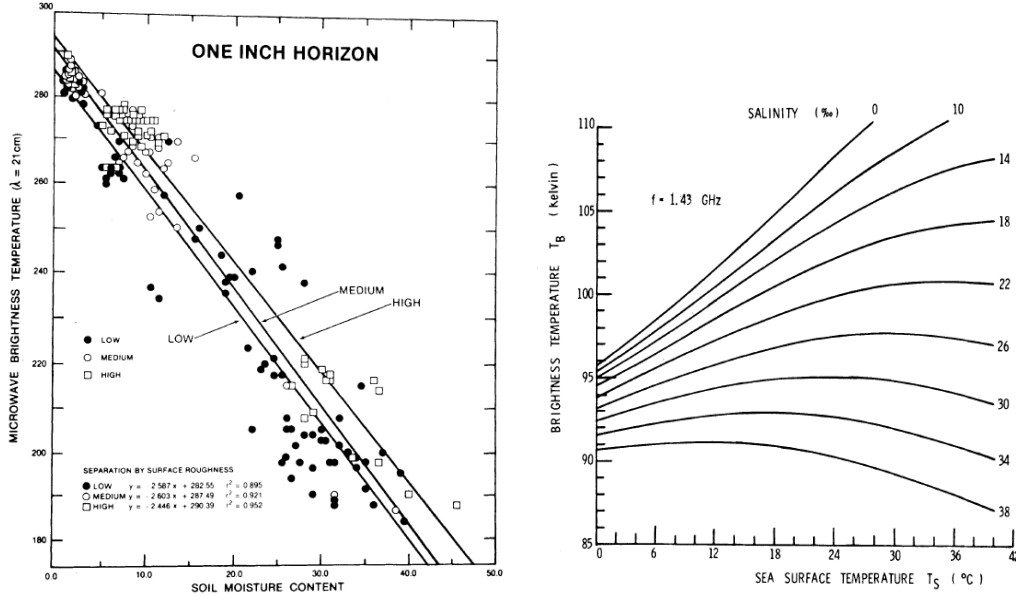
FIGURE 1.1: L-band airborne T_B measurements as a function of SM observations over the Hand County, South Dakota, USA [Schmugge *et al.*, 1986] (left) and L-band T_B curves as a function of sea surface temperature with SSS as a parameter [Swift, 1980] (right).

With respect to other sensing frequencies, main advantages of L-band are: i) it is significantly less affected by rain and atmospheric effects than higher microwave frequencies, being the atmosphere nearly transparent [Crane, 1971]; ii) the radiation emitted by the Earth's surface can also pass through sparse up to moderate canopies (i.e., those with vegetation water content (VWC) ≤ 5 kg/m^2, which corresponds to 70 % of non-frozen land areas on Earth, excluding dense forest); and iii) since L-band is part of the microwave frequency range, the measurements are also independent of solar illumination. In all these evidences, the scientific community considers L-band radiometry the optimal technology to globally measure SM and SSS.

Nowadays, there are two satellite missions in orbit providing unprecedent views of the Earth's surface using L-band radiometers: i) the Soil Moisture and Ocean Salinity (SMOS, 2009–2017) mission from the European Space Agency (ESA) [Kerr *et al.*, 2010, Font *et al.*, 2010, Mecklenburg *et al.*, 2016], and ii) the Soil Moisture Active Passive (SMAP, 2015–2018) mission from the U.S National Aeronautics and Space Administration (NASA) [Entekhabi *et al.*, 2010b, Chan *et al.*, 2016]. Additionally, a third L-band satellite was operational from 2011 until 2015: the Aquarius/*Satélite de Aplicaciones Científicas* (SAC)-D mission from the NASA and the Argentinian *Comisión Nacional de Actividades Espaciales* [Le Vine *et al.*, 2010].

1.2   Motivation and objectives

Although the amount of water on Earth remains constant along time, it is always in movement on, above, and below the Earth's surface, i.e., there is a continuous water exchange between the oceans, the land and the atmosphere [USGS, 2015]. In last years, climate change is having an impact in the Earth's water cycle. If there is a global increase of temperature, there is more evaporation from land and sea to the atmosphere. As air gets warmer, it can hold more water

vapor, which can lead to more intense rainstorms, increasing the risk of floods. During intense precipitation events, much of the water run off into rivers and streams, doing little to dampen soil. This, combined with higher temperatures and other processes (e.g., changes in global circulation, etc.), increase the risk of droughts and deforestation [Climate Reality, 2014]. The research line described in this Ph.D. Thesis is focused on studying the bio-geophysical information about the Earth's water cycle that can be estimated from L-band satellite observations over the continental surfaces on Earth, in the framework of SMOS, Aquarius, and SMAP missions. The activities are organized as follows:

- *Inter-comparison of radiometer brightness temperatures at selected targets*

  The combination of data from several sensors to obtain a longer data record requires a comprehensive knowledge of these datasets to verify the continuity and the consistency of the measurements. This study was performed using SMOS and Aquarius data, the only L-band spaceborne datasets available at that moment. There are significant differences between the radiometers on-board of SMOS [McMullan *et al.*, 2008] and Aquarius [Le Vine *et al.*, 2007a] satellites. Analyzing and comparing the radiometric measurements over the entire dynamic range of observations is of prime importance if data from both instruments are to be used in any long term enviromental, meteorological, hydrological, or climatological study. The specific objectives are:

  - Development of a new methodology to compare the T_B acquired by SMOS and Aquarius radiometers to verify the continuity and consistency of the data over the entire dynamic range of observations (land, ice, and ocean).
  - Analysis of the possible temporal and spatial differences at selected targets on Earth.

- *Ice thickness effects on passive remote sensing of Antarctic continental ice*

  Recent research has shown that the Arctic sea ice thickness can be estimated using SMOS [Kaleschke *et al.*, 2012] and Aquarius [De Matthaeis *et al.*, 2014] observations. Over Antarctica, L-band could also be potentially sensitive to changes in the ice sheet. The Antarctic continent has ∼98 % of its surface covered by ice. It comprises an area of almost 14 million km^2, being the largest reservoir of freshwater on Earth (∼90 % of the Earth's fresh water is held in the Antarctic ice sheet). The role of its ice sheet is crucial in the global climate system through multiple feedback mechanisms. It represents a sensitive indicator of the global warming and its changes have a critical impact on ocean circulation and global sea level rise [Pollard *et al.*, 2015, Paolo *et al.*, 2015]. Understanding how the system works and how it responds to human pressures is an important scientific challenge. Because of the difficult access, the complex logistics and the high budget required to perform field experiments, remote sensing observations offer a great opportunity to explore Antarctica from space. The specific objectives are:

  - Theoretical estimation of how deep, under the ice surface, the emissivity of the Antarctic ice layers originates and can be detected by an L-band radiometer.
  - Exploration of the relationship between the spatial variations of SMOS and Aquarius T_B over Antarctica and their sensitivity to geophysical parameters and processes such as ice thickness, presence of subglacial lakes, and possible bedrock and/or basal hydrological effects.

- *Microwave/optical synergy for multi-scale soil moisture sensing*

  Over land, L-band is sensitive to the surface SM [Schmugge *et al.*, 1974, 1986]. SM is an essential climate variable of the terrestrial water cycle [GCOS, 2010]. It controls the energy exchange at the land-atmosphere boundaries, linking the Earth's water and energy cycles. SM variations affect the evolution of weather and climate, and its knowledge is key for meteorological and hydrological modelling, monitoring of plant growth, and forecasting of hazardous events, such as floods and droughts. The spatial resolution of SMOS, Aquarius and SMAP SM is of ∼40–100 km. This resolution is enough for global applications [Ochsner *et al.*, 2013], but higher resolution (∼1–10 km) is needed for regional or local

studies [Entekhabi *et al.*, 1999]. In the last years, several approaches have been proposed to enhance the spatial resolution of these sensors using optical (for SMOS) or active (for Aquarius and SMAP) information. The specific objectives are:

- Analysis of the temporal correlation of SM and a variety of land surface temperature (LST) derived parameters at daily and seasonal scales to better understand the fundamental link of the SM–LST relationship through physical processes, such as the evapotranspiration and thermal inertia.

- Validation of high resolution SMOS SM datasets obtained from a SMOS SM downscaling algorithm. Implementation and validation of an improved approach of this algorithm and an averaged ensemble of high resolution SM estimates.

- *Comparison of passive and active microwave vegetation parameters*

  L-band is sensitive to SM, but also to vegetation characteristics [Jackson *et al.*, 1982, Jackson & Schmugge, 1991]. Consequently, the current passive SM retrieval algorithms employ *a priori* vegetation information (vegetation opacity and single-scattering albedo) to correct for the effects of the plant canopy in observed surface emissivity. This ancillary vegetation information is often land cover-based or derived from optical visible or infrared measurements. Recent research has shown that it is possible to directly retrieve these microwave vegetation parameters from L-band observations, alongside SM, using the multi-temporal dual channel algorithm (MT-DCA) [Konings *et al.*, 2016]. Also, vegetation estimations from passive and active microwave measurements could be related. This is of special interest in multi-resolution active-passive systems, where the link to the radar measurement allows estimation of these vegetation properties at high resolution. The specific objectives are:

  - Validation of the MT-DCA using airborne L-band observations from the SMAP Validation Experiment 2012 (SMAPVEX12) field campaign.

  - Comparison of retrieved passive vegetation parameters with co-located radar-based vegetation parameters.

The activities and original contributions contained in this Thesis path the way to advances in different scientific disciplines, including climate, cryosphere, hydrology and ecology.

1.3 Document organization

This Thesis is organized as follows:

Chapter 1 presents the context of the Thesis, its motivation and objectives, and the organization of this document.

Chapter 2 reviews the fundamentals of microwave radiometry, summarizes the theoretical background of passive remote sensing over continental ice and over land, and provides an overview of SMOS, Aquarius and SMAP L-band satellite missions.

Chapter 3 proposes a new technique to inter-compare SMOS and Aquarius T_B in any latitude/longitude. The radiometric observations, acquired independently for each instrument, are compared over four representative target regions that cover the entire dynamic range of observations (land, ice and sea). The comparison is based on the analysis of the level of linearity, the correlation, and the differences between SMOS and Aquarius T_B, using daily statistics along the whole year 2012.

Chapter 4 estimates the theoretical L-band penetration depth over the Antarctic ice sheet and explores the influence of ice thickness spatial variations on the measured SMOS and Aquarius T_B along a three-months no-daylight period in 2013. This ensures the independence of T_B changes

due to ice surface temperature variations. The possible effects of subglacial water and/or bedrock on the acquired radiometric signals is also analyzed.

Chapter 5 evaluates the temporal correlation of SM and LST using four years of *in situ* data from the Soil Moisture Measurement Stations Network of the University of Salamanca (REMED-HUS), in the Duero basin, Spain, and of spaceborne observations over the same region. The agreement of instantaneous SM with a variety of LST-derived parameters is analyzed. Also, the impact of using the different LST acquisition times in microwave/optical disaggregation algorithms is assessed with the validation of all possible downscaled SM estimates. An ensemble of averaged downscaled SM datasets is assessed to improve the coverage.

Chapter 6 validates the MT-DCA using airborne radiometric observations from SMAPVEX12. It is a new algorithm to simultaneously retrieve SM, VOD and ω, without using ancillary vegetation information. The SM retrievals are validated using *in situ* SM measurements. Later, the retrieved passive microwave vegetation parameters (VOD and ω) are compared to co-located active observations and the possible relations between active and passive vegetation parameters are analyzed.

Chapter 7 summarizes the main conclusions of this work, remarks its original contributions, and presents suggestions for follow-on research.

Chapter 2

Review of microwave radiometry & L-band satellite missions

2.1 Fundamentals of microwave radiometry

A brief explanation of the quantum theory for the thermal radiation and the emitted radiation of blackbodies and real materials is included. The measurement process to obtain the T_B of an observed body or scene using a radiometer is also described.

2.1.1 Quantum theory of thermal radiation

All bodies at a physical temperature above 0 K emit electromagnetic radiation at different frequencies or wavelengths. For example, in an atomic gas, each radiated spectral line corresponds to a specific transition of an electron from one atomic energy level ϵ_1 to a lower energy level ϵ_2. The frequency f [Hz] of the emitted radiation (photon) is given by the Bohr's equation:

$$f = \frac{\epsilon_1 - \epsilon_2}{h},\tag{2.1}$$

where the parameter h is the Planck's constant (h=6.63·10^{-34} J·s).

Planck's quantum theory defines the energy levels of an atom and the allowed transitions between them. When an atom absorbs the incident energy to move an electron to a higher energy level, the incident energy also satisfies the Bohr's equation. So, the absorption spectrum of an atomic gas is identical to its emission spectrum. This principle also applies to more complicated structures including molecular gases, liquids and solids.

Spontaneous emission of radiation by an atom is caused by a collision with another atom or particle. The probability of emission is higher for higher density of atoms and higher kinetic energy, which is associated to its absolute physical temperature. In a molecule, the vibrational, rotational and electronic motion of the atoms contribute to a more spectral lines than for an unique atom. In the liquids and the solids, which are composed of a continuoum of molecules, there is a large number of closely spaced spectral lines and the radiation spectrum becomes continuous.

2.1.2 Blackbody radiation

According to the Kirchhoff's law of thermal radiation, all the energy absorbed by a body in thermodynamic equilibrium is re-emitted. A blackbody is an idealized perfectly opaque material that absorbs all the incident radiation at all frequencies, reflecting none. Hence, a blackbody is a perfect absorber and a perfect emitter.

The blackbody emission follows the Planck's law; its radiation is uniform in all directions with a spectral brightness [W·m^{-2}·Hz^{-1}·sr^{-1}]:

$$B_f = \frac{2hf^3}{c^2} \frac{1}{e^{\frac{hf}{k_B T_{ph}}} - 1},$$
(2.2)

where h is the Planck's constant, f corresponds to the frequency [Hz], k_B is the Boltzmann's constant (k_B=1.38·10^{-23} J·K^{-1}), T_{ph} is the absolute physical temperature [K], and c is the speed of light in vacuum (c=3·10^8 m·s).

When $hf/k_B T_{ph} << 1$, the Planck's law described in Eq. (2.2) can be simplified using the Taylor's approximation $e^x - 1 = \left(1 + x + \frac{x^2}{2!} + ...\right) - 1 \approx x$, for $x << 1$, obtaining the Rayleigh-Jeans law:

$$B_f \approx \frac{2f^2 k_B T_{ph}}{c^2} = \frac{2k_B T_{ph}}{\lambda^2},$$
(2.3)

where $\lambda = c/f$ is the wavelenght.

In the microwave region, the Rayleigh-Jeans law is widely used since the spectral brightness is linearly related to the physical temperature. In fact, it has only a 1 % of deviation when $f <$117 GHz and T_{ph}=300 K.

When $hf/k_B T_{ph} >> 1$, the Planck's law in Eq. (2.2) is simplified using the approximation $\frac{1}{e^x - 1} \approx e^{-x}$, for $x >> 1$, obtaining the Wien's law:

$$B_f \approx \frac{2hf^3}{c^2} e^{-\frac{hf}{k_B T_{ph}}}.$$
(2.4)

A comparison of the spectral brightness of Planck's law (red solid line), Rayleigh-Jeans law (blue dashed line), and Wien's law (green dash-dotted line) is shown in Fig. 2.1 for T_{ph}=300 K (∼Earth's temperature) and T_{ph}=6000 K (∼Sun's temperature). Note that the two different approximations are appropiated to use in respective frequency ranges: Rayleigh-Jeans law for low frequencies and Wien's law for high frequencies.

Stefan-Boltzmann relates the total brightness of a blackbody B_{bb} [W·m^{-2}·sr^{-1}] with its physical temperature T_{ph} [K] by integrating Eq. (2.2) on the whole spectrum:

$$B_{bb} = \int\limits_0^\infty B_f df \approx \frac{\sigma T_{ph}^4}{\pi},$$
(2.5)

where the parameter σ is the Stefan-Boltzmann's constant (σ=5.67·10^{-8} W·m^{-2}·sr^{-1}·K^{-4}).
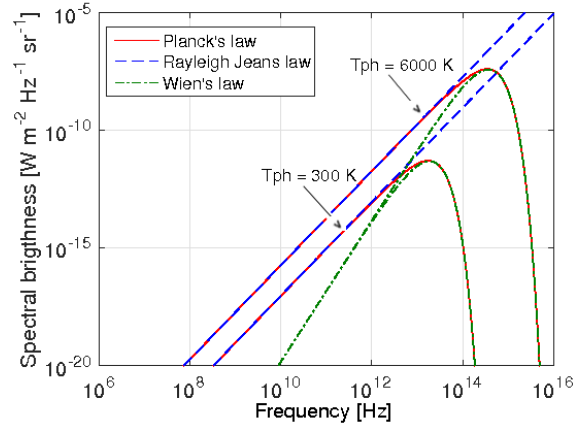
FIGURE 2.1: Comparison of spectral brigthness of Planck's law (red solid line), Rayleigh-Jeans law (blue dashed line), and Wien's law (green dash-dotted line) at T_{ph}=300 K ($\sim$Earth's temperature) and T_{ph}=6000 K ($\sim$Sun's temperature). Adapted from Ulaby & Long [2014].

2.1.3 Gray body radiation

The blackbody is a theoretical model used to describe the radiation process; it absorbs all the incident energy and, at thermodynamic equilibrium, all this energy is re-emitted. However, real materials or gray bodies emit less radiation than blackbodies since they do not necessarily absorb all the incident energy upon them. The incoming radiation of a gray body is partly reflected and partly absorbed. The absorbed radiation is then re-emitted and, in general, its emission is not omnidirectional. Due to that, the brightness of a gray body per unit area and solid angle $B(\theta, \phi)$ [W·m^{-2}·sr^{-1}] in the microwave region depends on directions θ and ϕ, which correspond to the incidence and azimut angle referred to nadir. Therefore, a blackbody equivalent radiometric temperature is defined as the brightness temperature of the material $T_B(\theta, \phi)$ [K], corresponding to the temperature that a blackbody should have in order to emit the same brightness.

The ratio of the brightness of a material to that of a blackbody at the same physical temperature is defined as the emissivity $e(\theta, \phi)$:

$$e(\theta, \phi) = \frac{B(\theta, \phi)}{B_{bb}} = \frac{T_B(\theta, \phi)}{T_{ph}}. \tag{2.6}$$

Since real materials radiate less than or equal to blackbodies $B(\theta, \phi) \leq B_{bb}$, therefore the emissivity is constrained to the range $0 \leq e(\theta, \phi) \leq 1$. A material with $e=0$ is a perfect reflector (a lossless conductor) while a material with $e=1$ is a perfect absorber (a blackbody). Hence, the brightness temperature of a material $T_B(\theta, \phi)$ is always lower than or equal to its physical temperature T_{ph}.

The microwave dielectric properties of the natural Earth materials are defined by their dielectric constant (ε). In general, ε is complex, consisting of a real part and an imaginary part, as follows:

$$\varepsilon = \varepsilon' - j\varepsilon'', \tag{2.7}$$

where ε' is the permittivity of the material, and ε'' corresponds to the loss factor.

The emissivity depends on several parameters such as the electrical properties of the material, the angle of observation, the surface's roughness, the polarization and the frequency. For the measurement of soil moisture and ocean salinity, the sensitivity of the dielectric constant to these geophysical parameters is maximum at L-band.

2.1.4   Brightness and power measured by an antenna

The simple case of an emitting source, which acts as transmitter, is considered. The radiation or brightness of the emitting source, with a normalized radiation pattern F_t [W·sr^{-1}] and an effective radiating area A_t [m^2] is defined as:

$$B = \frac{F_t}{A_t}. \tag{2.8}$$

The power P_r [W] collected by a lossless receiving antenna separated a distance d [m], oriented in the direction of maximum directivity with an effective area A_r [m^2], being R large enough to be considered constant power over a solid angle Ω_r [sr] is:

$$P_r = F_t \frac{A_r}{d^2} = BA_r \frac{A_t}{d^2} = BA_r \Omega_t, \tag{2.9}$$

where $\frac{A_t}{d^2}$ is replaced by the solid angle subtended by the source Ω_t [sr].

If the source is not observed by the receiving antenna in the direction of maximum directivity, the normalized receiving antenna pattern must be added in this way:

$$P_r = BA_r F_r \Omega_t. \tag{2.10}$$

Figure 2.2 shows the general case of a lossless receiving antenna surrounded by an extended source. In addition, the brightness is not constant with frequency. Taking into account for the directionality of the antenna, the expression in Eq. (2.10) is converted into a differential form that expresses the differential spectral power dP_f received through a differential solid angle $d\Omega$ along the direction (θ, ϕ), relative to the boresight direction of the antenna, as:

$$dP_f(\theta, \phi) = B_f(\theta, \phi)A_r F_r(\theta, \phi)d\Omega. \tag{2.11}$$
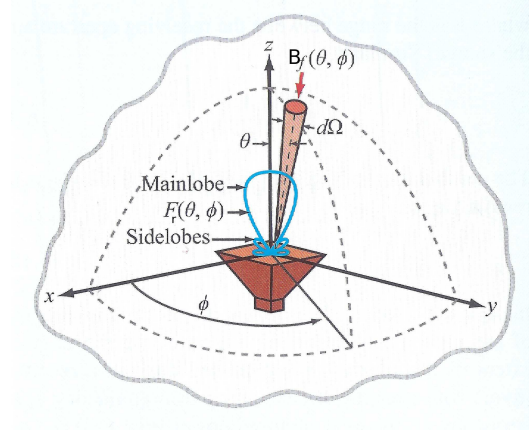
FIGURE 2.2: Geometry for calculating the received power measured by a lossless antenna from an emitting extended source (general case). Adapted from Ulaby & Long [2014].

The total amount of power received by the antenna can be obtained by integrating Eq. (2.11) over a bandwidth Δf (from f to $f + \Delta f$) and over the entire space 4π (for θ=0 to π and ϕ=0 to 2π):

$$P_r(\theta, \phi) = \frac{1}{2} A_r \int\limits_{f}^{f+\Delta f} \iint\limits_{4\pi} B_f(\theta, \phi)F_r(\theta, \phi)d\Omega df. \tag{2.12}$$

The term $\frac{1}{2}$ takes into account that, in general, the energy emitted is unpolarized, as occurs in the case of the Earth's surface and many other media, and the receiving antenna is polarized. Thus, on average, it can only detect half of the energy incident upon its aperture.

2.1.5 Power–temperature correspondence

In the microwave region, under the Rayleigh-Jeans law conditions given in Eq. (2.3), the brightness of a blackbody B_{bb} in a limited bandwidth Δf becomes:

$$B_{bb} = B_f(f, T_{ph})\Delta f = \frac{2k_B T_{ph}}{\lambda^2}\Delta f. \tag{2.13}$$

Therefore, the total power P_{bb} collected by an antenna in a limited bandwidth Δf, such that the spectral brightness is approximately constant over Δf, since $\Delta f << f$, with normalized radiation pattern $F_r(\theta, \phi)$ enclosed by a blackbody at a constant physical temperature is given by Eqs. (2.12) and (2.13):

$$P_{bb} = k_B T_{ph}\frac{A_r}{\lambda^2}\Delta f \iint\limits_{4\pi} F_r(\theta, \phi)d\Omega = k_B T_{ph}\Delta f, \tag{2.14}$$

where the integral $\iint\limits_{4\pi} F_r(\theta, \phi)d\Omega$ corresponds to the definition of the antenna solid angle $\Omega_r = \frac{\lambda^2}{A_r}$, which is canceled. Note that there is a linear relationship between power and the physical temperature. This is fundamental in microwave remote sensing, where the power received by an antenna is commonly given in units of temperature.

In a grey body, a similar expression to Eq. (2.13) can be obtained using the brightness temperature $T_B(\theta, \phi)$ instead of the physical temperature T_{ph}:

$$B(\theta, \phi) = \frac{2k_B T_B(\theta, \phi)}{\lambda^2}\Delta f. \tag{2.15}$$

Replacing $\frac{A_r}{\lambda^2}$ by $\frac{1}{\Omega_r}$, an analogous expression of the power for a grey body leads to:

$$P_r = \frac{1}{\Omega_r}k_B\Delta f \iint\limits_{4\pi} T_B(\theta, \phi)F_r(\theta, \phi)d\Omega = k_B T'_A\Delta f. \tag{2.16}$$

Then, the antenna temperature T'_A, defined as the apparent temperature of an equivalent lossless antenna such that the noise power delivered by the resistor of the receiver at that temperature is equal to P_r, can be expressed as:

$$T'_A = \frac{1}{\Omega_r}\iint\limits_{4\pi} T_B(\theta, \phi)F_r(\theta, \phi)d\Omega = \frac{\iint\limits_{4\pi} T_B(\theta, \phi)F_r(\theta, \phi)d\Omega}{\iint\limits_{4\pi} F_r(\theta, \phi)d\Omega}. \tag{2.17}$$

It is important to clarify that the brightness temperature $T_B(\theta, \phi)$ is referred to the emitted radiation from a body incident upon the antenna whereas the antenna temperature T'_A is referred to the radiation measured by the antenna (see Fig. 2.3).

2.1.6 Earth contributions to the brightness temperature

The case of interest in this Thesis is the passive remote sensing with an Earth-looking radiometer on-board a satellite, as shown in Fig. 2.3. In this case, the brightness temperature from the observed scene incident upon the antenna from any specific direction contain several contributions, since neither the radiometer nor the Earth's surface are isolated from radiation by other sources, such as the atmosphere.

Therefore, the radiation incident upon the antenna at the top of atmosphere (TOA) is a function of the land surface and the atmosphere contributions:

$$T_B^{TOA} = T_{UP} + \frac{1}{L_a}(T_{SE} + T_{SS}),\tag{2.18}$$

where $T_{UP}(\theta, \phi)$ is the self-emitted atmospheric upward brigthness temperature, L_a represents the atenuation of the atmosphere, $T_{SE}(\theta, \phi)$ corresponds to the brightness temperature self-emitted by the Earth's surface, and $T_{SS}(\theta, \phi)$ is the downward-emitted atmospheric brightness temperature $T_{DN}(\theta, \phi)$ reflected (scattered by the Earth's surface) in the direction of the antenna.
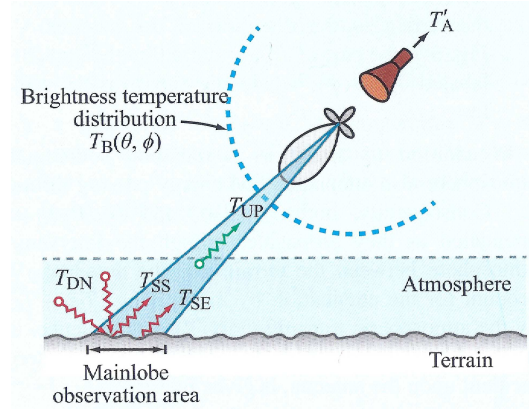
FIGURE 2.3: Radiation incident on an Earth-looking radiometer, from Ulaby & Long [2014].

2.1.7 Faraday rotation

The ionosphere, the part of the atmosphere placed at ~60–1000 km above the Earth's surface, consists of an ionized gas containing free electrons and positively charged ions. When propagating through the ionosphere, a radio wave with a certain polarization suffers a gradual rotation effect of its polarization plane, which is known as Faraday rotation. It depends on the wave frequency, its direction of propagation relative to the direction of the Earth's magnetic field, and the state of the ionosphere (free electron density profile). Faraday rotation affects the Earth observation systems above 60 km. For frequencies in the range $0.5 \leq f \leq 3$ GHz, as the case of the L-band, the Faraday rotation angle φ_F [rad] can be estimated as [ITU-RP.531-12, 2013]:

$$\varphi_F = 2.36 \cdot 10^{-14} \frac{B_{av} N_{TEC}}{f^2},\tag{2.19}$$

where B_{av} is the average Earth's magnetic field [Wb·m^{-2}] or [Teslas] along the propagation path, N_{TEC} [electrons·m^{-2}] stands for the total electron content (TEC) for a vertical column through the entire ionosphere, and f [GHz] is the frequency.

A typical averaged value of φ_F as a function of TEC and frequency is displayed in Fig. 2.4. TEC has significant temporal variations between day and night, and also varies with season and latitude. Assuming low latitudes, the Faraday rotation angle at L-band can be as low as 4° (TEC=10^{16} electrons·m^{-2}) at night, and as high as 30° (TEC=10^{18} electrons·m^{-2}) at noon. This

rotation angle also exhibits large fluctuation and may result in brightness temperature errors, producing inaccuracies in the geophysical parameters retrieved at the surface. An average value of φ_F at a given frequency can be predicted using polarimetric radiometers and compensated for [Yueh, 2000].

Faraday rotation as a function of TEC and frequency
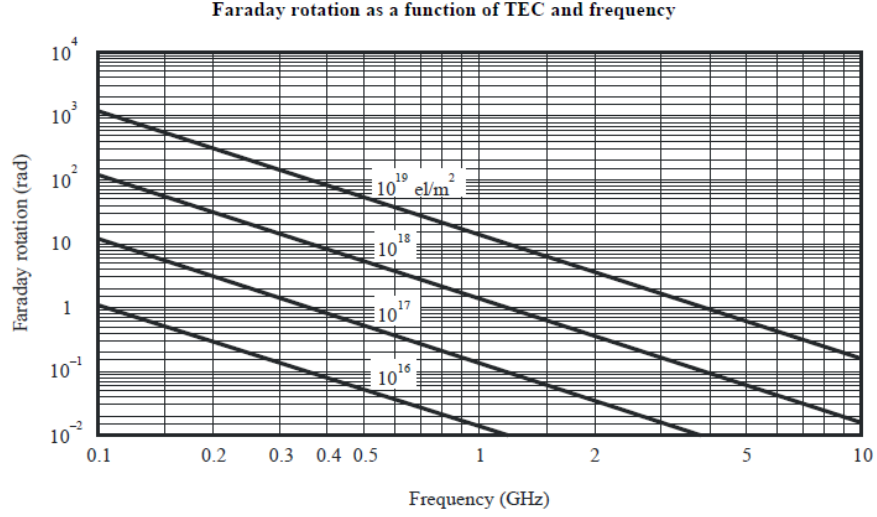
FIGURE 2.4: Typical averaged values of Faraday rotation angle [rad] as a function of TEC and frequency [ITU-RP.531-12, 2013].

The following expressions relate the brightness temperatures at TOA with the brightness temperatures at the antenna [Ulaby & Long, 2014]:

$$
\begin{aligned}
T_{B_H}^{TOA} &= \frac{1}{\cos^2(\varphi)-\sin^2(\varphi)}\left(\cos^2(\varphi)T_{B_X}^{ANT} - \sin^2(\varphi)T_{B_Y}^{ANT}\right), \\
T_{B_V}^{TOA} &= \frac{1}{\cos^2(\varphi)-\sin^2(\varphi)}\left(-\sin^2(\varphi)T_{B_X}^{ANT} + \cos^2(\varphi)T_{B_Y}^{ANT}\right),
\end{aligned}
\tag{2.20}
$$

where the rotation angle $\varphi = \varphi_G + \varphi_F$ is the sum of the geometric polarization angle of the antenna φ_G and the Faraday rotation angle due the ionosphere φ_F, $T_{B_X}^{ANT}$ and $T_{B_Y}^{ANT}$ are measured at the antenna plane according to X and Y-axis, and $T_{B_H}^{TOA}$ and $T_{B_V}^{TOA}$ correspond to the T_B at TOA for horizontal (H-pol) and vertical (V-pol) polarizations, respectively, as illustrated in Fig. 2.5.
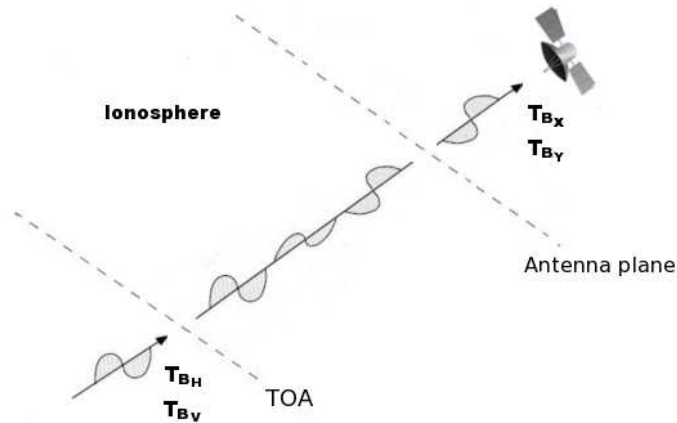
FIGURE 2.5: Faraday rotation effect of a polarized wave propagating through the ionosphere.

2.1.8 Space radiation

The measured antenna temperature contains the signal directly coming from the Earth's surface, but also includes different space radiations, such as the cosmic background, the galactic, the solar, and the lunar components. These contributions are direcly received by the antenna and also indirectly via Earth reflection and scattering. All possible radiation sources detected by the antenna are shown in Fig. 2.6.

- Direct Earth radiation: it is the brightness temperature of the Earth's surface entering into the main lobe of the antenna, also taking into account the contributions coming from the atmosphere (see Subsection 2.1.6).

- Sky radiation: it is a small amount of energy that includes the cosmic background, which is a residual from the origin of the universe in the Big Bang and has a constant value of ~2.7 K, and the direct galactic radiation from its own galaxy, the Milky Way, with a very small contribution (~0.3–0.9 K).

- Direct solar radiation: since the Sun is a localized source, its radiation is estimated considering the satellite orbit position and the time of the year and removed [Camps *et al.*, 2004, Le Vine *et al.*, 2005].

- Direct lunar radiation: it is completely negligible because this radiation is a factor of 10^{-4} lower than the solar radiation.

- Reflected galactic radiation: it is of ~2–10 K at L-band and can either be avoided by selecting a convenient orbit or corrected through the use of existing galactic noise maps [Tenerelli *et al.*, 2008].

- Reflected solar radiation: it is an important noise source that comes from the specular reflection of sunlight in a location on the Earth far away from the observation point, and enters into the antenna [Camps *et al.*, 2004, Le Vine *et al.*, 2005].

- Reflected lunar radiation: it occurs at each month when the moonlight reflected off the surface enters into the antenna lobes ($\leq$1 K).
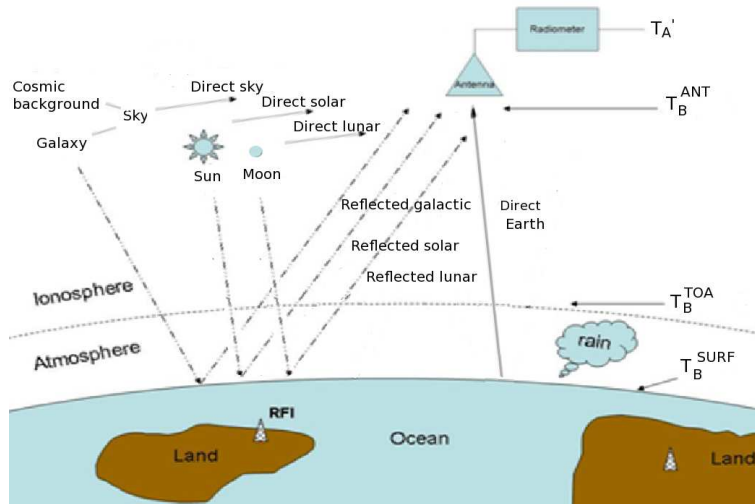
FIGURE 2.6: General scenario displaying all possible radiation sources detected by the antenna of a radiometer on-board a satellite.

2.1.9 Stokes parameters

The polarization of an electromagnetic wave can be completely described by the four Stokes parameters S_0, S_1, S_2, and S_3. The first Stokes parameter (S_0) describes the total intensity of the electromagnetic emission. The second Stokes parameter (S_1) is the difference between the intensity in two orthogonal directions at a given polarization frame, i.e., at V-pol and H-pol. The third (S_2) and fourth (S_3) Stokes parameters represent the real and the imaginary parts (denoted by $\Re$ and $\Im$) of the cross-correlation (denoted by $\langle \cdot \rangle$) between these orthogonal polarizations, respectively:

$$
\begin{aligned}
S_0 &= \tfrac{1}{\eta_0} \left(\langle |E_V|^2 \rangle + \langle |E_H|^2 \rangle \right), \\[6pt]
S_1 &= \tfrac{1}{\eta_0} \left(\langle |E_V|^2 \rangle - \langle |E_H|^2 \rangle \right), \\[6pt]
S_2 &= \tfrac{1}{\eta_0} \left(2\Re \langle E_V E_H^* \rangle \right), \\[6pt]
S_3 &= \tfrac{1}{\eta_0} \left(2\Im \langle E_V E_H^* \rangle \right),
\end{aligned}
\tag{2.21}
$$

where E_V and E_H are the electric field components at H-pol and V-pol, respectively, the asterisk as superscript (*) denotes complex conjugation, and $\eta_0 = 120\pi$ [Ω] is the intrinsic impedance of free space.

In polarimetric radiometry it is common to use the Stokes parameters in terms of brightness temperatures, as follows:

$$
\begin{aligned}
I &= T_{B_V} + T_{B_H} = \tfrac{\lambda^2}{k_B \Delta f} S_0, \\[6pt]
Q &= T_{B_V} - T_{B_H} = \tfrac{\lambda^2}{k_B \Delta f} S_1, \\[6pt]
U &= T_{B_{+45°}} - T_{B_{-45°}} = \tfrac{\lambda^2}{k_B \Delta f} S_2, \\[6pt]
V &= T_{B_{LHC}} - T_{B_{RHC}} = \tfrac{\lambda^2}{k_B \Delta f} S_3.
\end{aligned}
\tag{2.22}
$$

The scale factor $\frac{\lambda^2}{k_B \Delta f}$ relates the electric field [V·m^{-1}] to the brightess temperature [K], being λ the wavelenght, k_B the Boltzmann's constant, and Δf the radiometer bandwidth. The polarization of the corresponding brightness temperature is denoted by the subscrip: V-pol, H-pol, slant linear at +45°and at -45°, left-hand and right-hand circular. Note that the first and fourth Stokes parameters are invariant to rotations, whereas the second and third Stokes parameters are not.

The energy emitted by the Earth's surface is partly polarized, meaning that the vertical differs from the horizontal brightness temperature ($T_{B_V} \neq T_{B_H}$, except at nadir where $T_{B_V} = T_{B_H}$). Dual-polarized radiometers only measure the horizontal and vertical T_B related to the first and second Stokes parameters; full-polarized radiometers measure all the four Stokes parameters. A commonly used parameter related to T_{B_H} and T_{B_V} is the microwave polarization difference index (MPDI). It can be estimated as [Owe *et al.*, 2001]:

$$
MPDI = \frac{T_{B_V} - T_{B_H}}{T_{B_V} + T_{B_H}}.
\tag{2.23}
$$

The third and fourth Stokes parameters can be measured direct or indirectly by either coherent or incoherent detection [Ishimaru, 1991]. In general, the third Stokes parameter is used for estimating the Faraday rotation [Yueh, 2000]. A Faraday rotation correction is applied to the radiometers of the three L-band missions [Corbella *et al.*, 2015, Le Vine *et al.*, 2013, 2015]. In the case of remote sensing of oceans, information about wind direction is contained in the third and fourth Stokes parameters [Yueh *et al.*, 1995]. They have also been used to observe geophysical variations in structures over Greenland and the Antarctic ice sheets [Li *et al.*, 2008].

2.2 Passive remote sensing over continental ice

The cryosphere includes those portions of the Earth's surface where water is in solid form, including sea ice, lake ice, river ice, snow cover, glaciers, ice caps, ice sheets, permafrost, and frozen ground.

2.2.1 Penetration depth over ice

The penetration of microwave radiation decreases with increasing losses due to scattering and absorption, and thus increases as frequency decreases. For any material with $\frac{\varepsilon'}{\varepsilon''} < 0.01$, as it occurs in the case of the ice, the penetration depth is defined by [Ulaby & Long, 2014]:

$$\delta_p = \frac{\lambda\sqrt{\varepsilon'}}{2\pi\varepsilon''},\tag{2.24}$$

where λ corresponds to the electromagnetic wavelength.

2.2.2 Dielectric constant of pure ice

In the microwave region, the permittivity of pure ice ($\varepsilon'_{pi} \sim 3.15$) is nearly independent of frequency from 10 MHz to 300 GHz [Matzler & Wegmuller, 1987], and only exhibits a very small dependence on temperature (233.15 K $\leq T_{ph} \leq$ 273.15 K), on the form:

$$\varepsilon'_{pi} = 3.1884 + 9.1 \cdot 10^{-4}(T_{ph} - 273.15),\tag{2.25}$$

where T_{ph} is the ice physical temperature [K] and the subscript pi denotes pure ice.

By contrast, the loss factor of pure ice (ε''_{pi}) has a strong dependence with both frequency and physical temperature. Also, at L-band, ε''_{pi} is a very low magnitude ($\sim 10^{-5}$), which is difficult to estimate accurately. The loss factor model of pure ice from 0.1 MHz to 1 THz was proposed by Hufford [1991]. Later, it was adjusted by Matzler *et al.* [2006]. In this model, ϵ''_{pi} decreases with increasing frequency, with a minimum around 1 GHz, and then monotonically increases with frequency:

$$\varepsilon''_{pi} = \frac{\alpha_{pi}}{f} + \beta_{pi}f,\tag{2.26}$$

where f corresponds to the frequency [GHz]. The coefficients α_{pi} [GHz] and β_{pi} [GHz^{-1}] are given by semi-empirical expressions:

$$\begin{aligned}
\alpha_{pi} &= 0.00504 + 0.0062\left(\frac{300}{T_{ph}} - 1\right)e^{-22.1\left(\frac{300}{T_{ph}}-1\right)},\\
\beta_{pi} &= \frac{0.0207}{T_{ph}}\frac{e^{\frac{335}{T_{ph}}}}{\left(e^{\frac{335}{T_{ph}}}-1\right)^2} + 1.16\cdot 10^{-11}f^2 + e^{-9.963+0.0372(T_{ph}-273.15)}.
\end{aligned}\tag{2.27}$$

A comparison of two curves corresponding to the loss factor model of pure ice at two temperatures (258 K with black single line and 196 K with black double line) and several experimental measurements (depicted by markers) are shown in Fig. 2.7. In general, a good agreement can be observed between the model and experimental results, except for observations between 5–10 GHz at very low temperatures (190 K), which are lower than those predicted by the model [Matsouka *et al.*, 1996]. In addition, there are not direct measurements in 0.5–3 GHz. This suggests a lack of validation at these frequencies.
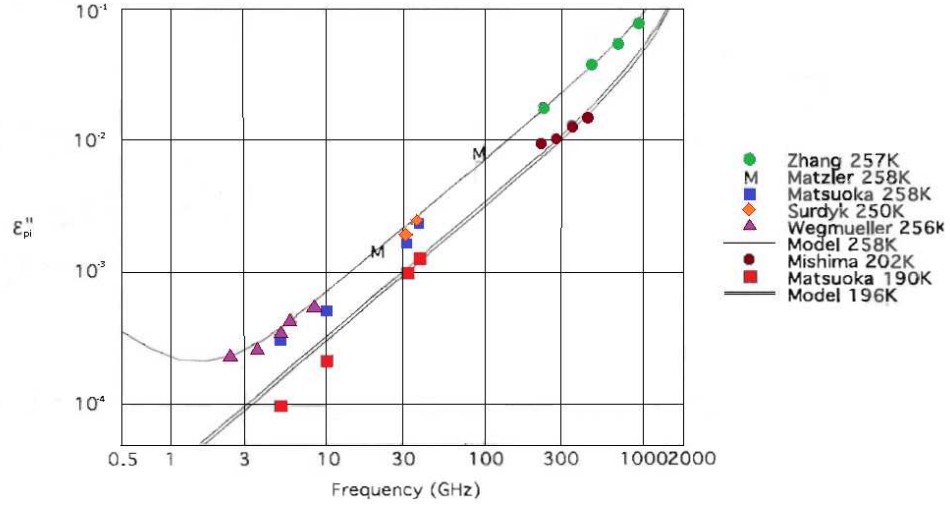
FIGURE 2.7: Comparison of loss factor model of pure ice (ε_{pi}'') at two different temperatures (258 K with black single line and 196 K with black double line) and experimental measurements (depicted by markers) *vs.* frequency. Reference to measurement is given by the name of first author and temperature. Adapted from Matzler *et al.* [2006].

2.2.3 Dielectric constant of the icepack

The equivalent dielectric constant of a heterogeneous material (mixture) consisting of two or more substances is related to the dielectric constant of the individual substances, their volume fractions, and their spatial distributions. A general formulation can be used to account for first-order inclusion interactions [Tinga *et al.*, 1973]. The Antarctic ice sheet is composed of a mixture of ice and air, called snowpack or icepack. Since the icepack is typically granular, the ice-air mixture model for spherical inclusions can be considered [Sihvola & Kong, 1988] to derive its equivalent dielectric constant (ε_i) as follows:

$$\varepsilon_i = \varepsilon_{pi} + \frac{3f_v\left(\varepsilon_a - \varepsilon_{pi}\right)\varepsilon_{pi}/\left(\varepsilon_a + 2\varepsilon_{pi}\right)}{1 - f_v\left(\varepsilon_a - \varepsilon_{pi}\right)/\left(\varepsilon_a + 2\varepsilon_{pi}\right)}, \tag{2.28}$$

where the subscript i denotes icepack, ε_{pi} is the dielectric constant of pure ice, $\varepsilon_a=1$ is the dielectric constant of air (the subscript a denotes air), and f_v stands for the relative volume of air, which can be calculated from the density of the ice with respect to the density of pure ice ($f_v = 1 - \rho/\rho_{pi}$).

2.2.4 Ice density

The icepack model takes into account that the density of the Antarctic ice sheet increases exponentially with depth, from 379 kg·m^{-3} at the surface, which corresponds to fresh snow, until 918 kg·m^{-3}, which corresponds to the density of pure ice (ρ_{pi}). The ice density profile can be therefore expressed as [Rist *et al.*, 2002]:

$$\rho(z) = 918 - 539e^{-(z/32.5)}, \tag{2.29}$$

where z is the depth [m] below the upper surface, generally defined as a positive value.

2.2.5 Internal ice temperature

The internal ice sheet temperature is an important factor to determine the ice sheet mass balance and dynamics [Rignot *et al.*, 2011]. Internal ice tempereatures are provided from the small

number of boreholes in which physical temperatures are direcly measured [Ritz, 1988, Price *et al.*, 2002]. In addition, a modeled physical temperature profile, which assumes a planar stratified medium with homogeneous thermal paramaters, is given as [Jezek *et al.*, 2015]:

$$T_{ph}(z) = T_{isurf} - \frac{G\sqrt{\pi}}{2k_c\sqrt{\frac{M}{2k_dH}}} \left[erf\left((H-z)\sqrt{\frac{M}{2k_dH}}\right) - erf\left(H\sqrt{\frac{M}{2k_dH}}\right) \right]. \qquad (2.30)$$

Here, erf is the error function, T_{isurf} is the ice surface temperature [K], G is the geothermal heat flux [W·m^{-2}], k_c is the ice thermal conductivity [W·m^{-1}·K^{-1}], k_d is the ice thermal diffusivity [m^2·year^{-1}], H stands for the ice thickness [m], M is the snow accumulation rate [m·year^{-1}], and z corresponds to the depth [m].

2.2.6 Ice grain size

The ice grain size is related to the correlation length. Its continuous profile can be estimated using the parametrization proposed by Zwally [1977]:

$$a(z) = \sqrt[3]{0.0377 + 0.00472z}, \qquad (2.31)$$

being z the depth [m] and a is the ice particle radius [mm].

2.2.7 Coherent and incoherent emissivity

The configuration of a two-layer structure, consisting of a top medium of air with ε_1=1, a dielectric medium of thickness d and dielectric constant ε_2, located above a homogeneuos medium of dielectric contant ε_3, is shown in Fig. 2.8. The upper and lower boundaries are electromagnetically flat and the three media are in thermodynamic equilibrium (at the same physical temperature). It is considered that the emission source contributes towards the total emission into the top medium along direction θ_1. The electric field of this emission source contains an infinite number of contributions, all interrelated by specific phase relationships, which are associated with the propagation delay between the two boundaries and the phase angles of reflection coefficients.
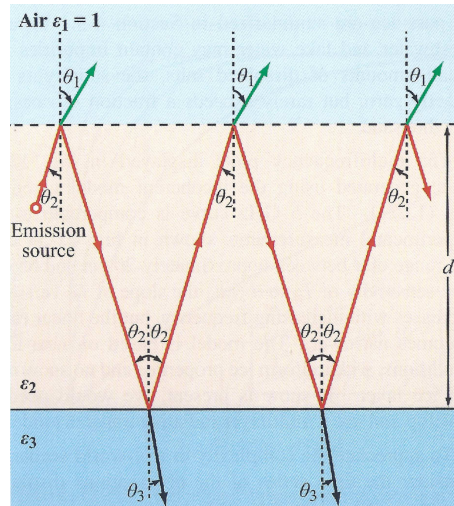
FIGURE 2.8: Configuration of a two-layer structure: air, dielectric medium and homogeneous medium [Ulaby & Long, 2014].

If the spatial scale of variations of the middle medium is much smaller than λ, the middle medium is equivalent to an homogeneous medium. In this case, the coherent emissivity at polarization p (H-pol and V-pol) can be expressed as:

$$e_{p,coh} = 1 - \Gamma_p = 1 - |\varrho_p|^2, \tag{2.32}$$

where Γ_p is the reflectivity and ϱ_p is the reflection coefficient at polarization p (H-pol and V-pol) given by:

$$\varrho_p = \frac{\varrho_{p,12} + \varrho_{p,23}e^{-2\gamma_2 d \cos(\theta_2)}}{1 + \varrho_{p,12}\varrho_{p,23}e^{-2\gamma_2 d \cos(\theta_2)}}. \tag{2.33}$$

Hence, $\varrho_{p,12}$ is the reflection coefficient for incidence in medium 1 onto medium 2 at angle θ_1, and $\varrho_{p,23}$ corresponds to the reflection coefficient for incidence in medium 2 onto the boundary of medium 3 at angle θ_2. Angles θ_1, θ_2 and θ_3 are related by the Snell's law, and γ_2 is the propagation constant of the middle medium ($\gamma = \alpha + j\beta$, being α the attenuation constant and β the phase constant).

If the middle medium has randomly distributed inhomogeneities whose dimensions are larger than $\lambda/100$, the phase relationships among the multiply-reflected contributions are no longer preserved. In this case, the incoherent emissivity at polarization p (H-pol or V-pol) is expressed as:

$$e_{p,inc} = \left(\frac{1 - \Gamma_{p,12}}{1 - \Gamma_{p,12}\Gamma_{p,23}\Upsilon^2}\right)[(1 + \Gamma_{p,23}\Upsilon)(1-\omega)(1-\Upsilon) + (1 - \Gamma_{p,23})\Upsilon], \tag{2.34}$$

where ω is the single scattering albedo of the middle layer, and $\Upsilon = e^{-k_e d/\cos(\theta_2)}$, being k_e the extinction rate [Np·m^{-1}] through layer.

If the random inhomogeneities in the middle medium are enough to destroy the phase coherence between multiple reflections, and simultaneously $\omega << 1$, the incoherent emissivity simplifies to:

$$e_{p,inc} = \left(\frac{1 - \Gamma_{p,12}}{1 - \Gamma_{p,12}\Gamma_{p,23}\Upsilon^2}\right)(1 - \Gamma_{p,23}\Upsilon^2). \tag{2.35}$$

Plots of both the coherent (blue line) and incoherent (red line) emissivities as a function of d are shown in Fig. 2.9 for a layer of ice over water at 1 GHz and normal incidence angle. The two emissivities have the same trend, but the coherent emissivity also displays an oscillatory behaviour, which manifest the constructive and destructive inferference associated with coherent addition of multiply-reflected contributions.
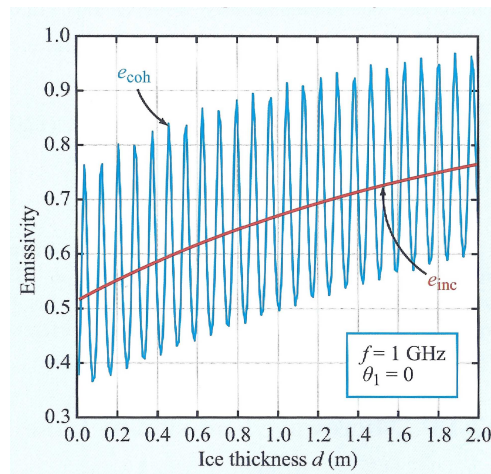
FIGURE 2.9: Coherent (e_{coh}, blue line) and incoherent (e_{inc}, red line) emissivities as a function of thickness d for a layer of ice over water [Ulaby & Long, 2014].

2.2.8 Ice emissivity models

Several models have been proposed to estimate microwave emission from an iced-covered surface. The radiative transfer theory is widely used to express the propagation of the energy flux through the icepack, which is represented as a stack of horizontal layers with homogeneous scattering and absorption coefficients. The different models using this theory, including the Helsinky University of Technology (HUT/TKK) snow emission model [Pulliainen *et al.*, 1999], the microwave emission model of layered snow-packs (MEMLS) [Wiesmann & Matzler, 1999], and the dense-medium radiative theory model based on quasicrystalline approximation (DMRT-QCA) [Tsang *et al.*, 2000], mainly differ in the relationship used to link the ice properties to the scattering and absorption coefficients. However, the interference phenomenon is ignored in all of these models and only the propagation of the incoherent wave is explicitly considered.

Interferences within the ice layers are particularly important when the thickness of the layer is on the order of or less than the wavelenght. This effect is more pronounced at L-band, where $\lambda \approx 21.2$ cm, than at higher frequencies. In order to account for the interference phenomenon, an alternative to the radiative transfer theory is to compute the emission and propagation of the waves, instead of the energy flux. This alternative, often called as coherent approach, is derived from Maxwell's equations; it requires considerable simplification of the medium description to be computationally realistic.

The multi-layer snow-pack dense media radiative transfer (DMRT-ML) model [Picard *et al.*, 2013] was also developed using a medium composed of several layers, where each of them are characterized by its thickness, temperature, density, grain size, stikiness parameter, and liquid water content. Additionally, this model includes the possibility of selecting the emissivity type (incoherent or coherent). The incoherent emissivity is primarily designed for microwave frequencies higher than L-band. The coherent emissivity is based on the coherent approach derived by [West *et al.*, 1996]. In this case, each layer is only characterized by its thickness, temperature and density. The most important simplification is to neglect the scattering of snow grain. This assumption is invalid at high frequencies. Nevertheless, at low microwave frequencies (<10 GHz), since the wavelength is several orders of magnitude larger than the grain size, scattering by grains is insignificant in comparison with the absorption and scattering caused by reflections at the interfaces between layers.

2.3   Passive remote sensing over land

In the microwave region, the dielectric constant of most natural materials is dominated by its water content. According to this, passive L-band radiometers are based on the large contrast between the dielectric properties of dry soil ($\varepsilon \sim 4$) and water ($\varepsilon \sim 80$). This contrast results in a broad range of dielectric values for soil–water mixtures ($\varepsilon_s \approx 4$–40, the subscript s denotes soil–water mixture), which is the primary influence on the natural microwave emission from the soil [Schmugge *et al.*, 1974, 1986].

A soil medium is a mixture of soil particles, air pockets, and liquid water. Usually, the water contained in the soil is divided in two fractions: bound water and free water. Bound water is the water contained in the first molecular layers surrounding the soil particles, i.e., the water absorbed by the soil surface due to the influence of matric and osmotic forces. Free water refers to the liquid water molecules located in the pore spaces, which are able to move within the soil medium. The amount of water contained in the soil is directly proportional to the total surface area of the soil particles contained in a unit volume. The total surface area is, in turn, a function of the size distribution and minerology of the particles.

2.3.1   Porosity and soil texture

The porosity of a soil determines the total volume occupied by pores per unit volume of soil. It is affected by soil texture, structure, compaction, and organic matter content. The porosity (P_s) can be defined as [Weil & Brady, 2016]:

$$P_s = 1 - \frac{\rho_b}{\rho_{sm}}, \tag{2.36}$$

where ρ_b is the bulk density of the dry soil [g/cm^3] and ρ_{sm} corresponds to the density of the associated solid material [g/cm^3].

Soils are classified as sand, silt, or clay, according to its particle-size distribution as shown in Fig. 2.10 (left). This classification determines the soil texture [Birkeland, 1974]. In addition, the soil textural triangle, displayed in Fig. 2.10 (right), is widely used to visualize the soil texture. Soils with small pores (clay) will hold more water per unit volume than soils with large pores (sand). While pore spaces of dry soils are mostly filled with air, pore spaces of wet soils are filled with water. Processes such as infiltration, ground-water movement and storage occur in these void spaces.
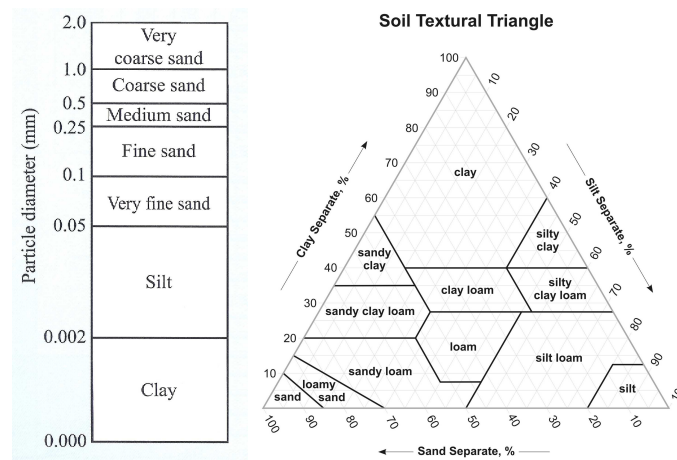
FIGURE 2.10: Particle-size classes (left) and soil texture classification triangle (right) of the U.S. Department of Agriculture (USDA).

2.3.2 Gravimetric and volumetric soil moisture

The soil moisture, or water in a soil, is expressed as a ratio, which can range from 0 (completely dry) to ∼0.6 (the value of porosity of the materials at saturation). The two terms commonly used to characterize the moisture content of a soil sample are gravimetric moisture and volumetric moisture.

Gravimetric soil moisture is defined as the mass of water per unit mass of dry soil. It can be calculated from the wet (W_{wet}) and dry (W_{dry}) weights of a soil sample, as:

$$m_g = \frac{W_{wet} - W_{dry}}{W_{dry}} = \frac{W_{water}}{W_{dry}}, \tag{2.37}$$

where W_{water} corresponds to the weight of the water in the soil sample.

Volumetric soil moisture is defined as the volume of water per unit volume of soil. It is determined from the volume of water (Vol_{water}) and the total volume (Vol_T), as:

$$m_v = \frac{Vol_{water}}{Vol_T} = \frac{Vol_{water}}{Vol_{dry}} = \frac{W_{water}/\rho_{water}}{W_{dry}/\rho_b} = \frac{W_{water}}{W_{dry}/\rho_b} = m_g \rho_b, \tag{2.38}$$

where the total volume includes the volumes of air, soil and water and is equal to the volume of the dry sample (assuming that when water is added to the sample, it fills air pockets, but does not increase the total volume), ρ_{water}=1 g/cm^3 is the density of water, and ρ_b is the bulk density of the dry soil. Although the ratio is unitless, it is often expressed in m^3/m^3, cm^3/cm^3 or g/cm^3.

Since precipitation, evapotranspiration and other water-related variables are commonly expressed in terms of flux, volumetric expressions for water content are often preferred in environmental studies. Furthermore, the *in situ* soil moisture observations used to validate remote sensing observations are generally acquired using dielectric probes, which directly provide volumetric measurements.

2.3.3 Penetration depth over land

The penetration depth over land, defined as the soil depth from above which 63 % (1-1/e) of the radiation emitted by the surface originates, is estimated using Eq. (2.24). The water content has an impact on the soil penetration depth through its relationship to the real and imaginary parts of the soil dielectric constant.

The penetration depth of microwaves rapidly decreases with increasing soil wetness. For a wavelength of 21.2 cm (L-band), it varies from approximately 75 cm for a dry soil (ε'_s=5 and ε''_s=0.1) to about 3.7 cm for a wet soil (ε'_s=30 and ε''_s=5). Knowledge of the penetration depth is important because it is an indicator of the thickness of the surface layer within which variations in moisture and temperature can significantly affect the emitted radiation. Consequently, the soil moisture measured using L-band passive radiometry is approximately in the top 5 cm of the soil [Ulaby & Long, 2014].

2.3.4 Field capacity and wilting point

The field capacity (FC) and wilting point (WP) are, among other hydrological parameters, involved in the soil dielectric constant. The FC is defined as the amount of soil moisture held in a soil after excess water has drained out. Physically, it is the water retained in a soil at a tension of 1/3 bar. Rawls *et al.* [1982] proposed an expression to estimate the FC of a soil from texture and organic matter content as:

$$FC = 0.2576 - 0.002 \cdot S + 0.0036 \cdot C + 0.0299 \cdot M_{org}, \tag{2.39}$$

where S and C correspond to the sand and clay contents [%] of dry soil, and M_{org} corresponds to the organic matter content [%].

The WP is defined as the level of soil moisture below which plants wilt. It is usually taken as the soil moisture at a tension of 25 bar. The WP can be estimated as [Rawls *et al.*, 1982]:

$$WP = 0.26 + 0.005 \cdot C + 0.0158 \cdot M_{org}. \tag{2.40}$$

The difference between FC and WP is the plant available water (PAW) content, defined as amount of water that can be stored in the soil and be available for plant growth.

2.3.5 Dielectric constant of soils

In the past few decades, several soil dielectric models were developed by the passive microwave remote sensing community [Birchak *et al.*, 1974, Wang & Schmugge, 1980, Dobson *et al.*, 1985, Hallikainen *et al.*, 1985, Roth *et al.*, 1990, Peplinski *et al.*, 1995a,b, Mironov *et al.*, 2009]. Although they differ in analytical forms, they generally share common dependence on soil moisture, soil texture, and frequency. In a heterogeneous medium such as the soil, the complex dielectric constant is a function of frequency, physical temperature, salinity, total volumetric water content, and relative fractions of bound and free water, which are, in turn, related to the texture, bulk soil density, shape of the soil particles, and shape of the water inclusions.
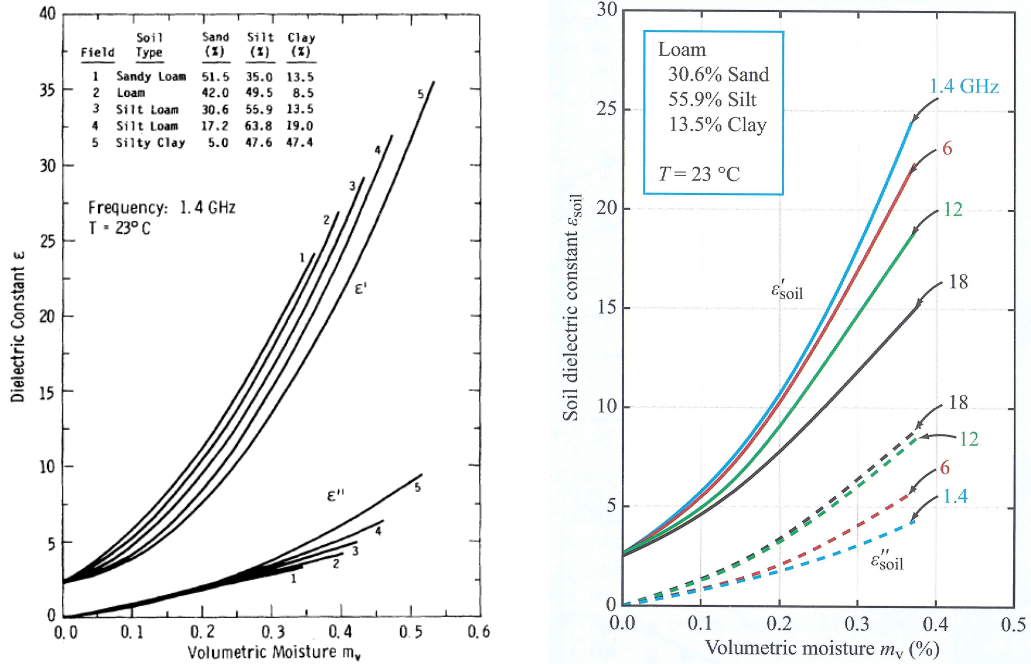
FIGURE 2.11: Soil dielectric constant as a function of volumetric soil moisture for five soil types at 1.4 Ghz and 23°C (left), and dielectric constant as a function of volumetric soil moisture for a silt loam soil at four microwave frequencies. Adapted from Hallikainen *et al.* [1985].

The measured soil dielectric constant as a function of the volumetric soil moisture is shown in Fig. 2.11 (left) for a variety of soil types at a frequency of 1.4 GHz and a temperature of 23°C. The dependence on soil type is due to the different percentages of water bound to the particle surfaces in the different soils. It is evident that clay soils hold greater percentages of bound water

and, therefore, have a lower dielectric constant than sandy or silty soils at the same moisture content. Also, the relationship between dielectric constant and volumetric soil moisture is almost linear, except at low moisture contents [De Jeu *et al.*, 2008]. Similar responses were measured at higher frequencies, such as 6, 12 and 18 GHz. The role of frequency for one of the soil types (field sample 3: silt loam) at 23°C is shown in Fig. 2.11 (right). It is observed that, increasing frequency from 1.4 to 18 GHz, ε_s' decreases whereas ε_s'' increases.

The dielectric constant of dry soils is almost independent of temperature. In wet soils, the dielectric constant is only weakly dependent on temperature, and for the range of temperatures encountered in nature this dependence may be ignored. Nevertheless, frozen soils have much lower dielectric constants than unfrozen soils, as the contained water is no longer in liquid phase. The measured permitivity and loss factor of a silt loam soil is shown in Fig. 2.12 for different temperatures over a wide frequency range extending from 3 GHz to 37 GHz. Above 0°C, the soil permittivity (ε_s', left) and loss factor (ε_s'', right) are weakly independent on physical temperature. However, as soil temperature crosses the frozen temperature of water, both ε_s' and ε_s'' values suffer a notable change. This feature has led to studies of microwave radiometry for detecting areas of permafrost and freeze-thaw boundaries in soils [England, 1990].
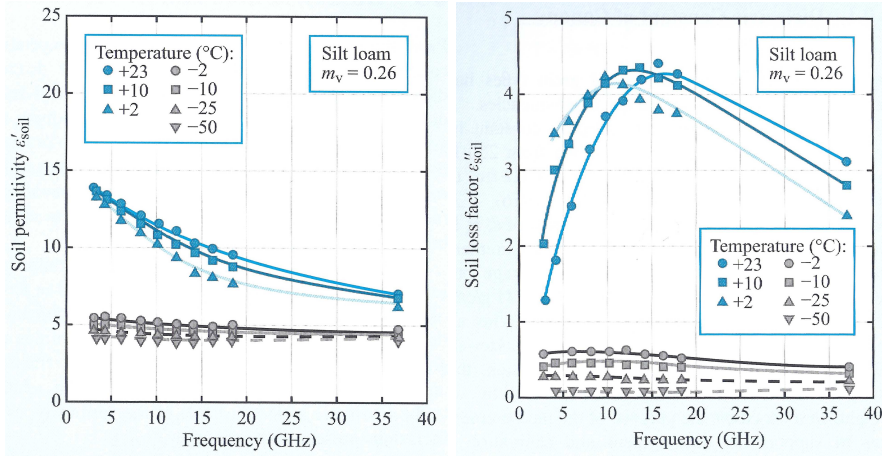
FIGURE 2.12: Measured permitivity (left) and loss factor (right) of a silt loam soil as a function of frequency with temperature as a parameter. Adapted from Hallikainen *et al.* [1984].

In L-band passive remote sensing, there are three soil dielectric constant models commonly used: i) Wang and Schmugge [Wang & Schmugge, 1980], ii) Dobson [Dobson *et al.*, 1985], and iii) Mironov [Mironov *et al.*, 2009]. In the first and the second models, the starting point is the four component mixing model consisting of solid material, air, free water, and bound water as [Birchak *et al.*, 1974]:

$$\varepsilon_s^{\alpha_1} = Vol_{sm}\varepsilon_{sm}^{\alpha_1} + Vol_a\varepsilon_a^{\alpha_1} + Vol_{fw}\varepsilon_{fw}^{\alpha_1} + Vol_{bw}\varepsilon_{bw}^{\alpha_1}, \tag{2.41}$$

where Vol_{sm} (ε_{sm}), Vol_a (ε_a), Vol_{fw} (ε_{fw}) and Vol_{bw} (ε_{bw}) are the volume fraction (or dielectric constant) of solid material, air, free water and bound water in the soil, respectively, and the α_1 is a semi-empirical coefficient.

The expression in Eq. (2.41) can be rewritten as a function of the soil bulk density (ρ_b) and volumetric soil moisture (m_v) as follows:

$$\varepsilon_s^{\alpha_1} = 1 + \frac{\rho_b}{\rho_s}(\varepsilon_{sm}^{\alpha_1} - 1) + Vol_{fw}\varepsilon_{fw}^{\alpha_1} + Vol_{bw}\varepsilon_{bw}^{\alpha_1} - m_v. \tag{2.42}$$

If $\alpha_1 = 0.5$, the model is known as refractive model.

Wang and Schmugge model

The soil dielectric model of Wang and Schmugge was proposed for 1.4 GHz and 5 GHz. It starts from Eq. (2.42) with $\alpha_1=1$. This model provides separate dielectric constant equations for volumetric water content lower than, or greater than the transition moisture (m_t). It is defined as the soil moisture at which the free water phase begins to dominate the soil hydraulics, and is strongly dependent on texture. The transition moisture is determined as [Wang & Schmugge, 1980]:

$$m_t = 0.49 \cdot WP + 0.165. \tag{2.43}$$

where WP is the wilting point.

The soil dielectric constant can be estimated as [Wang & Schmugge, 1980]:

$$\varepsilon_s = \begin{cases} m_v \varepsilon_x + (P_s - m_v)\varepsilon_a + (1 - P_s)\varepsilon_{rock} & \text{if } m_v \leq m_t \\ m_t \varepsilon_x + (m_v - m_t)\varepsilon_{fw} + (P_s - m_v)\varepsilon_a + (1 - P_s)\varepsilon_{rock} & \text{if } m_v > m_t \end{cases}, \tag{2.44}$$

with

$$\varepsilon_x = \begin{cases} \varepsilon_{ice} + (\varepsilon_{fw} - \varepsilon_{ice})\frac{m_v}{m_t}\Psi & \text{if } m_v \leq m_t \\ \varepsilon_{ice} + (\varepsilon_{fw} - \varepsilon_{ice})\Psi & \text{if } m_v > m_t \end{cases}, \tag{2.45}$$

and

$$\Psi = -0.57 \cdot WP + 0.481. \tag{2.46}$$

Here, P_s is the porosity of dry soil, ε_a, ε_{ice}, ε_{fw} and ε_{rock} are the dielectric constant of air, ice, free water and rock, respectively, and ε_x corresponds to the dielectric constant of the initially absorbed water.

Dobson model

The soil dielectric constant of Dobson also starts from Eq. (2.42), but considers that there is not difference between free and bound water, as follows:

$$Vol_{fw}\varepsilon_{fw}^{\alpha_1} + Vol_{bw}\varepsilon_{bw}^{\alpha_1} = m_v^{\beta}\varepsilon_w^{\alpha_1}, \tag{2.47}$$

where the subscript fw indicates free water, bw stands for bound water, and w denotes water.

Taking into account the assumption of Eq. (2.47), the expression for the soil dielectric constant, where the real and imaginary parts were developed, is [Dobson *et al.*, 1985]:

$$\begin{aligned} \varepsilon_s' &= [1 + 0.66\rho_b + m_v^{\beta_1}(\varepsilon_w')^{\alpha_1} - m_v]^{\frac{1}{\alpha_1}}, \\ \varepsilon_s'' &= m_v^{\beta_2}(\varepsilon_w''), \end{aligned} \tag{2.48}$$

where ρ_B is the soil bulk density, m_v is the volumetric moisture content and ε_w is the dielectric constant of water. The exponents α_1, β_1 and β_2 are empirically determined by soil properties, as follows:

$$\begin{aligned} \alpha_1 &= 0.65, \\ \beta_1 &= 1.27 - 0.519 \cdot S - 0.152 \cdot C, \\ \beta_2 &= 2.06 - 0.928 \cdot S - 0.255 \cdot C, \end{aligned} \tag{2.49}$$

where S and C represent the mass fraction of sand and clay, respectively, being $0 \leq S \leq 1$ and $0 \leq C \leq 1$.

The dielectric constant of water (ε_w) is given by the Debye equation for pure water with a modified electrical conductivity term as [Hasted, 1974]:

$$\begin{aligned} \varepsilon_w' &= \varepsilon_{w\infty} + \frac{\varepsilon_{w0} - \varepsilon_{w\infty}}{1 + (2\pi f \tau_w)^2}, \\ \varepsilon_w'' &= \frac{2\pi f \tau_w(\varepsilon_{w0} - \varepsilon_{w\infty})}{1 + (2\pi f \tau_w)^2} + \left(\frac{2.65 - \rho_b}{2.65 m_v}\right)\frac{\sigma_{eff}}{2\pi\varepsilon_0 f}, \end{aligned} \tag{2.50}$$

where ε_{w0} is the static dielectric constant of pure water, $\varepsilon_{w\infty}=4.9$ is the high frequency dielectric constant of pure water [Lane & Saxton, 1952], $\varepsilon_0=8.854\cdot10^{-12}$ [F/m], f is the frequency [Hz], τ_w correspond to the relaxation time of water [s], and σ_{eff} is the effective conductivity [S·m^{-1}], which can be expressed in the range of 0.3–1.5 GHz as [Peplinski *et al.*, 1995a,b]:

$$\sigma_{eff} = 0.0467 + 0.22 \cdot \rho_b - 0.411 \cdot S + 0.661 \cdot C. \tag{2.51}$$

Mironov model

The model of Mironov, which is formally known as the Mineralogy-Based Soil Dielectric Model (MBSDM), takes into account separately the free and bound water. In this model, the soil dielectric constant (ε_s) is expressed as [Mironov *et al.*, 2009]:

$$\begin{aligned} \varepsilon'_s &= n_s{}^2 - \kappa_s{}^2, \\ \varepsilon''_s &= 2n_s\kappa_s, \end{aligned} \tag{2.52}$$

with

$$n_s = \begin{cases} n_d + (n_{bw} - 1)m_v & \text{if } m_v \le m_{vt}, \\ n_d + (n_{bw} - 1)m_v + (n_{fw} - 1)(m_v - m_{vt}) & \text{if } m_v > m_{vt} \end{cases}, \tag{2.53}$$

$$\kappa_s = \begin{cases} \kappa_d + \kappa_{bw}m_v & \text{if } m_v \le m_{vt}, \\ \kappa_d + \kappa_{bw}m_v + \kappa_{fw}(m_v - m_{vt}) & \text{if } m_v > m_{vt} \end{cases}, \tag{2.54}$$

where n_d (κ_d), n_{bw} (κ_{bw}) and n_{fw} (κ_{fw}) are the refracive index (or normalized attenuation coefficient) of dry soil, bound water and free water, and m_{vt} is the value of the maximum bound water fraction of the soil.

The refractive index and normalized attenuation coefficient of dry soil (n_d and κ_d) can be expressed as a function of the clay content C [%] as follows [Mironov *et al.*, 2009]:

$$\begin{aligned} n_d &= 1.634 - 0.539 \cdot 10^{-2} \cdot C + 0.2748 \cdot 10^{-4} \cdot C^2 \\ k_d &= 0.03952 - 0.04038 \cdot 10^{-2}C \end{aligned}. \tag{2.55}$$

The maximum bound water fraction of the soil is estimated as [Mironov *et al.*, 2009]:

$$m_{vt} = 0.02863 + 0.30673 \cdot 10^{-2} \cdot C. \tag{2.56}$$

The values of refractive index and normalized attenuation coefficient for bound and free water (n_{bw}, κ_{bw}, n_{fw} and κ_{fw}) can be written through respective permittivity and loss factor, as follows:

$$\begin{aligned} n_{bw,fw}\sqrt{2} &= \sqrt{\sqrt{(\varepsilon'_{bw,fw})^2 + (\varepsilon''_{bw,fw})^2} + (\varepsilon'_{bw,fw})^2} \\ \kappa_{bw,fw}\sqrt{2} &= \sqrt{\sqrt{(\varepsilon'_{bw,fw})^2 + (\varepsilon''_{bw,fw})^2} - (\varepsilon'_{bw,fw})^2} \end{aligned}, \tag{2.57}$$

where the real and imaginary parts of the dielectric constant of bound and free water are expressed with the Debye equation [Hasted, 1974]:

$$\begin{aligned} \varepsilon'_{bw,fw} &= \varepsilon_{w\infty} + \frac{\varepsilon_{bw0,fw0} - \varepsilon_{w\infty}}{1 + (2\pi f \tau_{bw,fw})^2} \\ \varepsilon''_{bw,fw} &= \frac{2\pi f \tau_{bw,fw}(\varepsilon_{bw0,fw0} - \varepsilon_{w\infty})}{1 + (2\pi f \tau_{bw,fw})^2} + \frac{\sigma_{bw,fw}}{2\pi\varepsilon_0 f} \end{aligned}. \tag{2.58}$$

The expressions for the static dielectric constant, relaxation time and effective conductivity, depending on soil clay content, are given by [Mironov *et al.*, 2009]:

$$\begin{aligned}
\varepsilon_{bw0} &= 79.8 - 85.4 \cdot 10^{-2} \cdot C + 32.7 \cdot 10^{-4} \cdot C^2 \\
\tau_{bw} &= 1.062 \cdot 10^{-11} + 3.45 \cdot 10^{-14} \cdot C \\
\sigma_{bw} &= 0.312 + 0.467 \cdot 10^{-2} \cdot C
\end{aligned} \tag{2.59}$$

and

$$\begin{aligned}
\varepsilon_{fw0} &= 100 \\
\tau_{fw} &= 8.5 \cdot 10^{-12} \\
\sigma_{fw} &= 0.3631 + 1.217 \cdot 10^{-2} \cdot C
\end{aligned} \tag{2.60}$$

The impact of using Dobson or Mironov models was studied in SMOS [Mialon *et al.*, 2015] and SMAP [Srivastava *et al.*, 2015a]. Nowadays, the soil dielectric constant is estimated with the Mironov model in both missions. The advantages of Mironov model are that can be applied to a wide range of soil types and it only requires the clay percentage as input parameter.

2.3.6 Soil surface emissivity

The general case of a single interface between two media is considered. Medium 1 is located at the top and medium 2 at the bottom. From Snell's law, an incident wave is partially transmitted from medium 2 with a relative dielectric constant ε_2 at angle θ_2 into medium 1 with ε_1 at angle θ_1 such that:

$$\sqrt{\varepsilon_1} \sin(\theta_1) = \sqrt{\varepsilon_2} \sin(\theta_2). \tag{2.61}$$

Fresnel equations describe the behaviour of an electromagnetic wave at the specular boundary of the interface, obtaining the reflectivity at H-pol and V-pol as:

$$\begin{aligned}
\Gamma_{12,H,\theta_1} &= \left| \frac{\sqrt{\varepsilon_1} \cos(\theta_1) - \sqrt{\varepsilon_2} \cos(\theta_2)}{\sqrt{\varepsilon_1} \cos(\theta_1) + \sqrt{\varepsilon_2} \cos(\theta_2)} \right|^2, \\
\Gamma_{12,V,\theta_1} &= \left| \frac{\sqrt{\varepsilon_1} \cos(\theta_2) - \sqrt{\varepsilon_2} \cos(\theta_1)}{\sqrt{\varepsilon_1} \cos(\theta_2) + \sqrt{\varepsilon_2} \cos(\theta_1)} \right|^2.
\end{aligned} \tag{2.62}$$

In the case of the soil surface emissivity, the medium 1 is the air with ε_1=1 and the medium 2 is the soil with ε_2, called hereafter ε. Using Eq. (2.61) to express θ_2 as a function of θ_1, called hereafter θ, and combining with Eq. (2.62), the resulting surface reflectivity of flat soil at H-pol ($\Gamma_{H,\theta_{flat}}$) and V-pol ($\Gamma_{V,\theta_{flat}}$) is given by:

$$\begin{aligned}
\Gamma_{H,\theta_{flat}} &= \left| \frac{\cos(\theta) - \sqrt{\varepsilon - \sin^2(\theta)}}{\cos(\theta) + \sqrt{\varepsilon - \sin^2(\theta)}} \right|^2, \\
\Gamma_{V,\theta_{flat}} &= \left| \frac{\varepsilon \cos(\theta) - \sqrt{\varepsilon - \sin^2(\theta)}}{\varepsilon \cos(\theta) + \sqrt{\varepsilon - \sin^2(\theta)}} \right|^2,
\end{aligned} \tag{2.63}$$

where θ is the incidence angle and ε is the complex dielectric constant of the soil, which is in turn governed by the moisture content and the soil type.

The surface emissivity of flat soil at polarization p is defined as:

$$e_{p,\theta_{flat}} = 1 - \Gamma_{p,\theta_{flat}}, \tag{2.64}$$

being $\Gamma_{p,\theta_{flat}}$ the surface reflectivity of flat soil at polarization p (H-pol or V-pol), and incidence angle θ.

2.3.7 Surface roughness

The electromagnetic roughness of a surface is measured in relative terms to the wavelength. If the surface is perfectly flat, the electric fields of two reflected rays are in-phase ($\Delta\phi$=0). In the case of a random surface with a root-mean-square (rms) height σ_s due to the surface roughness, the associated phase difference between two reflected rays is expressed as:

$$\Delta\phi = 2k\sigma_s \cos(\theta) = \frac{4\pi\sigma_s}{\lambda}\cos(\theta), \qquad (2.65)$$

where k is the wavenumber, being $k = \frac{2\pi}{\lambda}$, and θ corresponds to the incidence angle. Additionally, the electromagnetic roughness of a surface is defined as:

$$k_s = \frac{2\pi}{\lambda}\sigma_s. \qquad (2.66)$$

When modeling the emission and scattering of natural surfaces in the microwave region, the Fraunhofer criterion was adopted to distinguish between a smooth and a rough surface. It defines that the maximum phase difference between the electric fields of rays coming from the center and the edge of the antenna must be less than $\pi/8$. With this requirement, the Fraunhofer roughness criterion leads to the condition:

$$\sigma_s < \frac{\lambda}{32\cos(\theta)}, \qquad (2.67)$$

which is equivalent to k_s <0.2 at normal incidence (θ=0).

For a perfectly smooth surface with rms height σ_s=0 or k_s=0, the incident electromagnetic wave at polarization p is reflected along the specular direction, which corresponds to the coherent component of the scattering pattern at polarization p. If the surface is slightly rough with $k_s \sim 0.1$, the scattering continues to be dominated by its coherent component along the specular direction, but it also includes a non-coherent component along all other directions. Furthermore, the incoherent component contains not only waves with the same polarization as that of the incident wave, but also waves with the orthogonal polarization. That is, if the incident wave is at H-pol, the scattering incoherent component consist of both H-pol (co-polar component) and V-pol (cross-polar component). If the surface roughness is increased to $k_s \sim 0.2$, the coherent component becomes negligible small in comparison with the incoherent, which becomes dominant, including the specular direction.
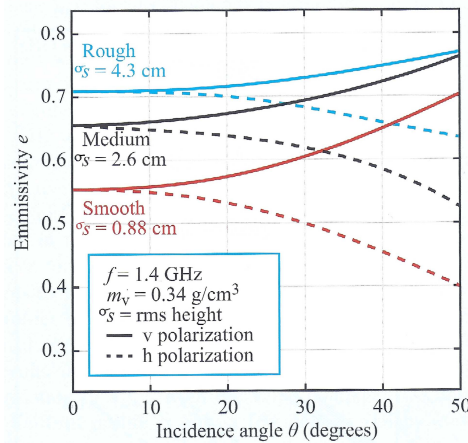
FIGURE 2.13: Emissivity *vs.* incidence angle at 1.4 GHz for three bare-soil fields with different surface roughness [Newton & Rouse, 1980].

The surface roughness has an impact on the microwave emission from bare soils, as shown in Fig. 2.13. It displays the measured emissivity at 1.4 GHz under three different soil surface roughness conditions [Newton & Rouse, 1980]. It is evident that surface roughness increases the emissivity of natural surfaces, due to the increase in the soil area interacting with the atmosphere, and reduces the difference between the vertical and horizontal polarizations. Hence, the sensitivity of the emissivity to soil moisture variations decreases significantly as the surface roughness increases, since it reduces the range of measurable emissivity from dry to wet soil conditions [Wang, 1983].

The effect of surface roughness on soil emissivity has been an issue widely addressed in literature [Choudhury *et al.*, 1979, Wang & Choudhury, 1981, Wang, 1983, Mo & Schmugge, 1987, Wigneron *et al.*, 2001, Escorihuela *et al.*, 2007, Wigneron *et al.*, 2011, Lawrence *et al.*, 2013]. A simple semi-empirical expression of an effective rough surface reflectivity ($\Gamma_{p,\theta}$) was proposed by Choudhury *et al.* [1979]:

$$\Gamma_{p,\theta} = \Gamma_{p,\theta_{flat}} e^{-h_s \cos^2(\theta)}, \tag{2.68}$$

where $\Gamma_{p,\theta_{flat}}$ is the reflectivity at polarization p (H-pol or V-pol) of a flat surface given by Eq. (2.63), h_s corresponds to the roughness parameter, and θ is the incidence angle. The roughness parameter, which is an equivalent rms height, is defined as [Choudhury *et al.*, 1979]:

$$h_s = (2k\sigma_s)^2, \tag{2.69}$$

being k the wavenumber and σ_s the rms roughness height.

A more elaborated formulation of the rough surface reflectivity, taking into account the effects of the polarization mixing, was proposed by Wang & Choudhury [1981]:

$$\Gamma_{p,\theta} = [(1 - Q_s)\Gamma_{p,\theta_{flat}} + Q_s\Gamma_{q,\theta_{flat}}]e^{-h_s \cos^{x_s}(\theta)}, \tag{2.70}$$

where p is the polarization (H-pol and V-pol, or *vice versa*), $\Gamma_{p,\theta_{flat}}$ and $\Gamma_{q,\theta_{flat}}$ are the flat surface reflectivities, Q_s is a polarization mixing factor, and x_s expresses the angular dependence of roughness.

The first value proposed for the Q_s parameter at L-band was zero for all surfaces [Wang, 1983]. The value proposed for the angular dependence was $x_s=2$ [Choudhury *et al.*, 1979], but this value was considered to be too strong for L-band [Mo & Schmugge, 1987]. A detailed analysis showed that both Q_s and x_s could be set equal to zero at L-band and a global h_s could be semi-empirically estimated comprising most surface roughness conditions [Wigneron *et al.*, 2001]. According to this, $Q_s=0$ and $x_s=0$, 1 or 2 are considered both in SMOS and SMAP. Different parameterizations of Q_s and x_s were proposed in several experimental studies [Escorihuela *et al.*, 2007, Wigneron *et al.*, 2011, Lawrence *et al.*, 2013]. However, these studies have been performed under very local conditions, and there is no evidence of the potential benefits that they may introduce at global scale.

The soil emissivity of rough surface at polarization p (H-pol or V-pol) and incidence angle θ is defined as:

$$e_{p,\theta} = 1 - \Gamma_{p,\theta}, \tag{2.71}$$

being $\Gamma_{p,\theta}$ the rough surface reflectivity.

2.3.8   Vegetation effects

When the soil is covered by vegetation, its emission is affected by the canopy layer: it absorbs and scatters the radiation emanating from the soil and also adds its own contribution. The magnitude of the absorption and scattering by the canopy depends upon the wavelength and the vegetation content. At frequencies above 10 GHz, the presence of a vegetation layer masks most of the emission contributed by the underlaying soil surface. Exceptions include very short, very sparse or very dry vegetation covers. As vegetation elements contain water and because water

is very lossy at the low end of the microwave spectrum, the vegetation is qualified as a weakly scattering medium, ignoring contributions related directly to the volume scattering.

Several models have been developed to account for the effects of vegetation on the observed signal [Kirdiashev *et al.*, 1979, Mo *et al.*, 1982, Burke & Schmugge, 1982, Ulaby & Wilson, 1985, Jackson & Schmugge, 1991, Wigneron *et al.*, 1995, Burke *et al.*, 2001, Meesters *et al.*, 2005]. Most of passive microwave soil moisture retrieval algorithms are based on a zero-order radiative transfer model, the so-called τ-ω model, which considers two discrete layers: the soil surface and the vegetation. Using this model, the observed brightness temperature at polarization p and incidence angle θ ($T_{Bp,\theta}$) is expressed as [Mo *et al.*, 1982]:

$$T_{Bp,\theta} = T_s e_{p,\theta} \Upsilon + T_v (1 - \omega)(1 - \Upsilon) + T_v (1 - e_{p,\theta})(1 - \omega)(1 - \Upsilon)\Upsilon, \tag{2.72}$$

where T_s and T_v are the effective temperature of the soil and the vegetation, respectively, $e_{p,\theta}$ is the emissivity at polarization p for incidence angle θ, ω is the single-scattering albedo, and Υ corresponds to the transmissivity of the vegetation layer.

Components of Eq. (2.72) include three contributions as shown in Fig. 2.14. The first term (1) defines the radiation from the soil as attenuated by the overlying vegetation. The second term (2) accounts for the upward radiation directly from the vegetation. The third term (3) defines the downward radiation from the vegetation, reflected upward by the soil and again attenuated by the canopy.
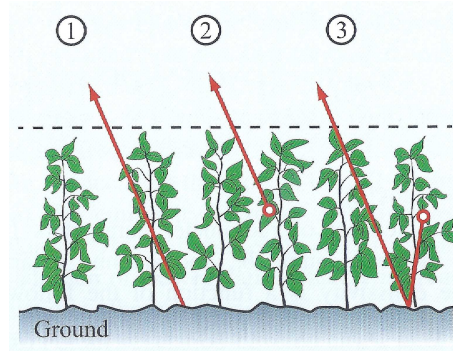
FIGURE 2.14: Three emissivity contributions of a vegetation covered soil: (1) direct emission of the soil attenuated by the overlying vegetation, (2) direct upward emission of the vegetation, and (3) downward emission of the vegetation, reflected and attenuated by the vegetation layer [Ulaby & Long, 2014].

The single-scattering albedo describes an effective scattering for the vegetation cover, representing the fractional radiation scattered (i.e. deflected in many directions). At L-band, ω is often considered almost transparent and set to a very low constant value, either global or land cover dependent.

The transmittivity of the vegetation can be further defined in terms of τ or vegetation optical depth (VOD) and the incidence angle (θ) as:

$$\Upsilon = e^{\frac{-VOD}{\cos(\theta)}}. \tag{2.73}$$

The vegetation optical depth principally describes the attenuation of the soil surface emission by the vegetation layer, but also accounts for the emission of the vegetation layer itself. It is a frequency-dependent parameter, which provides information on water content, structure and density of the vegetation canopy [Pampaloni & Paloscia, 1986]. It can also be used to derive estimates of aboveground biomass [Jones *et al.*, 2011]. It is assumed to be linearly related to the total vegetation water content (VWC [kg/m²]) through a constant of proportionality b that depends on frequency, polarization and canopy structure, according to [Jackson *et al.*, 1982,

Van de Griend & Wigneron, 2004]:

$$VOD = b \cdot VWC. \tag{2.74}$$

There is some experimental evidence indicating possible polarization and angle dependence of both VOD and ω. However, this dependence has been observed mainly during field experiments over vegetation that exhibits a predominant orientation, such as vertical stalks in grass, corn, and soybeans [Kirdiashev *et al.*, 1979, Brunfeldt & Ulaby, 1986, Wigneron *et al.*, 1995, Hornbuckle *et al.*, 2003, Schwank *et al.*, 2005], whereas canopy and stem structure of most vegetation covers are randomly oriented. However, the effects of any systematic orientation of vegetation elements would most likely be minimized at satellite scales [Owe *et al.*, 2001, Martínez-Vázquez *et al.*, 2009].

At 6 A.M./6 P.M., the vertical profiles of soil temperature and soil dielectric properties are likely to be more uniform than at other times of the day [Basharinov & Shutko, 1975]. This minimizes the temperature gradients between soil and land cover types [Hornbuckle & England, 2005], as shown in Fig. 2.15. For this reason, SMOS, Aquarius and SMAP orbits were chosen with local overpass times of 6 A.M./6 P.M. Assuming that the vegetation temperature is in thermal equilibrium with the soil temperature ($T_v \approx T_s$), the expression in Eq. (2.72) can be simplified to:

$$T_{Bp,\theta} = T_s[e_{p,\theta}\Upsilon + (1-\omega)(1-\Upsilon) + (1-e_{p,\theta})(1-\omega)(1-\Upsilon)\Upsilon]. \tag{2.75}$$
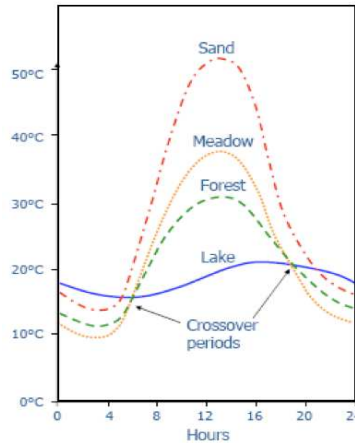
FIGURE 2.15: Diurnal temperature variation and thermal crossover times at approximately 6 A.M./6 P.M. local time for various broad classes of land surface covers. Adapted from Fagerlund *et al.* [1970].

The dependence of brightness temperature with incidence angle and polarization for six main surface conditions, combining bare and vegetation-covered soil with dry, moist and wet moisture conditions is shown in Fig. 2.16. Note that in bare soils (left), T_{B_H} decreases, whereas T_{B_V} increases with the incidence angle. In vegetation-covered soils (right), the vegetation canopy produces an increase of T_B and the difference between T_{B_V} and T_{B_H} decreases. The difference between T_B from dry, moist and wet conditions also decreases in vegetation-covered soils. This indicates that correction for the vegetation effects is necessary to obtain accurate soil moisture estimates. Furthermore, retrievals become increasingly unreliable as the opacity of the vegetation layer increases [Jackson & Schmugge, 1991]. Additionally, it is observed that the emissivity of dry soils is larger than the emissivity of wet soils, with a T_B variation at nadir of $\sim$80 K and of $\sim$40 K in bare and vegetation-covered soils, respectively. This variation is much larger than the noise sensitivity threshold of a microwave radiometer (typically <1 K), so that a large signal-to-noise ratio is obtained. This is a major advantage of the passive microwave technique for soil moisture remote sensing.
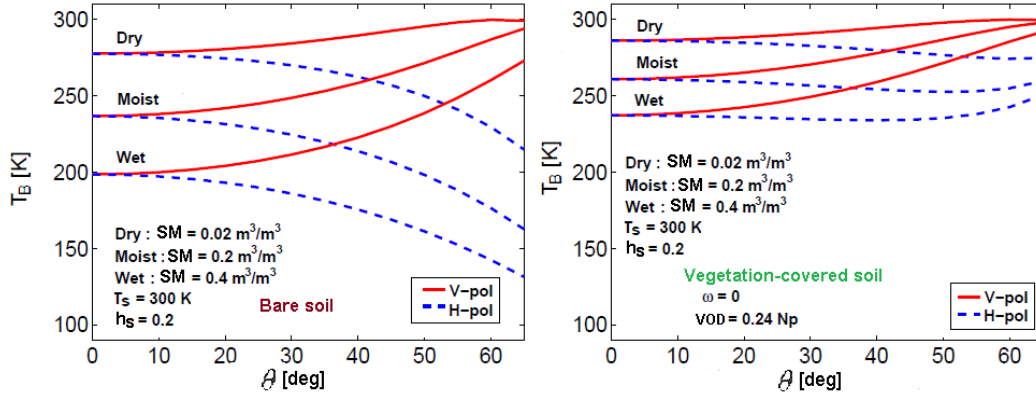
FIGURE 2.16: Brightness temperature at horizontal (blue dashed lines) and vertical (red solid lines) polarizations *vs.* incidence angle for bare (left) and vegetation-covered soil (right) under different soil moisture conditions: dry, moist and wet. Adapted from Piles *et al.* [2010].

2.3.9 Water bodies correction

At the satellite observations scale, a significant part of the footprints contain not only land but also some open fresh water due to the presence of lakes, rivers, wetlands, and transient flooding. For soil moisture retrieval purposes, the presence of open water within the radiometer footprint is undesirable. It dramatically lowers the brightness temperature and results in anomalously high retrieved soil moisture. This results in a bias which degrades the overall soil moisture retrieval accuracy. Fortunately, a correction for water bodies can be applied, since the observed T_B is an areal weighted sum of the land and water T_B contributions as:

$$T_B^{obs} = (1 - \alpha_w)T_B^{land} + \alpha_w T_B^{water}, \tag{2.76}$$

where α_w is the areal water fraction within the antenna footprint, T_B^{land} is the land emission (desired term), and T_B^{water} denotes the water emission computed from a theoretical model. Usually, T_B^{water} is estimated using the model of Klein & Swift [1977], assuming that the water temperature is approximately the same as soil temperature, and its salinity is 0.5 ppt.

2.3.10 Soil moisture retrieval

Most of soil moisture retrieval algorithms are based on the inversion of a geophysical function or so-called forward model, which is usually the τ-ω model [Mo *et al.*, 1982]. In the inversion, the mismatch between the observed ($T_{B_p}^{obs}$) and the modeled brightness temperature ($T_{B_p}^{mod}$) is minimized to determine the vector of unknown parameters ($\vec{X}$) from a set of observations as:

$$\vec{X} = \min_{\vec{X}} J = \sum_{p=H,V} (T_{B_p}^{obs} - T_{B_p}^{mod})^2, \tag{2.77}$$

where J represents the cost function and p denotes the polarization (H-pol and V-pol).

There are a variety of inversion algorithms that differ in how many unknows are included in $\vec{X}$ and in how many observations are combined, whether the sum over polarization is included or whether additional summations are made over different incidence angles, frequencies or overpasses. The cost function in Eq. (2.77) can also incorporate additional terms to account for *a priori* information of the unknown parameters and its associated uncertainty [Piles *et al.*, 2010]. The brightness temperature is influenced by two soil-related parameters, namely soil moisture (SM) and roughness (represented by h_s), and two-vegetation-related parameters, namely vegetation optical depth (VOD) and albedo (ω). SM is a key unknown and is always retrieved. By

constrast, additional parameters such as h_s, VOD and ω can be assigned either dependent on ancillary information or retrieved alongside SM. The challenge of the SM retrieval algorithms is to reconstruct the maximum environmental parameters from the observed signal by using a minimum of ancillary data. A disadvantage of the inversion techniques is that possible errors of the forward model lead to errors in the retrievals.

The earliest inversion approach proposed to retrieved SM is the single-channel algorithm (SCA), which uses T_B acquired at one polarization (H-pol or V-pol) [Jackson, 1993]. The SCA needs ancillary data to account for vegetation and/or roughness. SCA is the current SMAP algorithm, which uses an incidence angle (40°), the V-pol, land cover-based values for h_s and ω, and a NDVI climatology for VOD [O'Neill *et al.*, 2015, Chan *et al.*, 2016]. The same approach is used in Aquarius to retrieved SM [Bindlish *et al.*, 2015]. An extension of the SCA is the dual-channel algorithm (DCA), which uses T_B at two polarizations (H-pol and V-pol) to simultaneously retrieve SM and VOD [Njoku & Li, 1999, Jackson *et al.*, 2002, Yueh *et al.*, 2008]. Other parameters (h_s and ω) are provided as ancillary data. The use of an additional channel in the DCA may bring in additional T_B errors (uncorrelated between V-pol and H-pol) that may affect retrieval accuracy [Ulaby & Long, 2014]. A commonly used variant of the DCA is the land parameter retrieval model (LPRM) [Owe *et al.*, 2008]. It uses the H-pol in the cost function, but also uses the V-pol as an additional information by algrebraically re-arranging the model to provide a direct relationship between the ε_s and VOD as a function of the MPDI [Meesters *et al.*, 2005].

The SMOS algorithm uses the T_B measured at multiple incidence angles and two polarizations (H-pol and V-pol) [Kerr *et al.*, 2012, 2016]. The inversion is performed by minimizing the cost function using an iterative method [Marquartd, 1963]. The τ-ω model is the core of the forward model used to obtain the Earth's emission at L-band, known as L-MEB model [Wigneron *et al.*, 2007]. It considers a variety of land cover types and climatic conditions, while accounting for the pixel heterogeneity. The h_s is estimated with a linear function depending on SM. This function is defined by the transitional moisture point, the FC, and minimum and maximum land cover-based h_s values. The ω is also a land cover-based value. In areas of low vegetation density, VOD is retrieved as an inversion residual alongside SM, but it generally results in a noisy VOD [Patton & Hornbuckle, 2013]. Otherwise, *a prior* VOD value is estimated from a linear relationship between the VOD and Leaf Area Index (LAI) from ECOCLIMAP database [Masson *et al.*, 2003]. Some changes were applied to the new processor (v.620), specially focused on developing a better forward model for densely vegetated areas, which improves both the VOD and SM retrievals [Rahmoune *et al.*, 2013]. Alternatively, a new approach was developed to retrieve VOD from data at H-pol and different incidence angles [Cui *et al.*, 2015a].

Ideally, if four or more independent channels (multiple combinations of incidence angles, frequencies or polarizations) of radiometric data are available, it may be possible to invert a model without recourse to ancillary data. However, T_B measurements at H-pol and V-pol are highly correlated and contain redundant information [Konings *et al.*, 2015]. To overcome this limitation, a new multi-temporal dual-channel algorithm (MT-DCA) has recently been developed for simultaneous retrievals of SM, VOD and ω, using time-series of passive microwave measurements, without reliance on ancillary soil or vegetation information [Konings *et al.*, 2016, Piles *et al.*, 2016a].

Appart from the inversion, other retrieval techniques were developed. The first one is based on deriving an empirical regression between the geophysical variables and the radiative transfer equation [Wigneron *et al.*, 2003, Saleh *et al.*, 2006]. However, it has a limited applicability, since the regression is often valid only for the test sites. The second one is based on the use of neural networks, with satisfactory results in SM retrievals [Del Frate *et al.*, 2003, Rodríguez-Fernández *et al.*, 2015], but they need a training phase that is not always feasible.

2.4 L-band satellite missions

This Ph.D. Thesis makes use of data from three L-band satellite missions: SMOS, Aquarius and SMAP. A brief introduction of these missions is provided in this section.

2.4.1 The SMOS mission

The SMOS satellite was launched from Plesetsk, Russia, on November 2, 2009. It is the second ESA's Earth Explorer Opportunity mission selected in the framework of the Living Planet Programme (https://earth.esa.int/web/guest/missions/esa-operational-eo-missions/smos) [Kerr *et al.*, 2010, Font *et al.*, 2010, Mecklenburg *et al.*, 2016] and its operation has recently been extended until the end of 2017.

The biggest challenge of the SMOS mission was to demonstrate an innovative technology that has never been used before on a satellite platform: a two dimensional (2-D) radiometer based on interferometry, with a large effective antenna aperture synthesized through a distributed network of small physical antennas. While a real aperture antenna obtains a single pixel image, a synthetic aperture antenna obtains a snap-shot image that is composed of multiple pixels, as illustrated in Fig. 2.17.
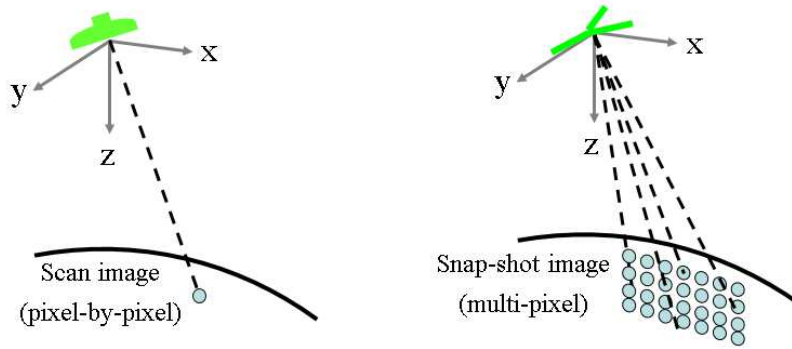
FIGURE 2.17: Single pixel image obtained from a real aperture antenna (left) and multi-pixel image obtained from a synthetic aperture antenna (right). Credits: UPC.

The synthetic aperture technology was originally developed for radio-astronomy research [Ryle, 1952, Ryle & Hewish, 1960, Napier *et al.*, 1983] and was later adopted in Earth remote sensing to improve the spatial resolution of passive microwave imagers that operate at low microwave frequencies. The objective was to avoid the large, mechanically steered physical aperture that would otherwise be required [Le Vine & Good, 1983, Ruf *et al.*, 1988]. However, its application in radiometry led to the development of complex calibration and image reconstruction procedures [Camps, 1996, Ribó, 2005, Camps *et al.*, 2008, Corbella *et al.*, 2009, González-Gambau, 2012]. In radio-astronomy the scene is a point source, which allow the use of highly directive antennas and an accurate measurement of the antenna patterns in the field of view (FOV). Instead, in Earth observation the scene is an extended source, which requires a wider FOV, individual antenna patterns must be taken into account, and the antenna spacing is shorter in order to prevent the aliasing in the image reconstruction process, increasing the antenna coupling and self-interferences.

Early demonstrators were made by some L-band airborne radiometers, such as the Electronically Steered Thinned Array Radiometer (ESTAR), developed by NASA and Goddard Space Flight Center (GSFC) to validate the one dimensional (1D) aperture synthesis concept [Le Vine *et al.*, 2001], and the 2D-ESTAR with two dimensional aperture synthesis [Le Vine *et al.*, 2007b]. Additionally, a small scale prototype of SMOS, the Airborne Microwave Imaging Radiometer by

Aperture Synthesis (AMIRAS), was developed by ESA and tested in the framework of the SMOS mission [Martín-Neira *et al.*, 2008].

The Microwave Imaging Radiometer by Aperture Synthesis (MIRAS) is the single payload of the SMOS satellite [McMullan *et al.*, 2008]. This passive sensor operates at 1.413 GHz and consists of a central structure or hub and three deployable arms that form angles of 120° to each other, in a Y-shape, as shown in Fig. 2.18. Each arm is ∼4.5 m length. MIRAS has 69 antennas in total, equally distributed over the three arms and the hub and separated at a distance of 0.875λ. Each arm has 18 antennas (6 antennas per each segment) and the hub has 15 antennas. There are two antenna types: 66 are Lightweight Cost Effective Front-end (LICEF) with two polarizations, but only one receiver, and 3 are Noise Injection Radiometer (NIR) with two polarizations and two receivers, one for each polarization, being a total of 72 receivers.
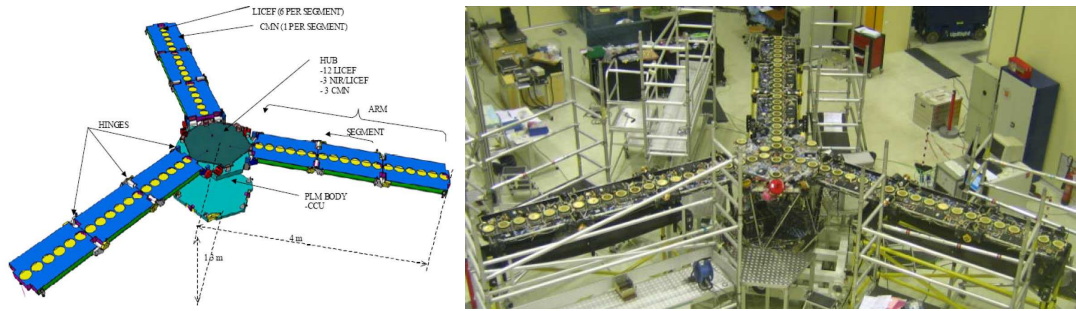
FIGURE 2.18: SMOS architecture diagram (left), from McMullan *et al.* [2008]. Photograph of the SMOS instrument at EADS-CASA Espacio facilities (right). Credits: ESA.

The individual measurement of SMOS is the baseline, formed by a pair of receivers. The signals acquired by each baseline are transmitted to a digital correlator unit, which performs cross-correlations between all possible combinations of receiver pairs to compute the visibilities at the spatial frequency domain ($u=\frac{x_k-x_j}{\lambda}$, $v=\frac{y_k-y_j}{\lambda}$). The brightness temperatures at the coordinates $\xi=\sin(\theta)\cos(\phi)$, $\eta=\sin(\theta)\sin(\phi)$ are obtained after applying the Fourier Synthesis methodology described by Camps [1996]. The spatial frequency domain (u,v) of the visibility samples and the coordinates (ξ,η) where the T_B are retrieved, as well as the Earth and unit circle aliases, are observed in Fig. 2.19. The alias free field of view (AF-FOV) and the extended alias-free field of view (EAF-FOV) are also shown.
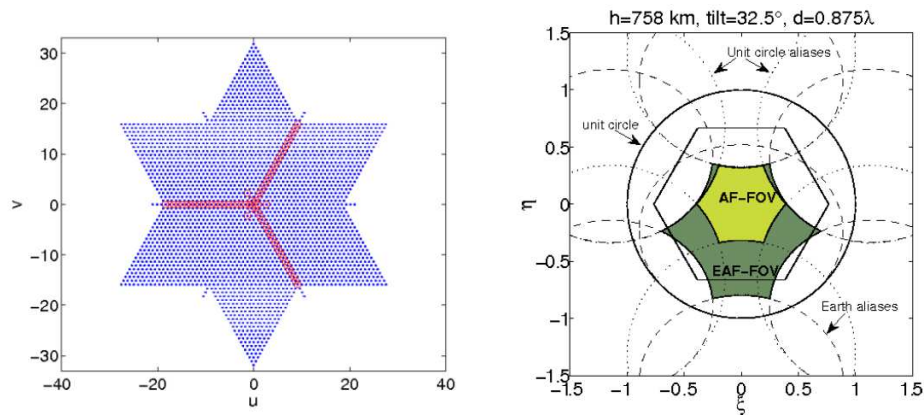
FIGURE 2.19: SMOS spatial frequency domain (u,v) of the visibility samples (left) and the coordinates (ξ,η) where the T_B are retrieved. Earth disks (dashed ellipses), the unit circle (solid circle), the basic period (hexagon) and the 6 closest replicas of the unit circle are also represented (dotted circles). The alias-free field of view (AF-FOV, in light green) and the extended one (EAF-FOV, in dark green) are marked [González-Gambau, 2012].

SMOS takes a T_B image every 1.2 seconds with a characteristic irregular curved hexagon-shaped FOV of ∼1000 km swath width at the Earth reference frame. As the satellite flies along its Sun syncronous orbital path at a mean altitude of 758 km and tilt angle of 32.5°, each pixel is observed under different viewing angles, from 0° to 65°. Its spatial resolution also varies from ∼35 km at nadir to ∼70 km at the upper borders. In addition, the radiometric sensitivity ranges from 2 K at boresight to 4.5 K [Corbella *et al.*, 2011]. Consequently, SMOS observations are characterized by a different incidence angle, pixel size and spatial resolution depending on the pixel's location within the instrument FOV, as shown in Fig. 2.20. SMOS measures the four Stokes parameters. The main instrumental features of the SMOS radiometer as well as the mission objectives are summarized in Table 2.1.
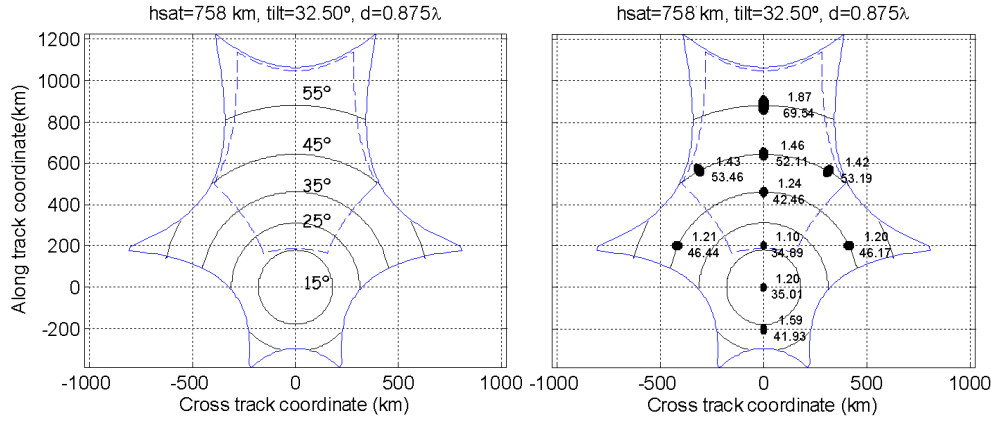
FIGURE 2.20: Incidence angles (left), and axis ratios and spatial resolution in km (right) within the SMOS AF-FOV (blue dashed contour) and the EAF-FOV (blue solid contour) at the Earth reference frame. Credits: UPC.

2.4.2 The Aquarius/SAC-D mission

The Aquarius/SAC-D satellite was launched from Vanderberg Air Force Base, California, on June 10, 2011. It was a partnership between the U.S. NASA and the Argentinian CONAE (http://aquarius.nasa.gov/). The main objective was to monitor the seasonal and inter-annual variation of the large-scale features of the SSS in the open ocean during 3–5 years [Le Vine *et al.*, 2010]. Unfortunately, a failure related to the power supply electronics led to the loss of several key systems needed to the satellite control. Consequently, the mission ended its operation on June 7, 2015, after an Aquarius SSS data record of approximately three years and nine months.

The mission was composed of two parts: the NASA's Aquarius instrument, which was a combination of a real aperture passive/active sensor [Le Vine *et al.*, 2007a, Lagerloef *et al.*, 2008], and the CONAE's SAC-D spacecraft platform and associated instruments, as shown in Fig. 2.21. In this Thesis, only data from the Aquarius instrument were used.

The Aquarius instrument included a 2.5 m offset parabolic reflector with three feed horns (see Fig. 2.21). It was flying in a Sun synchronous orbit at a mean altitude of 657 km. The three beams were arranged in a push-broom fashion pointed across track, with respect to the satellite nadir direction, pointing to the right of the orbit (nighttime side) to avoid Sun glint, with a different look-angle: 29.36°, 38.49°, and 46.29° for the inner, middle and outer beams, respectively. There were three radiometers operating at 1.413 GHz (each feed had a dedicated radiometer). The spatial resolution of the three radiometer beams were 76 x 94 km (inner), 84 x 120 km (middle), and 96 x 156 km, covering a swath width of ∼390 km. The radiometers were Dicke units and measured T_B at H-pol and V-pol, and the third Stokes parameter [Le Vine *et al.*, 2014]. There was only one scatterometer, which cycled among the three feeds and two polarizations. It was a total power radar system operating at 1.26 GHz, that provided backscatter measurements to estimate the ocean surface roughness [Freedman *et al.*, 2006]. The radiometers
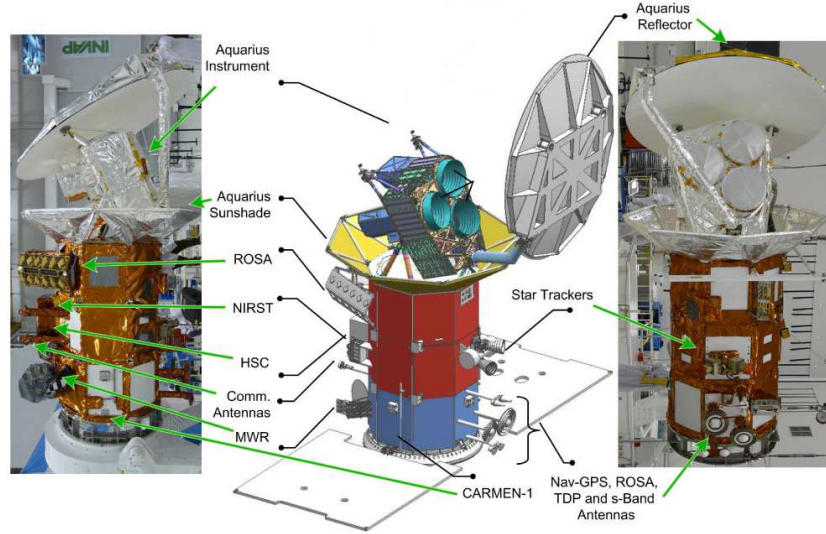
FIGURE 2.21: Deployed configuration of the ESA's Aquarius and CONAE's SAC-D instruments, and photographs of the Aquarius/SAC-D satellite at the Argentinian *Investigación Aplicada* (INVAP) facilities. Credits: NASA.

and scatterometer beams were aligned and had approximately the same shape at the 3-dB level, as shown in Fig. 2.22. The fundamental timing unit was 10 ms (9 ms of observation time for the radiometer and 1 ms for the scatterometer transmit pulse). The main characteristics of the Aquarius instrument and the science objectives are summarized in Table 2.1.
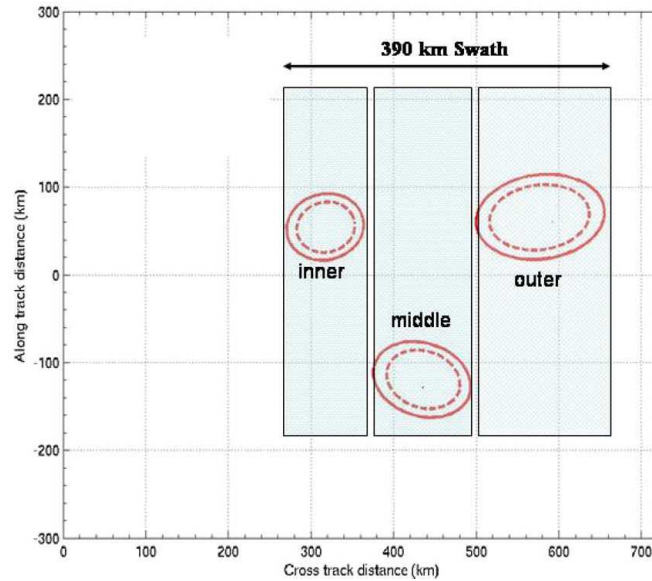
FIGURE 2.22: Aquarius radiometer 3-dB footprint (red solid lines) and scatterometer 3-dB footprint (red dashed lines) of the three beams (inner, middle, and outer), with a swath width of ∼390 km [Le Vine *et al.*, 2007a].

The Aquarius team is now undertaking a task to generate SSS data from the NASA's SMAP mission. The SMAP SSS data is generated using the same algorithm as Aquarius, and will be distributed in a similar manner. The objective is to make the Aquarius and SMAP datasets as seamless as possible, and provide uninterrupted data continuity between the missions.

2.4.3 The SMAP mission

The NASA's SMAP satellite was launched from Vanderberg Air Force Base, California, on January 31, 2015 (https://smap.jpl.nasa.gov/). The main objective is to mesure the global SM and the freeze/thaw state of the soil during 3 years [Entekhabi *et al.*, 2010b].

Currently, SM is measured at scales ranging from point (*in situ* observations) to satellite footprint ($\sim$40 km, as SMOS) at various temporal resolutions. An L-band radiometer measures T_B with high accuraccy, being clearly sensitive to SM, but presents a coarse spatial resolution. An L-band synthetic aperture radar (SAR) provides backscatter measurements at high spatial resolution, with a limited accuraccy to SM sensing due to its high sensitivity to surface roughness and vegetation scattering. These individual technologies can only partially satisfy the criterion for an optimal SM sensing approach. The SMAP instrument is a combination of a passive/active sensor at the same satellite. It takes advantage of the concurrent L-band measurements: high accuracy (radiometer) and high spatial resolution (SAR) [Spencer *et al.*, 2010].
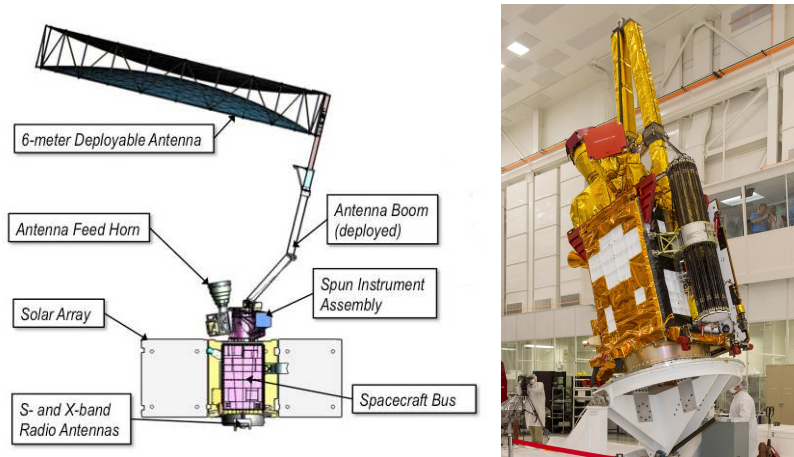
FIGURE 2.23: Diagram of the SMAP architecture (left) and photograph of the instrument at NASA's Jet Propulsion Laboratory (JPL) with the antenna folded before its launch (right). Credits: NASA.

SMAP flies in a Sun syncronous orbit at a nominal altitude of 658 km. The SMAP architecture diagram is shown in Fig. 2.23. Both the radiometer and radar share a single feedhorn and reflector. The feedhorn is a large cone visible on the outside of the spacecraft. The deployable mesh antenna of 6 m is shown in Fig. 2.24 (left). It is an offset reflector from nadir and rotates about the nadir axis at 14.6 rpm. It provides a conically scanning antenna beam at a constant Earth's surface incidence angle of 40°with a swath width of $\sim$1000 km, as displayed in Fig. 2.24 (right). While the radiometer resolution is defined by the real aperture with $\sim$40 km 3-dB footprint, the high radar resolution of $\sim$1–3 km is obtained by synthetic aperture processing. The Dicke radiometer operates at 1.413 GHz, measuring the T_B at H-pol and V-pol, and also the third and the fourth Stokes parameters [Kim *et al.*, 2013], obtaining full-polarimetric capabilities. The SAR operates at 1.26 GHz, providing the backscatter measurements at HH-pol, VV-pol and HV-pol [West, 2012].

Additionally to the passive-only SM and the active-only SM estimations, SMAP planned to provide a 9-km SM product using a disaggregation algorithm that combines active and passive observations [Piles *et al.*, 2009, Das *et al.*, 2011, 2014]. However, the SMAP SAR ended its operation on July 7, 2015 due to a failure in the data transmission. Due to that, the production of the active SM and active-passive SM products ceased abruptly after about ten weeks. Although this duration is limited, the global SMAP measurements during early spring and summer allow new insights about the passive/active combination for SM mapping. Currently, the C-band SAR on-board of ESA's Sentinel 1 is proposed to use in tandem with the SMAP radiometer to provide the 9-km active-passive SM product [Leone, 2015]. The SMAP mission also provides

added value products, such as the SM at the surface and the root-zone, and the carbon ecosystem exchange [Entekhabi *et al.*, 2014]. The main features of SMAP and the scientific requirements are summarized in Table 2.1.
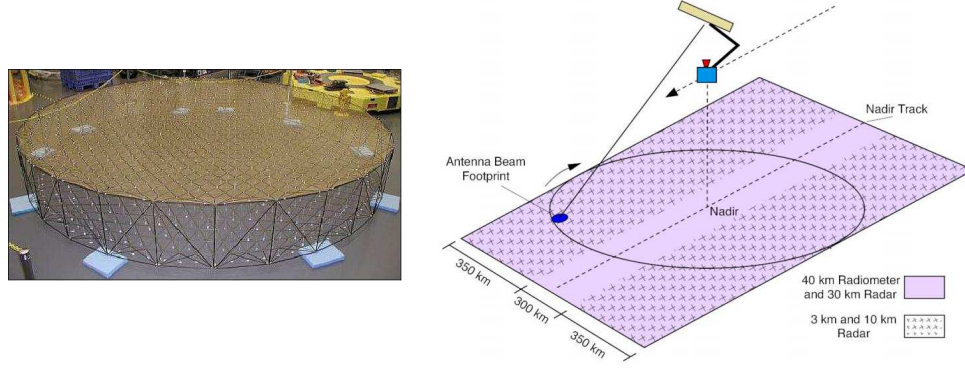
FIGURE 2.24: SMAP deployable antenna at the ground of the JPL facilities (left) and schematic of the conically scanning antenna beam mapping out a swath width of ∼1000 km at Earth's surface (right) [Spencer *et al.*, 2010].

TABLE 2.1: Main features of SMOS, Aquarius and SMAP instruments

	SMOS	**Aquarius**	**SMAP**
Scientific requirements	SM: 4% SSS: 0.5–1.5 psu (single observation) or 0.2 psu (monthly average of a 100 x 100 km area)	SSS: monthly average accuraccy of 0.2 psu and spatial resolution of 150 km	SM: 0.04 m^3/m^3
Orbit height	758 km	657 km	685 km
Local solar time at ascending node	6 A.M.	6 P.M.	6 P.M.
Topology (radiometer) (radar)	synthetic aperture	real aperture real aperture	real aperture synthetic aperture
Incidence angle	0°–65°(multi-angular)	29.36° (inner) 38.49° (middle) 46.29° (outer)	40°(constant angle)
Radiometric accuracy	∼2–4.5 K	∼1–1.5 K	∼1.3 K
Spatial resolution	∼35–70 km	76 x 94 km (inner) 84 x 120 km (middle) 96 x 156 km (outer)	40 km (radiometer) 1–3 km (radar)
Swath coverage	∼1000 km	∼390 km	∼1000 km
Revisit time	3 days	7 days	3 days

Chapter 3

Inter-comparison of SMOS & Aquarius brightness temperatures

For nearly four years, there were two satellite missions in orbit providing frequently and globally unprecedented observations of the Earth's surface using L-band radiometers on board: the ESA's SMOS [Kerr *et al.*, 2010, Font *et al.*, 2010, Mecklenburg *et al.*, 2016] and the NASA's Aquarius [Le Vine *et al.*, 2010]. The evaluation of the continuity and the consistency between SMOS and Aquarius T_B is paramount if data from both radiometers are to be used in any long term environmental, meteorological, hydrological, or climatological study.

Although Aquarius is no longer in operation, the scientific community considers that its T_B dataset is still very useful to further improve our knowledge of the Earth's water cycle. Additionally, the inter-comparison is a fundamental issue that can also be applicable to SMAP, the current NASA's L-band mission in orbit [Entekhabi *et al.*, 2010b, Chan *et al.*, 2016].

3.1   State of the art

SMOS and Aquarius instruments operate at the same frequency band, centered at 1.413 GHz. However, they have important differences (see Section 2.4), such as the architecture of their radiometers (synthetic aperture *vs.* real aperture), their operation principles (interferometric radiometer *vs.* Dicke radiometer), their spatial resolutions ($\sim$40 km *vs.* $\sim$100 km), their swath coverages (1000 km *vs.* 390 km), and their revisit times (3 days *vs.* 7 days).

Both instruments are calibrated to obtain their T_B products within the mission requirements, using different procedures. In SMOS, there are two types of calibration: the internal and the external. The internal calibration is based on the injection of uncorrelated noise which compensates for offset terms, and correlated noise at two known levels, which compensates for amplitude and phase terms. The external calibration uses cold sky maneouvers to calibrate the injected noise level [Brown *et al.*, 2008, Martín-Neira *et al.*, 2016]. Likewise, Aquarius had an internal calibration (injecting correlated and uncorrelated noise) and used the cold sky as external calibration. Additionally, a vicarious calibration was performed using models over the ocean, Antarctica and Amazon rainforest [Piepmeier *et al.*, 2013].

After calibration, some corrections are applied to SMOS and Aquarius T_B to obtain the signal from the Earth's surface and to filter signal contributions from sky and celestial bodies (galaxy, Sun and Moon). The main differences in the corrections applied are summarized in Table 3.1. In both instruments, the T_B are already corrected for the direct sky radiation. SMOS Level 1 (L1) data contain flags indicating the Sun and Moon corrections/detections in presence of direct/reflected radiations, respectively. Corrections for reflected galaxy [Tenerelli *et al.*, 2008]

are applied at SMOS Level 2 Ocean Salinity (L2OS) processor before retriving the sea surface salinity (SSS) [Font *et al.*, 2014]. In Aquarius, the distributed T_B were already corrected for sky, galaxy, Sun and Moon signal contributions.

TABLE 3.1: Corrections applied to SMOS and Aquarius radiometers.

Correction type	SMOS	Aquarius
Direct sky	Yes	Yes
Reflected galaxy	No	Yes
Direct Sun	Yes	Yes
Reflected Sun	No	Yes
Direct Moon	Yes	Yes
Reflected Moon	No	Yes

Direct comparison of SMOS and Aquarius observations is challenging, since both are Sun syncronous Low Earth Orbits (LEO) satellites at similar heights ($\sim$758 km and $\sim$675 km, respectively), but they have opposite equatorial ascending crossing times: approximately 6 A.M. for SMOS and 6 P.M. for Aquarius. Due to this, cross-overs only occur near the equator and at the poles.

Previous studies have shown an increase interest in comparing SMOS and Aquarius T_B. Firstly, a resampling and multi-windowing method to obtain SMOS T_B at the incidence angles and ground resolution of Aquarius was proposed [Anterrieu *et al.*, 2011]. Later, a method based on co-located overpasses (with at least 20 SMOS grid points inside the Aquarius footprint) and a 30-minutes time criterion to eliminate the effect of physical temperature drifts was used, but this approach limits the observations to low latitudes between [20°S, 40°N] [Bindlish *et al.*, 2012]. Finally, simultaneous observations over the same place (with a distance less than 2.5°) were also used, resampling SMOS data at the resolution and incidence angles of Aquarius and obtaining a limited number of co-locations ($\sim$750 overpasses in 500 days) [Cabot *et al.*, 2013] .

The proposed inter-comparison approach is based on the study of one year of measurements over key target regions selected as representative of land, ice, and sea surfaces. The level of linearity, the correlation, and the differences between the SMOS and Aquarius T_B are analyzed to detect possible differences or biases. Also, this methodology does not present latitudinal constraints, allowing to collect a fair amount of data for robust statistics. The content of this Chapter has been published in a workshop [Pablos *et al.*, 2013a], a symphosium [Pablos *et al.*, 2013b], and a journal [Pablos *et al.*, 2014b].

3.2   Datasets

3.2.1   SMOS data

The SMOS T_B are obtained from the L1C v.505 products, which are provided by the European Space Astronomy Centre (ESAC), Madrid. They are located at the antenna reference plane. These T_B have been first screened out for all the Radio-Frequency Interferences (RFI) detected (strong, point source and tails), and also for the Sun (glint area, aliases and tails), and Moon (aliases) contamination, using the corresponding flags. Later, geometric and Faraday corrections have been applied to obtain T_B at the top of the atmosphere (TOA), using Eq. (2.20).

All SMOS T_B in an incidence angle range of $\theta\pm5°$ have been linearly interpolated to obtain them at the Aquarius incidence angles (see Table 2.1). Finally, T_B at the Icosahedral Snyder Equal Area (ISEA) 4H9 grid [Sahr *et al.*, 2003] have been interpolated to a 0.25° regular latitude-longitude grid, which is easier to manipulate.

3.2.2 SMOS spatial bias correction over ocean

SMOS' synthetic imagery can be interpreted as obtained by an array of antennas located in each spatial frequency point [Bará *et al.*, 1998]. The incidence angle, the spatial resolution, and the radiometric accuracy vary depending on the position of each pixel within the field of view (FOV) (see Fig. 2.20). The differences between pixels that remain after calibration are the so-called pixel biases or spatial errors.

It is known that SMOS pixel biases are significantly affecting ocean observations, since they have an important impact in sea surface salinity (SSS) retrievals. Several studies characterized these spatial errors and described methods to mitigate their effects on the T_B images. An improved reconstruction algorithm that decomposes the visibility samples in ocean and land/sea ice, instead of just the Earth and the sky, was proposed [Camps *et al.*, 2008]. It was demonstrated that SMOS pixel biases are not zero mean and produce visible artifacts along-track, which could be minimized over the ocean using a multiplicative mask [Torres *et al.*, 2012]. The spatial errors were distinguished by azimuth dependence/independence and an empirically fitted pattern that could be applied over ocean, ice and land was estimated [Gourrion *et al.*, 2014].

In this study, the so-called Ocean Target Transformation (OTT) [Tenerelli & Reul, 2010] that models the instrumental spatial pattern of the FOV has been applied to SMOS data over South Pacific region, as it is currently applied operationally in the L2 Ocean Salinity processor [Font *et al.*, 2014]. As a result, the errors in the FOV become practically random, preserving the geophysical variation in the scene.

3.2.3 Aquarius data

The Aquarius T_B used are L2 v.2 products, which are provided by the Physical Oceanography Distributed Active Archive Center, managed and located at NASA's Jet Propulsion Laboratory (JPL), California. They are directly T_B at TOA and have been masked out for RFI, reflected Sun, glint and Moon contamination (moderate and severe flags), and also for direct Sun contamination (severe flag). No gridding was performed.

3.3 Methodology

3.3.1 Selection of target regions

The inter-comparison procedure involves identifying locations on Earth that could serve as target regions to assess the behaviour of both SMOS and Aquarius instruments. The main goal is to evaluate the T_B acquired independently over several relatively stable and homogeneous targets at scales compatible with both sensors. They should have nearly constant observed T_B over time and cover, as much as possible, the whole dynamic range of T_B observations from the cold to the hot end (sea, ice and land). Attending to these criteria, four locations have been selected: the Amazon rainforest, the Sahara desert, the South Pacific Ocean, and the Dome-C zone in the Antarctica as shown in Fig. 3.1. Specific locations, areas and number of observations selected from each radiometer are included in Table 3.2. Observations from cold sky views have not been used in this study since both radiometers have different antenna patterns and also different scenes entering into the back lobes that could severely affect the T_B measurements from the main lobe (∼3-10 K).

The four target regions selected for the present study have different radiometric characteristics:

1. The Amazon tropical forest has a very stable temperature and its surface is covered by a heavily vegetated layer that provides a feasible approximation to a blackbody at L-band. However, its surface contains rivers and it rains almost the whole year.
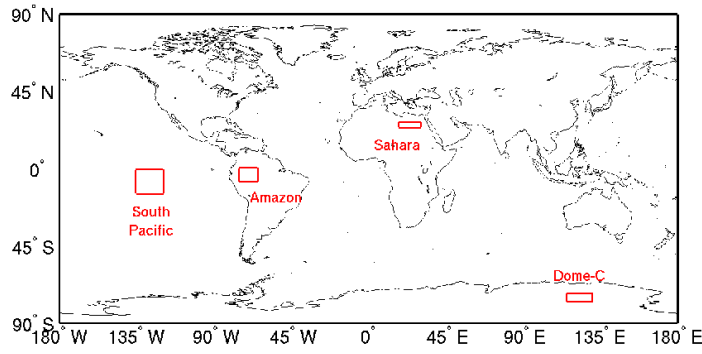
FIGURE 3.1: World map showing location and extention of target regions: Amazon rainforest and Sahara desert (land), South Pacific Ocean (sea), and Dome-C in Antarctica (ice)

2. The Sahara's surface is very dry, sandy, and without presence of vegetation. It is characterized by a dry atmosphere and high daily surface temperature variations. In the Sahara desert, the area has been selected to ensure total absence of precipitation during the study period. It was checked using the total precipitation in [mm/month] of the Global Precipitation Climatology Centre (GPCC) using a 1° regular grid product based on quality-controlled data from Earth's stations.

3. The South Pacific ocean is an ice-free region on the sea, with low or moderate wind speed (WS<12 m/s), an almost constant sea surface temperature (SST) of ∼26.5°C, and a SSS of ∼35 psu.

4. The Dome-C in the Antarctica is considered a very stable region on Earth. Also, the Dome-C region has been suggested as a reference target over ice for several experimental campaigns [Macelloni *et al.*, 2006, 2013].

TABLE 3.2: Description of selected target areas

Location	Latitude	Longitude	Area [km^2]	Beam	SMOS / Aquarius [pixels]
Amazon	8°S, 1°N	75°W, 65°W	1113·10^3	inner	294697 / 22618
				middle	289987 / 26886
				outer	335133 / 23001
Sahara	23.5°N, 27.5°N	18°E, 30°E	593·10^3	inner	164074 / 11485
				middle	162554 / 11216
				outer	181238 / 10485
South Pacific	15°S, 0°N	135°W, 120°W	2782·10^3	inner	712923 / 66141
				middle	711083 / 64374
				outer	793666 / 62707
South Pacific *(with OTT applied to SMOS data)*	15°S, 0°N	135°W, 120°W	2782·10^3	inner	712925 / 66141
				middle	706166 / 64374
				outer	793577 / 62707
Dome-C	78°S, 72°S	116°E, 130°E	1039·10^3	inner	1450060 / 30994
				middle	1444861 / 34732
				outer	1737110 / 38305

3.3.2 Study period and data selection

All SMOS and Aquarius radiometric observations measured over the selected target areas have been analyzed at the three Aquarius Earth incidence angles along the year 2012. For Aquarius, only the footprints which are entirely enclosed within the target areas' boundaries have been considered. In SMOS, the orbits covering at least 20% of the total number of ISEA 4H9 grid points within the region have been taken into account. Both ascending and descending orbits have been used. The use of ascending and descending separately has been checked not to affect the results.

3.3.3 Length of the averaging window

Temporal window averaging is needed to reduce the noise in the measurements. To select an appropriate length for this window, the Allan variance has been computed over each target region, both for SMOS and for Aquarius. Allan variance determines the stability and drifts of the measurement time series as a function of the integration time (in this study from 2 to 100 days). Plots of the Allan variance obtained for Aquarius (top) and SMOS (bottom) over all targets using the middle beam of the half first Stokes parameter ($I/2 = (T_{B_H} + T_{B_V})/2$) are shown in Fig. 3.2. Other beams (not included) present similar behavior. It could be observed that Aquarius has a stability period of $\sim$7 days over land and ice, in agreement with its revisit time. Over ocean, the stability period is not clear enough. SMOS has a stability period of $\approx$6 to 10 days over land, $\approx$3 to 7 days over ice, and $\approx$5 to 8 days over ocean. In view of these results, a 7-day averaging window has been selected in this study for all target regions and both instruments.
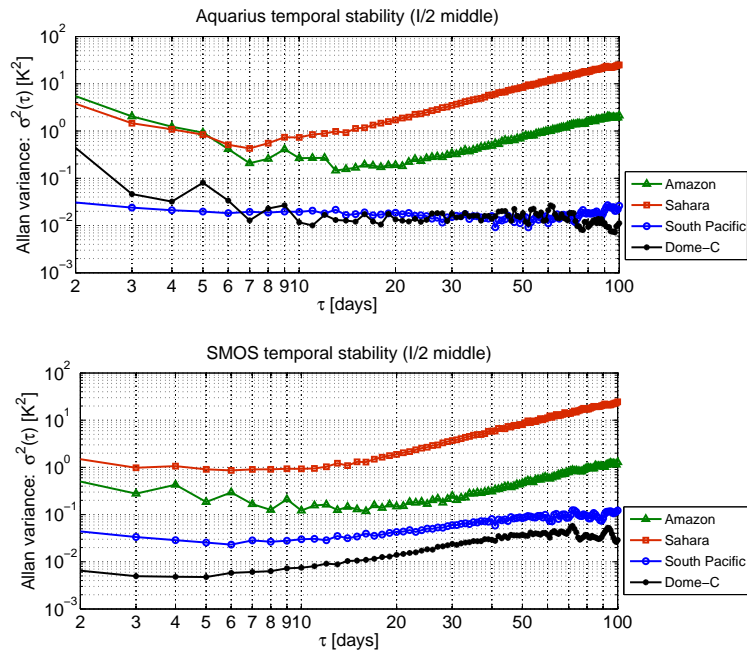
FIGURE 3.2: Aquarius (top) and SMOS (bottom) Allan variance for each target region: Amazon (green), Sahara (red), South Pacific (blue) and Dome-C (black) using only middle beam of the First Stokes (I/2). Other beams present similar behaviours.

SMOS and Aquarius T_B have been compared at TOA for H-pol and V-pol separately, at the three Aquarius incidence angles: $\sim$29.36° (inner), $\sim$38.49° (middle) and $\sim$46.29° (outer) beams. Half of First Stokes has also been analyzed to discard errors due to Faraday rotation.

3.4 Results and discussion

3.4.1 Global overview

A global view of the results over all the study areas (Amazon, Sahara, South Pacific Ocean, and Dome-C) is provided in Fig. 3.3. The yearly mean Aquarius T_B are presented as a function of the yearly mean SMOS T_B for each beam, polarization and region. Each beam is depicted using a different colour and symbol. Ideally, the yearly mean values within the dynamic range (70 K to 310 K) should be on the 1:1 line (dashed line).

In South Pacific, Dome-C and Sahara, higher incidence angles imply lower T_{B_H}, and higher T_{B_V}. However, in the Amazon, the T_B variation with incidence angle and polarization is not clear due to the vegetation scattering; the signal emitted by the Amazon's surface is highly affected by multiple reflections when is travelling upward through the vegetation canopy, and coherent effects appear when the distance between vegetation scatterers becomes comparable to the wavelength ($\sim$21 cm). As expected, there is a small difference between polarizations ($T_{B_V} - T_{B_H}$) for vegetation-covered soils.
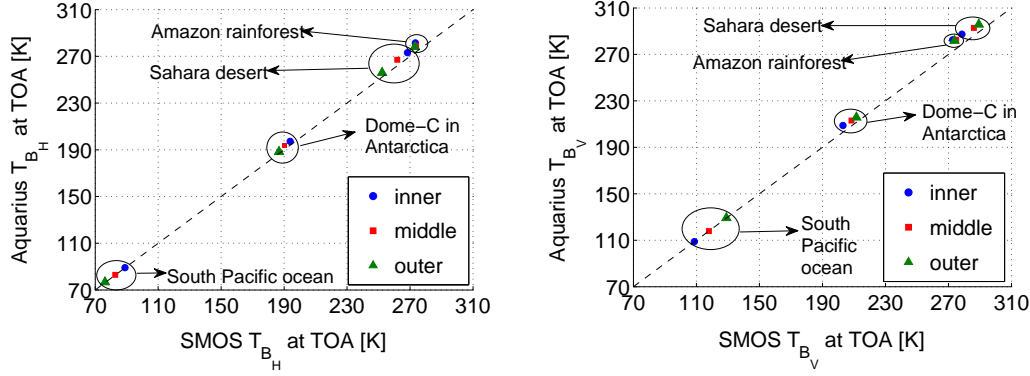
FIGURE 3.3: Aquarius T_B *versus* SMOS T_B over land $\sim$250-300 K (Amazon rainforest and Sahara desert), over ice $\sim$180-220 K (Dome-C in Antarctica) and over sea $\sim$70-130 K (South Pacific ocean) for H (left) and V polarizations (right). Different symbols represent inner (blue circles), middle (red squares) and outer (green triangles) beams.

3.4.2 Linearity analysis

To study the linearity between the two radiometers along 2012, representative scatter plots of Aquarius T_B *vs.* SMOS T_B (7-days averaged) are presented for H-pol and V-pol in Figs. 3.4 and 3.5, respectively. Regions are sorted by rows and beams are assigned by columns. Dynamic ranges are fixed for each area to show full T_B variability with enough detail. The slope (s) is estimated through a robust linear fit [DuMouchel & O'Brien, 1989].

Over land, the slopes are close to 1 (Amazon: $s\approx$0.94 to 1.21, Sahara: $s\approx$0.86 to 1.05). Over sea, slopes are low and only slightly increase after the pixel bias correction (South Pacific: before OTT $s\approx$0.08 to 0.37, after OTT $s\approx$0.30 to 0.42). It is evident from these results that there is a better agreement between SMOS and Aquarius T_B over land than over sea. The obtained differences over sea could be due to Aquarius T_B are corrected for the reflected galactic radiation. However, this correction is not applied to SMOS T_B. In the case of Dome-C, the scatter plots show an unusual distribution and two slopes (opposite in sign) have been identified. The subset of points from the summer months (from December the 21st to March the 21st) match with positive slopes (Dome-C Austral summer: $s\approx$0.30 to 1.66) whereas the other points match with negative slopes (Dome-C other seasons: $s\approx$-0.11 to -0.58). Note that some slopes over ice are non-significant (p_{value} >0.05, at the 95 % of significance level) for middle and outer beams. Focusing on a single target area and comparing the different polarizations, it can be noted that T_{B_H} slopes are higher than T_{B_V} slopes. Also, the slope values obtained at higher incidence angles are closer to 1 (ideal slope) than lower incidence angles in most cases.

The linearity is also assessed with scatter plots of Aquarius $I/2$ *vs* SMOS $I/2$. Note that $I/2$ is independent of the Faraday rotation. The obtained results, included in Appendix B (see Fig. B.1), are consistent with those obtained at H-pol and V-pol. This confirms that differences in Faraday correction are not affecting the inter-comparison analysis.

Updated data versions are explored to analyze the unusual distribution of the scatter plots over Dome-C in Antarctica. The results are included in Appendix B (see Fig. B.2). They show that

a similar behaviour is present along different data versions and further research is needed to understant its origin.
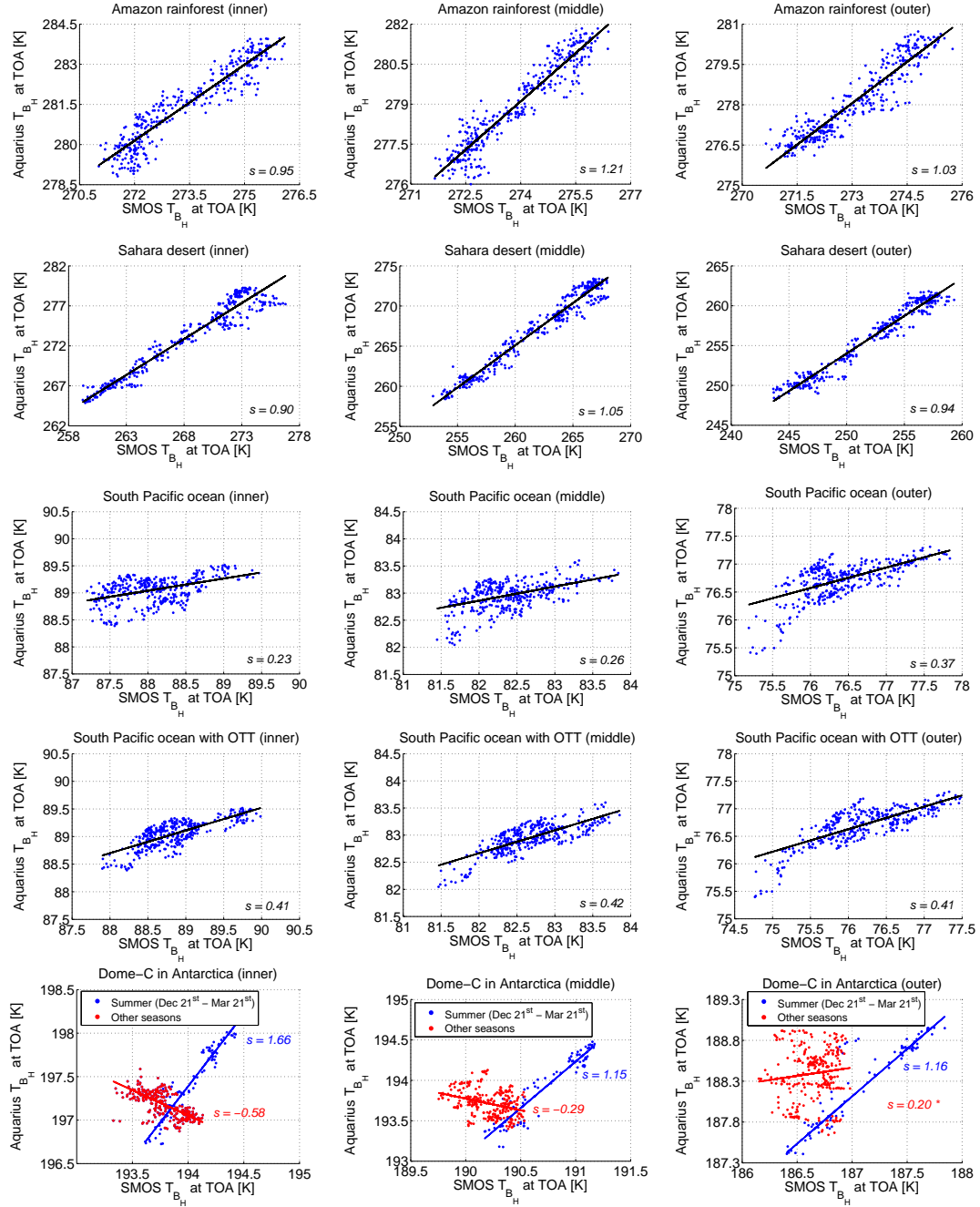
FIGURE 3.4: Scatter plots of Aquarius T_{B_H} *vs* SMOS T_{B_H} over target areas sorted by rows: Amazon rainforest (first row), Sahara desert (second row), South Pacific Ocean (third row), South Pacific ocean with OTT applied to SMOS data (fourth row), and Dome-C in the Antarctica (fifth row). Different incidence angles are placed by columns: inner ~29.36° (left), middle ~38.49° (centre) and outer ~46.29° (right) beams. Dynamic ranges are fixed, being 6 K for Amazon, 20 K for Sahara, 3 K for South Pacific, and 2 K for Dome-C. Over Dome-C, the Austral summer (in blue) is distinguished from the rest of the seasons (in red). The solid line represents the robust linear regression. Slope values s from the linear fit are shown in the plots. Non-significant slopes ($p_{value} > 0.05$) are marked with an asterisk.
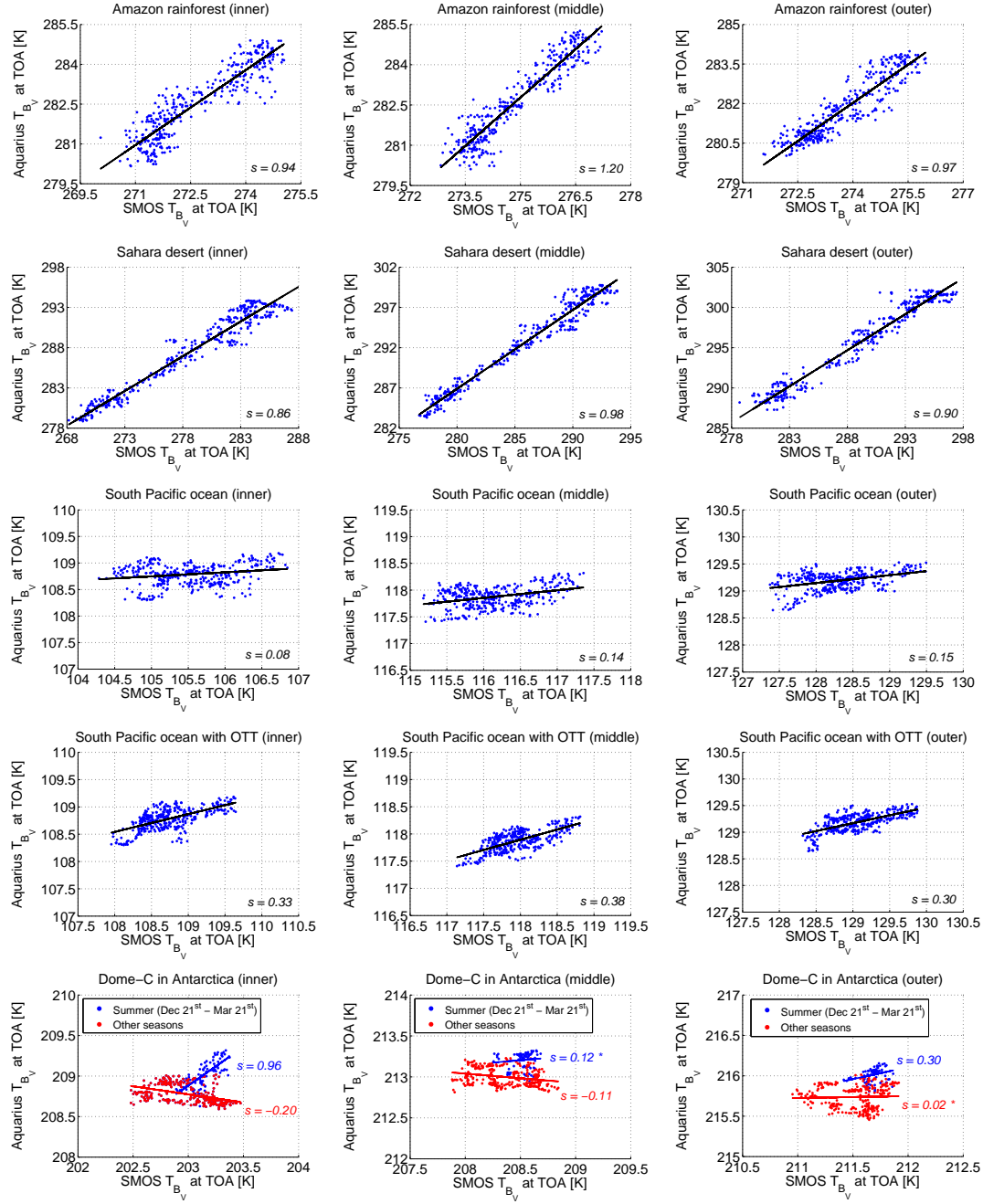
FIGURE 3.5: Same as for Fig. 3.4 , but for V-pol (T_{B_V}).

3.4.3 Statistical analysis

Statistical scores, namely, the mean, the standard deviation (std), the Root Mean Square Difference (RMSD), the correlation (R), the T_B difference (Aquarius T_B minus SMOS T_B), and the slope (s) are summarized in Tables 3.3 and 3.4 for H-pol and V-pol, respectively. Non-significant correlations or slopes are marked with an asterisk. Results are in agreement with the corresponding scatter plots in Figs. 3.4 and 3.5. Correlation is very strong over land (R>0.9) and decreases over sea (before OTT: R≈0.23 to 0.68, after OTT: R≈0.63 to 0.80). Over ice, the correlations are R≈0.74 to 0.96 in the Austral summer and R≈0.24 to 0.65 during other seasons. Correlation and slope values are systematically higher at H-pol than at V-pol, revealing that there is a higher degree of linearity between SMOS and Aquarius at H-pol than at V-pol.

TABLE 3.3: Statistics for horizontal polarization (T_{B_H})

Target region	Beam	Aquarius mean ± std [K]	SMOS mean ± std [K]	Aquarius-SMOS RMSD [K]	R	Difference [K]	Slope s
Amazon	inner	281.46 ± 2.49	273.41 ± 6.48	8.07	0.94	8.05	0.95
	middle	278.93 ± 3.76	273.88 ± 5.69	5.09	0.94	5.05	1.21
	outer	278.18 ± 3.17	273.12 ± 6.52	5.08	0.93	5.05	1.03
Sahara	inner	273.15 ± 1.20	268.38 ± 7.31	4.95	0.97	4.77	0.90
	middle	267.05 ± 1.17	261.89 ± 6.97	5.25	0.98	5.16	1.05
	outer	256.05 ± 1.98	252.22 ± 8.96	3.94	0.98	3.83	0.94
South Pacific	inner	89.04 ± 0.29	88.08 ± 1.88	1.06	0.48	0.96	0.23
	middle	82.95 ± 0.29	82.39 ± 2.16	0.69	0.56	0.56	0.26
	outer	76.70 ± 0.32	76.40 ± 1.88	0.49	0.68	0.30	0.37
South Pacific *(with OTT applied to SMOS data)*	inner	89.04 ± 0.29	88.85 ± 1.06	0.35	0.76	0.19	0.41
	middle	82.95 ± 0.29	82.67 ± 1.04	0.42	0.78	0.28	0.42
	outer	76.70 ± 0.32	76.20 ± 1.13	0.63	0.80	0.50	0.41
Dome-C *(Austral summer)*	inner	197.45 ± 3.07	194.04 ± 4.80	3.42	0.96	3.41	1.66
	middle	193.93 ± 2.81	190.74 ± 4.78	3.19	0.95	3.19	1.15
	outer	188.32 ± 2.67	187.12 ± 5.50	1.21	0.91	1.20	1.16
Dome-C *(other seasons)*	inner	197.18 ± 2.78	193.78 ± 4.86	3.41	0.65	3.40	-0.58
	middle	193.72 ± 2.64	190.21 ± 4.81	3.52	0.33	3.51	-0.29
	outer	188.38 ± 2.40	186.64 ± 5.47	1.77	0.07*	1.74	0.20*

* Non-significant values of correlations or slopes (p_{value} >0.05).

TABLE 3.4: Statistics for vertical polarization (T_{B_V})

Target region	Beam	Aquarius mean ± std [K]	SMOS mean ± std [K]	Aquarius-SMOS RMSD [K]	R	Difference [K]	Slope s
Amazon	inner	282.55 ± 2.19	272.70 ± 5.63	9.86	0.91	9.85	0.94
	middle	282.67 ± 3.31	274.92 ± 5.17	7.77	0.94	7.75	1.20
	outer	281.84 ± 2.39	273.80 ± 4.57	8.05	0.92	8.03	0.97
Sahara	inner	287.37 ± 1.17	278.50 ± 7.43	8.97	0.97	8.87	0.86
	middle	292.88 ± 1.06	286.10 ± 7.89	6.86	0.98	6.78	0.98
	outer	295.86 ± 1.76	289.27 ± 9.30	6.69	0.98	6.59	0.90
South Pacific	inner	108.78 ± 0.29	105.52 ± 1.94	3.30	0.23	3.26	0.08
	middle	117.87 ± 0.28	116.13 ± 2.01	1.80	0.38	1.74	0.14
	outer	129.19 ± 0.27	128.31 ± 1.63	0.97	0.43	0.88	0.15
South Pacific *(with OTT applied to SMOS data)*	inner	108.78 ± 0.29	108.74 ± 1.04	0.30	0.63	0.04	0.33
	middle	117.87 ± 0.28	117.94 ± 1.02	0.27	0.69	-0.07	0.38
	outer	129.19 ± 0.27	129.06 ± 1.09	0.31	0.67	0.13	0.30
Dome-C *(Austral summer)*	inner	209.02 ± 2.22	203.15 ± 3.93	5.87	0.74	5.87	0.96
	middle	213.20 ± 1.52	208.52 ± 3.65	4.68	0.09*	4.68	0.12*
	outer	216.00 ± 1.18	211.68 ± 3.15	4.33	0.27	4.32	0.30
Dome-C *(other seasons)*	inner	208.78 ± 2.03	202.99 ± 3.81	5.79	0.42	5.79	-0.20
	middle	213.00 ± 1.45	208.36 ± 3.63	4.65	0.24	4.64	-0.11
	outer	215.73 ± 1.17	211.52 ± 2.95	4.22	0.03*	4.21	0.02*

* Non-significant values of correlations or slopes (p_{value} >0.05).

Note that Aquarius T_B are warmer than SMOS T_B over all study areas. The difference is higher over warmer targets with ∼5 K (∼8 K) for H-pol (V-pol) polarization over land. This difference decreases with colder targets being ∼3 K (∼5 K) for H-pol (V-pol) polarization over ice and ∼0.6 K (∼2 K) for H-pol (V-pol) polarization over sea. In the latter, the difference decreases significantly after applying the pixel bias correction down to ∼0.3 K (∼0.1 K) for H-pol (V-pol) polarization. It has been checked that differences over sea are not due to different wind conditions, affecting SMOS and Aquarius during the 7-day period. Since the difference between SMOS and Aquarius T_B is found to be target dependent, it can be argued that there is a bias and also a non-linear effect between the two instruments.

Statistics are also computed using $I/2$. The obtained results, included in Appendix B (see Table B.1), are in line with those obtained for H-pol and V-pol. This ensures that the differences in the SMOS and Aquarius Faraday corrections does not have any impact in the inter-comparison analysis. Additionally, statistics obtained over Dome-C region using different data versions at H-pol are summarized in Appendix B (see Table B.2). They show that a similar behaviour is

present along different data versions, with a better agreement between SMOS and Aquarius T_B during the Austral summer than in the other seasons.

The noise level of each instrument is calculated from the temporal standard deviation (std) of the observations. In percent (std divided by mean), Aquarius noise varies from $\approx$0.2 to 0.4% over sea, from $\approx$0.5 to 1.5% over ice and from $\approx$0.4 to 1.4% over land. SMOS noise varies from $\approx$1.3 to 2.5% over sea, from $\approx$1.5 to 3% over ice and from $\approx$1.7 to 3.5% over land. This is consistent with the topology of the radiometers, since Aquarius is a real aperture Dicke radiometer and SMOS is a synthetic aperture radiometer, which involves T_B image reconstruction. Currently, the OTT reduces the image pixel biases within the FOV to a large extent. In this study, the application of the OTT results in an improvement of $\sim$30-40% in South Pacific, obtaining a noise level from $\approx$0.8 to 1.5% over sea.

3.4.4   Temporal analysis

Temporal evolution of SMOS and Aquarius T_B during year 2012 have also been analyzed. The T_B variations are displayed in Fig. 3.6. The corresponding yearly mean value has been subtracted ($\Delta T_{B_{pol}} = T_{B_{pol}} - \overline{T_{B_{pol}}}$, where the subscript *pol* indicates the polarization (H-pol or V-pol, respectively), in order to show the full variability with enough detail. Dynamic ranges are also fixed, being 6 K for Amazon, 20 K for Sahara, 3 K for South Pacific, and 2 K for Dome-C. Results show that SMOS T_B present higher temporal fluctuations than Aquarius ones over all regions due to the nature of the instrument.

Over land, SMOS and Aquarius T_B have a similar seasonal behaviour. In the Amazon, lower T_B are obtained with the two radiometers during the first half of the year, coincident with the rainy season, than in the second half of the year, corresponding to the not-so-rainy season. In the Sahara, higher T_B are observed both in SMOS and Aquarius from April to November due to the very high temperatures at that time of the year. Over sea, SMOS T_B show higher seasonal variability than over land. In the South Pacific, SMOS T_B have a lower variability after applying the pixel bias correction, particularly at vertical polarization. In Dome-C, both radiometers show a more stable T_B at V-pol than at H-pol, which may be due to Sun scattering contributions, since the reflection coefficient is larger at H-pol than at V-pol. A seasonal phenomenon is also observed. The SMOS and Aquarius T_B vary in phase along time during the Austral summer. In contrast, SMOS and Aquarius T_B vary in opposite phase in the other seasons. One reason for this may be that Sun zenith angle variations are affecting SMOS and Aquarius observations in a different way, depending on the period of the year. Also, the upper 10 m experience seasonal temperature changes in the order of 30 °C [Floury *et al.*, 2002]. We assume that these temperature variations could affect the ice crystal size and shape, modifying the microwave emission of the ice surface in scales resolved by SMOS and not by Aquarius. Spatial inhomogeneities over the Dome-C area were found during an airborne campaign using the EMIRAD-2 L-band radiometer [Kristensen *et al.*, 2013]. Expected high values of T_B appeared in the Northern side, while other unexpected inhomogeneities were observed around Concordia station and the Western side.

Theoretically, the L-band penetration depth of ice and snow is of hundreds of meters. As ice and snow at Dome-C are very dry, we thought that L-band penetration in this area could be more than hundreds of meters. In view of the results presented in this study, we hypothesize the penetration depth may be significantly higher and T_B observations are being influenced by geophysical elements greatly affecting emissivity, such as the bedrock surface [Fretwell *et al.*, 2013] or the presence of subglacial lakes [Wright & Siegert, 2012].
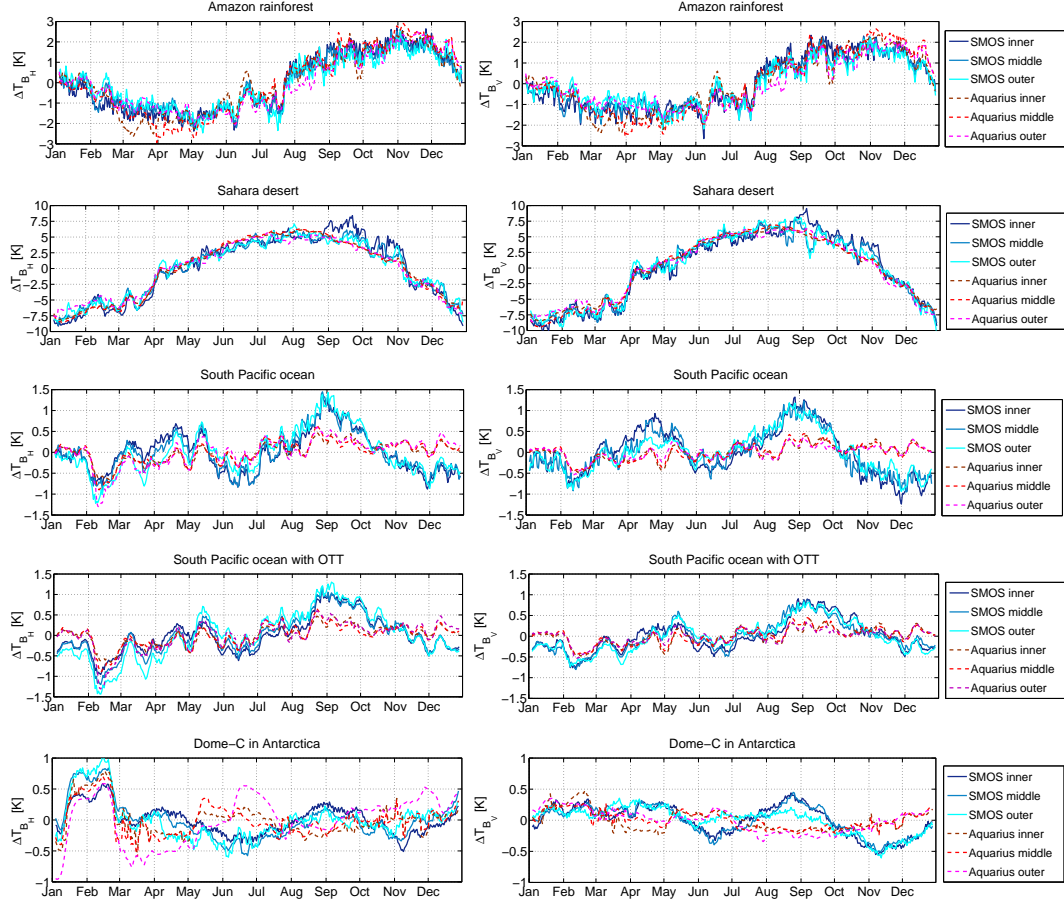
FIGURE 3.6: SMOS (bluish solid lines) and Aquarius (reddish dashed lines) T_B variations subtracting the corresponding yearly mean value ($\Delta T_{B_{pol}} = T_{B_{pol}} - \overline{T_{B_{pol}}}$, where the subscript *pol* indicates the polarization, H-pol or V-pol, respectively) over target areas sorted by rows: Amazon rainforest, Sahara desert, South Pacific ocean without OTT applied to SMOS data, South Pacific with OTT applied in SMOS data, and Dome-C in Antarctica. Polarizations are by columns: horizontal (left) and vertical (right). Different beams (inner, middle and outer) are shown by colours on graduated shading.

3.5   Conclusions

For the first time, there were two satellite missions in orbit with L-band radiometers on-board: SMOS and Aquarius. In this work, an inter-comparison of SMOS T_B *vs* Aquarius T_B has been performed over four selected targets: the Amazon rainforest, the Sahara desert, the Dome-C in Antarctica, and the South Pacific ocean. Radiometric observations along 2012, acquired independently for each instrument, are therefore compared over land, ice and sea areas, covering a large dynamic range.

This paper differs from previous works on SMOS and Aquarius comparisons on the use of a 7-day window averaging. The proposed technique allows to do inter-comparison in any latitude and to collect a fair amount of data for robust statistics. The length of the window should be chosen to ensure that T_B values are preserved when averaging. Both ascending and descending orbits are used. The comparison is based on the analysis of the level of linearity, the correlation and the differences between SMOS and Aquarius T_B, using statistics along the whole year 2012.

There is a high correlation over land (R>0.9) and it decreases over sea (R≈0.23 to 0.68). Slope values obtained from a robust linear fit are close to 1 over land (s≈0.86 to 1.21) and lower over

sea ($s \approx 0.08$ to 0.37). Slopes are systematically higher at horizontal than at vertical polarizations. Also, slopes are higher at high incidence angles.

The Aquarius L2 T_B product has been produced using an ocean model as a reference during its calibration. In this study, an OTT obtained from an ocean model has been applied to SMOS data to reduce the pixel bias existing in the FOV. Results show the inter-comparison is significantly improved over sea when applying the OTT, with increasing correlation ($R \approx 0.63$ to 0.80) and slope values ($s \approx 0.30$ to 0.42). Also, Aquarius T_B are corrected for the reflected galactic radiation, but this correction is not applied to SMOS T_B.

Aquarius is systematically measuring warmer T_B than SMOS. There is a higher difference over land targets ($\sim$5-8 K). This difference decreases over colder targets ($\sim$3–5 K over ice, and $\sim$0.1–0.3 K over sea, after OTT). This indicates there may be a non-linear effect between the two radiometers, and not only a bias.

SMOS and Aquarius T_B have similar seasonal cycles over land. Nevertheless, SMOS T_B show higher seasonal variability than Aquarius over sea. In addition, a seasonal effect is observed in the Dome-C region. The correlation associated to the Austral summer is high ($R \approx 0.74$ to 0.96) and it decreases in the other three seasons ($R \approx 0.24$ to 0.65). Also, two different slopes are shown in opposite sign (Dome-C Austral summer: $s \approx 0.30$ to 1.56, other seasons: $s \approx -0.11$ to -0.77).

The East Antarctic Plateau, particularly the Dome-C area has been used as a test site for calibrating and validating data of satellite-borne microwave radiometers since the 1970's [Hollinger *et al.*, 1990, Fily & Benoist, 1991, Macelloni *et al.*, 2006, 2013]. However, the analysis performed in this work evidences some spatial inhomegeneities in this area that can be detected with L-band radiometers, in line with the conclusions achieved in an airborne experiment [Kristensen *et al.*, 2013]. Consequently, some studies for having a better understanding of Dome-C emissivity at L-band are required before using this area as a calibration target.

Any study using a long term enviromental data record that spans multiple L-band missions requires consistent input observations. Results presented on this work are a contribution to understand the differences between SMOS and Aquarius measurements. Also, they could help in deciding future target areas for a vicarious calibration or to validate in a better way the T_B products from both radiometers using *in situ* measurements of a particular area. These results could also help the definition of the calibration and/or validation of the SMAP radiometer as well.

Chapter 4

SMOS & Aquarius brigthness temperature sensitivity over continental ice

Although SMOS and Aquarius missions were primarily designed for monitoring surface soil moisture (SM) and/or sea surface salinity (SSS), respectively, they are also sensitive to radiation emitted by ice surfaces. That sensitivity, together with the large number of observations due to their polar orbits, make them suitable for cryospheric studies. The sea ice thickness over the Artic Ocean has been estimated using SMOS [Kaleschke *et al.*, 2012] and Aquarius observations [De Matthaeis *et al.*, 2014]. In addition, an experimental SMOS SSS product over ocean at high latitudes and in the Arctic Sea is recently being distributed at the Barcelona Expert Centre (BEC) [BEC Team, 2016].

Since ground-based measurements over Antarctica are very sparse, remote sensing is particularly important for the study of the continental ice. It is known that microwave observations are affected by different physical characteristics of the icepack, such as ice density, physical temperature, grain size, etc., and their variations along depth [Jezek, 2012, Brogioni *et al.*, 2014, Brucker *et al.*, 2014, Macelloni *et al.*, 2015a, Brogioni *et al.*, 2015]. Here, SMOS and Aquarius data are used to investigate the Antarctica, the largest ice sheet on Earth, from an instrumental point of view.

4.1 State of the art

The Dome-C region, located at the East Antarctic Plateau, is regarded as an ideal natural laboratory for calibration/validation of space-borne microwave radiometers. This region was analyzed as a potential satellite calibration site [Six *et al.*, 2004, Cao *et al.*, 2010]. During last decades, it has been used as test site for different microwave radiometers, such as the Special Sensor Microwave Imager (SSM/I) [Hollinger *et al.*, 1990] and the Scanning Multichannel Microwave Radiometer (SMMR) [Fily & Benoist, 1991], as well as for comparing data of these radiometers [Jezek *et al.*, 1991]. Later, the Dome-C region has been used for calibration of the ESA's SMOS radiometer through several experimental campaigns [Macelloni *et al.*, 2006, 2013, 2015b]. At L-band, the thermal stability of this area has been confirmed [Macelloni *et al.*, 2006]. However, its use as an independent external calibration target has recently been questioned.

An inter-comparison study between SMOS and Aquarius observations over the Dome-C area revealed a seasonal effect producing an unusual distribution of the measured T_B (see Chapter3 and [Pablos *et al.*, 2014b]). In this line, some spatial inhomegeneities around Dome-C were detected using L-band airborne observations from the DOMECair campaign [Kristensen *et al.*, 2013] and also with satellite observations [Pablos *et al.*, 2014b]. These results suggest that a better understanding of the Antarctic ice emissivity would be needed in order to use Dome-C as a reference calibration target for present and upcoming L-band missions.

This study evidences the influence of the Antarctic ice thickness spatial variations on the measured SMOS and Aquarius T_B. The theoretical maximum L-band penetration depth has been estimated to understand the possible contributions to the observed signals. A 3-months no-daylight period during the Austral winter has been selected to ensure that spatial variations are independent of surface temperature changes and four transects over East Antarctica have been used to study these variations. The possible effects of bedrock and/or basal hydrology on the acquired radiometric signals have also been analyzed. The content of this Chapter has been published in a journal [Pablos *et al.*, 2015a] and a symposium [Pablos *et al.*, 2015b].

4.2 Datasets

4.2.1 Antarctic ice sheet

The Antarctic continent is considered as a cold desert because is extremely dry, with only 166 mm of average annual precipitation. Also, its air relative humidity is often as low as 0.03 %, the temperature is always below freezing (with a yearly average of -48°C), even during the Austral summer, and the snow on the surface never melts, but accumulates year-by-year forming stratigraphic layers [BAS, 2009]. An scheme of the bed topography, sea level, and ice sheet from the Western to the Eastern part of Antarctica is shown in Fig. 4.1, where it can be observed that the West Antarctic ice sheet is grounded below sea level.
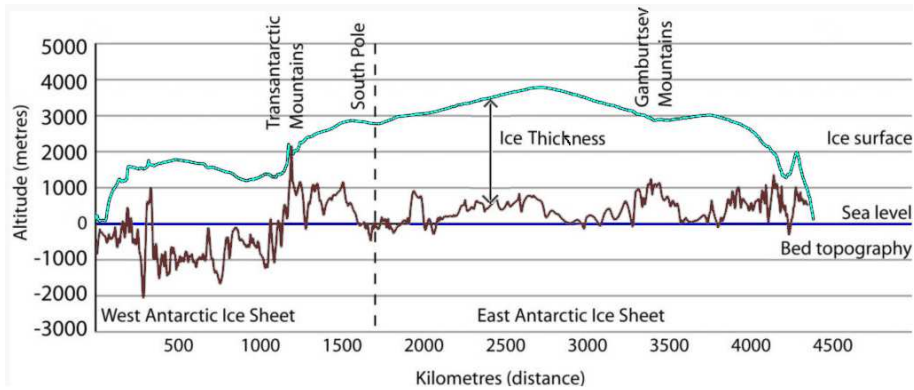
FIGURE 4.1: Scheme of the bed topography, sea level, and ice sheet from the Western to the Eastern part of Antarctica. Adapted from Fretwell *et al.* [2013].

The Antarctic ice sheet datasets used in this study are obtained from the Bedmap2 project [Fretwell *et al.*, 2013]. It contains a suite of 1-km regular gridded products for ice surface elevation, ice thickness and subglacial bedrock elevation of the Antarctica. The mean uncertainty for both the subglacial bedrock elevation and ice thickness is ∼250 m. The most recent Antarctic subglacial lakes inventory obtained from [Wright & Siegert, 2012] is also used. Currently, this dataset includes the location for 379 known subglacial lakes.

4.2.2 SMOS data

The SMOS T_B at the antenna reference plane are obtained from the L1C v.505 products. Firstly, these T_B have been screened out for detected RFI (strong, point source and tails), and also for the Sun (glint area, aliases and tails), and Moon (aliases) contamination, using the corresponding flags provided with the products. Later, geometric and Faraday corrections have been applied to obtain T_B at the top of the atmosphere (TOA), using Eq. (2.20). Finally, all SMOS T_B in an incidence angle range of $\theta\pm5°$ have been linearly interpolated to obtain them at the Aquarius incidence angles (see Table 2.1).

4.2.3 Aquarius data

The Aquarius T_B used are the L2 v.3 products, already provided at TOA. Additionally, they are filtered for RFI, reflected Sun, glint and Moon contamination (using the moderate and severe flags), and also for direct Sun contamination (using severe flag).

4.2.4 ECMWF ice surface temperature

The ice surface temperature over the Antarctica along 2013 has been used. It is provided by the European Centre for Medium-Range Weather Forecasts (ECMWF) from the ERA-Interim dataset. This dataset is a global atmospheric reanalysis covering the period since 1979 until June 2016. Its products can be freely downloaded through: `http://apps.ecmwf.int/datasets/`. Berrisford *et al.* [2011] provides detailed information about the available ERA-Interim products. In this study, the ice surface temperature used is, specifically, the skin temperature at thermal equilibrium corresponding to the top layer of the snowpack in a 0.125° regular grid.

4.3 Methodology

4.3.1 Study period for surface temperature independence

To minimize the impact of ice surface temperature changes on T_B variations and maximize the number of observations, both ascending and descending SMOS and Aquarius orbits during a 3-months no-daylight period at latitudes below 65° S for all possible longitudes have been selected (from May 6 to August 6, 2013) [Glarner, 2006]. This period contains June 21, the Austral winter solstice, as the center of the dataset, which corresponds to the day of the year with the largest latitude coverage at the Southern hemisphere without Sun ilumination. All observations from this period have been averaged to obtain mean SMOS and Aquarius T_B maps for each beam at H-pol and V-pol. Although Aquarius T_B are corrected for the reflected galactic contribution and SMOS T_B are not corrected, this difference does not affect observations over Dome-C due to its negligible impact at latitudes above 60° N and below 60° S [Tenerelli *et al.*, 2008]. Half of the First Stokes parameter ($I/2$) has also been used to analyze possible errors due to Faraday corrections.

4.3.2 Gridding procedure

A gridding procedure has been applied to data of both instruments. The spatial sampling has been selected to fulfill the Nyquist criterium according to the spatial resolution of each radiometer ($\sim$50 km in SMOS and $\sim$100 km in Aquarius). SMOS T_B have been projected from the ISEA 4H9 gridpoints [Sahr *et al.*, 2003] to a 25-km Equal Area Scalable Earth (EASE) grid [Brodzik & Knowles, 2002]. The T_B value of each cell was obtained as the average of all

observations that fall within the cell. The Aquarius T_B were defined by a latitude-longitude point at the center and four latitude-longitude points at the edges (-3dB) of its footprint, along and across beam tracks. Firstly, they have been projected to a 50-km EASE grid, using the cooordinates of the center and the edges, and observations within each cell have been averaged to obtain its T_B value. Secondly, they have been resampled to the 25-km EASE grid, the same grid used in SMOS, using a nearest-neighbour approach. The Antarctic datasets and the ECMWF ice surface temperature have also been projected to the same 25-km EASE grid.

4.3.3   Transects for spatial analysis

To assess the spatial variations on T_B, four transects (T1, T2, T3, and T4) over East Antarctica have been selected in representative areas with: (i) significant ice thickness variations, (ii) different ice thickness ranges, (iii) no correspondence between ice thickness and bedrock elevation, and (iv) presence of known subglacial lakes. Under these assumptions, the selected transects include most of the possible combinations of ice thickness and bedrock elevation (see Fig. 4.3).

4.3.4   Statistics to assess the ice effects

The correlation of SMOS and Aquarius T_B with two Antarctic geophysical variables (subglacial bedrock elevation and ice thickness) has been calculated. Also, the slope between the mean SMOS and Aquarius T_B and the ice thickness (s_i), including their standard deviation (std), has been estimated through a robust linear fit [DuMouchel & O'Brien, 1989] for all pixels in the map. Statistical scores with ice thickness have also been computed taking into account the presence of known subglacial lakes. They are displayed separately for the pixels with known subglacial lakes and for a representative selection of a comparable number of pixels without lakes, using a random selection of 172 pixels and 1000 Monte Carlo simulations. The selection of these 172 pixels has been performed in the same ice thickness range covered by pixels with lakes (from -4.1 km to -1.4 km), binned in 4 parts, and 43 pixels have been selected from each part, to ensure covering the entire range. Note this selection is needed to make statistics comparable, since only ∼154–193 out of ∼7664–9871 pixels contain known subglacial lakes.

4.3.5   Filtering of sea area and land-sea transitions

The sea area around the Antarctic continent has been removed to have only measurements over the continental ice sheet. In general, the SMOS and Aquarius orbit tracks are closer at the Poles than at the Equator. A circular area without data at the South Pole is produced in both radiometer observations due to their inclination (98.44° in SMOS and 98.0° in Aquarius). The different incidence angle is responsible for the slightly different unobserved area per beam. In SMOS, the Southernmost observable latitudes are 85.05° S for the inner, 86.31° S for the middle and 87.53° S for the outer beams. In Aquarius, they are 79.01° S for the inner, 77.90° S for the middle, and 76.55° S for the outer beams. Aquarius tracks produce a larger unobserved area at the South Pole that SMOS tracks. However, the same region without data has been considered in both SMOS and Aquarius for the spatial and statistical analysis. Also, coastal areas over land (∼150 km, approximately six 25-km EASE pixels) have been filtered to avoid the land-sea contamination effect.

4.4   Results and discussion

4.4.1   Overview of Antarctica

The ECMWF ice surface temperature over Antarctica has firstly been analyzed. Its mean and std for the entire year 2013 and the selected 3-months no-daylight period are shown in Fig. 4.2. It can be seen that the spatial distribution of the mean surface temperature is similar in both periods, having the warmer values at the coastal areas and the colder values over the East Antarctic Plateau. As expected, the ice surface temperatures are colder during the no-daylight period, and more stable (with lower std than the entire year 2013). This result supports the applied criterium for the temporal data selection and, therefore, it can be safely assumed that T_B variations are not due to ice surface temperature variations. Note that Dome-C is located in a region with low ice surface temperature.
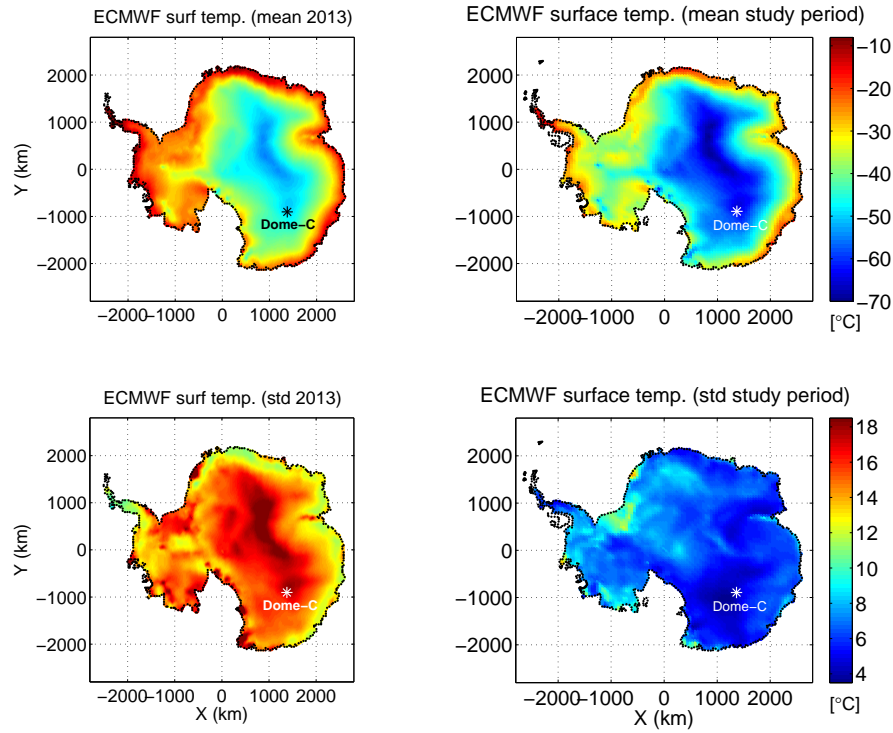
FIGURE 4.2: ECMWF mean (top) and std (bottom) ice surface temperature for entire year 2013 (left) and no-daylight period (right). The asterisk marks the location of Dome-C.

The Antarctic datasets used to analyze the sensitivity of T_B variations to geophysical variables (such as ice surface elevation, subglacial bedrock elevation and ice thickness) are displayed in Fig. 4.3. Ice surface elevation varies from 0 to $\approx$4 km above the sea level defined by the WGS-84 geoid and it is always positive. Subglacial bedrock elevation varies from $\approx$-2.2 km below to $\approx$2.2 km above the WGS-84 sea level and it could be positive or negative. Ice thickness, referred to the surface with positive axis defined upwards, called hereafter ice thickness level (IceTL), varies from 0 (at the coast) to $\approx$-4.3 km (around Dome-C area) and it is always negative. The negative sign has been included to better compare with the SMOS and Aquarius T_B. Then, the ice surface elevation is related to the IceTL and the bedrock elevation as:

$$IceTL = -(Surface - Bedrock).\tag{4.1}$$

A map showing the location of the selected transects as well as the pixels including at least one of the reported subglacial lakes is included. Two of the four transects (T1 and T2) are placed

along areas without known subglacial lakes, others (T3 and T4) are located in areas with a great amount of known subglacial lakes.
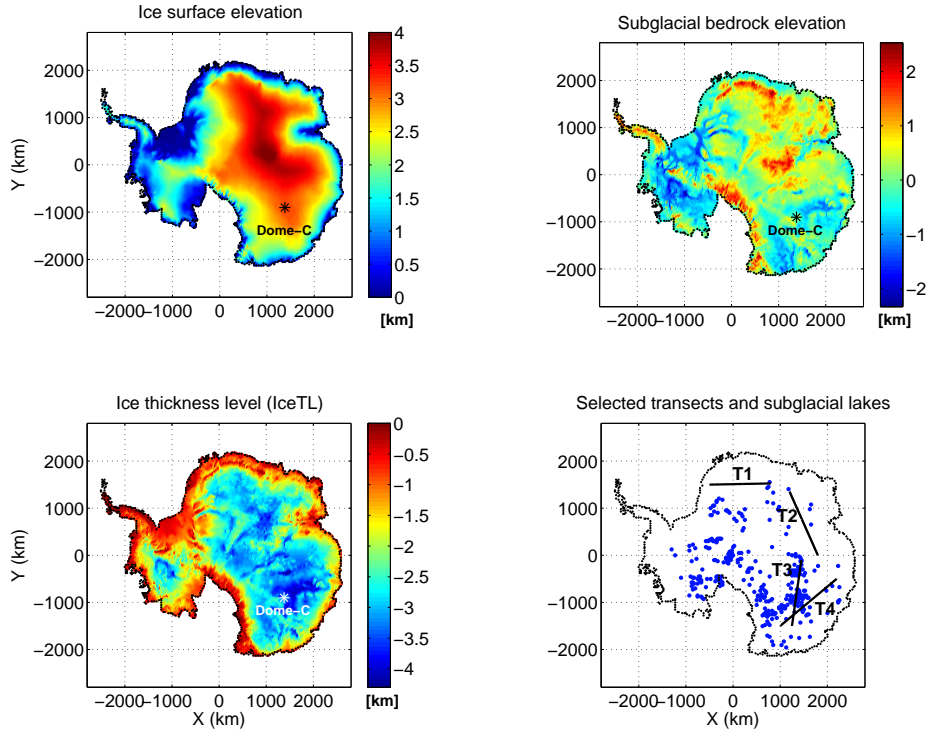
FIGURE 4.3: Ice surface elevation referred to WGS-84 (top left), subglacial bedrock elevation referred to WGS-84 (top right), and ice thickness level referred to surface (bottom left). The asterisk marks the location of Dome-C. Map of selected transects T1, T2, T3 and T4 in black solid lines and subglacial lakes depicted with blue squares (bottom right).

4.4.2 Maximum L-band penetration depth

Our approach to compute the maximum L-band penetration depth (δ_p) over the Antarctic ice sheet is mainly based on the estimation of the imaginary part of the ice dielectric constant, the so-called loss factor (ε''), and the use of Eq. 2.24 (see Subsection 2.2.1). At L-band, ε'' is a very low magnitude ($\sim 10^{-5}$), which is difficult to estimate accurately. Two models of ε'' for the Antarctic ice have been considered in this study: the pure ice model [Matzler *et al.*, 2006] and the icepack model [Sihvola & Kong, 1988]. A detailed description of these models is included in Subsections 2.2.2 and 2.2.3, respectively. The icepack model takes into account that the density of the Antarctic ice sheet increases exponentially with depth, from 379 kg·m^{-3} corresponding to the fresh snow up to 918 kg·m^{-3} corresponding to pure ice [Rist *et al.*, 2002] (see Subsection 2.2.4). The possible influence of fluctuations in the ice density profile and the snow grain size with depth, which may affect the estimation of ε'', are not considered in this study. A more complex formulation would be needed to include these effects, as described in Leduc-Leballeur *et al.* [2015]. Nevertheless, these fluctuations are important near the surface and tend to disappear with depth [Leduc-Leballeur *et al.*, 2015].

In both models, there is a strong dependence of ε'' on the physical temperature. Nevertheless, the lowest temperature is associated to the lowest ε'' for a constant frequency and, consequently, to the largest δ_p. For the pure ice model, the maximum δ_p has been estimated considering the ice surface temperature, which corresponds to the lowest value within the vertical ice profile. For the icepack, the temperature model described in Jezek *et al.* [2015] (see Subsection 2.2.5) has been used with the following parameters: ice surface temperature (-70° C, from ECMWF), geothermal

heat flux (47 mW·m^{-2}), ice thermal conductivity (2.7 W·m^{-1}.K^{-1}), ice thermal diffusivity (45 m^2·year^{-1}), ice thickness (4300 m, from Fretwell *et al.* [2013]), and snow accumulation rate (0.025–0.035 m·year^{-1}, from Macelloni *et al.* [2006]). In this model, the internal ice temperature is propagated from the surface to the bedrock with an exponential profile that increases with depth, in agreement with measurements from boreholes at the Vostok lake [Ritz, 1988] and at the Antarctic Moun and Neutrino Detector Array (AMANDA) observatory [Price *et al.*, 2002]. Theoretical estimations of δp may be dependent on the accuracy of the temperature dataset and/or model employed. The use of alternative datasets or *in situ* ice temperature observations will be considered subject of further research.

First of all, the consistency between the estimated δ_p using the two different models has been assessed. To do so, the icepack model has been applied using the density of the pure ice, to better compare with the pure ice model. As expected, the same δ_p values are obtained with both models at extreme ECMWF surface temperatures over Antarctica: $\delta_p \approx$204 m (-10° C) to 1258 m (-70° C). Also, δ_p is larger at lower temperatures in agreement with the theoretical background.
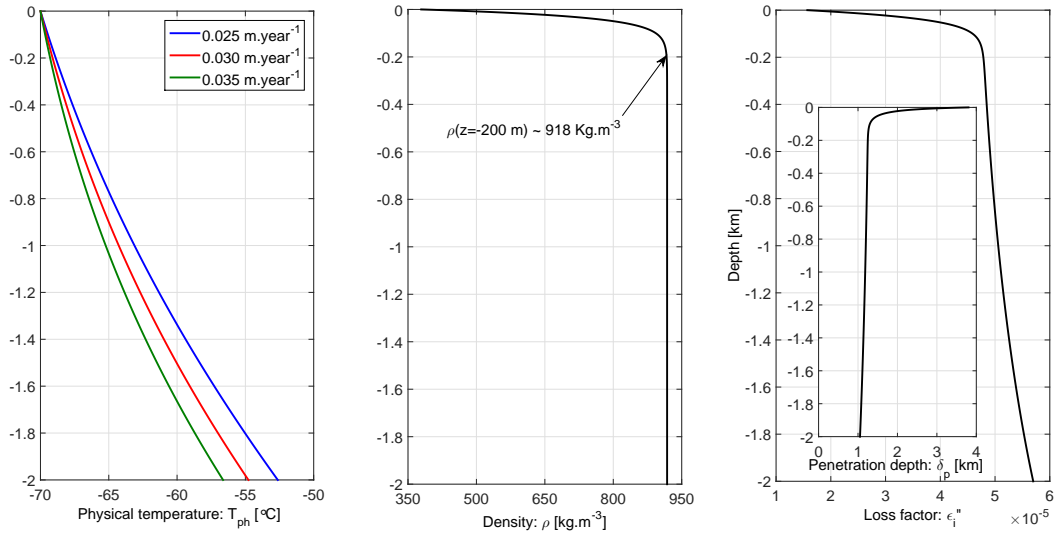
FIGURE 4.4: Physical temperature profiles (left) depending on the snow accumulation rate (blue: 0.025 m·year^{-1}; red: 0.030 m·year^{-1}; green: 0.035 m·year^{-1}). Exponential vertical ice density profile (middle), where the arrow marks the value of snow density at 200 m depth. Loss factor of the icepack model as a function of depth (left) using 0.03 m·year^{-1}. The corresponding penetration depth for each value of ε_i'' is included inside.

Figure 4.4 shows the internal ice temperature profiles depending on the snow accumulation rate (left), the vertical ice density profile (middle), and the loss factor of the icepack model (ε_i'') as a function of depth (right) using a snow accummulation rate of 0.03 m·year^{-1}. Its corresponding δ_p for each ε_i'' is included inside. It can be observed that the exponential internal ice temperature profile slightly increases with decreasing accumulation rates, having a low impact in the estimation of the penetration depth. Note that the exponential ice density profile increases very fast, up to a value of $\sim$918 kg·m^{-3} at 200 m depth that remains constant. The loss factor also has a quick increase from $\sim$1.6·10^{-5} at the surface to $\sim$4.8·10^{-5} at 200 m depth. This behaviour in the ε_i'' produces a very fast decrease of the δ_p up to a value $\sim$1.25 km at 200 m depth. Then, the maximum theoretical L-band penetration depth is estimated to be $\approx$1 to 1.5 km.

Results obtained in Fig. 4.4 (right) suggest that the subglacial bedrock is not contributing to the measured SMOS and Aquarius T_B, since it lies deeper ($\approx$2 to 4.3 km below the ice surface, except in the coastal areas) than the estimated maximum theoretical L-band penetration depth in the East Antarctic Plateau. In an experimental study carried out at Dome-C during December 2009 (Austral summer), in collaboration with the DOMEX-2 experiment [Macelloni *et al.*, 2013],

the δ_p of L-band Global Navigation Satellite Systems-Reflectometry (GNSS-R) signals into the ice was estimated to be $\approx$200 to 300 m [Fabra, 2013]. In this case, the reflected signals were acquired with an elevation angle of $\sim$45°, after travelling through the ice an approximate length of $\approx$570 to 850 m, considering both downward and upward paths. Nevertheless, our estimation was assuming the lowest ice surface temperature (-70° C) and nadir. These differences (incidence angle and ice surface temperature) may be responsible for the different predicted δ_p with respect to the estimation by the experimental study.

4.4.3 Aquarius & SMOS brightness temperature maps

The mean SMOS and Aquarius T_B maps over Antarctica at middle beam for the no-daylight period are presented in Fig. 4.5 at H-pol and V-pol. Color scale is adjusted from 170 K to 240 K to show the full spatial T_B variability over the continental ice sheet. It can be seen the different unobserved area depending of the instrument. As expected, vertical T_B are notably higher than horizontal T_B, but both polarizations and instruments reveal similar spatial patterns, presenting the warmer values at the coastal areas and colder values over the East Antarctic Plateau. In general, areas with subglacial lakes (see Fig. 4.3 (bottom right)) correspond to areas with the minimum values of ice surface temperatures (see Fig. 4.2 (top right)), minimum values of T_B and maximum ice thickness in absolute value (see Fig. 4.3 (bottom left)). Note that Aquarius T_B are slightly higher than SMOS T_B at both polarizations, which agrees with previous studies [Pablos *et al.*, 2014b]. Aquarius results are very similar to those provided by an independent study [Brucker *et al.*, 2013]. Also, similar results are obtained with the other two beams; they are included in Appendix C (see Figs. C.1 and C.4 for inner and outer beam, respectively).
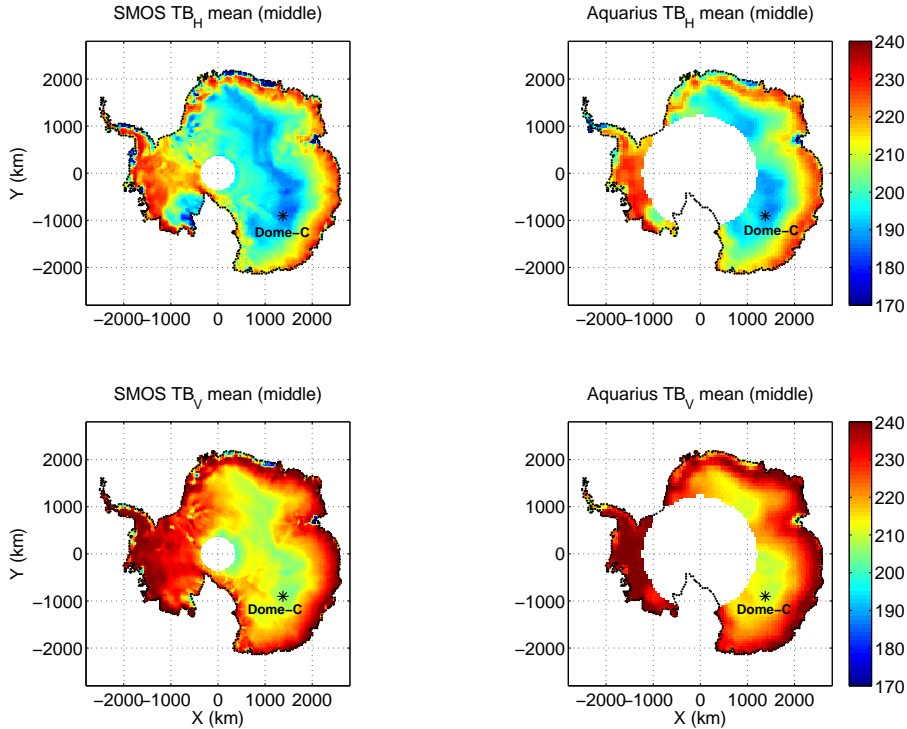
FIGURE 4.5: Mean SMOS (left) and Aquarius (right) T_B maps at middle beam over Antarctica during the no-daylight period at horizontal (top) and vertical (bottom) polarizations. The asterisk marks the location of Dome-C.
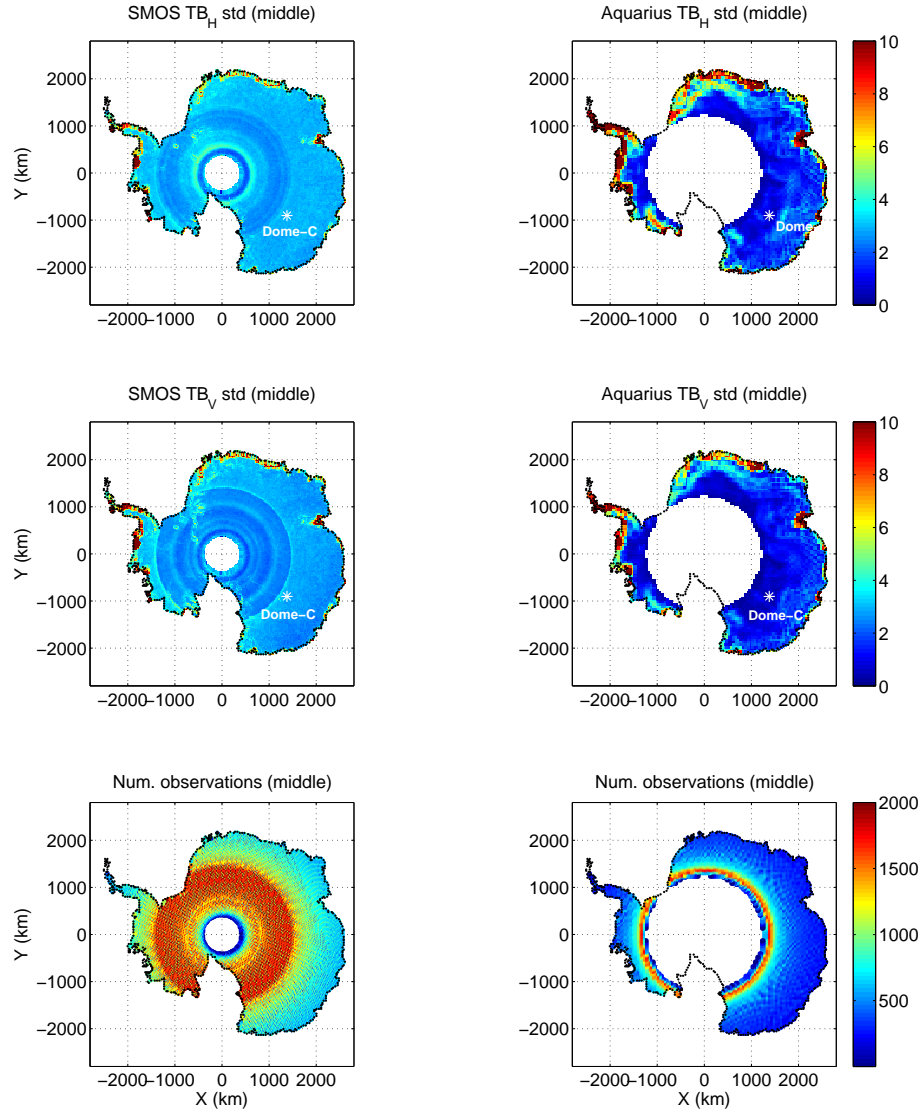
FIGURE 4.6: Std SMOS (left) and Aquarius (right) T_B maps at middle beam over Antarctica during the no-daylight period at horizontal (top) and vertical (center) polarizations, and number of observations within each 25-km EASE pixel (bottom). The asterisk marks the location of Dome-C.

Figure 4.6 shows the std SMOS and Aquarius T_B maps over Antarctica at middle beam for the no-daylight period at H-pol and V-pol polarizations, and the number of averaged observations within each 25-km EASE pixel. The vertical is more stable than the horizontal polarization in both instruments, in agreement with results obtained during DOMEX-2 experiment [Macelloni *et al.*, 2013]. Aquarius presents lower std values than SMOS. This fact is consistent with their instrument types, since Aquarius is a real aperture radiometer whereas SMOS is a synthetic aperture radiometer, inherently noisier due to the image reconstruction procedure. The Aquarius std maps exhibit some features of high T_B error values above the mean std, particularly in the coastal areas. This may be an incidence angle effect produced by abrupt ice surface changes due to strong topography or a physical effect by the ice dynamics of East Antarctica [Rignot *et al.*, 2011]. These features are not so remarkable in SMOS and the reason for that is not clear. In the SMOS std maps, the different number of averaged observations per cell is responsable of the non-geophysical circular artifacts with high std values. Note the different number of averaged observations and also the different unobserved area depending of the instrument. Similar results are obtained with the other two beams; they are included in Appendix C (see Fig.C.2 and C.5 for inner and outer beam, respectively).

4.4.4 Ice effects on SMOS and Aquarius brightness temperatures

SMOS and Aquarius T_B variations ($\Delta T_B = T_B - \overline{T_B}$) for the middle beam at H-pol and V-pol, and IceTL along the four transects are shown in Fig. 4.7. The T_B values along each transect are computed from the mean SMOS and Aquarius T_B maps. The corresponding mean value ($\overline{T_B}$, included between brackets in the legends) has been subtracted to better compare the variations of both instruments at the same plot. It is assumed that the impact of changes on ice surface temperature, accumulation rate, and snow density is negligible through transects during the winter period relative to the IceTL variations. The subglacial bedrock and ice surface elevations have been included. Also, the location of known subglacial lakes along the transects is marked with a blue bar in the X-axis to assess its impact on the observed T_B. Note that the T_B changes of both radiometers follow the overall trend in all transects, with a closer agreement when the IceTL presents slow spatial variations, as occur in T1. In the other transects (T2, T3, and T4), the agreement is limited, since IceTL exhibits fast spatial variations that cannot be resolved by SMOS and Aquarius. Nevertheless, SMOS T_B have a better agreement with the IceTL variations than Aquarius T_B, which can be explained by its higher spatial resolution ($\sim$50 km in SMOS *vs.* $\sim$100 km in Aquarius). Similar results are observed at both polarizations.

When analyzing the influence of subglacial water in Fig. 4.7, it is important to note that transects T3 and T4 have the highest presence of known subglacial lakes (see Fig. 4.3 (bottom right)). We hypothesize that the subglacial lakes and possible water connections between them may have an influence on the vertical physical temperature profile, and consequently, modify the dielectric properties and the emissivity of the ice layers overlaying these lakes. However, there is not a clear response of measured T_B at the subglacial lakes location during the spatial analysis. Ice surface elevation presents smoother variations than the observed T_B in all transects. Note that T1 differs from the other three transects in the larger dynamic range of the ice surface elevation (from 0.5 km to 3.5 km). Also, the ice surface elevation monotonically increases in T1 and T3, whereas it decreases and later increases in T2, or viceversa, in T4. Note that the IceTL and bedrock elevation have similar variations in T2, T3 and T4, but not in T1, covering most of possible scenarios. A similar behaviour is obtained with the other two beams, as shown in Appendix C (see Fig.C.3 and C.6 for inner and outer beam, respectively). Therefore, the use of a different incidence angle is not affecting the spatial analysis. Additionally, a similar behaviour is observed when using the half of First Stokes (see Fig. C.7). Then, results are not affected by Faraday rotation.

The correlation of SMOS and Aquarius T_B for the middle beam at H-pol and V-pol with subglacial bedrock (R_b) and IceTL (R_i) over the whole Antarctica, and the slope of the linear regression respect to the IceTL (s_i) for all pixels in the map and the error estimation (std) are summarized in Table 4.1. As expected from the maximum theoretical estimation of δ_p, no correlation is observed with the bedrock in SMOS neither in Aquarius ($R_b \approx$0.15 to 0.19). Instead, correlations with IceTL are $R_i \approx$0.61 to 0.72, being similar for both instruments and higher at V-pol than at H-pol. Slopes indicate that there is a sensitivity of $\approx$8.7 to 9.8 K/km to variations in IceTL.

Table 4.1 also presents statistical scores with IceTL considering separately pixels with known subglacial lakes and a representative selection of a comparable number of pixels without lakes. Although the number of data points is considerably reduced in these cases, statistics are significant ($p_{value} <$0.05, at a 95 % of significance level). Results show that the presence of subglacial water does not have an important impact in terms of correlation both in SMOS and Aquarius. However, lower slopes are obtained considering the pixels with known subglacial lakes in both polarizations (with $s_i \approx$5.7 to 7.6 K/km *vs.* without $s_i \approx$9.0 to 9.9 K/km). The estimated errors in the slopes (std values) are higher than when all pixels are considered, but remain within reasonable bounds. These results suggest that the presence of subglacial water may be affecting the measured T_B. It is known that Antarctica has a rich basal hydrological system, with water transferring events among its many subglacial lakes. The spatial distribution of the physical temperature near the ice-bedrock interface depends on the geothermal heat flux and this basal system. We hypothesize that the presence of subglacial lakes and the possible water connections between them may have an effect on the vertical temperature profile and, consequently, may

modify the dielectric properties and the emissivity of the ice layers overlaying these lakes. A dedicated study would be needed to obtain conclusive results regarding the effect of the presence of subglacial lakes on L-band Antarctica's emissivity, which is out of the scope of this research. Similar results are obtained with the other two beams and when using the half of First Stokes, as shown in Appendix C (see Tables C.1, C.2 and C.3 for inner and outer beams, and $I/2$, respectively). In general, the correlation with bedrock decreases whereas correlations with IceTL increases with higher incidence angles in both polarizations and when using $I/2$. The influence of the ice surface topography on the SMOS and Aquarius T_B, that could be related to the impact of the ice thickness, would be subject of further research. Only results with $I/2$ and middle beam will be shown hereafter.
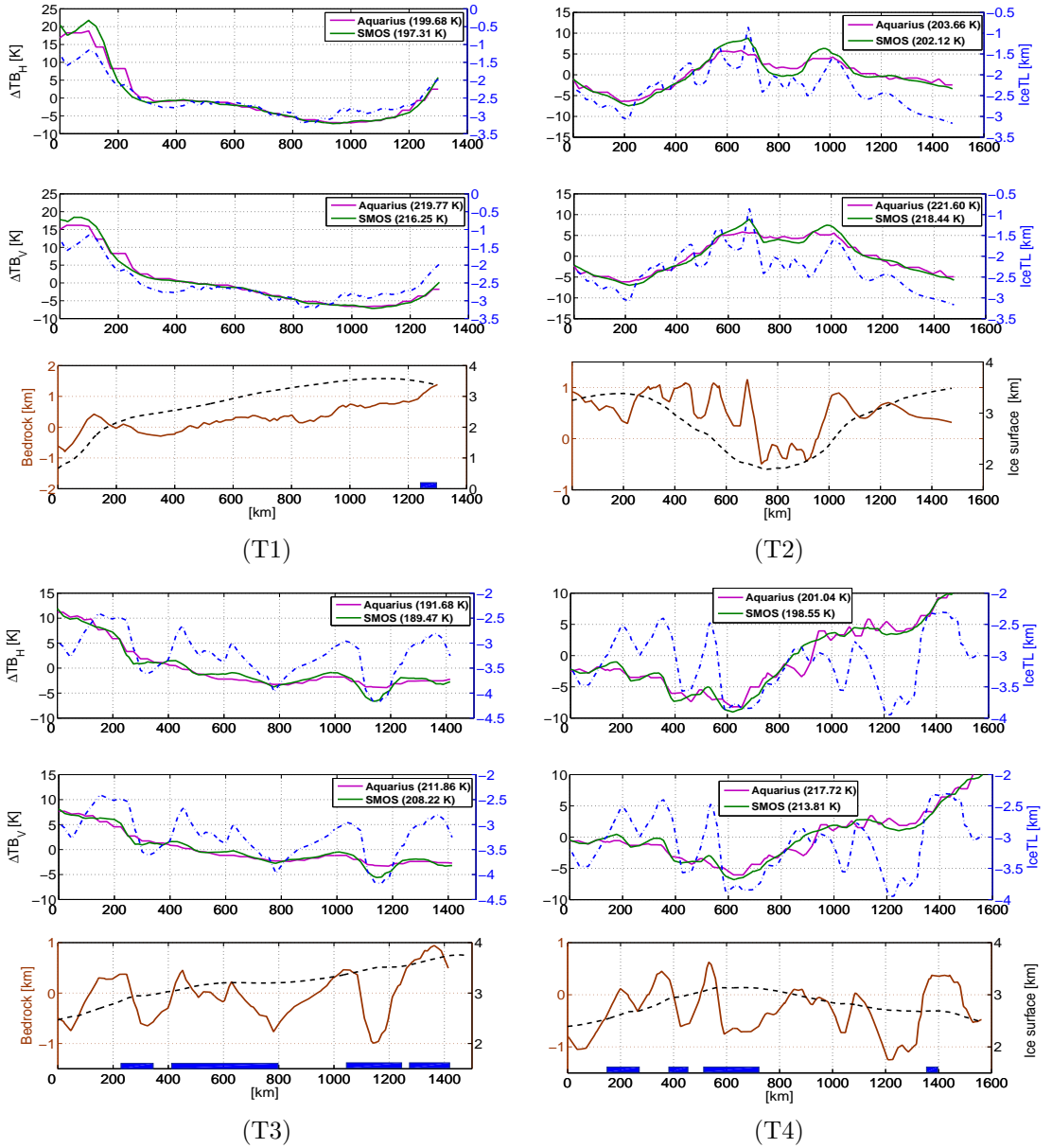
FIGURE 4.7: SMOS and Aquarius T_B variations ($\Delta T_B = T_B - \overline{T_B}$) for the middle beam (pink and green solid lines, respectively) at horizontal and vertical polarizations, and ice thickness level (blue dashed line) along each transect. Legends display $\overline{T_B}$ values subtracted. The bedrock (brown solid line), the ice surface (black dashed line) and the presence of subglacial lakes (marked with a blue bar in the X-axis) are also displayed.

TABLE 4.1: Correlation of SMOS and Aquarius T_B at middle beam with subglacial bedrock (R_b) and ice thickness (R_i), and slope respect to the ice thickness (s_i) and the error estimation for all pixels. Statistics with ice thickness are also displayed separately for pixels with known subglacial lakes and for a representative selection of a comparable number of pixels without lakes. All values are significant (p_{value} <0.05).

Radiometer	Polarization		All pixels		Pixels with lakes		Pixels without lakes	
		R_b	R_i	s_i [K/km]	R_i	s_i [K/km]	R_i	s_i [K/km]
SMOS	Horizontal	0.15	0.63	9.8±0.1	0.67	7.6±0.6	0.67	9.9±0.8
	Vertical	0.16	0.72	9.2±0.1	0.72	6.0±0.4	0.77	9.4±0.6
Aquarius	Horizontal	0.18	0.61	9.3±0.1	0.66	6.4±0.5	0.66	9.5±0.8
	Vertical	0.19	0.69	8.7±0.1	0.70	5.7±0.4	0.75	9.0±0.6

Figure 4.8 shows the scatter plots of SMOS and Aquarius $I/2$ at middle beam *vs.* subglacial bedrock and IceTL. In the case of IceTL, pixels without and with known subglacial lakes (red and blue asterisk, respectively) are distinguished. Note that the $I/2$ as a function of bedrock seems to be random in both radiometers, in agreement with results of Table 4.1. This, together with the maximum estimated L-band penetration depth, supports that the bedrock is not contributing to the Antarctica's emissivity. Instead, a linear trend could be identified in $I/2$ and IceTL distributions both in SMOS and Aquarius. Also, it can be observed that the pixels with subglacial lakes are, in general, concentrated in the lower values of $I/2$, specially for Aquarius. This seems to indicate that the presence of water underneath the ice influences the measured $I/2$. Similar results are obtained at H-pol and V-pol and when using other beams (not shown).
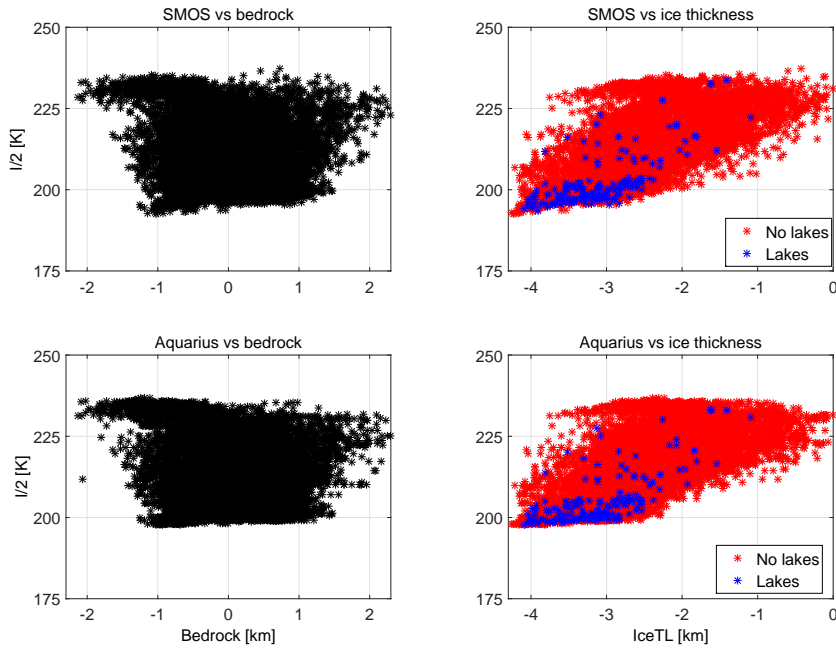
FIGURE 4.8: SMOS (top) and Aquarius (bottom) $I2$ at middle beam *vs.* subglacial bedrock elevation (left) and ice thickness level (right). In the last case, pixels without known subglacial lakes (red asterisks) and with lakes (blue asterisks) are distinguished.

As shown in Figs. 4.7 and 4.8, and in Table 4.1, there is a significant correlation between SMOS and Aquarius T_B and IceTL changes over Antarctica (R≈0.6 to 0.7). No significant correlation has been found with the bedrock (R≈0 to 0.2). Some studies pointed out the relationship between the bedrock and the measured SMOS T_B at the Dome-C region [Macelloni *et al.*, 2014, Skou *et al.*, 2015]. Hence, we looked at correlations over Dome-C and obtained values of R_i ≈0.5 to 0.6 for IceTL and R_b ≈0.4 to 0.5 for bedrock elevation. At Dome-C, there is a high degree of similarity between the bedrock and the IceTL variations as shown in Fig. 4.9, and this explains

the correlations found between T_B and the bedrock in this particular region. However, this relation was not found considering the entire Antarctica.
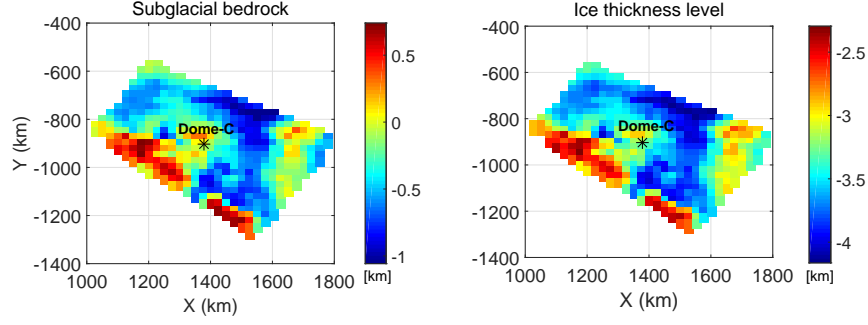
FIGURE 4.9: Subglacial bedrock elevation (left) and ice thickness level (right) at the Dome-C region defined by latitudes [78°S–72°S] and longitudes [116°E–130°E]
.

Figure 4.10 shows the spatial patterns of L-band T_B (left) and gravity (right) measurements acquired during an airborne field campaign carried out at Dome-C in Antarctica [Steinhage, 2013]. The images also show the flight tracks during the campaign. Note that there is a remarkable similarity between both patterns. This could be related to our findings. In addition, this would lead to new scientific discoveries beneath the surface of the Antarctic ice.
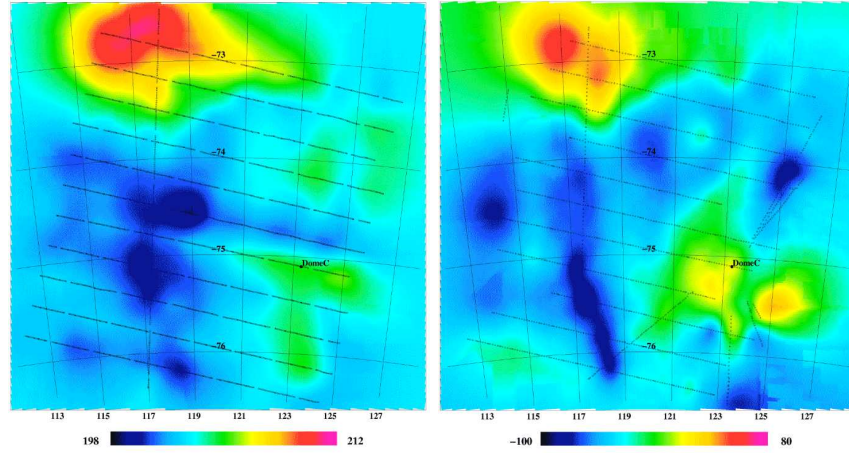
FIGURE 4.10: L-band T_B (left) and gravity (right) measurements acquired during an airborne field campaig at Dome-C [Steinhage, 2013].

4.5 Conclusions

The influence of the Antarctic ice thickness spatial variations in measured SMOS and Aquarius T_B changes has been explored. A 3-months no-daylight period during the Austral winter has been selected to ensure T_B variations are independent of ice surface temperature changes. The maximum theoretical L-band penetration depth has been estimated to understand the possible contributions to the observed signals. Spatial and statistical analysis have been performed, comparing both SMOS and Aquarius T_B changes with ice thickness and subglacial bedrock.

The L-band penetration depth over the Antarctic ice sheet has been estimated to be $\approx$1 to 1.5 km using the icepack dielectric constant model, and ice density and internal ice temperature profiles. Therefore, the subglacial bedrock, which lies deeper $\approx$2 to 4.3 km below the ice surface, seems that is not affecting the observed T_B.

A good agreement has been observed between SMOS and Aquarius T_B and ice thickness variations over the four selected transects on East Antarctica, except for the case of fast spatial variations, which are not resolved by SMOS neither Aquarius. Nevertheless, SMOS resolves better the ice thickness variations than Aquarius due to its higher spatial resolution. A linear trend has been identified between ice thickness changes and T_B of both instruments with slopes of ≈9.2 to 9.8 K/km for SMOS and ≈8.7 to 9.3 K/km for Aquarius. Correlations vary from R≈0.6 to 0.7, and they are higher for vertical than for horizontal polarizations, and increase with higher incidence angles. No correlation has been found between SMOS and Aquarius T_B and the bedrock elevation (R≈0 to 0.2) and its data distribution exhibits a random behaviour. Then, the Antarctica's emissivity seems to depend on the emission from ice layers well below the surface, but, in general, not from the subglacial bedrock which is much deeper than the estimated L-band penetration depth. Results show that the presence of subglacial lakes, which are generally located at ∼3 km depth, may influence the internal ice temperature profile and/or the dielectric properties of the ice layers above, affecting the observed T_B. This would be subject of further research.

This study could help in deciding future target areas over Antarctica for upcoming L-band missions. In view of the presented results, minimum ice thickness spatial variations is an additional aspect that should be considered when selecting a suitable Antarctic calibration/validation site for microwave radiometers, apart from temporal stability and spatial homogeneity. Also, this study could contribute to improve our understanding of the Antarctica's emissivity as a necessary step for the potential use of L-band radiometric observations in cryospheric studies.

Chapter 5

Microwave/optical synergy for multi-scale soil moisture sensing

Both SMOS and SMAP missions provide SM maps at a spatial resolution of ~40 km from passive L-band observations [Kerr *et al.*, 2016, Chan *et al.*, 2016]. This spatial resolution is enough for global-scale applications, such as flood and drought monitoring, and meteorological, ecological and hydrological model and forecasting [Ochsner *et al.*, 2013]. However, it is limited for regional and local-scale studies, where ~1–10 km are required. Different SM disaggregation algorithms have been developed to bridge this gap. For SMOS, most approaches are based on the synergy of passive microwave with ancillary data from optical visible/thermal infrared (VIS/TIR) observations, where the land surface temperature (LST) is a fundamental input variable measured at high spatial resolution, together with the Normalized Difference Vegetation Index (NDVI) [Piles *et al.*, 2011, Merlin *et al.*, 2012, Piles *et al.*, 2012, Song & Jia, 2013, Sánchez-Ruiz *et al.*, 2014, Piles *et al.*, 2014, Fang & Lakshmi, 2014, Piles *et al.*, 2016b]. For SMAP, disaggregation approaches are based on the synergy of passive with high spatial resolution active observations [Piles *et al.*, 2009, Das *et al.*, 2011, Guo *et al.*, 2013, Das *et al.*, 2014, Bruscantini *et al.*, 2015].

It is known that LST is related to SM (e.g., via its influence on the soil emission). Therefore, changes in SM significantly affect LST, and *vice versa*. Both SM and LST vary temporally, with the time of the day and the seasons, and spatially, with soil type and land cover. A better knowledge of the fundamental SM–LST link is required for refining the current SM retrieval or microwave/optical disaggregation algorithms related to evapotranspiration (ET) and vegetation status, and may also contribute to improve the representation of LST in hydrological and climate prediction models.

5.1 State of the art

Remotely sensed LST, acquired with TIR sensors, are routinely used in many operational applications, including weather forecasting. Polar orbiting satellites, such as NASA's Terra (1999–2020) and Aqua (2002–2020) missions, provide global LST maps at 1 km every 1-2 day using the Moderate-resolution Imaging Spectroradiometer (MODIS) sensor [Wan & Snyder, 1999]. Geostationary satellites (i.e., those with the same orbital period as the Earth's rotation) are able to provide continental coverage at a higher temporal resolution. The Spinning Enhanced Visible and InfraRed Imager (SEVIRI) sensor from the Meteosat Second Generation (MSG) mission (2002–2021) of ESA & European Organisation for the Exploitation of Meteorological Satellites (EUMETSAT) provides continental LST maps at 3 km every 15 min [Aminou *et al.*, 1997]. However, the effective temporal resolution of both polar and geostationary LST observations can be much lower than the theoretical value since optical observations, and particularly TIR observations, are masked in presence of cloud cover.

SM and LST are closely inter-related and their link is central to land-surface variables and processes such as soil emission, ET and thermal inertia. Soil emission is influenced by the SM and soil physical temperature. Owing to this relationship, LST is a necessary input of any microwave SM retrieval algorithm. SM and LST are also related through ET, which is a fundamental variable in hydrological and water/energy balance studies [Crow *et al.*, 2008, Er-Raki *et al.*, 2008, Seneviratne *et al.*, 2010]. According to the latter, there are two different ET regimes: the energy-limited and the water-limited. In the energy-limited regime, SM is above a certain SM value (critical SM) and ET is mainly controlled by the available energy (not by the soil water content). In the water-limited regime, in contrast, SM is below the critical SM and acts as the main driver of the ET process. The critical SM is known to be bounded by the soil wilting point (WP) and the soil field capacity (FC) (see Subsection 2.3.4), and typically lies between the 50 % to 80 % of FC [Shuttleworth, 1993]. The thermal inertia describes the resistence of a material to temperature variations and is proportional to the material's thermal conductivity, density and specific heat capacity. In general, a decrease in SM produces an increase in LST diurnal range, and the maximum LST under moist conditions occurs later than under dry conditions (with a time lag within the day) [Sun & Pinker, 2004]. This is because the specific heat capacity of water is typically higher than that of bare soil and, consequently, dry soils respond faster than wet soils to temperature variations.

Several studies have been focused on the indirect estimation of SM using TIR remote sensing. Because the surface brightness temperature depends on its physical temperature and also on the surface water content and vegetation, most of these approaches are based on the so-called triangle or trapezoidal method of the LST/vegetation index space [Price, 1980, Carlson *et al.*, 1994, Moran *et al.*, 1994, Gillies & Carlson, 1995, Anderson *et al.*, 1997, Sandholt *et al.*, 2002, Anderson *et al.*, 2007, Carlson, 2007, Stisen *et al.*, 2008, Petropoulos *et al.*, 2009]. Usually, the LST/VI method is also used with an ET model or the thermal inertia. An intercomparison study showed that SM estimates from microwave and TIR provide complementary information [Hain *et al.*, 2011]. Microwave retrievals are optimal for measuring accurate SM under all-weather conditions, but the spatial resolution obtained is limited (around tens of km). TIR retrievals, in turn, provide high resolution (from tens of meters to several km), but are sensitive to atmospheric effects. To benefit from the advantages of both SM retrieval techniques, several pixel disaggregation algorithms have been developed for SMOS [Piles *et al.*, 2011, Merlin *et al.*, 2012, Piles *et al.*, 2012, Song & Jia, 2013, Sánchez-Ruiz *et al.*, 2014, Piles *et al.*, 2014, Fang & Lakshmi, 2014, Piles *et al.*, 2016b]. In these methods, LST and NDVI are fundamental input variables. A recent review describes these relationships and the synergistic use of passive microwave and VIS/IR for multi-scale SM estimation [Piles & Sánchez, 2016].

Most radiometer-based and TIR-based SM retrieval algorithms employ the instantaneous LST in the inversion. However, some studies have revealed that the maximum temperature (or a composite of the maximum temperature) provides a closer representation of land surface conditions of a particular day [Cihlar *et al.*, 1994, Fisher *et al.*, 2008]. The above-mentioned studies suggest that daily maximum LST is more closely linked to instantaneous SM than collocated LST. In this regard, gaining understanding of the SM–LST link could be useful refining SM retrieval or microwave/optical disaggregation algorithms. It may be also useful for improving the representation of LST in hydrological and climate models. Additionally, an ensemble created from the average of several disaggregated SM estimates could allow for improved coverage in case of optical data masked by presence of clouds. As a first step, different combinations of SMOS morning and afternoon passes with 3 days of MODIS Terra and Aqua day were composited into an averaged disaggregated SM [Merlin *et al.*, 2012]. Alternatively, the synergy of microwaves (SMOS) and geostationary optical data (MSG SEVIRI) was recently assessed [Piles *et al.*, 2016b].

In this study, an evaluation of SM and LST dynamics using *in situ* and satellite observations over the central part of the river Duero basin, in Spain, is presented. The study period comprises four years (2011–2014). The *in situ* data include SM and LST observations from the Soil Moisture Measurement Stations Network of the University of Salamanca (REMEDHUS) Sánchez *et al.* [2012b]. The satellite data used are the SMOS Barcelona Expert Centre (BEC) Level 3 (L3) SM [BEC Team, 2015] and the MODIS Terra/Aqua LST. The temporal correlation of instantaneous SM and a variety of LST-derived parameters is analyzed at the daily scale to better

understand the fundamental SM–LST link through ET and thermal inertia physical processes. The seasonal dependence is evaluated using a modeled ET obtained from the Hydrological Model for Operational estimates of Recharge and actual Evapotransporation (HidroMORE) as supporting information [Sánchez *et al.*, 2010, 2012a]. A method to estimate the critical SM from the SM–LST coupling/decoupling transitions has been developed and effectively applied to *in situ* and spaceborne measurements. Additionally, a SMOS/MODIS SM downscaling algorithm has been been applied to two years (2012–2013) of SMOS and MODIS data [Piles *et al.*, 2014]. The performance of all possible SMOS SM-MODIS LST combinations has been separately evaluated for each downscaled SM estimate and compared to *in situ* data from the REMEDHUS network. An averaged ensemble of four downscaled SM datasets (using all available MODIS LST) has also been evaluated. The content of this Chapter has been published in a symposium [Pablos *et al.*, 2014a] and two journals [Pablos *et al.*, 2016, In review].

5.2 Datasets

5.2.1 *In situ* data

The REMEDHUS network is located at the central part of the river Duero basin, in Spain [Sánchez *et al.*, 2012b] (see Fig. 5.1). It covers a semi-arid continental-Mediterranean agricultural region of 35 km x 35 km [41.1–41.5°N, 5.1–5.7°W], with an area of approximately 1300 km^2. It is a member of the International Soil Moisture Network (ISMN, `https://ismn.geo.tuwien.ac.at`, [Dorigo *et al.*, 2011]). REMEDHUS includes 21 permanent stations providing hourly SM and LST measurements in the top 5 cm of the soil. Both are acquired with Hydra Probes that measure with an accuracy of 0.003 m^3/m^3 for SM and 0.6°C for LST [Hydra Probe, 2008].
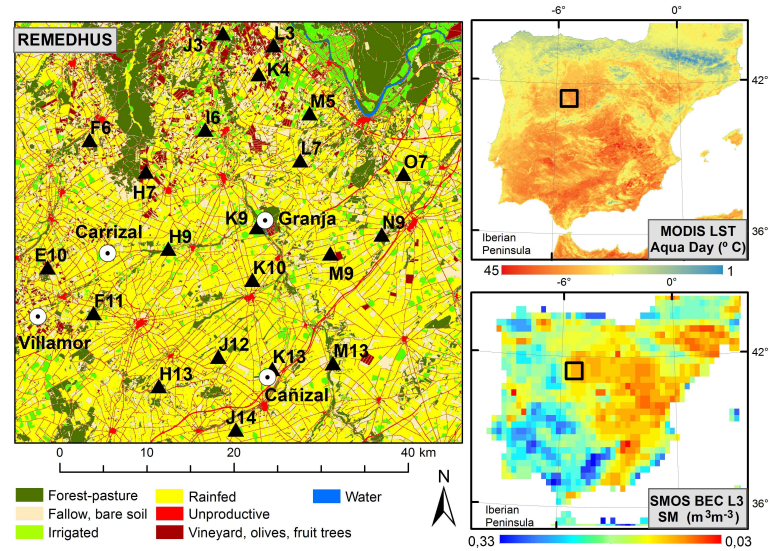
FIGURE 5.1: Land use map of the REMEDHUS network (left) at the river Duero basin, Spain, including the location of the 21 stations for measuring SM and LST (black triangles) and the 4 weather stations (white dartboards). Time-averaged 1-km MODIS LST Aqua day (top right) and 25-km SMOS BEC L3 SM (bottom right) maps during the study period.

The main land uses in this area are vineyard (stations E10, F6, H7, K6, J3, and L3), rainfed cereals or fallow (stations F11, H13, J12, J14, K9, K10, K13, L7, M5, M9, N5, and O7), and forest-pasture (stations H9 and M13). During the study period, station K4 changes its land use from vineyard (2011) to rainfed cereals or fallow (2012, 2013 and 2014). The SM and LST measurements of REMEDHUS from a particular year corresponding to stations over irrigated crops (K9 during 2012, K13 during 2013 and 2014) have been removed from the dataset. The reason for filtering irrigated crops is the quick SM fluctuations related with the high frequency

of water supply (less than 12 h, specially during the summer), which are not captured by the SMOS 3-day repeat. Stations with corrupted LST (J12 during 2011) or corrupted SM (M13 during 2014) have also been discarded.

In REMEDHUS there are also four automatic weather stations that measure air temperature, relative humidity, precipitation, solar radiation, reference or potential evapotranspiration (ET_0) and wind speed. The monthly accumulated ET_0 and the daily mean precipitation have also been used in this study. A land use map of the REMEDHUS region is shown in Fig. 5.1 (left) including the location of the 21 SM and LST stations and the 4 weather stations, depicted with black triangles and white dartboards, respectively.

5.2.2 Satellite data

The SMOS BEC L3 SM v.1 products acquired over the Iberian Peninsula are freely distributed at BEC (`http://cp34-bec.cmima.csic.es`). These products were obtained by quality-filtering and re-gridding from the operational ESA SMOS L2 v.5.51 products. Grid points affected by radio frequency interference (RFI) and/or SM with Data Quality Index (DQX, defined as the error standard deviation) greater than 0.07 m^3/m^3 are discarded. A DQX-inverse weighted average is applied to bin the data from the Icosahedral Snyder Equal Area (ISEA 4H9) grid to the global cylindrical 25-km Equal-Area Scalable Earth (EASE ML) grid. More details are available in BEC Team [2015]. A validation of SMOS L2 and L3 SM products using two complementary small-scale and large-scale *in situ* networks (REMEDHUS and Inforiego, respectively) and a surface water balance model was performed [González-Zamora *et al.*, 2015]. The SMOS equatorial crossing times are: 6:00/18:00 UTC for morning (ascending)/afternoon (descending) orbits.

The MODIS LST v.5 products of Terra/Aqua (MOD11A1/MYD11A1) are provided by the U.S. Land Processes Distributed Active Archive Center (LP DAAC, `https://lpdaac.usgs.gov`). They have 1 km of spatial resolution and a nominal accuracy of 1°C under clear sky conditions. Higher error (from 4°C to 10°C) could be expected in presence of clouds and heavy aerosols. The MODIS equatorial crossing times are: 10:30/22:30 for Terra day (descending)/night (ascending), and 13:30/01:30 for Aqua day (ascending)/night (descending). Figure 5.1 also displays maps of 1-km MODIS LST Aqua day (top right) and 25-km SMOS BEC L3 SM (bottom right) over the Iberian Peninsula, both time-averaged during the study period. Note the different size of MODIS and SMOS pixels.

5.2.3 HidroMORE model

The real or actual evapotranspiration (ET_a) during 2014 is obtained from the HidroMORE hydrological model [Sánchez *et al.*, 2010, 2012a]. It is an operational distributed model based on the water balance equation [Allen *et al.*, 1998]. HidroMORE provides daily estimates of deep percolation (DP), water storage (WS) and ET after considering effective precipitation (P), surface runoff (RO) and irrigation (IRR):

$$P + IRR - RO - ET - DP = \pm \Delta WS, \qquad (5.1)$$

where $\pm \Delta WS$ is a residual of the balance and expresses the rate of change in soil moisture content or water storage [mm]. The calculation in Eq. (5.1) accounts for the effective root zone.

The estimation of ET_a is based on the dual crop coefficient–reference ET methodology [Allen *et al.*, 1998]:

$$ET_a = ET_0(K_s K_{cb} + K_e), \qquad (5.2)$$

where ET_0 stands for the reference or potential evapotranspiration, K_s is the water stress co-efficient, K_{cb} is the basal crop coefficient, and K_e is the soil evaporation coefficient. The K_{cb}

is calculated on the basis of the daily NDVI retrieved from temporal series of optical imagery (NDVI–K_{cb} approach), K_e is computed from the Food and Agriculture Organization (FAO) water balance procedure, and water stress conditions are applied to estimate K_s. The outputs of HidroMORE are obtained at the same spatial resolution than the optical images used to derive the NDVI.

The K_{cb} approach has been previously applied with different formulations (linear and exponential) and also using different indirect growing parameters, such as the Leaf Area Index (LAI), the Fractional Vegetation Cover (FVC) or the NDVI. Results show that the linear approach is adequate for SM estimation at the root zone, which is denoted by $\pm \Delta WS$ (see Eq. (5.1)). The ET_a differences produced by the indirect growing parameter are lower than 3 mm of the total annual ET_a) [Sánchez *et al.*, 2012c]. Ground-based SM measurements from REMEDHUS have also been used for validating these results [Mahmood & Hubbard, 2007]. The higher correlations obtained between *in situ* SM and HidroMORE SM at the root-zone (R≈0.78 to 0.95) indicate that the model was well calibrated and working correctly [Sánchez *et al.*, 2012c].

5.2.4 SMOS/MODIS SM downscaling algorithm

A SMOS/MODIS SM downscaling algorithm based on the LST–NDVI relationship was proposed by Piles *et al.* [2011] proposed. The algorithm uses a linear regression linking model to relate the coarse resolution (∼40 km) SMOS SM and T_B at horizontal polarization in a single incidence angle (θ_i=42.5°) with the high resolution (∼1 km) MODIS LST and NDVI. Later, The impact of adding multi-angular observations and full-polarimetric information to the linking model was evaluated in Piles *et al.* [2012]. Finally, the algorithm was modified with a remarkable improvement in the modeling, including the T_B at horizontal (H-pol) and vertical (V-pol) polarizations, and three incidence angles. The updated linear linking model for relating the variables across spatial scales can be expressed as [Piles *et al.*, 2014]:

$$sm = a_0 + a_1 LST_N + a_2 NDVI_N + \sum_{i=1}^{3} a_{3i} T_{BH}(\theta_i)_N + \sum_{i=1}^{3} a_{4i} T_{BV}(\theta_i)_N, \qquad (5.3)$$

where a_0, a_1, a_2, a_{3i} and a_{4i} are the regression coefficients, sm stands for SM, LST_N is the normalized LST, $NDVI_N$ is the normalized NDVI, and $T_{BH}(\theta_i)_N$ and $T_{BV}(\theta_i)_N$ are the normalized H-pol and V-pol brightness temperatures, respectively, at incidence angles θ_i=32.5°, 42.5°, and 52.5°. The normalization of each variable is performed for a specific SMOS morning/afternoon pass and scene, using:

$$X_N = \frac{X - X_{min}}{X_{max} - X_{min}}, \qquad (5.4)$$

where X corresponds to the variable itself, and X_{min} and X_{max} are its minimum and maximum values.

The use of NDVI and others VI from ShortWave InfraRed (SWIR) at different spatial (500 m *vs.* 1 km) and temporal (8 days *vs.* 16 days) resolutions was explored in Sánchez-Ruiz *et al.* [2014]. Nowadays, the approach of Piles *et al.* [2014] is the operational disaggregation algorithm used to produce daily 1-km SM maps over the Iberian Peninsula (SMOS BEC L4 SM products). In its first version (SMOS BEC L4 SM v.1), the SMOS SM was combined with the closest MODIS LST acquisition: SMOS morning (6:00) with MODIS LST Aqua night (1:30) or Terra day (10:30), and SMOS afternoon (18:00) with MODIS LST Aqua day (13:30) or Terra night (22:30). During their validation with *in situ* data, the SMOS BEC L4 SM v.1 products in the afternoon passes showed better temporal correlations than in the morning passes (R$_{Terra}$ ≈0.30 to 0.70/0.37 to 0.78 and R$_{Aqua}$ ≈0.31 to 0.64/0.49 to 0.73 for morning/afternoon passes). The use of MODIS LST Terra day was preferred, although results from downscaled SM maps using LST Aqua were broadly consistent [Piles *et al.*, 2014].

5.3 Methodology

5.3.1 Analysis of SM–LST relationship

Ground-based SM measurements from the REMEDHUS network have been time-averaged to mimic the instantaneous SM acquired during SMOS morning/afternoon passes over the region. Ground-based LST measurements at a variety of acquisition times have also been selected, leading to six LST-derived parameters: i) instantaneous T_i, ii) daily mean $\overline{T}$, iii) daily median T_{med}, iv) daily maximum T_{max}, v) daily minimum T_{min}, and vi) diurnal range $\Delta T = T_{max} - T_{min}$.

Regarding satellite data, the four 25-km SMOS L3 SM pixels covering the REMEDHUS area have been extracted in both morning and afternoon SMOS passes. In the case of MODIS LST, all 1-km MODIS LST pixels ($\approx$552 to 576) within the corresponding SMOS pixel have been averaged in order to obtain four aggregated 25-km LST pixels per each MODIS platform (Terra and Aqua) and overpass (day and night). The aggregated 25-km MODIS pixels with a LST lower than -5°C have been filtered to screen out measurements affected by frozen soil. In addition, a 3-day averaging window has been applied to SMOS and MODIS data to reduce the noise in the time-series. The longitude of the averaging window corresponds to the SMOS revisit time. It has been checked that this averaging does not affect results and neither conclusions obtained from satellite data analysis.

In order to evaluate the SM–LST relationship, the temporal correlation of the two variables has been computed at the daily and at the seasonal scale for two different scenarios: i) *in situ* SM and LST from the REMEDHUS stations and ii) satellite SMOS SM and MODIS LST over the REMEDHUS network. As SM and LST annual cycles are expected to be highly related, their anomaly values have been used to detrend the time-series and perform a separate analysis. The anomaly has been obtained by subtracting the mean seasonal cycle of each variable, which represents the annual cycle. This mean seasonal cycle (or seasonal climatology) has been computed as the monthly mean value of the variable during the entire study period. In all cases, non-significant correlations ($p_{value} >$0.05, at the 95 % of significance level) have been discarded. Normalized occurrence frequency density diagrams of the SM–LST space of both *in situ* and satellite data have also been computed.

5.3.2 Analysis of SM–LST coupling/decoupling and critical SM

The temporal evolution of SM and LST has been analyzed using time-series of *in situ* and satellite observations together with the daily mean precipitation. The latter is computed from the average of the four weather stations located within the REMEDHUS area. A method to get an estimate of the critical SM, i.e., the SM value at the SM–LST coupling/decoupling transitions, is proposed. As a first step, both SM and LST time-series are normalized using Eq. (5.4). As a second step, the SM–LST transition points are identified as those in which the normalized SM and LST have a difference of less than 0.01. Then, the SM and LST values of these transition points are denormalized to compute their maximum, minimum, mean and standard deviation. The critical SM and its uncertainty can be inferred from these statistics.

5.3.3 Analysis of water/energy-limited ET regimes

In this study, 11 images from Landsat 8 at Level 1T during 2014 have been used in the Hidro-MORE simulation. Firstly, we have obtained reflectances at the top of the atmosphere (TOA). They have been converted to bottom of the atmosphere (BOA) reflectances through a relative atmospheric correction and the NDVI has been obtained and cloud-masked at a spatial resolution of 30 m. Later, the NDVI maps from Landsat together with other datasets, such as a land cover map at the same spatial resolution, climatic data and soil data, have been used as input for HidroMORE. The climatic data has been obtained from the REMEDHUS

weather stations. The soil database came from the Sistema de Información Agroclimática para el Regadío (SiAR) service of the Spanish Ministry of Agriculture, Food and Environment (`http://eportal.magrama.gob.es/websiar/Inicio.aspx`).

A linear relationship between the bassal crop coefficient K_{cb} and NDVI has been computed. This NDVI–K_{cb} approach has been applied in the HidroMORE simulation as follows:

$$K_{cb} = 1.36 \cdot NDVI - 0.03. \tag{5.5}$$

The water balance has been calculated for each day and cell, and results at each REMEDHUS station location have been extracted. Runoff has not been considered in this simulation, owing that in this area, the topographic features and the soil properties make the infiltration the predominant process. HidroMORE considers the root-zone soil layer and calculates SM and ET_a, but our interest lies in the comparison between ET and the SM at the surface layer. Thus, the SM at root-zone from HidroMORE has not been used.

Since the SM–LST coupling/decoupling periods are an indicator of a different ET regime (water-limited or energy-limited, respectively), the behaviour of the ET has been studied over the year 2014, comparing the mean potential evapotranspiration (ET_0) of the four weather stations from the REMEDHUS network with the actual evapotranspiration (ET_a) obtained from the HidroMORE hydrological model. The correlation between the ET_a from HidroMORE and SM from REMEDHUS has also been analyzed for the different ET regime periods during 2014.

5.3.4   Validation of disaggregated SM estimates

The SMOS/MODIS SM downscaling algorithm of Piles *et al.* [2014] has been applied to produce eight datasets of daily 1-km disaggregated SM maps over the Iberian Peninsula during 2012 and 2013, using all possible SMOS–MODIS combinations. These eight disaggregated SM estimates have been validated with ground-based data by means of Taylor diagrams that show the correlation (R), the standard deviation (std) and the unbiased Root Mean Square Difference (ubRMSD) respect to the REMEDHUS network. In addition, the *in situ* SM value of each REMEDHUS station has been compared with the 1-km SM pixel covering the corresponding station. During this validation, the following statistics have been computed, both at each station and at the network scale: i) correlation (R), ii) unbiased Root Mean Square Difference (ubRMSD), iii) bias, iv) slope estimated from a robust linear regression [DuMouchel & O'Brien, 1989], and days of coverage (N) along along two years. Statistical metrics at the network scale are computed after averaging all stations of the disaggregated SM estimates. The used statistics are widely employed to assess the accuraccy of satellite-based SM estimates [Entekhabi *et al.*, 2010a].

5.3.5   Analysis of coverage improvement

An averaged ensemble of four disaggregated SM datasets (using all available MODIS LST) has been produced for SMOS morning and afternoon passes. The ensemble has also been validated at each station and at the network scale using *in situ* data from the REMEDHUS network. Statistical scores have been compared with those obtained from the validation of disaggregated SM using MODIS LST Aqua day (the SMOS BEC L4 SM v.2 product), specially the days of coverage (N).

5.4 Results and discussion

5.4.1 Characterization of SM and LST over the study area

Figure 5.2 (left) shows the diurnal cycle of *in situ* SM (blue line) and LST (red line) observations from the REMEDHUS network during the study period (2011–2014) averaged over all stations. The error bar indicates the standard deviation (std) among the 21 stations. Note that the hourly mean LST exhibits a considerable diurnal range (from ~13°C to ~19°C), and the daily minimum and maximum LST (T_{min} and T_{max}) occur at 7 h and at 16 h, respectively. These times approximately correspond to the SMOS morning and afternoon passes over the REMEDHUS region. Additionally, the LST variability among the stations is higher when the LST is high (std LST~2°C) than when the LST is low (std LST~1°C). By contrast, the hourly mean SM remains almost constant (~0.13 m^3/m^3); its variation along the day is within the accuracy of the sensor, and the SM variability among the stations is low (std SM~0.09 m^3/m^3). The stability of the daily SM indicates that a unique SM value per day could be representative of the entire day, except when rainfall events occur. In this line, previous research studied the temporal evolution of SM in this region and verified its persistence for a few hours per day, and even during a few days [Martínez-Fernández & Ceballos, 2003]. Also, in a SMOS L2 SM validation study at the same area, no differences where detected between using the time-overpass or the daily average of the *in situ* SM values [Sánchez *et al.*, 2012b].

The annual cycle of *in situ* SM and LST observations from the REMEDHUS network is displayed in Fig. 5.2 (right). The monthly mean of SM and LST present opposite behaviours, with the lowest SM and the highest LST during summer months (June, July and August), and the highest SM and the lowest LST during winter months (December, January and February). The SM annual cycle ranges from ~0.07 m^3/m^3 to ~0.2 m^3/m^3 and the LST annual cycle ranges from ~6°C to ~27.7°C. The variability in SM is higher in winter (std SM~0.12 m^3/m^3) and lower in summer (std SM~0.05 m^3/m^3), whereas variability in LST is lower in winter (std LST~0.8°C) and higher in summer (std LST~2°C). These values are consistent with the temporal evolution of SM from the ground-based measurements from the last 15 years of data recorded in REMEDHUS and the climate type of this region [Martínez-Fernández & Ceballos, 2005].
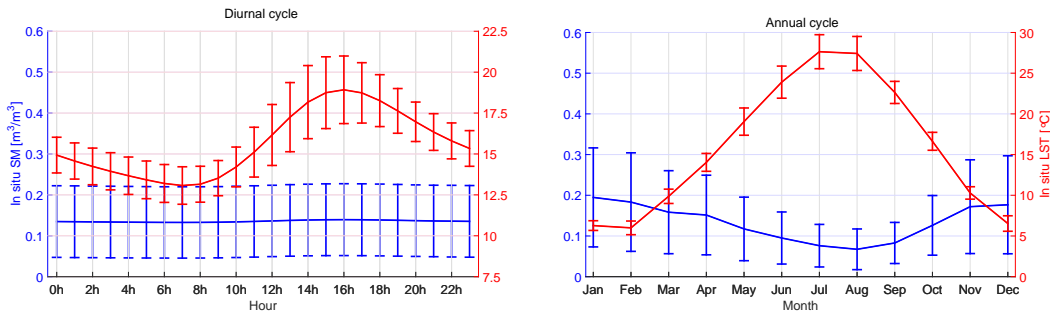
FIGURE 5.2: Diurnal (left) and annual (right) cycles of *in situ* SM (blue line) and LST (red line) from the REMEDHUS network during the study period. The error bar indicates the standard deviation (std) among the 21 stations.

The possible relation of SM and LST dynamic ranges with soil texture is explored in Fig. 5.3. For the case of SM (left), a very strong anticorrelation with the soil sand content (red asterisks, R=-0.93) and a strong correlation with the soil clay content (blue crosses, R=0.86) is observed. Two stations (H9 and M13) present a higher ΔSM compared with the other stations. This can be explained by the fact that they are forest-pasture stations. Also, they are located at the bottom of valleys where the water table is shallow in winter, and where occassional flooding occurs [Sánchez *et al.*, 2012b]. In the case of LST (right), a non-significant correlation of LST dynamic range with the soil sand or clay content is found.
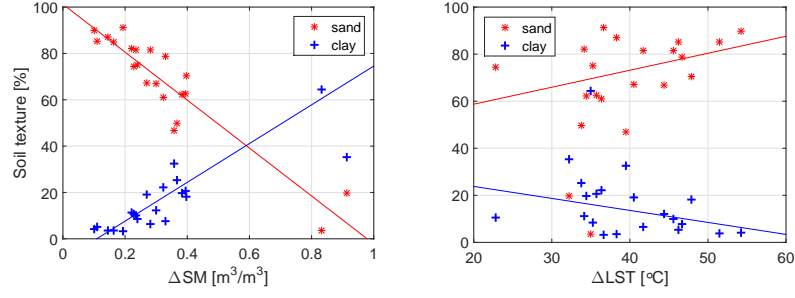
FIGURE 5.3: Comparison of *in situ* SM (left) and LST (right) dynamic ranges with soil texture: sand content (red asterisks) and clay content (blue crosses). Segments show the linear regression fitting lines.

5.4.2 SM–LST relationship at the daily scale

The correlation of ground-based SM acquired at SMOS morning/afternoon passes and LST-derived parameters is shown in Fig. 5.4 (left). In the boxplot, the central mark indicates the median, and the bottom and top edges of the box indicate the 25th and 75th percentiles, respectively. The whiskers extend to the most extreme data points not considered outliers, and the outliers are plotted individually using red crosses. Considering the entire study period, SM and LST variables are in general anticorrelated: if SM decreases, LST increases, and *vice versa*. This result agrees with those obtained in Fig. 5.2 (right). There is a single outlier with a very low correlation (R≈-0.2 to 0.1) corresponding to H7, a vineyard station that recorded extremely dry conditions (with SM ranging from 0 to 0.08 m³/m³ along the four years). In the morning passes, the anticorrelation values (in median) sorted from strong to weak are obtained for: daily maximum LST and daily mean LST ($R_{T_{max}, \overline{T}} \approx$-0.71), daily median LST ($R_{T_{med}} \approx$-0.70), instantaneous LST and daily minimum LST ($R_{T_i, T_{min}} \approx$-0.68), and LST diurnal range ($R_{\Delta T} \approx$-0.59). In the afternoon passes, the sorted R values are obtained for: daily median LST ($R_{T_{med}} \approx$-0.70), daily mean LST ($R_{\overline{T}} \approx$-0.69), daily maximum LST and instantaneous LST ($R_{T_{max}, T_i} \approx$-0.68), daily minimum LST ($R_{T_{min}} \approx$-0.66), and LST diurnal range ($R_{\Delta T} \approx$-0.55). Note that the correlation obtained for instantaneous LST becomes equal to the correlation obtained for daily minimum LST in the morning, and equal to the correlation obtained for daily maximum LST in the afternoon. This could be due to T_i being closer in time and similar to T_{min} values at the morning, and to T_{max} values at the afternoon passes, respectively. Considering the percentiles and wiskers, the strongest anticorrelation is obtained for the daily maximum LST (T_{max}) both in morning and afternoon passes. This can be explained by the time of T_{max} being also the time of maximum potential evapotranspiration, i.e, when there is a higher atmospheric demand of water and the air turbulence (uplift) is maximum.

When analyzing the detrended *in situ* time-series, Fig. 5.4 (right) shows that, as expected, correlations are weaker than when using the variables directly. In the morning passes, the sorted R values (in median) from strong to weak are: LST diurnal range ($R_{\Delta T} \approx$-0.33), daily maximum LST ($R_{T_{max}} \approx$-0.31), daily mean LST ($R_{\overline{T}} \approx$-0.26), daily median LST ($R_{T_{med}} \approx$-0.25), and instantaneous LST and daily minimum LST ($R_{T_i, T_{min}} \approx$-0.20). In the afternoon passes, the sorted R values are obtained for: LST diurnal range ($R_{\Delta T} \approx$-0.31), instantaneous LST ($R_i \approx$0.30, daily maximum LST ($R_{T_{max}} \approx$-0.29), daily mean LST and median LST ($R_{\overline{T}, T_{med}} \approx$-0.24), and daily minimum LST ($R_{T_{min}} \approx$-0.19). The strongest anticorrelation is obtained for the LST diurnal range both in morning and afternoon passes. This agrees with previous literature [Dai *et al.*, 1999, Durre *et al.*, 2000, Braganza *et al.*, 2004], in which a relation between SM and near-surface air temperature diurnal range was reported. However, this air temperature is usually measured at 1.5 m above the ground level, not in the top 5 cm of the soil. Results indicate that maximum LST and LST diurnal range provide complementary information of the SM–LST relationship. Since results obtained at the SMOS morning and afternoon are very similar using both the direct variables and their anomalies, hereafter only results at morning passes are presented. In the *in situ* analysis, only daily maximum LST will be shown.
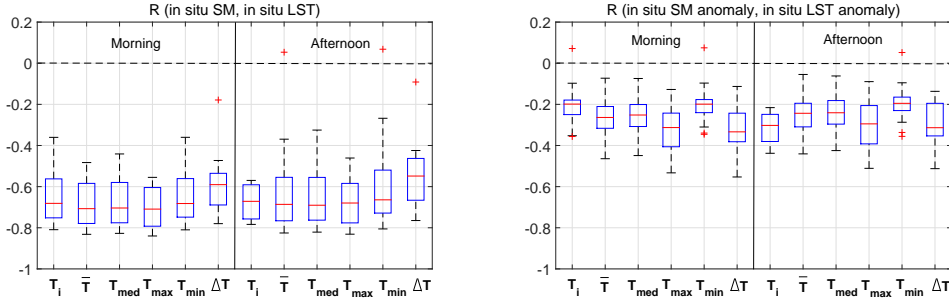
FIGURE 5.4: Correlation (R) of *in situ* SM acquired at the SMOS morning/afternoon passes and LST derived parameters (left) and their anomalies (right) during the study period for: i) instantaneous T_i, ii) daily mean $\overline{T}$, iii) daily median T_{med}, iv) daily maximum T_{max}, v) daily minimum T_{min}, and vi) diurnal range $\Delta T = T_{max} - T_{min}$. Outliers are depicted with red crosses.

Figure 5.5 (left) shows the correlation of SMOS SM at the morning passes and MODIS LST at different platforms and acquisition times over the REMEDHUS network during the study period. Correlations are less variable for satellite than for *in situ* observations, likely due to their different spatial scales; satellite observations represent the four 25-km pixels covering the REMEDHUS area whereas ground-based measurements are made at point scale. The correlation values obtained are: Terra day (R≈-0.68 in median), Terra night (R≈-0.54), Aqua day (R≈-0.70), and Aqua night (R≈-0.44). The strongest anticorrrelations are obtained for MODIS LST day times, both for Terra and Aqua satellites. We hypothesize that MODIS LST from day overpasses captures better the spatial pattern induced by topography that may not be captured at night time. Note that the anticorrelation for Aqua day is slightly stronger than for Terra day. This can be explained by Aqua day passes being closer to T_{max} over the REMEDHUS region than Terra day passes. These results agree with those obtained with *in situ* data (see Fig. 5.4 (left)). Further research using a geostationary satellite as MSG SEVIRI, which has a temporal resolution of 15 min, would be needed to analyze the relationship of SM with LST diurnal range.

When analyzing the anomaly time-series, Fig. 5.5 (right) displays correlations that are weaker than using the direct variables in absolute value, as expected, but significant: Terra day (R≈-0.47 in median), Terra night (R≈-0.13), Aqua day (R≈-0.46), and Aqua night (R≈+0.17). Note that Terra/Aqua at night overpasses produce very weak correlations, suggesting that only Terra/Aqua at day times maintain their relationship with the SM under anomalous conditions. Similar behaviour is obtained at the afternoon passes (not shown).
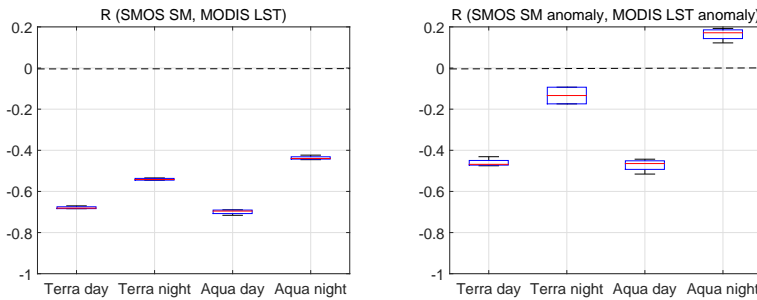
FIGURE 5.5: Correlation (R) of SMOS SM at the morning passes and MODIS LST (left) and their anomalies (right) over the REMEDHUS network for different MODIS platforms and passes: i) Terra day, ii) Terra night, ii) Aqua day, and iv) Aqua night. Similar behavior is obtained at the afternoon passes.

Two-dimensional frequency density diagrams of *in situ* SM acquired at the SMOS morning passes and T_{max}, and SMOS SM at the morning passes and MODIS LST Aqua day over the REMEDHUS network during the study period are displayed in Fig. 5.6. They inform of the frequency of occurrence of all SM–LST combinations. The normalized SM–LST space visually

shows the relationship between the two variables through its distributions. A triangular shape emerges from the SM–LST relationships, with sharper edges when using *in situ* data (left) than when using satellite data (right). This is likely to the fact that MODIS LST Aqua day is not acquired at the maximum daily LST time, when the strongest SM–LST correlation is obtained. It is important to note that MODIS LST measurements are obtained at the skin level whereas the ground-based LST observations are acquired at 0-5 cm below the land surface. Also, daily LST fluctuations are less pronounced with depth [Van De Griend *et al.*, 1984]. These differences could explain the higher MODIS LST Aqua day than T_{max} during very dry conditions (0–0.1 m^3/m^3). Similar triangles are obtained at the afternoon passes (not shown) and when using Terra day, as shown in Appendix D (see Fig. D.1). The triangle (or trapezoid) was also obtained when plotting the LST–NDVI space, which is used to indirectly estimate SM from TIR observations [Carlson, 2007, Anderson *et al.*, 2007, Sandholt *et al.*, 2002, Petropoulos *et al.*, 2009], or to disaggregate SM from the microwave/optical synergy [Piles *et al.*, 2014, 2016b]. To also evaluate the SM–LST relationship in a larger area than the REMEDHUS network, an additional analysis at daily scale with satellite data is performed over the Iberian Peninsula, as shown in Appendix D (see Figs. D.2 and D.3). Only SMOS morning passes and MODIS LST Aqua day over the REMEDHUS network will be shown hereafter for the satellite analysis at the seasonal scale.
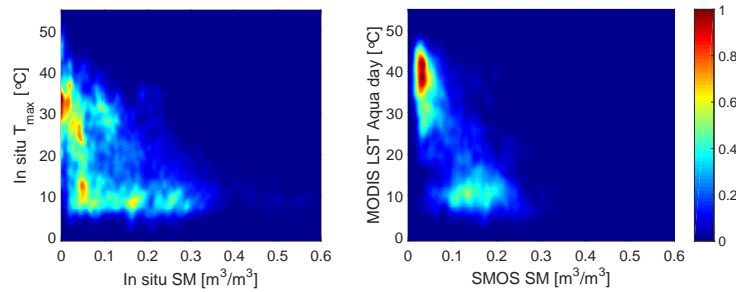
FIGURE 5.6: Normalized occurrrence frequency density diagrams of *in situ* SM at the SMOS morning passes and T_{max} (left), and SMOS SM at the morning passes and MODIS LST Aqua day (right) during the study period. Similar behaviour is obtained at the afternoon passes and/or using Terra day.

5.4.3 SM–LST relationship at the seasonal scale

The correlation of *in situ* SM at the SMOS morning passes and T_{max} from the REMEDHUS network for each season is shown in Fig. 5.7 (left). Note that the strongest anticorrelation is obtained in autumn (September-October-November, SON) with R≈-0.68 in median, followed by spring (March-April-May, MAM) with R≈-0.51, and summer (June-July-August, JJA) with R≈-0.48. Hence, the strongest SM–LST relationship is observed in transitional seasons (i.e., autumn and spring) because the SM is sufficiently dynamic to affect air temperature, and also LST. As expected from results explained in [Seneviratne *et al.*, 2010], this result agrees with those obtained in [Miralles *et al.*, 2012], where the SM–air temperature coupling was shown to be higher in transitional zones between wet and dry climates. However, a low correlation is obtained in winter (December, January, February, DJF) with R≈+0.30. This suggests that SM and LST are not coupled during winter. This could also explain the low performance of disaggregated SM products based on soil evaporation efficiency models in winter [Merlin *et al.*, 2012].

Figure 5.7 (right) shows the correlation between ground-based SM anomaly at the morning passes and T_{max} anomaly for each season. A low correlation is also observed in winter (R≈+0.27 in median) and the strongest anticorrelation is obtained in summer (R≈-0.49), which is the driest season, followed by spring (R≈-0.43) and autumn (R≈-0.31). It can be related to the fact that, under very dry conditions, an increase of SM from an individual precipitation event has an important impact on LST, due to its low thermal inertia. Also, since ET is regulated by the SM content under water-limited conditions in summer, the SM increase produces an ET increase and

there is enough energy to maintain the high rate of ET until the SM content decreases. Obviously, this effect is less important in wet seasons, specially in winter, due to the lower available energy involved in the ET process and the higher thermal inertia. These results suggest that the annual cycle contains most of the SM–LST relationship information of transitional seasons, particularly in autumn. By contrast, the anomaly contains most of the SM–LST relationship information during summer. Similar behavior is obtained with *in situ* SM at the SMOS afternoon passes (not shown). Further research is needed to confirm these results in other regions with different climates.
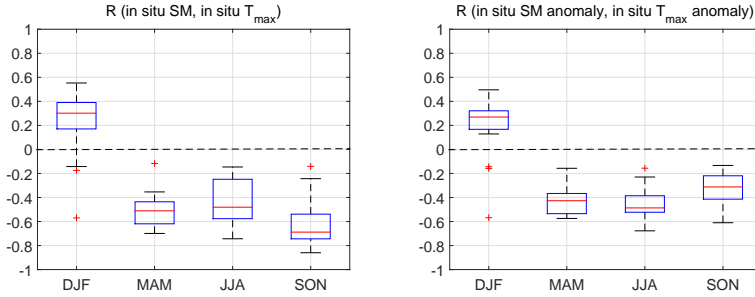
FIGURE 5.7: Correlation (R) of *in situ* SM at the SMOS morning passes and T_{max} (left) and their anomalies (right) for each season: winter (December-January-February, DJF), spring (March-April-May, MAM), summer (June-July-August, JJA) and autumn (September-October-November, SON). Outliers are depicted with red crosses. Similar behavior is obtained with *in situ* SM acquired at the SMOS afternoon passes (not shown).

The correlation of SMOS SM at the morning passes and MODIS LST Aqua day for each season is displayed in Fig. 5.8 (left). In this case, all correlations are negative, including winter. The anticorrelations sorted from strong to weak are obtained in autumn (SON: R≈-0.69 in media), spring (MAM: R≈-0.66), summer (JJA: R≈-0.39) and winter (DJF: R≈-0.34). Thus, the transitional seasons also present the strongest anticorrelation and other seasons the weakest. We hypothesize that differences between *in situ* and satellite results during winter could be due to the more frequent presence of clouds than during other seasons, which produces a lower coverage and a higher LST uncertainty that could be up to 10°C. Another reason may be a side effect of the different spatial scales represented by the remotely sensed data and ground-based data.

Figure 5.8 (right) shows the correlation of the detrended spaceborne time-series. The sorted anticorrelations are obtained in spring (MAM: R≈-0.62), autumn (SON: R≈-0.61), summer (JJA: R≈-0.39) and winter (DJF: R≈-0.26). The lowest SM–LST relationship is obtained during winter, in agreement with results of Fig. 5.7 (right). Similar behavior is obtained with the afternoon passes and/or using Terra day (not shown).
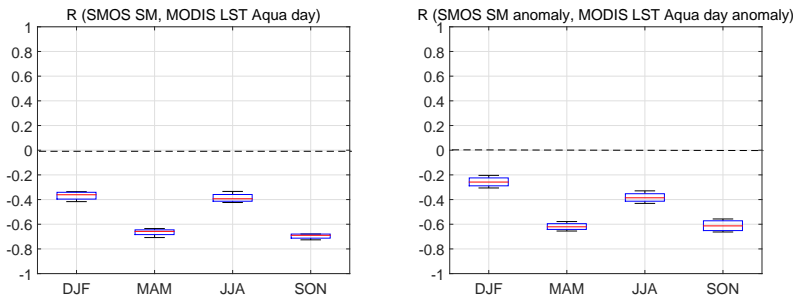
FIGURE 5.8: Correlation (R) of SMOS SM at the morning passes and MODIS LST Aqua (left) and their anomalies (right) for each season: winter (December-January-February, DJF), spring (March-April-May, MAM), summer (June-July-August, JJA) and autumn (September-October-November, SON). Similar behaviour is obtained at the afternoon passes and/or using Terra day (not shown).

Normalized occurrence frequency density diagrams of *in situ* SM at the SMOS morning passes and T_{max} (top row), and SMOS SM at the morning passes and MODIS LST Aqua day (bottom row) are displayed in Fig. 5.9 for each season. Using *in situ* data, SM exhibits a similar dynamic range in winter than in other seasons, but there is a very low dynamic range in T_{max} since there is a minimum thermal gradient of the soil in this area. This leads to the appearance of a line instead of a triangle in the SM–LST space. By contrast, satellite data have a higher dynamic range of LST Aqua day, showing a small triangle in the SM–LST space. The triangle shape is clearly visible in transition seasons (autumn and spring) both using *in situ* and satellite data due to the high SM and LST dynamic ranges. In summer, it is better identified using *in situ* than satellite data. Differences between ground-based and satellite data could be due to the different soil layer sensed by MODIS (skin) and captured by *in situ* LST measurements (0-5 cm) as well as to the higher thermal inertia of ground-based observations, particularly in wet soils during winter. These results are consistent with those obtained in Fig. 5.7 and 5.8. Similar behavior is obtained at the afternoon passes and when using Terra day (not shown).
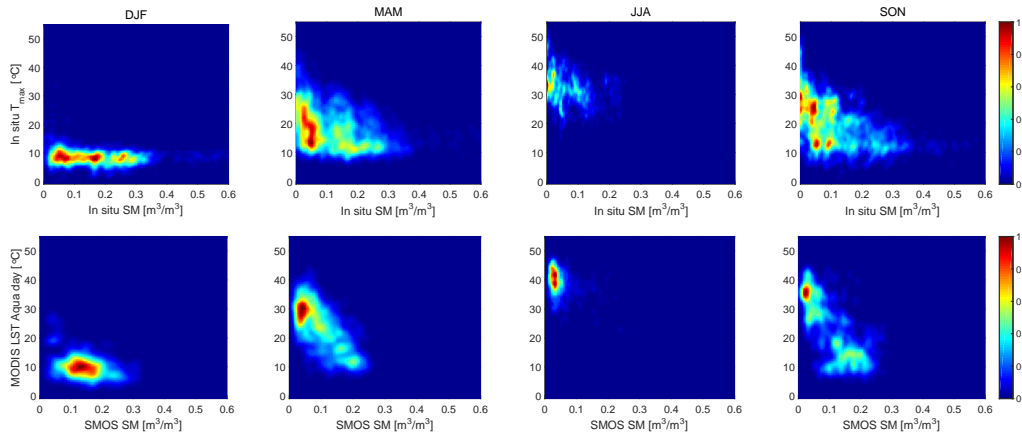

FIGURE 5.9: Normalized occurrence frequency density diagrams of *in situ* SM at the SMOS morning passes and T_{max} (top row), and for SMOS SM at the morning passes and MODIS LST Aqua day (bottom row) for each season (by columns): winter (December-January-February, DJF), spring (March-April-May, MAM), summer (June-July-August, JJA) and autumn (September-October-November, SON), respectively. Similar behaviour is obtained at the afternoon passes and/or using Terra day (not shown).

5.4.4 SM–LST coupling/decoupling and critical SM estimation

Figure 5.10 (top) shows time-series of *in situ* SM at the SMOS morning passes and T_{max} (blue and red solid lines, respectively), and SMOS SM at the morning passes and MODIS LST Aqua day (cyan and magenta dashed lines, respectively). Daily mean precipitation from the REMEDHUS network is also shown (bottom). Winter seasons defined as December, January and February (DFJ) are shaded in light green colour. Although there is a different temporal resolution for *in situ* and satellite data (daily *vs.* 3-day averages, respectively), both SM estimations are consistent with precipitation and capture wetting and drying events. The SMOS SM has a dry bias with respect to *in situ* SM. This dry bias has been previously reported [Jackson *et al.*, 2012, Sánchez *et al.*, 2012b, González-Zamora *et al.*, 2015] and remains almost constant along time. However, the MODIS LST Aqua day is very similar to T_{max} during winter and is higher in other seasons, in agreement with results shown in Figs. 5.6 and 5.9. Note that the SM–LST relationship presents two different behaviours in both datasets. On one hand, there is SM–LST coupling (when SM decreases LST increases and *vice versa*), aproximately corresponding to the spring, summer and autumn seasons, in which a strong anticorrelation is obtained (R≈-0.5 to -0.7/R≈-0.4 to -0.7 from *in situ*/satellite data in Figs. 5.7 and 5.8, respectively). This is related to a water-limited ET regime. On the other hand, there is SM–LST decoupling (when SM and LST do not show a clear relation between them) approximately corresponding to the winter

seasons, in which a weak correlation is obtained (R≈+0.30/R≈-0.3). This is related to an energy-limited ET regime. The discrepancy in the sign of the correlation during winter could be due to the different spatial scales represented by the remotely sensed data and ground-based data. In addition, SM–LST decoupling periods vary from one year to another and include, in most cases, around one month after and before the defined winter (DJF). Similar behavior is obtained at the afternoon passes and/or using Terra day (not shown). Time-series of the normalized variables used to determine the crossing points of SM and LST are included in Appendix D (see Fig. D.4).
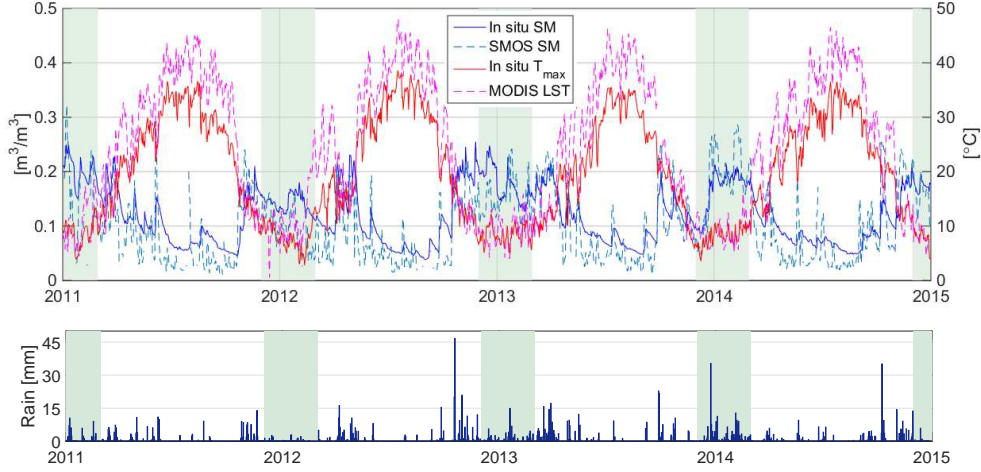
FIGURE 5.10: Time-series of *in situ* SM at the SMOS morning passes and T_{max} (top; blue and red solid lines, respectively), SMOS SM at the morning passes and MODIS LST Aqua day (top; cyan and magenta dashed lines, respectively), and daily mean precipitation of the REMEDHUS network (bottom). Winter seasons (defined as December, January and February, DFJ) are shaded in light green colour. Similar behaviour is obtained at the afternoon passes and/or using Terra day.

Minimum, maximum, mean and standard deviation (std) of SM and LST values obtained at the SM–LST coupling/decoupling transitions are summarized in Table 5.1. Note that the same mean SM is estimated in both datasets (mean SM~0.12 m³/m³), which corresponds to the critical SM over the study area. Taking into account its variability (*in situ* std SM~0.06 m³/m³; satellite std SM~0.05 m³/m³), the estimated critical SM remains within reasonable boundaries (≈0.10 to 0.16 m³/m³ *vs.* ≈0.08 to 0.22 m³/m³). In addition, the estimated critical SM lies between WP and FC over the REMEDHUS network (WP~0.08 m³/m³ and FC~0.16 m³/m³) and is between the 50 % and the 80 % of FC (~75%), in agreement with [Shuttleworth, 1993]. The proposed methodology could be an interesting technique to measure critical SM using remote sensing. In the SM–LST crossings, the mean LST from *in situ* (mean LST~16.4°C) has a good agreement with the mean LST from satellite data (mean LST~15.2°C). It is observed that spaceborne LST measurements have a higher upper limit (max. LST~32.7°C) than ground-based measurements (max LST~22.6°C). This can be explained by the fact that MODIS LST Aqua day observations have also a higher dynamic range than *in situ* observations, in agreement with results shown in Figs. 5.6 and 5.9. Considering the LST variability in both datasets (std LST≈4.4 to 5.9°C) the minimum LST value is also similar (*in situ* min. LST~12.4°C *vs.* satellite min. LST~8.4°C). Other regions with different climates should be analyzed in further research studies.

TABLE 5.1: Statistics obtained from SM–LST coupling/decoupling transitions.

| | *In situ* data | | Satellite data | |
	SM [m³/m³]	T_{max} [°C]	SMOS SM [m³/m³]	MODIS LST Aqua day [°C]
minimum	0.10	12.4	0.08	8.4
maximum	0.16	22.6	0.22	32.7
mean	0.12	16.4	0.12	15.2
std	0.06	5.9	0.05	4.4

5.4.5   Critical SM and ET regimes during 2014

Figure 5.11 shows the monthly actual evapotranspiration (ET_a) from HidroMORE, the potential evapotranspiration (ET_0) and the *in situ* SM from the REMEDHUS network along year 2014. It can be observed that ET_0 and ET_a are very similar in some months of the year (NDJF: November, December, January, and February) and the SM is larger than the estimated critical SM in Table 5.1. This result reveals an energy-limited ET regime. In this regime, the temperature regulates the ET, the ET_0 is very low since there is not enough energy and the ET_a is almost able to reach its maximum possible value (i.e. ET_0) because there is enough SM (SM>estimated critical SM). Thus, the ET process is independent of the SM content and has an important dependence on the sensible heat flux, which impacts on the air temperature and the LST. By contrast, ET_0 and ET_a have a different behaviour in the other months (MAMJJASO: March, April, May, June, July, August, September, and October) and the SM is lower than the critical SM, indicating a water-limited ET regime. In this case, the ET_0 increases from March to July and decreases from July to September, according to the temperature variation in this area. The ET_a is always lower than the ET_0 because the SM controls the ET process. Note that ET_a minimum is in August, corresponding to the minimum SM, and the driest month in semi-arid climates. The energy-limited and the water-limited periods found for 2014 approximately agree with the SM–LST transitions of Fig. 5.10 (top).
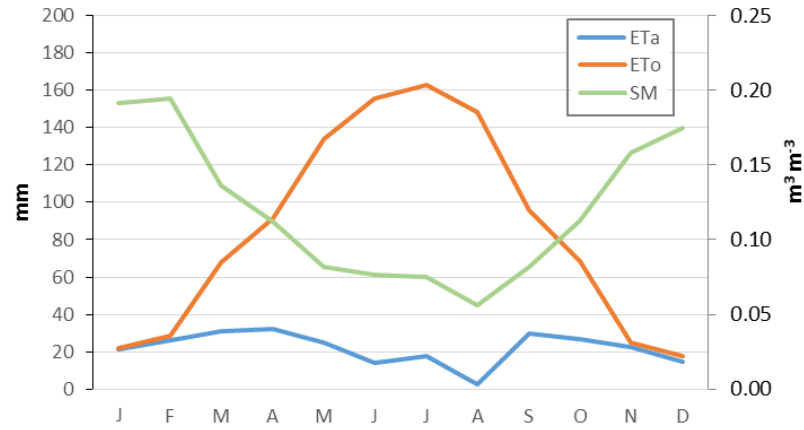
FIGURE 5.11: Monthly actual evapotranpiration (ET_a, blue line) from HidroMORE, potential evapotranspiration (ET_0, red line), and SM (green line) from the REMEDHUS network along 2014.

Table 5.2 summarizes the correlation between daily *in situ* SM from the REMEDHUS network and ET_a from HidroMORE, and the number of observations (N) for the energy-limited (NDJF) and water-limited (MAMJJASO) periods along 2014. As the persistence of SM is an important component in land–atmosphere interactions [Martínez-Fernández & Ceballos, 2003, Seneviratne *et al.*, 2010], the correlation has been computed considering the delayed SM with respect to the ET_a day (with a delay between 0 to 5 days, 0 days corresponds to the same day). In the energy-limited period, most correlation values are very weak (|R| ≤0.2) and others are non-significant. This result supports the argument that there is not a clear relationship between the SM and ET_a under energy-limited conditions due to SM–LST decoupling. Instead, correlations obtained in the water-limited period (R≈0.54 to 0.62) reveal an important relation of SM and ET_a due to SM–LST coupling. Since the SM of a particular day is related to the amount of previously lost water, the correlation increases considering the SM of one or two days after the ET_a day. This result indicates that there is a temporal lag between the ET behaviour and its impact on the SM.

TABLE 5.2: Correlation (R) between ET_a from HidroMORE and *in situ* SM from the REMED-HUS network, and number of observations (N) under energy-limited and water-limited conditions along 2014, considering the delayed SM with respect to the ET_a day (delay=0,1,2,3,4 or 5 days). Non-significant correlation values (p_{value} >0.05) are marked with an asterisk.

Delay in SM respect to ET_a	Energy-limited (NDJF)		Water-limited (MAMJJASO)	
	R	N [days]	R	N [days]
Same day	0.05*	120	0.54	245
1 day after	-0.07*	119	0.59	244
2 days after	-0.08*	118	0.61	243
3 days after	-0.17*	117	0.62	242
4 days after	-0.18	116	0.62	241
5 days after	-0.20	115	0.62	240

5.4.6 Validation of 1-km disaggregated SM estimates

Figure 5.12 shows the Taylor diagrams obtained from the validation of 1-km disaggregated SM estimates using all combinations of MODIS LST Terra/Aqua day/night with SMOS morning (left) and afternoon (right) passes at each REMEDHUS station. The std of the reference (depicted with a star) has been computed as the mean SM of the 21 REMEDHUS stations at morning and afternoon time-overpasses, respectively. The ubRMSD is measured with the dashed line circles around the reference, the std is measured with the pointed line arches, and the correlation (R) is measured with radial lines (not shown). In general, the disaggregated products using MODIS LST Terra day or Aqua day exhibit lower ubRMSD and higher correlation to ground-based measurements than the disaggregated product using MODIS LTS Terra night and Aqua night. This agrees with results previously obtained in Fig.5.5. Note that station H7 exhibits the highest ubRMSD ($\sim$0.08 m^3/m^3) and the lowest correlation (R$\sim$0.30) compared to the other REMEDHUS stations (ubRMSD$\approx$0.04 to 0.06 m^3/m^3; R$\approx$0.55 to 0.85), in agreement with results from Fig. 5.7 (left). No significant differences are found between morning and afternoon passes. Since the disaggregated SM using MODIS LST Aqua day displays a lower std compared to the *in situ* reference (yellow star) than the disaggregated SM using Terra day, the use of MODIS LST Aqua day is recommended for producing these downscaled SMOS SM (the current SMOS BEC L4 SM v.2), independently of the SMOS time-overpass. However, MODIS LST Terra day can also be used in the downscaling SM algorithm when Aqua day is not available.
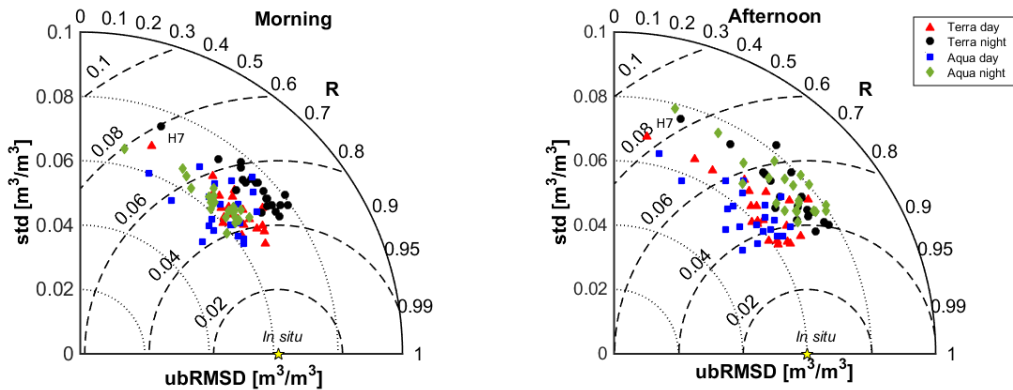
FIGURE 5.12: Taylor diagrams obtained from the validation of 1-km disaggregated SM estimates using MODIS LST Terra day (red triangles), Terra night (black circles), Aqua day (blue squares), and Aqua night (green diamonds) for each REMEDHUS station at the SMOS morning (left) and afternoon (right) passes.

Statistical scores (R, ubRMSD, bias, slope and coverage) obtained from the validation of the two 1-km disaggregated SM datasets using MODIS LST Aqua day are summarized in Tables 5.3 and 5.4 for morning and afternoon passes, respectively. In the analysis at the station scale, higher correlations are obtained for morning (R≈0.36 to 0.83) than for afternoon passes (R≈0.22 to 0.82). The ubRMSD is similar (ubRMSD≈0.04 to 0.10 m^3/m^3 *vs.* ubRMDS≈0.04 to 0.11 m^3/m^3) and the bias is also similar (bias≈-0.16 to 0.08 m^3/m^3 *vs.* bias≈-0.12 to 0.12 m^3/m^3). Slopes are slightly better for morning than for afternoon passes (s≈0.30 to 1.92 *vs.* s≈0.32 to 2.17). However, the coverage in the morning is lower than in the afternoon passes (N≈155 to 202 days *vs.* N≈174 to 228 days). Some REMEDHUS stations have a particular behavior, such as H9 and M13 with forest-pasture land use that have a higher ubRMSD ($\approx$ 0.10 to 0.11 m^3/m^3) and bias ($\approx$-0.16 to 0.15 m^3/m^3), and a very low slope (s ≈0.30 to 0.38) than the other stations. They are located in valley bottoms and flooded-prone areas, which could explain these differences. Additionally, H7 exhibit a very low correlation (R≈0.22 to 0.36) compared to the other stations. This agrees with results obtained in Figs. 5.4 (left) and 5.12, where H7 behaves as an outlier. Station K4 presents a high slope (s ≈1.92 to 2.17). This could be explained by the change of land use respect to the previous years 2010 and 2011, when it was vineyard. In the analysis at the network scale, the correlations are similar (R∼0.76 *vs.* R∼0.78). The ubRMSD is also similar ubRMSD≈0.05 m^3/m^3 *vs.* ubRMSD≈0.06 m^3/m^3) and no bias is found. Slopes are better in morning (s ∼1.05) than in afternoon passes (s ∼1.20). Nevertheless, the coverage is higher in afternoon than in morning (N≈278 days *vs.* N≈310 days). Therefore, no significant differences are found between the analysis at the station and the network level. Statistics from the validation of the other six 1-km disaggregated SM estimates (with MODIS LST Aqua night, Terra day and Terra night) are summarized in Appendix D (see Tables D.1, D.2, D.3, D.4, D.5, and D.6).

TABLE 5.3: Statistics from the validation of 1-km disaggregated SM using SMOS SM at the morning passes and MODIS LST Aqua day: correlation (R), unbiased Root Mean Square Difference (ubRMSD), bias, slope (s), and coverage (N).

Station	R	ubRMSD [m^3/m^3]	bias [m^3/m^3]	Slope s	N [days]
E10	0.70	0.06	0.07	1.56	179
F6	0.78	0.04	-0.04	0.82	194
F11	0.82	0.04	0.03	0.97	176
H7	0.36	0.06	0.05	1.48	175
H9	0.73	0.11	-0.15	0.38	155
H13	0.68	0.05	-0.01	0.79	177
I6	0.51	0.05	0.06	1.42	167
J3	0.63	0.05	0.08	1.59	179
J12	0.80	0.04	-0.15	0.87	171
J14	0.73	0.04	0.03	0.86	170
K4	0.62	0.06	0.06	1.92	194
K9	0.76	0.04	0.03	1.24	165
K10	0.83	0.04	0.05	1.40	165
K13	0.54	0.07	-0.11	0.43	190
L3	0.70	0.04	0.02	1.21	179
L7	0.77	0.05	-0.08	0.53	202
M5	0.66	0.06	0.00	1.12	184
M9	0.71	0.05	-0.07	0.56	161
M13	0.73	0.10	-0.16	0.30	200
N9	0.76	0.05	-0.05	0.64	193
O7	0.73	0.04	0.01	0.67	170
Network	0.76	0.05	0.00	1.05	278

TABLE 5.4: Same as Table 5.3, but for afternoon passes and MODIS LST Aqua day.

Station	R	ubRMSD [m³/m³]	bias [m³/m³]	slope s	N [days]
E10	0.73	0.06	0.11	1.59	201
F6	0.77	0.04	-0.02	0.80	219
F11	0.81	0.04	0.06	1.06	196
H7	0.22	0.06	0.09	0.72	205
H9	0.77	0.10	-0.11	0.35	181
H13	0.60	0.05	0.02	0.61	204
I6	0.36	0.05	0.09	0.78	190
J3	0.54	0.06	0.12	1.58	214
J12	0.81	0.04	-0.12	0.94	191
J14	0.74	0.04	0.05	0.94	200
K4	0.63	0.05	0.09	2.17	228
K9	0.70	0.04	0.06	0.80	189
K10	0.82	0.04	0.09	1.40	192
K13	0.74	0.05	-0.08	0.69	215
L3	0.63	0.05	0.05	0.97	198
L7	0.78	0.05	-0.05	0.57	227
M5	0.62	0.05	0.03	1.02	220
M9	0.67	0.04	-0.04	0.39	174
M13	0.71	0.10	-0.12	0.32	226
N9	0.79	0.04	-0.02	0.58	210
O7	0.78	0.04	0.03	0.63	190
Network	0.78	0.05	0.00	1.20	310

5.4.7 Coverage improvement

Scatter plots showing a comparison of the correlation (R, left), ubRMSD (middle) and bias (right) obtained from the validation of the disaggregated SM using MODIS LST Aqua day (the SMOS BEC L4 SM v.2 product) and the averaged ensemble of four disaggregated SM datasets are displayed in Fig. 5.13 for morning and afternoon passes. Note that the correlation (left) is similar in both SM estimates in the morning passes. Instead, it is slightly higher for the ensemble than for the disaggregated SM using Aqua day in the afternoon passes. However, in the analysis of the ubRMSD (middle), it is clearly seen that there is a lower ubRMSD for the disaggregated SM using Aqua day than for the ensemble both in the morning and afternoon passes. The bias (rigth) is similar considering both SM estimates and there are not significant differences between morning and afternoon passes. Results indicate that both SM estimates perform similar statistical scores, except for the ubRMSD, which is lower when only MODIS LST Aqua day is used in the SM downscaling algorithm.
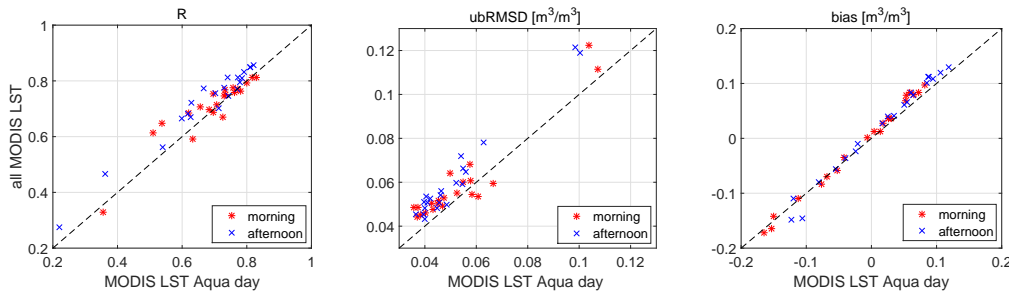
FIGURE 5.13: Scatters of correlation (R, left), unbiased Root Mean Square Difference (ubRMSD, middle), and bias (right) from the validation of disaggregated SM using MODIS LST Aqua day, and the averaged ensemble of four disaggregated SM datasets at the SMOS morning (red asterisks) and afternoon (blue crosses) passes.

Statistical scores (R, ubRMS, bias, slope and coverage) obtained from the validation of the averaged ensemble of four disaggregated SM datasets are summarized in Tables 5.5 and 5.6 for morning and afternoon passes, respectively. They are compared with those obtained from the validation of the disaggregated SM using MODIS LST Aqua day (the SMOS BEC L4 SM v.2 product) in Tables 5.3 and 5.4. In the analysis at the station scale, the correlations are similar in the morning passes, but they are slightly higher for the ensemble than when only using MODIS LST Aqua day in the downscaling algorithm in the afternoon passes (Aqua day R≈0.36 to 0.83/0.22 to 0.82; ensemble R≈0.33 to 0.81/0.27 to 0.86 for morning/afternoon), in agreement with results obtained in Fig. 5.13 (left). The ubRMSD is slightly lower for the disaggregated SM using MODIS LST Aqua day than for the ensemble (Aqua day ubRMSD≈0.04 to 0.11/0.04 to 0.10 m^3/m^3; ensemble ubRMSD≈0.04 to 0.12/0.04 to 0.12 m^3/m^3), in aggrement with results derived from Fig. 5.13 (middle). The bias is similar (Aqua day bias≈-0.16 to 0.08/-0.12 to 0.12 m^3/m^3; ensemble bias≈-0.17 to 0.10/-0.15 to 0.14 m^3/m^3), in aggrement with results obtained in Fig. 5.13 (right). Better slopes are obtained when using only MODIS LST Aqua day for the disaggregation (Aqua day s≈0.30 to 1.92/0.32 to 2.17; ensemble s≈0.30 to 2.79/0.35 to 2.53). There is a coverage improvement of ∼20 % when using the ensemble (Aqua day N≈155 to 202/174 to 224 days with ∼25 % of coverage along two years; ensemble N≈303 to 335/334 to 346 with ∼45 %). In the analysis at the network scale, the correlation is similar (Aqua day R≈0.76/0.78; ensemble R≈0.77/0.79) and the ubRMSD is equal (Aqua day ubRMSD∼0.05/0.05 m^3/m^3; ensemble ubRMSD∼0.05/0.05 m^3/m^3). The bias is higher for the ensemble in the afternoon passes (Aqua day bias∼0.00/0.00 m^3/m^3; ensemble bias∼0.00/0.04 m^3/m^3), but the slopes are similar (Aqua day s ∼1.05/1.20; ensemble s ∼1.04/1.21). Nevertheless, there is a coverage improvement of ∼15 % when using the ensemble (Aqua day N∼278/310 days with ∼40 % of coverage; all N∼385/411 days with ∼55 %).

TABLE 5.5: Same as Table 5.3, but for the averaged ensemble at the morning passes.

Station	R	ubRMSD [m^3/m^3]	bias [m^3/m^3]	Slope s	N [days]
E10	0.75	0.05	0.08	1.57	306
F6	0.76	0.05	-0.04	0.96	323
F11	0.81	0.05	0.04	1.08	311
H7	0.33	0.07	0.08	1.93	319
H9	0.75	0.11	-0.16	0.33	303
H13	0.70	0.05	0.00	0.93	310
I6	0.61	0.06	0.08	2.79	322
J3	0.59	0.06	0.10	1.53	325
J12	0.79	0.04	-0.14	0.93	317
J14	0.75	0.05	0.04	1.03	310
K4	0.69	0.06	0.08	2.21	329
K9	0.76	0.05	0.04	1.14	311
K10	0.81	0.05	0.07	1.44	320
K13	0.65	0.06	-0.11	0.63	335
L3	0.69	0.05	0.03	1.32	310
L7	0.77	0.05	-0.08	0.58	335
M5	0.71	0.05	0.01	1.19	324
M9	0.71	0.05	-0.07	0.70	313
M13	0.67	0.12	-0.17	0.30	333
N9	0.78	0.05	-0.06	0.68	331
O7	0.77	0.05	0.01	0.74	324
Network	0.77	0.05	0.00	1.04	385

TABLE 5.6: Same as Table 5.3, but for the averaged ensemble at the afternoon passes.

Station	R	ubRMSD [m^3/m^3]	bias [m^3/m^3]	slope s	N [days]
E10	0.78	0.06	0.12	1.81	340
F6	0.77	0.05	-0.01	1.01	358
F11	0.85	0.05	0.08	1.32	344
H7	0.27	0.08	0.11	1.53	352
H9	0.81	0.12	-0.15	0.32	339
H13	0.67	0.06	0.03	1.10	334
I6	0.47	0.07	0.11	2.12	347
J3	0.56	0.06	0.13	1.83	347
J12	0.85	0.05	-0.11	1.14	343
J14	0.81	0.05	0.07	1.25	339
K4	0.67	0.07	0.11	2.53	356
K9	0.76	0.05	0.08	1.23	339
K10	0.86	0.05	0.10	1.69	351
K13	0.75	0.05	-0.08	0.77	353
L3	0.72	0.05	0.06	1.50	340
L7	0.81	0.05	-0.06	0.66	359
M5	0.68	0.06	0.04	1.35	346
M9	0.77	0.05	-0.04	0.83	338
M13	0.70	0.12	-0.15	0.35	353
N9	0.83	0.04	-0.02	0.78	352
O7	0.80	0.05	0.04	0.84	346
Network	0.79	0.05	0.04	1.21	411

5.5 Conclusions

Nowadays, most of radiometric soil moisture (SM) retrieval and disaggregation algorithms employ the instantaneous land surface temperature (LST). Alternative LST-derived parameters, such as the daily maximum LST, may provide a better representation of the SM–LST relationship than the instantaneous LST. To analyze this hypothesis, the SM and LST dynamics at daily and seasonal scales were evaluated using four years of data (2011–2014) from both *in situ* and satellite observations. The study site is the REMEDHUS network, located at the central part of the river Duero basin, in Spain. The objective was to better understand the fundamental SM–LST link and assess this relationship through the SM–LST coupling/decoupling, the evapotranspiration and the thermal inertia. The SM–LST interaction was studied with the direct variables in absolute values and with their anomalies, to separate out seasonality. Additionally, a validation of the eight 1-km disaggregated SM estimates using all possible combinations of SMOS SM morning/afternoon–MODIS LST Terra/Aqua day/night and an averaged ensemble with ground-based data was also performed using two years of data (2012–2013).

Considering the entire study period, SM and LST are, as expected, anticorrelated. At the daily scale, results from *in situ* data show that instantaneous SM exhibits stronger anticorrelation to daily maximum LST (R≈-0.7) than to the other LST-derived parameters (i.e., instantaneous LST, daily mean LST, daily median LST, daily minimum LST and LST diurnal range). When using satellite data, stronger anticorrelation is obtained between SMOS SM and MODIS LST Aqua (or Terra) day (R≈-0.7) than night (R≈-0.4 to -0.5). This is consistent with the *in situ* analysis, since the time of MODIS LST Aqua (or Terra) day is closer to the time of daily maximum LST, which is also the time of maximum potential evapotranspiration (i.e., when there is a higher atmospheric demand of water). For the anomaly time-series, results from *in situ* data show that LST diurnal range presents the strongest anticorrelation with SM (R≈-0.3), followed by daily maximum LST (R≈+0.3). This indicates that maximum LST and LST diurnal range provide complementary information on the SM-LST relationship. When using satellite data, the strongest anticorrelation is obtained with MODIS LST Aqua (or Terra) day (R ≈-0.5). Further research using a geostationary satellite such as MSG SEVIRI with a temporal resolution of 15 min. would be needed to further evaluate the relationship of SM with LST diurnal range. In addition, the SM–LST space of the normalized occurrence frequency density diagrams display a triangular shape in both ground-based and spaceborne observations.

The seasonal dependency of the correlation was also studied. Results from *in situ* data show a strong anticorrelation between instantaneous SM and daily maximum LST in spring, summer and autumn seasons (R≈-0.5 to -0.7), revealing a SM–LST coupling. By contrast, a very low correlation is obtained in winter (R≈+0.3), which indicates a clear SM–LST decoupling. When using satellite data, results confirm a SM–LST coupling in spring, summer and autumn (R≈-0.4 to -0.7), and a SM–LST decoupling in winter (R≈-0.3). For the anomaly time-series, the highest correlation is obtained in summer for *in situ* data (R≈-0.5). This can be related to the fact that an increase of SM from an individual precipitation event has an important impact on LST in very dry conditions due to its low thermal inertia. Differences in the correlation during winter with the direct variables and during summer with the anomalies could be due to the different spatial scales represented by the remotely sensed and ground-based data. Similar conclusions could be extracted from the normalized occurrence frequency density diagrams displayed per seasons, where the triangular shape is better defined in transitional seasons (autumn and spring) due to the higher dynamic range of SM and LST.

Collocated SM and LST time-series display SM–LST coupling periods, approximately corresponding to spring, summer and autumn, and SM–LST decoupling periods, approximately corresponding to winter. These two behaviors can be identified in both *in situ* and satellite measurements. A method to estimate the critical SM from the crossing points of these SM–LST coupling/decoupling transitions was proposed. A critical SM of ∼0.12 m^3/m^3 is estimated using both *in situ* and spaceborne observations. This value is consistent with field measurements of soil field capacity and wilting point.

Since the SM–LST coupling/decoupling periods are related to water/energy-limited regimes, respectively, the temporal evolution of the evapotranspiration is further analyzed for a specific year (2014). The actual evapotranspiration is simulated using the regional hydrological model HidroMORE. The correlation between the daily SM and the modeled actual evapotranspiration ET_a confirm that SM and ET_a only interact under water-limited conditions (with R∼0.6) with a temporal lag between them of 2–3 days. A non-significant correlation between SM and ET_a is observed under energy-limited conditions.

When validating the 1-km disaggregated SM estimates, higher correlation and lower ubRMSD and std are obtained in the Taylor diagrams when using MODIS LST Aqua (or Terra) day than when using Aqua (or Terra) night in the SM downscaling algorithm. This agrees with results derived from the analysis of the SM–LST relationship. Therefore, the use of MODIS LST Aqua (or Terra) day for SM downscaling is recommended.

Considering the statistical scores of the 1-km disaggregated SM using MODIS LST Aqua day at the network scale, the correlation, ubRMSD and bias are similar both for morning and afternoon passes (R≈0.76 to 0.78, ubRMSD≈0.05 m^3/m^3 and bias≈0 m^3/m^3). Better slopes are obtained for morning than for afternoon (*s*∼1.05 *vs.* *s*∼1.20), and lower coverage is found in the morning than in the afternoon (N≈278 *vs.* N≈310), but this difference in coverage is low (∼5 %). These results reveal that no significant differences are obtained between morning and afternoon passes. Similar results are obtained at the station scale. Comparing these statistics with those obtained from the averaged ensemble, similar correlation, ubRMSD, bias and slopes are obtained at the network scale (R≈0.76 to 0.78, ubRMSD≈0.05 m^3/m^3, bias≈0 m^3/m^3 and *s*≈1.04 to 1.21). At the station scale, the ubRMSD is slightly lower in the disaggregated SM using MODIS LST Aqua day than in the ensemble (Aqua day ubRMSD≈0.04 to 0.11 m^3/m^3; ensemble ubRMSD≈0.04 to 0.12 m^3/m^3). However, there is a coverage improvement of ∼15–20 % in the ensemble respect to the disaggregated SM using MODIS LST Aqua day.

This study contributes to furthering present knowledge of SM and LST interactions in land surface, hydrological and climate models. Results presented could be applicable to microwave/optical synergistic SM retrieval algorithms and, particularly, for the improvement of applications based on the SM–LST link, related to evapotranspiration. Also, an ensemble composed of an average of all available disaggregated SMOS/MODIS SM data could be useful for enhancing the coverage. Further research is needed to study the possible dependency of the different Earth's land covers/climate types in the SM–LST relationship, and also to analyze this relationship and

the performance of the disaggregated SM using geostationary LST data. Nevertheless, the application of geostationary LST data to an operational SM disaggregation algorithm requires more time and a higher computation capacity than the use of the averaged ensemble from MODIS.

Chapter 6

Passive and active microwave vegetation parameters

Passive sensors (radiometers) consist only of a receiver that measures the radiation naturally emitted from the scene under observation, while active sensors (radars) consist of a transmitter and a receiver that measures the signal that is reflected, refracted or scattered. Microwave observations between 1 and 10 GHz are sensitive to SM, but are also sensitive to vegetation characteristics [Jackson & Schmugge, 1991]. Traditional passive soil moisture (SM) retrieval algorithms require *a priori* vegetation information as ancillary input, which is partially or fully used to correct for the attenuation and scattering effects of the plant canopy on the observed signal. The ancillary vegetation information is usually land cover-based or derived from optical visible/infrared (VIS/IR) indices, as occurs in both SMOS [Kerr *et al.*, 2012, 2016] and SMAP [O'Neill *et al.*, 2015, Chan *et al.*, 2016].

Based on the degrees of information framework [Konings *et al.*, 2015], a new multi-temporal dual-channel algorithm (MT-DCA) has recently been developed for simultaneous retrievals of SM and vegetation optical depth (VOD), together with a static single-scattering albedo (ω), all based on microwave measurements alone and without reliance on optical information or land use assumptions. This approach uses time-series of passive L-band observations in a single incidence angle at both polarizations [Konings *et al.*, 2016]. Hence, it is applicable to the three L-band missions: SMOS, Aquarius and SMAP. The first year of passive SMAP data was processed with the latest implementation of MT-DCA and the results are very optimistic to be an alternative to traditional approaches [Piles *et al.*, 2016a].

6.1 State of the art

Whether with multi-angular or with fixed-angle measurements, passive microwave SM retrievals are generally based on the τ-ω model [Mo *et al.*, 1982] (see Eq. (2.72)). In this model, two parameters are used to describe how the vegetation affects the observed signal: i) tau (τ) or vegetation optical depth (VOD), and ii) single-scattering albedo (ω). These two parameters characterize the absorption and the scattering effects, respectively, within the vegetation canopy and must be accounted for in SM retrieval algorithms (see Subsection 2.3.8).

VOD is usually assumed to be linearly related to the total vegetation water content (VWC) (see Eq. (2.74)). Although SMOS algorithm attempts to retrieved VOD based on the multi-angular information, *a prior* VOD value based on optical data is used when not enough angular measurements are available [Kerr *et al.*, 2012, Rahmoune *et al.*, 2013, Kerr *et al.*, 2016]. The SMAP algorithm estimates VOD based on a Normalized Difference Vegetation Index (NDVI) climatology, which does not provide interannual variability of VWC or variations in hydraulic state

depending on recent water supply [O'Neill *et al.*, 2015, Chan *et al.*, 2016]. The ω is commonly set to a constant value, either global or land cover dependent, in both the SMOS [Kerr *et al.*, 2012, 2016] and SMAP [O'Neill *et al.*, 2015, Chan *et al.*, 2016] algorithms.

Active vegetation measurements are also sensitive to vegetation scattering and water content. At L-band, cross-polarized backscattering observations (σ_{HV}) are relatively insensitive to SM [Le Toan *et al.*, 1992, Dubois *et al.*, 1995], and can thus be potentially used as a vegetation indicator analogous to VOD. In addition, a previous study has used the Radar Vegetation Index (RVI) as an indicator of vegetation growth [Kim & Van Zyl, 2009]. Also, vegetation indices from radar observations were evaluated to represent VWC with a ground-based SMAP simulator [Srivastava *et al.*, 2015b]. Recently, a relationship between the MT-DCA VOD retrievals and σ_{HV} has been found using three years of Aquarius data. Although validations at the spatial scale of Aquarius ($\sim$100 km) are difficult, the VOD based on passive observations and the VOD predicted by active measurements are comparable globally [Rötzer *et al.*, In review]. These studies suggest the potential of using combined active-passive microwave vegetation parameters.

In this study, the MT-DCA is applied to the radiometer observations acquired by the Passive/Active L-band Sensor (PALS) [Wilson *et al.*, 2001] during the SMAP Validation Experiment 2012 (SMAPVEX12) campaign [McNairn *et al.*, 2015]. *In situ* SM and vegetation measurements as well as satellite vegetation observations are used for validating MT-DCA retrievals. The main objective is to explore the possible relationships between retrieved airborne radiometer-based VOD and ω and co-located radar measurements. The relations obtained may be used to provide a better representation of VOD and ω in passive SM retrievals, which are at present estimated using optical VIS/IR vegetation indices. This may be of special interest in multi-resolution active-passive systems, where the link to the radar measurement allows estimation of these vegetation properties at high resolution. The content of this Chapter has been published in a journal [Pablos *et al.*, Submitted]

6.2 Datasets

6.2.1 SMAPVEX12: Satellite and *in situ* data

The SMAPVEX12 campaign took place in Southern Manitoba (Canada), in the Red River watershed, around the town of Elm Creek (see Fig. 6.1). This region was selected due to its wide range of soil and vegetation conditions, with clay soil in the East (agricultural use), and loam and sandy loam soils in the West (forested area and some agricultural fields). These diverse conditions lead to significant spatial and temporal variability of SM and vegetation cover which are ideally suited for field campaigns that are limited in duration and extent. SMAPVEX12 was carried out during the growing season, from June 7 to July 19, 2012 (6 weeks).

A land cover classification map of the SMAPVEX12 region at 20 m of spatial resolution, derived from satellite images of the RADARSAT-2, Système Pour l'Observation de la Terre (SPOT-4), and DMC International Imaging Ltd (DMCii) [McNairn *et al.*, 2014], is shown in Fig. 6.1. The principal domain, enclosed in the black rectangle, is 70.4 km long x 12.8 km wide, covering an area of approximately a SMAP radiometer pixel at coarse resolution (36 km). It can be divided in 22 square cells of 6.4 km of side, which are close to a SMAP pixel at medium (M) resolution (9 km) of the active-passive baseline.

The land cover data are used to estimate the fraction of agricultural crop cover for each M-scale pixel. The agricultural crop types include forage, barley, oat, rye, triticale, wheat, corn, canola/rapeseed, flaxseed, sunflowers, soybeans, peas, potatoes, other vegetables, and berries. Figure 6.2 shows the agricultural fraction of each M-cell (in percent, from dark green to red), where two groups can be clearly distinguished: <50% (from 1 to 10) and >50% (from 11 to 22) of agricultural fraction. This classification approximately follows soil texture regions [McNairn *et al.*, 2015]. Cells with more agricultural activity are located in regions with more clay content. Natural vegetation and trees dominate the remainder of the domain. The contrast

of forest and cropland are important to interpreting the temporal and spatial patterns of the retrieved vegetation parameters.
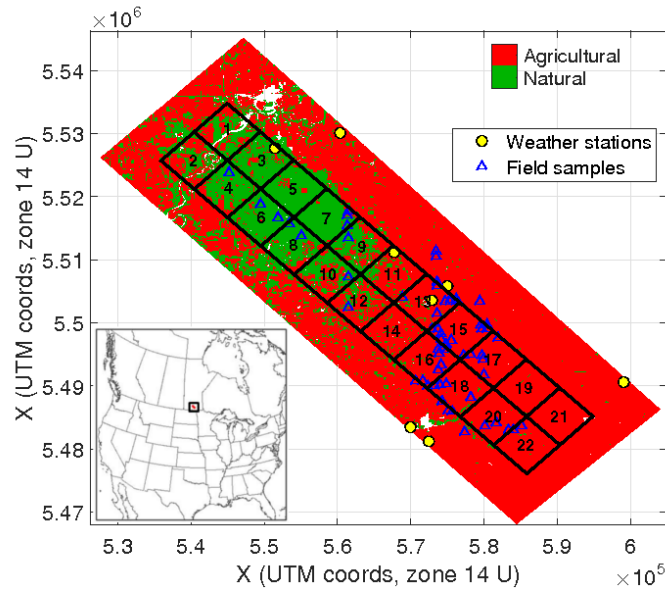
FIGURE 6.1: SMAPVEX12 experimental site in the Red River watershed, Southern Manitoba, in Canada. The spatial domain shows the 22 M-cells. The land cover classification displays areas with agricultural (red) and natural vegetation or forests (green). The location of the 8 weather stations (yellow points) and the 60 field samples (blue triangles) is marked.
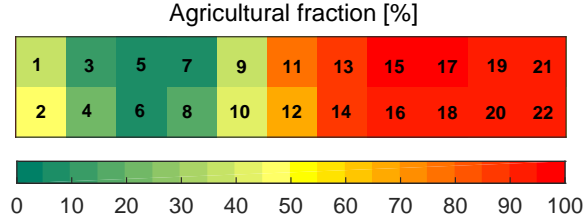
FIGURE 6.2: Map of agricultural fraction (%) of each M-cell of the SMAPVEX12 domain.

Satellite maps of VWC at very high resolution (5 m), based on the Normalized Difference Water Index (NDWI) from SPOT and RapidEye instruments are obtained during the field experiment [Cosh, 2014]. In this study, all VWC_{NDWI} pixels within the same M-cell are averaged.

During the SMAPVEX12 experiment, *in situ* data was collected over 55 agricultural fields [Wiseman *et al.*, 2014a,b] and 5 forested fields [Moghaddam & Berg, 2014], both depicted with blue triangles in Fig. 6.1. The crop type distribution of the agricultural fields is: 19 soybeans fields, 16 cereal (13 spring wheat, 1 oat and 2 winter wheat), 8 corn, 7 canola, 4 pasture, and 1 forage. The mean crop height along time, obtained after averaging all data samples within the same M-cell, is used in this study. The forested sites are a mix of broadleaf forest and perennial grasslands and pastures. The main tree species included are Trembling Aspen, Bur Oak and Balsam Poplar. The mean height of trees is between 6.6 and 10.1 m, and remains stable along time.

The SM ground sampling days were synchronized with the aircraft flight days. In the agricultural fields, 16 sampling observations, with 3 replicas of each sample point, were acquired to capture a representative soil moisture value of the field at 0–5 cm. In the forested sites, one sampling observation was selected to be representative of the entire site. For each day, all field observations within the same cell are averaged to obtain a single value at M-scale.

There are different weather stations around this area, but only stations within the domain or at less than 10 km of its edges are considered in this study. These are eight stations: Wingham Farms Ltd., Elm Creek A, Manitoba Water Stewardship Elm Creek, Sperling, Syngenta Portage la Prairie, Portage Southport, Carman U of M CS, and Agrotak Carman, marked with yellow circles in Fig. 6.1. The accumulated daily precipitation is computed as the sum of daily rain observations of these eight stations.

6.2.2 Airborne data from PALS

The airborne PALS instrument provides coincident radiometer and radar observations with an effective spatial resolution of ∼1.3 km at a fixed 40°incidence angle. The radiometer operates at 1.413 GHz, measuring the brightness temperatures (T_B) at both horizontal (H-pol) and vertical (V-pol) polarizations [Colliander, 2014b]. The radar operates at 1.26 GHz and measures the backscatter cross-sections at H-pol (σ_{HH}), V-pol (σ_{VV}) and HV-pol (σ_{HV}) polarizations [Colliander, 2014a]. The land IR surface temperature is also measured.

PALS was flown over the SMAPVEX12 area on 17 deployments (spread over 43 days), following eight lines spaced 1.6 km apart along the largest dimension of the experimental domain. However, only 14 days have coincident and well-calibrated radiometer and radar data. PALS data were acquired at two different altitudes: high (1750 m) and low (1200 m). In this study the high altitude data are used since they cover an area equivalent to a SMAP radiometer pixel and allow replicating the SMAP active-passive measurement geometry. PALS observations within each cell are averaged for each flight-day to obtain active and passive datasets at M-scale.

6.2.3 Estimation of RVI

RVI is a normalized cross-polarization backscatter estimation. The cross-polar backscatter (σ_{HV}) has higher sensitivity to vegetation (i.e. volume scattering) than the co-polar backscatters (σ_{HH} and σ_{VV}) and is relatively insensitive to surface reflectivity and surface soil moisture [Le Toan *et al.*, 1992, Dubois *et al.*, 1995]. The RVI measures the volume scattering typically caused by structural elements of vegetation canopies (e.g., branches), independently of its greenness as [Kim & Van Zyl, 2009]:

$$RVI = \frac{8\sigma_{HV}}{\sigma_{HH} + \sigma_{VV} + 2\sigma_{HV}}, \tag{6.1}$$

where radar backscatter values are expressed in units of power. RVI is an index that varies from 0 to 1, increasing with the amount of vegetation on the land surface. If the vegetation canopy is composed of long and randomly-oriented lossy dielectric cylinders (branches), the limiting values of σ_{HH} and σ_{VV} are the same and equal to three times σ_{HV} (then, RVI=1). Detailed information on RVI errors due to radar speckle noise and miscalibration can be found in McColl *et al.* [2014].

6.3 Methodology

6.3.1 Implementation of MT-DCA

The MT-DCA is based on the minimization of the quadratic difference between the observed and the modeled T_B, for two consecutive passes, using two polarizations and a single look-angle, although it can be adapted to multi-angular observations. The modeled T_B are obtained from the modeled reflectivities, which are estimated using Fresnel equations [Ulaby & Long, 2014] and the measured IR surface temperature. Roughness effects are incorporated in the modeled reflectivity through the roughness parameter h_s using Eq. (2.68) [Choudhury *et al.*, 1979]. The Root Mean Square (RMS) roughness measured in the field is ∼0.94 cm, which corresponds to

a value of h_s=0.31 at the wavelength of the observations according to Eq. (2.69). A constant h_s=0.31 is therefore used in this study.

An updated implementation of the MT-DCA, which uses a gradient optimization technique, is applied to SMAPVEX12 T_B time-series at H-pol and V-pol without use of ancillary data besides the IR surface temperature. Since PALS acquisitions started approximately at 6:30 A.M. local time, it is assumed that the vegetation temperature is in thermal equilibrium with the soil temperature [Hornbuckle & England, 2005]. In the algorithm, two consecutive observations are used to estimate two values of dielectric constant (ϵ_{MT}) and one VOD$_{MT}$ (subscript denotes multi-temporal retrieval) at each M-cell for all possible ω values. Later, the ω_{MT} value per cell that minimizes the quadratic difference between the observed and the modeled MPDI is estimated (see Eq. (2.23)). Therefore, MT-DCA assumes a constant VOD between time-adjacent observations and a constant ω over the entire period of record. For SMAPVEX12 data, two consecutive observations of the same cell can be separated from 2 up to 5 days. The histogram and the map of the VOD differences between consecutive passes over the same cell are shown in Appendix E (see Fig. E.1). They have a mean of $7.3 \cdot 10^{-4}$ and a standard deviation (std) of 0.05. The elapsed time between time-adjacent observations is short enough to avoid major changes in vegetation conditions. However, some crops during the growing season may change enough to question the constant ω assumption along the study period.

The retrieved SM is obtained from the retrieved ϵ_{MT} after applying the Mironov mixing dielectric model [Mironov *et al.*, 2009], using the in *situ* clay fraction data as input. This is the dielectric model currently adopted in SMOS and SMAP algorithms [Kerr *et al.*, 2012, O'Neill *et al.*, 2015]. As a result of the moving window, two SM retrievals are estimated for each day and cell. The histogram and the map of the differences between the two estimates are shown in Appendix E (see Fig. E.2). They have a mean of 0.0015 m^3/m^3 and a std of 0.012 m^3/m^3. The resulting SM$_{MT}$ is obtained after averaging the two soil moisture values corresponding to the same day and cell.

6.3.2   Statistical analysis

In order to assess the impact of the vegetation cover on multi-temporal retrievals (SM$_{MT}$, VOD$_{MT}$ and ω_{MT}), the entire analysis has been performed for all M-cells as well as for the combined groups of croplands and forests, according to the land cover classification.

The retrieved SM$_{MT}$ was compared to ground-based SM measurements for each M-cell and day. This analysis includes the computation of: i) correlation (R), ii) bias, iii) Root Mean Square Difference (RMSD), iv) unbiased RMSD (ubRMSD), and v) slope (s) estimated through a robust linear regression [DuMouchel & O'Brien, 1989]. They are the statistical metrics generally used to assess the accuracy of the satellite-based SM estimates [Entekhabi *et al.*, 2010a]. It is important to note that certain cells (1, 2, 3, 5, 11, 14, 19, and 21) do not have field SM samples. Also, even though several ground-based observations are averaged per field and cell, there may still be representative error between the M-cell spatial domain and the *in situ* measurements. Nevertheless, all the statistics obtained were significant (p_{value} <0.05, 95 % of significance level).

The retrieved VOD$_{MT}$ was analyzed for each day and M-cell. It was compared to co-located radar measurements σ_{HV} and RVI, and also to satellite VWC$_{NDWI}$. In the comparison to active vegetation parameters, a robust linear regression fit was estimated. The b parameter relating the VOD to VWC$_{NDWI}$ was also estimated and compared with the land-cover based b values used in the SMAP mission [O'Neill *et al.*, 2015]. Additionally, the covariability (as measured by R and RMSD) between the retrieved VOD$_{MT}$ and the VOD estimates (VOD$_{\sigma_{HV}}$, VOD$_{RVI}$, and VOD$_{NDWI}$) was analyzed.

The retrieved static ω_{MT} was compared to the land cover-based ω values used in the SMAP mission [O'Neill *et al.*, 2015] as well as to the temporal mean of co-located radar measurements σ_{HV} and RVI. Also, a robust linear fit was estimated with the radar parameters and statistical

scores (R and RMSD) between ω_{MT} and the ω estimates ($\omega_{\sigma_{HV}}$ and ω_{RVI}) were computed for all M-cells.

6.4   Results and discussion

6.4.1   MT-DCA retrievals

The retrieved SM_{MT} for each cell (top) and accumulated daily precipitation (bottom) along time over SMAPVEX12 domain are shown in Fig. 6.3. The color bar indicates the agricultural fraction within each M-cell. Note the missing data on July 8 is due to the aircraft measuring only half of the SMAPVEX12 domain, specifically over even numbered cells. Cells with a higher agricultural area exhibit a larger dynamic range ($SM_{MT} \approx 0.02$ to 0.31 m^3/m^3) than the forested cells ($SM_{MT} \approx 0.05$ to 0.19 m^3/m^3). The higher SM content reached by croplands could be due to the larger soil clay content in these cells, which could lead to a higher water retention; the lower SM values could be, in turn, related to the higher absorption of the water content in the crop plants during the growing stages [Brouwer & Heibloem, 2001]. The temporal evolution of SM_{MT} is consistent with the daily precipitation, with a general decreasing trend during the summer period and rainfall events captured in June 16, June 22, July 4, July 12 and July 15.
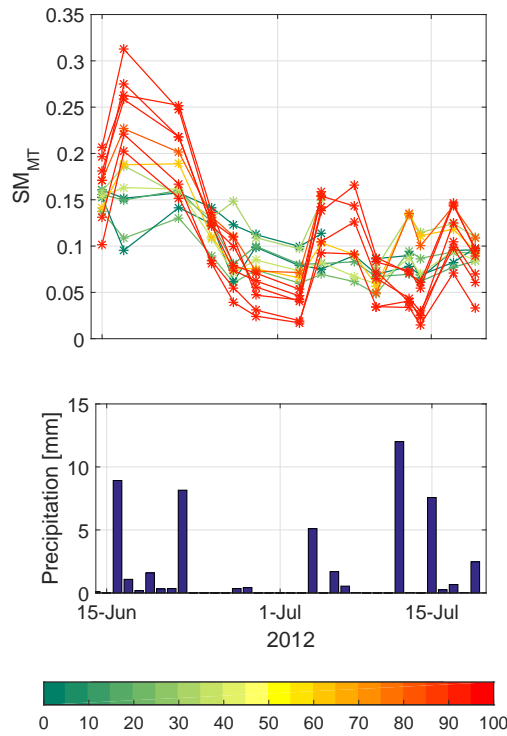
FIGURE 6.3:   Retrieved SM_{MT} (top) and accumulated daily precipitation over the SMAPVEX12 domain (bottom) along time. The color bar indicates the agricultural fraction within each M-cell.

Figure 6.4 displays the retrieved VOD_{MT} (top), mean crop vegetation height from *in situ* measurements (middle) and accumulated daily precipitation (bottom) over SMAPVEX12 along time. Forested cells have the highest values ($VOD_{MT} \approx 0.15$ to 0.50, with a mean of 0.27) and agricultural cells the lowest ($VOD_{MT} \approx 0$ to 0.32, with a mean of 0.09). There are two distinctive peaks of VOD_{MT} in two different periods (from June 22 to July 3 and from July 8 to 14), which are more pronounced in croplands than in forests. In contrast, the crop height (ground-based measurements) are monotonically increasing. This result agrees with the fact that the experiment

was performed during the growing season and no harvesting was carried out [McNairn *et al.*, 2015]. Therefore, there is a crop development and a biomass increase that appear to be affecting the VOD_{MT} evolution, particularly in the last part of the study period. In addition, the two peaks of VOD_{MT} approximately correspond to the two rainfall events with a certain delay implying an increase in water vegetation content but not height. This is explained by the fact that VOD_{MT} does not immediate decline after the last rainfall event as stomatal closure acts to maintain relative water content. The relative water content effect on VOD_{MT} is initially masked by continuing biomass growth. In a recent study, the global mean values of SMOS VOD over two years (2010-2011) are of 0.219 for croplands, 0.179 for grassland, 0.710 for evergreen broadleaf forest, and 0.575 for deciduous broadleaf forest [Cui *et al.*, 2015b], which are higher than those obtained in this study. The possible reason for this discrepancy is the limited study period of the SMAPVEX12 field campaign, covering only a month and a half during summer 2012.
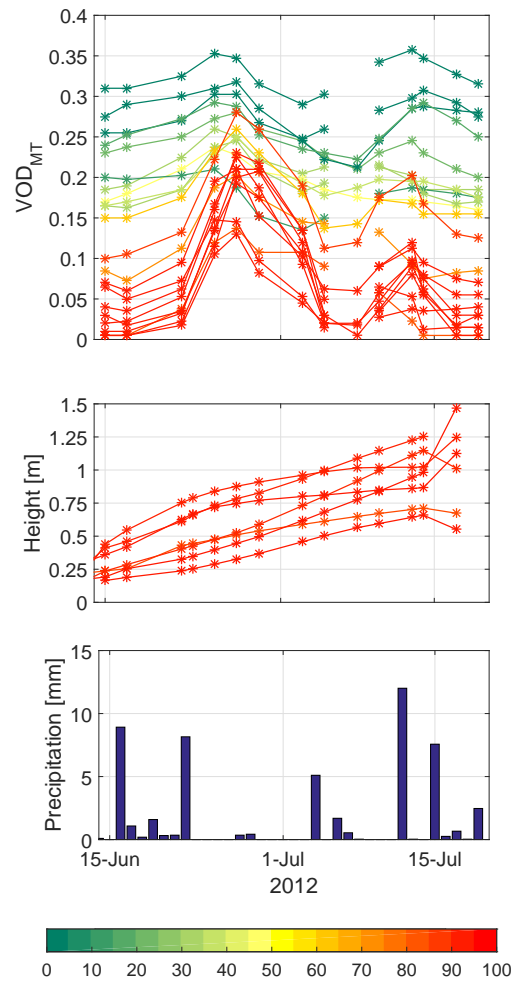
FIGURE 6.4: Retrieved VOD_{MT} (top), mean crop height from *in situ* measurements (middle), and accumulated daily precipitation (bottom) over the SMAPVEX12 domain along time. The color bar indicates the agricultural fraction within each M-cell.

The retrieved ω_{MT} for each M-cell is shown in Fig. 6.5, separating croplands (red circles) and forests (green triangles). In general, forested cells are grouped in the highest values of ω_{MT} with a mean of 0.145, which indicates more vegetation density and microwave scattering due to the presence of woody trees in these areas. Agricultural cells have the lowest values of ω_{MT} with a mean of 0.083. Note that these values are higher than those defined in the SMAP mission for broadleaf forests (ω=0.12) and grassland/croplands (ω=0.05). The retrieval of a static albedo may not be adequate in agricultural regions where significant crop growth can lead to albedo variations over time. However, the limited duration of the field experiment does not

allow a dynamic albedo retrieval. The dynamic albedo retrievals, using SMAP time-series with a modified MT-DCA method is under development and would be of special interest for croplands.
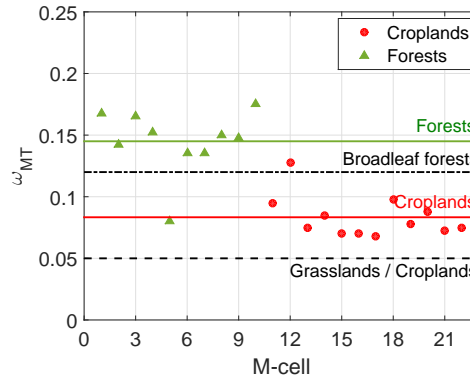
FIGURE 6.5: Retrieved static ω_{MT} over the SMAPVEX12 domain for each M-cell. The mean ω of croplands (red line and circles) and forests (green line and triangles), and the SMAP ω values for broadleaf forests (pointed black line) and grasslands/croplands (dashed black line) are included.

6.4.2 Soil moisture validation

A scatter plot of the retrieved SM_{MT} and co-located *in situ* SM observations is shown in Fig. 6.6. It includes linear regressions of all M-cells (black line), croplands (red line and circles) and forests (green line and triangles). A dry bias is evident in SM_{MT}, both in croplands and forests. The linear regression for croplands is close to the one obtained considering all cells.
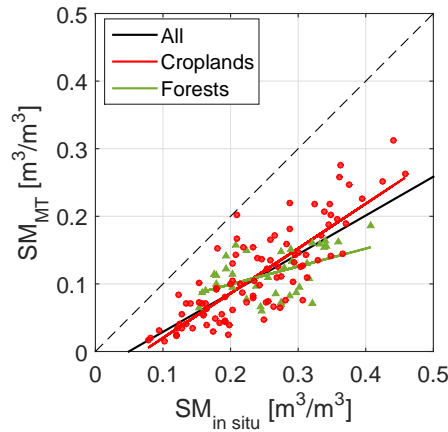
FIGURE 6.6: Comparison of retrieved SM_{MT} and *in situ* SM. The linear regressions of all M-cells (black line), croplands (red line and circles) and forests (green line and triangles) are included.

Statistics obtained from the SM validation for all M-cells, and for croplands and forests separately, are summarized in Table 6.1. It also contains statistics for a particular group of M-cells (13, 15, 16 and 17), which were used in a previous study [Leroux *et al.*, 2016]. Note that there is a stronger correlation in croplands (R~0.83) than in forests (R~0.47) and across all cells (R~0.78). There is a large bias in all cases (bias≈-0.13 to -0.15 m^3/m^3), as was already seen in Fig. 6.6. The RMSD and ubRMSD are lower in croplands (~0.134 m^3/m^3 and ~0.047 m^3/m^3, respectively) than in forests (~0.157 m^3/m^3 and ~0.056 m^3/m^3) and considering all cells (~0.141 m^3/m^3 and ~0.051 m^3/m^3), indicating a better agreement with *in situ* data for agricultural areas. Additionally, the slope is higher in croplands (s ~0.66) than in forests (s ~0.57) and considering all

cells ($s \sim 0.25$). This could be due to the lower number of *in situ* data samples available for the validation of forested cells, which may not be representative of the scales observed by the remote sensing data. In the particular group of M-cells, statistics obtained with MT-DCA ($R \sim 0.87$, ubRMSD~ 0.042 m^3/m^3) have an important improvement relative to those obtained with the single-channel algorithm (SCA) approach ($R \sim 0.61$, ubRMSD~ 0.072 m^3/m^3). However, the bias is lower using SCA (-0.056 m^3/m^3) than using MT-DCA (-0.110 m^3/m^3) [Leroux *et al.*, 2016].

TABLE 6.1: Statistics from SM validation for all M-cells, croplands, forests, and group of M-cells*.

	R	bias [m^3/m^3]	RMSD [m^3/m^3]	ubRMSD [m^3/m^3]	Slope s
All	0.78	-0.131	0.141	0.051	0.57
Croplands	0.83	-0.125	0.134	0.047	0.66
Forests	0.47	-0.146	0.157	0.056	0.25
Group of M-cells	0.87	-0.110	0.118	0.042	0.72

All statistics are significant ($p_{value} <0.05$).
*Group of M-cells (13, 15, 16 and 17) used in a previous study [Leroux *et al.*, 2016].

Figure 6.7 shows the mean *in situ* SM (blue line and asterisks) and SM$_{MT}$ (pink line and crosses) over the SMAPVEX12 region over time. The error bar indicates the std among the 22 M-cells. Both time-series exhibit the same behavior, although they have different mean values (≈ 0.17 to 0.35 m^3/m^3 for *in situ* and ≈ 0.06 to 0.20 ^{3}/m^3 for multi-temporal retrievals). This bias is consistent with results shown in Fig. 6.6 and Table 6.1. Additionally, the spatial variability is lower in SM$_{MT}$ (std≈ 0.02 to 0.06 m^3/m^3) than using *in situ* SM observations (std≈ 0.04 to 0.08 m^3/m^3).
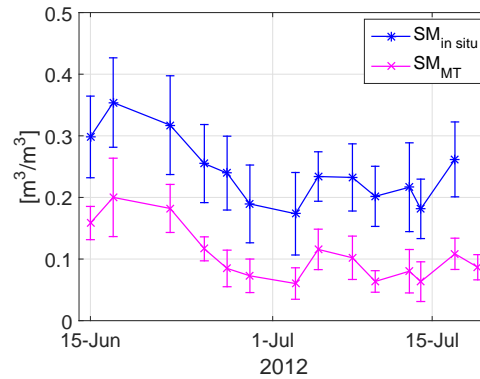
FIGURE 6.7: Mean *in situ* SM (blue line and asterisks) and retrieved SM$_{MT}$ (pink line and crosses) over the SMAPVEX12 domain along time. The error bar indicates the std among the 22 M-cells.

6.4.3 Comparison of passive and active vegetation parameters

The comparison between the retrieved VOD$_{MT}$ *versus* σ_{HV} (top left), RVI (top right) and VWC$_{NDWI}$ (bottom) is shown in Fig. 6.8. It includes the linear regressions of all M-cells (black line), croplands (red line and circles) and forests (green line and triangles). A first-order polynomial seems to be adequate to represent the relationship of VOD$_{MT}$ to σ_{HV} (with σ_{HV} ranging between 0.004 and 0.059 in linear units, which approximately corresponds to the global dynamic range) and for the relationship of VOD$_{MT}$ to RVI (with RVI ranging between 0.43 and 0.89). When relating VOD$_{MT}$ to VWC$_{NDWI}$, the linear regression is forced to have a zero intercept and the slope corresponds to the b parameter. In the comparison with σ_{HV}, agricultural cells present a high dispersion whereas forested cells exhibit a better agreement. In the comparison with RVI, both datasets show a good agreement. In the comparison with VWC$_{NDWI}$,

the datasets have very different b values but a similar dynamic range ($VWC_{NDWI} \approx 1.3$ to 5.1 kg/m^2). The obtained b parameter is larger in forests ($b \sim = 0.101$, with a confidence interval of 0.094–0.109) that in croplands ($b \sim 0.031$, with a confidence interval of 0.027–0.034), confirming a dependence of VOD–VWC relationship with land cover type. The b values in croplands are lower than those used in SMAP for croplands ($b=0.11$), but in forests are similar to those obtained for evergreen broadleaf forests ($b=0.10$), deciduous broadleaf forests ($b=0.12$), and grasslands ($b=0.13$) [O'Neill *et al.*, 2015].
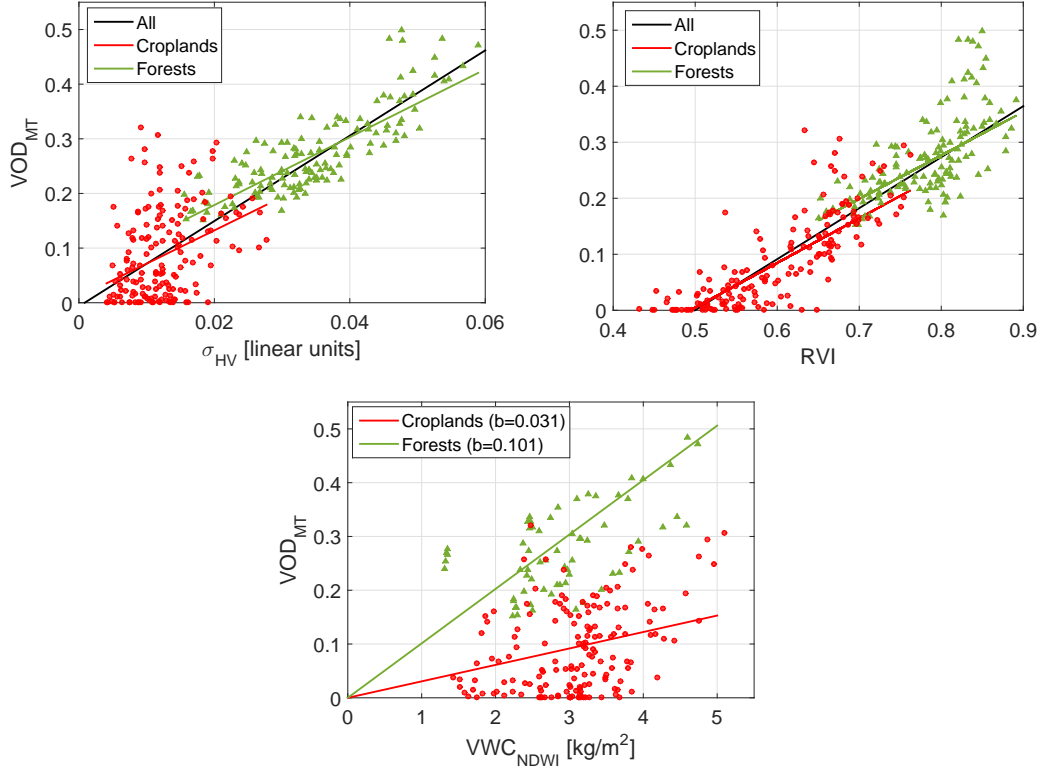
FIGURE 6.8: Retrieved VOD_{MT} *versus* σ_{HV} (top left), RVI (top right) and VWC_{NDWI} (bottom). The linear regression of all M-cells (black line), croplands (red line and circles) and forest (green line and triangles) are included. In the bottom plot, the estimated b parameter is included in the legend for the two land cover types.

The statistics of the relationships between the VOD_{MT} and the three VOD estimates are summarized in Table 6.2. Best scores are highlighted in bold type. Considering all M-cells, the VOD_{RVI} estimation has the best agreement with the retrieved VOD_{MT} (R$\sim$0.90 and RMSD$\sim$0.054) and results with $VOD_{\sigma_{HV}}$ are also good (R$\sim$0.84 and RMSD$\sim$0.065). This supports a direct relation between the passive (VOD) and active (RVI and σ_{HV}) microwave vegetation observations, in line with results shown in [Rötzer *et al.*, In review]. Time-series of both VOD and σ_{HV} vegetation parameters are shown in Appendix E (see Fig. E.3). In croplands, the best statistics are obtained for VOD_{RVI} (R$\sim$0.81 and RMSD$\sim$0.049) and poor statistics are obtained for $VOD_{\sigma_{HV}}$ and VOD_{NDWI} (R$\approx$0.36 to 0.40 and RMSD$\sim$0.076). RVI is the best estimator in agricultural regions. This is in line with a recent study, where the RVI is found better correlated with VWC over wheat than over pasture, suggesting a better relation between these variables in vegetation types having a greater dynamic range [Huang *et al.*, 2016]. Additionally, the L-band RVI was found to be a better predictor for VWC retrievals in rice and soybean than the RVI obtained from other frequency bands, such as C-band and X-band [Kim *et al.*, 2012]. In the case of forested cells, $VOD_{\sigma_{HV}}$ has the best agreement (R$\sim$0.83 and RMSD$\sim$0.043), followed by the VOD_{NDWI} (R$\sim$0.69 and RMSD$\sim$0.074) and VOD_{RVI} (R$\sim$0.67 and RMSD$\sim$0.059). This indicates that σ_{HV} is the best VOD predictor in forests, where volume scattering dominates. Overall results suggest that VIS/IR frequencies have a different sensitivity to the vegetation land cover than

the microwave frequencies and the active microwave-based measurements could be a better VOD estimator than optically-based indices.

TABLE 6.2: Statistics between retrieved VOD_{MT} and the three VOD estimates for all M-cells, croplands and forests.

		Polynomial fit	R	RMSD
All	$\mathbf{VOD}_{\sigma_{HV}}$	$7.81 \cdot \sigma_{HV}$-0.01	0.84	0.065
	$\mathbf{VOD}_{RVI}$	$0.91 \cdot$RVI-0.46	**0.90**	**0.054**
Croplands	$\mathbf{VOD}_{\sigma_{HV}}$	$6.09 \cdot \sigma_{HV}$+0.01	0.36	0.076
	$\mathbf{VOD}_{RVI}$	$0.80 \cdot$RVI-0.39	**0.81**	**0.049**
	$\mathbf{VOD}_{NDWI}$	$0.031 \cdot \text{VWC}_{NDWI}$	0.40	0.076
Forests	$\mathbf{VOD}_{\sigma_{HV}}$	$6.21 \cdot \sigma_{HV}$+0.05	**0.83**	**0.043**
	$\mathbf{VOD}_{RVI}$	$0.78 \cdot$RVI-0.35	0.67	0.059
	$\mathbf{VOD}_{NDWI}$	$0.101 \cdot \text{VWC}_{NDWI}$	0.69	0.074

All statistics are significant (p_{value} <0.05).
Best scores are highlighted in bold type.

The scatter plots of the retrieved static ω_{MT} *versus* the temporal mean of σ_{HV} (left) and RVI (right) are shown in Fig. 6.9. The variability of σ_{HV} and RVI during the field campaign are std~0.013 and std~0.113, respectively. The ω_{MT} is positively correlated with both σ_{HV} and RVI for all M-cells (black line), with a higher dispersion for σ_{HV} than for RVI. The distribution of the forested cells (green triangles) is almost constant for dynamic ranges of σ_{HV} ≈0.018 to 0.052 and RVI≈0.69 to 0.86, respectively. By contrast, the distribution of the agricultural cells (red circles) seems to display a positive trend. This results suggests that the assumption of a constant ω_{HV} is valid for forests whereas croplands, which experience more rapid growth and fallow cycles, may need dynamic albedo retrievals. This is now being assessed in a follow-on study with SMAP data [Piles *et al.*, 2016a]. There are similarities between the spatial patterns of ω_{MT} and the temporal mean of σ_{HV} and RVI, as shown in Appendix E (see Fig. E.4).
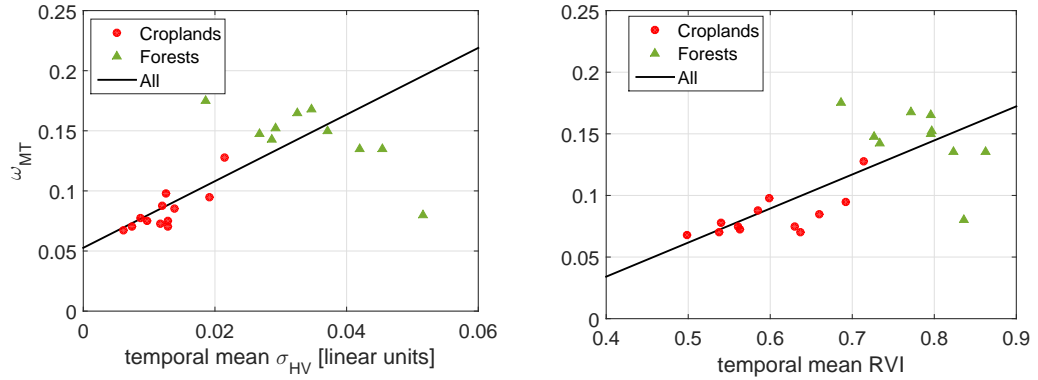
FIGURE 6.9: Retrieved static ω_{MT} *versus* the temporal mean of σ_{HV} (left) and RVI (right) for croplands (red circles) and forests (green triangles). The linear regression for all cells M-cells (black line) is included.

Table 6.3 summarizes the polynomial fit and statistics between the retrieved static ω_{MT} and the two ω estimates for all M-cells. Note that the best agreement is obtained using ω_{RVI} (R~0.71 and RMSD~0.026) and is highlighted in bold type. This result indicates that, in general, RVI is a better ω predictor than σ_{HV}.

TABLE 6.3: Statistics between retrieved static ω_{MT} and the two ω estimates for all M-cells.

	Polynomial fit	R	RMSD
$\omega_{\sigma_{HV}}$	$2.77 \cdot \sigma_{HV} + 0.05$	0.59	0.033
ω_{RVI}	$0.28 \cdot RVI - 0.08$	**0.71**	**0.026**

All statistics are significant ($p_{value} < 0.05$).
Best scores are highlighted in bold type.

6.5 Conclusions

This study evaluates the retrievals of SM, vegetation optical depth (VOD) and effective single-scattering albedo (ω) from airborne L-band microwave radiometer observations of SMAPVEX12 using the multi-temporal dual-channel algorithm (MT-DCA). In comparison with classical retrieval approaches, the MT-DCA has the advantage of not requiring *a priori* vegetation information, which is often land cover-based or derived indirectly from optical visible/infrared (VIS/IR) indices. This study also compares retrieved passive microwave vegetation VOD and ω parameters with simultaneous active microwave vegetation measurements, namely the cross-polarized backscatter (σ_{HV}) and the radar vegetation index (RVI).

The retrieved SM_{MT} is validated using ground-based observations. MT-DCA SM estimates are consistent with *in situ* SM measurements and also with the accumulated daily precipitation. Statistics obtained with MT-DCA (R~0.87, ubRMSD~0.042 m^3/m^3) have an important improvement relative to those obtained with the single-channel algorithm (SCA) approach (R~0.61, ubRMSD~0.072 m^3/m^3). This indicates the robustness of the MT-DCA approach as an alternative SM retrieval algorithm. However, the bias is lower using SCA (-0.056 m^3/m^3) than using MT-DCA (-0.110 m^3/m^3). The retrieved VOD_{MT} is consistent with the accumulated daily precipitation (with delay) and is also affected by the vegetation growth, more particularly in crop regions. As expected, both the biomass increase and precipitation have an impact on the L-band VOD parameter. The retrieved static ω_{MT} is lower in croplands than in forests, where the presence of woody and dense vegetation increase the microwave scattering. The retrieved ω_{MT} is larger than the values used in the SMAP mission for similar land cover types. This could be due to the scaling differences between airborne and satellite data. Also, we would like to emphasize that the MT-DCA computes a unique ω per pixel, whereas a dynamic ω may be needed in agricultural regions with quick or abrupt changes in the vegetation to capture crop growth. The implementation of MT-DCA with dynamic ω on SMAP is under development. However, the duration of SMAPVEX12 is too short to test this approach.

VOD_{MT} retrievals are compared with co-located σ_{HV} and RVI measurements, and with VWC derived from the optical Normalized Difference Water Index (NDWI). A linear function adequately relates σ_{HV} and RVI to VOD. Their corresponding VOD estimates ($VOD_{\sigma_{HV}}$ and VOD_{RVI}) are analyzed for all M-cells as well as for croplands and forests separately. The b parameter that relates VOD to VWC (VOD=$b \cdot$VWC) is computed and its VOD estimate (VOD_{NDWI}) is also analyzed in the two land cover types. Considering all cells, there is a robust correspondence between the radiometer-derived VOD and VOD_{RVI} (R~0.90 and ubRMSD~0.054). When separating by land cover type, the highest relation is found with $VOD_{\sigma_{HV}}$ (R~0.83 and ubRMSD~0.043) in forests and the highest relationship is observed with VOD_{RVI} (R~0.81 and ubRMSD~0.049) in croplands. These results suggest that both active microwave parameters could be better predictors of passive microwave VOD than optical parameters. Further studies are required to establish an active-passive relationship covering a wider range of vegetation types and phenology.

For the first time, there is a method to obtain spatially varying ω retrievals, instead of using a land cover-based or a constant value for all land cover types. The retrieved ω_{MT} is compared with the temporal mean of σ_{HV} and RVI. In both cases, a linear function is obtained to relate ω_{MT} with σ_{HV} and RVI. The two ω estimates ($\omega_{\sigma_{HV}}$ and ω_{RVI}) are analyzed for all cells. The

best statistical scores are obtained with ω_{RVI} (R∼0.71 and RMSD∼0.026). Therefore, RVI could be a good predictor of ω.

Results from this study support the use of VOD as a complementary vegetation indicator alongside VIS/IR indices such as Normalized Difference Vegetation Index (NDVI), NDWI, and Leaf Area Index (LAI) to monitor water content and stress in total aboveground vegetation. Unlike optical indices, the microwave vegetation parameters are available regardless of solar illumination and cloud cover. Passive microwave VOD and ω estimates (or active RVI or σ_{HV} measurements) could be an alternative to the ancillary optical vegetation information used in the current passive SM retrieval algorithms of SMOS and SMAP missions.

Chapter 7

Conclusions and future lines

Remotely sensed measurements made by radiometers and radars in the low microwave frequency range (L-band) are sensitive to soil moisture, vegetation water content, and ice thickness variations. During the last decade, three satellite missions have been launched providing unprecedent views of the Earth's surface at L-band or "water frequency channel": SMOS (2009–2017), Aquarius (2011–2015) and SMAP (2015–2018). New observational datasets at L-band are expected to further our understanding of the Earth's water, energy and carbon cycles. This Ph.D. Thesis is focused on analyzing the geophysical information that can be obtained from these three missions over the continental areas on Earth. This Chapter summarizes the main conclusions, remarking its original contributions and presenting suggestions for follow-on studies.

7.1   Main conclusions

Chapter 3 presents a new methodology to compare SMOS and Aquarius brightness temperatures (T_B). The T_B measured by each instrument are compared at the Top of the Atmosphere (TOA) over relative stable and homogeneous targets: the Amazon rainforest, the Sahara desert, the Dome-C in the Antarctica, and the South Pacific ocean. The inter-comparison covers the entire dynamic range of observations (land, ice and sea), using data of both ascending and descending orbits acquired during a full annual cycle (year 2012). The level of linearity, correlation and differences are analyzed at horizontal (H-pol) and vertical (V-pol) polarizations, and also using First Stokes ($I/2$), for the three Aquarius incidence angles (29.36°, 38.49° and 46.29°). The main conclusions of this Chapter are:

- Over land, there is a very high correlation (R>0.9), both in vegetation-covered soils and very dry soils. Over ocean, Aquarius T_B were produced using an ocean model as a reference during its calibration. Due to that, an ocean model should be applied to the SMOS T_B over ocean to compare with the Aquarius T_B. Ater that, high correlations are obtained (R≈0.6 to 0.8). Over ice, correlations show a seasonal effect with two different behaviours over Dome-C (Austral summer R≈0.7 to 1; other seasons R≈0.2 to 0.7).

- The level of linearity is systematically higher at H-pol than at V-pol. Also, higher agreement is obtained at higher incidence angles. The results with $I/2$ are in line with those obtained for H-pol and V-pol, confirming that the Faraday correction does not affect the inter-comparison.

- Aquarius T_B are systematically higher than SMOS T_B. This difference is higher over warmer targets with ∼5–8 K over land, and decreases with colder targets, being ∼3–5 K over ice and ∼0.1–0.3 K over sea. This suggests that there may be a non-linear effect between the two radiometers, and not only a bias.

- The agreement between SMOS and Aquarius T_B is target dependent. This fact should carefully taken into account if data from both radiometers are to be used in any long term environmental, meteorological, hydrological, or climatological study.

Chapter 4 explores the influence of the Antarctic ice thickness spatial variations on the measured SMOS and Aquarius T_B. A 3-months no-daylight period (from May 6 to August 6, 2013) is selected to safely assume that T_B changes are not due to surface temperature variations. A spatial and a statistical analysis are performed to relate SMOS and Aquarius T_B changes to a dataset of Antarctic ice thickness and subglacial bedrock. The theoretical L-band penetration depth is estimated to distangle the role of the different contributions to the microwave observed signal. The main conclusions of this Chapter are:

- The L-band penetration depth over the Antarctic ice sheet is estimated to be $\approx$1 to 1.5 km. The subglacial bedrock, which lies depper ($\approx$2 to 4.3 km under the ice surface) is not affecting the observed T_B. No correlation is found between SMOS and Aquarius T_B and the bedrock elevation (R$\approx$0 to 0.2).

- An good agreement between SMOS and Aquarius T_B changes and ice thickness spatial variations is observed in selected transects over the East Antarctica, except for the case of fast spatial variations, which are not resolved by any of the two radiometers. SMOS shows a better agreement than Aquarius due to its higher spatial resolution ($\sim$50 km *vs.* $\sim$100 km). A linear trend of $\sim$9 K/km can be identified between ice thickness variations and T_B changes. Correlations with ice thickness vary from R$\approx$0.6 to 0.7. They are higher at V-pol than at H-pol, and are higher for higher incidence angles.

- The presence of subglacial lakes, located at $\sim$3 km below the ice surface, may have an impact on the internal ice temperature and/or the dielectric properties of the ice layers above and, consequently, affect the measured T_B. Further research is needed to confirm this hypothesis.

- The sensitivity of SMOS and Aquarius T_B observations to the Antarctic ice thickness show the potential of using L-band radiometric observations in cryospheric studies.

Chapter 5 evaluates the soil moisture (SM) and land surface temperature (LST) dynamics at daily and seasonal scales through the physical processes of SM–LST coupling/decoupling, evapotranspiration (ET) and thermal inertia. The study is performed using four years (2011–2014) of *in situ* and satellite data. The study site is the REMEDHUS network, located at the central part of the river Duero basin, in Spain. The temporal correlation of the SM–LST link is analyzed for a variety of LST-derived parameters. The modeled ET, simulated with HidroMORE, is also assessed. Additionally, a SMOS/MODIS downscaling algorithm is applied to all possible SMOS SM–MODIS LST combinations and the 1-km disaggregated SM estimates are compared with ground-based data. The main conclusions of this Chapter are:

- Instantaneous SM shows a stronger anticorrelation to daily maximum LST (R$\approx$-0.7) than to the other LST-derived parameters (instantaneous, daily mean, daily median, daily minimum and diurnal range). This can be explained by the fact that the time of maximum LST corresponds to the time of maximum potential ET and thus the time of highest atmospheric demand of water. Also, stronger anticorrelation is obtained between SMOS SM and MODIS LST Aqua (or Terra) day than night.

- A stronger SM–LST anticorrelation is observed in autumn, spring and summer (R$\approx$-0.4 to 0.7) than in winter (R$\approx$-0.3 to +0.3). These two behaviours are related to a change from water-limited (SM–LST coupling) to energy-limited conditions (SM–LST decoupling) in the region accross seasons.

- In water-limited periods, SM is extracted from the soil through ET until critical SM is reached. The critical SM is estimated to be $\sim$0.12 m^3/m^3. This value is consistent with *in situ* and spaceborne data, and with the field capacity and the wilting point measured in the REMEDHUS network.

- A better agreement (lower ubRMSD and higher correlation) is obtained between disaggregated SMOS/MODIS SM and *in situ* SM when using MODIS LST Aqua (or Terra) day than when using MODIS LST Aqua (or Terra) night in the downscaling algorithm, independently of the SMOS time-overpass.

- An ensemble composed of an average of all available disaggregated SMOS/MODIS SM estimates per day is shown to improve the coverage in $\sim$15–20 %.

- Further knowledge of the SM–LST relationship from remotely sensed observations is paramount in the microwave/optical synergy for disaggregation algorithms.

Chapter 6 validates the multi-temporal dual channel algorithm (MT-DCA) using airborne L-band data from the SMAP Validation Experiment 2012 (SMAPVEX12) campaign. The MT-DCA allows to simultanously retrieve SM, vegetation optical depth (VOD) and a static single-scattering albedo (ω), without using *a priori* vegetation information. The retrieved passive vegetation parameters (VOD and ω) are compared with collocated airborne radar measurements, namely the cross-polar backscatter cross-section (σ_{HV}) and the radar vegetation index (RVI). The possible relationships between the passive and active microwave vegetation parameters are analyzed. The main conclusions of this Chapter are:

- The retrieved SM is consistent with *in situ* SM and precipitation. During its validation, statistics show an important improvement (higher R and lower ubRMSD) relative to those obtained with the single channel algorithm (SCA), which is currently used as SMAP baseline. However, the bias is higher using MT-DCA than using SCA.

- The retrieved VOD and ω show distinctive characteristics in crops and forests. Over forests, the σ_{HV} seems to be a better predictor of VOD than RVI. By constranst, RVI seems to be a better predictor of VOD than σ_{HV} in croplands.

- The retrieved static ω is lower in croplands than in forest, where the presence of woody and dense vegetation increase the microwave scattering.

- New ecological variables related to vegetation water content and structure can be estimated from L-band observations. The MT-DCA is now validated with Aquarius, SMAP and airborne data.

7.2 Original contributions

The original contributions of this Thesis are summarized below:

- A new inter-comparison methodology has been proposed to compare T_B measurements from satellites with opposite ascending crossing times, as is the case of SMOS and Aquarius. The proposed approach uses a 7-day averaging window and allows to perform the inter-comparison without the limitation of finding a statistically significant dataset of co-located observations. The longitude of the averaging window was selected to ensure that T_B values are preserved when averaging. Results have contributed to the improvement of the operational SMOS, Aquarius and SMAP T_B products, with the development of more consistent releases, specially for the Aquarius T_B.

- A relationship between the Antarctic ice thickness spatial variations and the measured SMOS and Aquarius T_B changes is shown for the first time. The subglacial bedrock elevation is discarded as a geophysical variable contributing to the observed signal at L-band. Results have contributed to improve our knowledge about the Antarctica's emissivity and to help deciding future calibration/validation sites over Antarctica for present and upcoming L-band missions. Results provide evidence that, appart from temporal stability and spatial homogeneity, minimum ice thickness variation should be a feature required when selecting a target area to be used as a reference calibration site for microwave rediometers.

- The daily maximum LST is suggested to be used in hydrological and climate models based on the SM–LST relationship for providing a closer representation of LST conditions of a particular day than the instantaneous LST. A method to estimate the critical SM from the SM–LST coupling/decoupling transitions is proposed. This method can be applied to both *in situ* and satellite observations. The SMOS/MODIS downscaling algorithm has been improved with the use of the MODIS LST Aqua day (closer to the daily maximum LST) in both the SMOS morning and afternoon passes. Also, a new release of the SMOS BEC L4 SM maps (v.2) over the Iberian Peninsula has been produced.

- The use of airborne data to validate the MT-DCA with *in situ* data is completely new. The MT-DCA is an alternative to the classical passive approaches, where ancillary vegetation information from optical measurements is used to obtain the SM retrievals. It allows retrieving two passive microwave vegetation parameters (VOD and ω) alongside SM. They are complementary vegetation indicators to VIS/IR indices, such as NDVI, NDWI and LAI, to monitor water content and stress in total aboveground vegetation. The relations obtained between the passive and active vegetation parameters may be used to provide a better representation of VOD and ω in SM radiometric retrievals.

7.3 Future research lines

The future research lines arising from the work presented in this Thesis are:

- Application of the inter-comparison methodology to SMOS, Aquarius and SMAP T_B products. Creation of a consistent global long-term dataset from L-band T_B.

- Analyze the possible influence of the subglacial lakes on the observed L-band T_B.

- Selection of a new independent target area over Antarctica to be used as calibration/validation site of L-band radiometers.

- Generalize the use of L-band observations for cryospheric studies, taking advantage of the continuous observations of SMOS, Aquarius and SMAP around the North and South Poles.

- Study the possible dependence of different Earth's land covers and/or climate types in the SM–LST link.

- Evaluation of the relationship between the instantaneous SM and the LST diurnal range using remotely LST data from a geostationary satellite, such a MSG SEVIRI.

- Use the passive L-band SM measurements of SMOS, Aquarius and SMAP as reference in the Climate Change Initiative (CCI) to provide a new long-term global SM data record based on passive microwave sensors.

- Develop a cloud-free ensemble composed of averaged disaggregated SM estimates using MODIS and SEVIRI LST in the SMOS SM downscaling algorithm, instead of using a modeled LST to produce the current SMOS BEC L4 SM maps v.3 over the Iberian Peninsula.

- Creation of a global high resolution SM dataset based on the synergy of microwave/optical observations, integrating SMOS and SMAP SM, and MODIS and SEVIRI LST for agricultural and water management purposes.

- Implementation of the MT-DCA approach to SMOS and SMAP data.

- In-depth study to establish active-passive relationships covering a wider range of vegetation types and phenology.

- Use of the active-passive relationships to estimate VOD and ω properties at high spatial resolution using radar measurements from Sentinel 1 with SMOS and SMAP.

Appendix A

List of publications

A.1 Journal papers

1. **Pablos, M.**, Piles, M., Konings, A.G., Entekhabi, D., & Leroux, D.J. (Submitted), "Comparison between Active and Passive Vegetation Parameters derived from SMAPVEX12 Time-series Retrievals", *IEEE Transacctions on Geoscience and Remote Sensing*.

2. **Pablos, M.**, Piles, M., Sánchez, N., Vall-llossera, M., Martínez-Fernández, J., & Camps, A. (In review), "Impact of Day/Night Time Land Surface Temperature in Soil Moisture Dissagregation Algorithms", *European Journal of Remote Sensing*.

3. Camps, A., Park, H., **Pablos, M.**, Foti, G., Gommenginger, C., Liu, P.W., & Judge, J. (July 2016), "Sensitivity of GNSS-R Spaceborne Observations to Soil Moisture and Vegetation", *IEEE Journal of Selected Topics in Applied Earth Observations and Remote Sensing*, 1–12.

4. **Pablos, M.**, Martínez-Fernández, J., Piles, M., Sánchez, N., Vall-llossera, M., & Camps, A. (July 2016), "Multi-Temporal Evaluation of Soil Moisture and Land Surface Temperature Dynamics Using in Situ and Satellite Observations", *Remote Sensing*, 8(7), 587–596.

5. Piles, M., McColl, K.A., Entekhabi, D., Das, N., & **Pablos, M.** (August 2015), "Sensitivity of Aquarius Active and Passive Measurements Temporal Covariability to Land Surface Characteristics", *IEEE Transactions on Geoscience and Remote Sensing*, 53(8), 4700–4711.

6. **Pablos, M.**, Piles, M., González-Gambau, V., Camps, A., & Vall-llossera, M. (April 2015), "Ice Thickness Effects on Aquarius Brightness Temperatures over Antarctica", *Journal of Geophysical Research–Oceans*, 120(4), 2856–2868

7. **Pablos, M.**, Piles, M., González-Gambau, V., Vall-llossera, M., Camps, A., & Martínez, J. (September 2014), "SMOS and Aquarius Radiometers: Inter-Comparison Over Selected Targets", *IEEE Journal of Selected Topics in Applied Earth Observations and Remote Sensing*, 7(9), 3833–3844.

8. Nova, E., Romeu, J., Torres, F., **Pablos, M.**, Riera, J.M., Broquetas, A., & Jofre, L. (April 2013), "Radiometric and Spatial Resolution Constraints in Millimeter–Wave Close–Range Passive Screener Systems", *IEEE Transactions on Geoscience and Remote Sensing*, 51(4), 2327–2336.

9. Font, J., Ballabrera-Poy, J., Camps, A., Duffo, N., Durán, I., Emelianov, M., Enrique, L., Fernández, P., Gabarró, C., González-Haro, C., González-Gambau, V., Gourrion, J., Guimbard, S., Hoareau, N., Julià, A., Kalaroni, S., Konstantinidou, A., Aretxabaleta, A.L., Martínez, J., Miranda, J., Monerris, A., Montero, S., Mourre, B., **Pablos, M.**,

Pérez, F., Piles, M., Portabella, M., Sabia, R., Salvador, J., Talone, M., Torres, F., Turiel, A., Vall-llossera, M., & Villarino, R. (September 2012), "A New Space Technology for Ocean Observation: SMOS Mission", *Scientia Marina*, 76S1, 249–259.

10. Camps, A., Font, J., Corbella, I., Vall-llossera, M., Portabella, M., Ballabrera-Poy, J., González-Gambau, V., Piles, M., Aguasca, A., Acevo, R., Bosch, X., Duffo, N., Fernández, P., Gabarró, C., Gourrion, J., Guimbard, S., Marín, A., Martínez, J., Monerris, A., Mourre, B., Pérez, F., Rodríguez, N., Salvador, J., Sabia, R., Talone, M., Torres, F., **Pablos, M.**, Pérez, F., Turiel, A., Valencia, E., Martínez-Fernández, J., Sánchez, N., Pérez-Gutiérrez, C., Baroncini-Turricchia, G., Rius, A., & Ribó, S. (May 2012), "Review of the CALIMAS Team Contributions to European Space Agency's Soil Moisture and Ocean Salinity Mission Calibration and Validation" *Remote Sensing*, 4 (5), 1272–1309.

11. Corbella, I., Torres, F., Duffo, N., González-Gambau, V., **Pablos, M.**, Durán, I., & Martín-Neria, M. (September 2011), "MIRAS Calibration and Performance: Results from the SMOS In-orbit Commissioning Phase", *IEEE Transactions on Geoscience and Remote Sensing*, 49 (9), 3147–3155.

A.2 Conference proceedings

1. Camps, A., Park, H., **Pablos, M.**, Foti, G., Gommenginger, C., Liu, P.W., & Judge, J. (July 2016), "Soil Moisture and Vegetation Impact in GNSS-R TechDemoSat-1 Observations", *IEEE International Conference on Geoscience and Remote Sensing Symposium (IGARSS) 2016*, Beijing, China.

2. **Pablos, M.**, Piles, M., González-Gambau, V., Camps, A., & Vall-llossera, M. (July 2015), "Influence of Ice Thickness on SMOS and Aquarius Brightness Temperatures over Antarctica", *IEEE International Conference on Geoscience and Remote Sensing Symposium (IGARSS) 2015*, Milán, Italy, 5178–5181.

3. Sánchez, N., Alonso-Arroyo, A., González-Zamora, A., Martínez-Fernández, J., Camps, A., Vall-llossera, M., **Pablos, M.**, & Herrero-Jiménez, C.M. (July 2015), "Airbone GNSS-R, Thermal and Infrared Data Relationships for Soil moisture Retrievals", *IEEE International Conference on Geoscience and Remote Sensing Symposium (IGARSS) 2015*, Milán, Italy, 4785–4788.

4. Alonso-Arroyo, A., Camps, A., Sánchez, N., **Pablos, M.**, González-Zamora, A., Martínez-Fernández, J., & Vall-llossera, M. (July 2015), "An Airbone GNSS-R Field Experiment over a Vineyard for Soil Moisture Estimation and Monitoring", *IEEE International Conference on Geoscience and Remote Sensing Symposium (IGARSS) 2015*, Milán, Italy, 4761–4764.

5. Sánchez, N., Alonso-Arroyo, A., Martínez-Fernández, J., González-Zamora, A., **Pablos, M.**, & Gumuzzio, A. (May 2015), "Multisensor Airbone Experiments over Vineyard: New Challenges for the GNSS-R Technique", *The 36th International Symposium on Remote Sensing of Environment (ISRSE) 2015*, Berlin, Germany, XL-7/W3.

6. **Pablos, M.**, Piles, M., Sánchez, N., González-Gambau, V., Vall-llossera, M., Camps, A., & Martínez-Fernández, J. (July 2014), "A Sensitive Study of Land Surface Temperature to Soil Moisture using *in-situ* and space-borne observations", *IEEE International Conference on Geoscience and Remote Sensing Symposium (IGARSS) 2014*, Quebec, Canada, 3267–3269.

7. **Pablos, M.**, Piles, M., González-Gambau, V., Vall-llossera, M., Camps, A., & Martínez, J. (July 2013), "Inter-Comparison of SMOS and Aquarius Brightness Temperatures over Selected Targets", *IEEE International Conference on Geoscience and Remote Sensing Symposium (IGARSS) 2013*, Melbourne, Australia, 386–389.

8. Corbella, I., Torres, F., Duffo, N., Durán, I., **Pablos, M.**, & Martín-Neira, M. (July 2012), "Enhanced SMOS Amplitude Calibration using External Target", *IEEE International Conference on Geoscience and Remote Sensing Symposium (IGARSS) 2012*, Munich, Germany, 2868–2871.

9. Dávila, R., Torres, F., Duffo, N., Corbella, I., **Pablos, M.**, & Martín-Neira, M. (July 2011), "Phase Error Assessment of MIRAS/SMOS by means of Redundant Space Calibration", *IEEE International Conference on Geoscience and Remote Sensing Symposium (IGARSS) 2011*, Vancouver, Canada, 3756–3759.

10. Corbella, I., Torres, F., Duffo, N., González-Gambau, V., Durán, I., **Pablos, M.**, & Martín-Neira, M. (July 2010), "Some Results on SMOS-MIRAS Calibration and Imaging", *IEEE International Conference on Geoscience and Remote Sensing Symposium (IGARSS) 2010*, Honolulu, Hawai, USA, 3768–3771.

11. Corbella, I., Torres, F., Duffo, N., González-Gambau, V., **Pablos, M.**, Durán, I., Closa, J., & Martín-Neira, M. (June-July 2010), "SMOS-MIRAS Calibration and Performance", *ESA Living Planet Symposium 2010*, Bergen, Norway, ESA SP-686.

12. Corbella, I., Torres, F., Duffo, N., González-Gambau, V., **Pablos, M.**, Durán, I., & Martín-Neira, M. (March 2010), "First Results on MIRAS Calibration and overall SMOS Performance", *11th Specialist Meeting on Microwave Radiometry and Remote Sensing of the Environment (MicroRad) 2010*, Washington DC, USA.

13. Torres, F., Corbella, I., Duffo, N., González-Gambau, V., Durán, I., **Pablos, M.**, & Martín-Neira, M. (March 2010), "One Point Calibration in Interferometric Radiometers: MIRAS/SMOS Preliminary Results", *11th Specialist Meeting on Microwave Radiometry and Remote Sensing of the Environment (MicroRad) 2010*, Washington DC, USA.

A.3   Workshops

1. **Pablos, M.**, Piles, M., González-Gambau, V., Vall-llossera, M., & Camps, A. (Apr. 2013), "Inter-Comparison of SMOS and Aquarius Brightness Temperatures over Selected Targets", *SMOS & Aquarius Science Workshop 2013*, Brest, Francia.

Appendix B

Additional results of inter-comparison of SMOS & Aquarius

B.1 Results using First Stokes

The obtained statistical scores using $I/2$ are summarized in Table B.1.

TABLE B.1: Statistics for half First Stokes ($I/2$)

Target region	Beam	Aquarius mean ± std [K]	SMOS mean ± std [K]	Aquarius-SMOS RMSD [K]	R	Difference [K]	Slope s
Amazon	inner	282.00 ± 2.33	273.12 ± 5.19	8.90	0.93	8.88	0.96
	middle	280.80 ± 3.54	274.44 ± 4.84	6.38	0.95	6.36	1.20
	outer	280.00 ± 2.77	273.55 ± 4.31	6.46	0.94	6.45	1.05
Sahara	inner	280.26 ± 1.15	273.42 ± 5.77	6.96	0.97	6.84	0.88
	middle	279.97 ± 0.99	274.06 ± 5.91	5.97	0.99	5.91	1.01
	outer	275.96 ± 1.76	270.73 ± 7.26	5.30	0.98	5.23	0.92
South Pacific	inner	98.91 ± 0.27	96.80 ± 1.15	2.16	0.37	2.11	0.15
	middle	100.41 ± 0.26	99.43 ± 1.13	1.07	0.52	0.98	0.23
	outer	102.94 ± 0.27	102.34 ± 1.22	0.72	0.59	0.60	0.27
South Pacific *(with OTT applied to SMOS data)*	inner	98.91 ± 0.27	98.79 ± 0.77	0.32	0.71	0.12	0.38
	middle	100.41 ± 0.26	100.32 ± 0.77	0.31	0.75	0.09	0.40
	outer	102.94 ± 0.27	102.63 ± 0.83	0.46	0.76	0.31	0.37
Dome-C *(Austral summer)*	inner	203.23 ± 2.64	198.55 ± 3.68	4.68	0.93	4.68	1.53
	middle	203.56 ± 2.14	199.61 ± 3.80	3.95	0.87	3.95	1.19
	outer	203.16 ± 1.90	199.38 ± 3.63	2.79	0.85	2.78	1.25
Dome-C *(other seasons)*	inner	202.98 ± 2.39	198.35 ± 3.61	4.63	0.63	4.63	-0.43
	middle	203.35 ± 2.01	199.27 ± 3.74	4.09	0.47	4.08	-0.31
	outer	202.06 ± 1.76	199.05 ± 3.57	3.03	0.55	3.01	-0.77

Scatter plots of Aquarius $I/2$ *vs.* SMOS $I/2$ are shown in Fig. B.1.
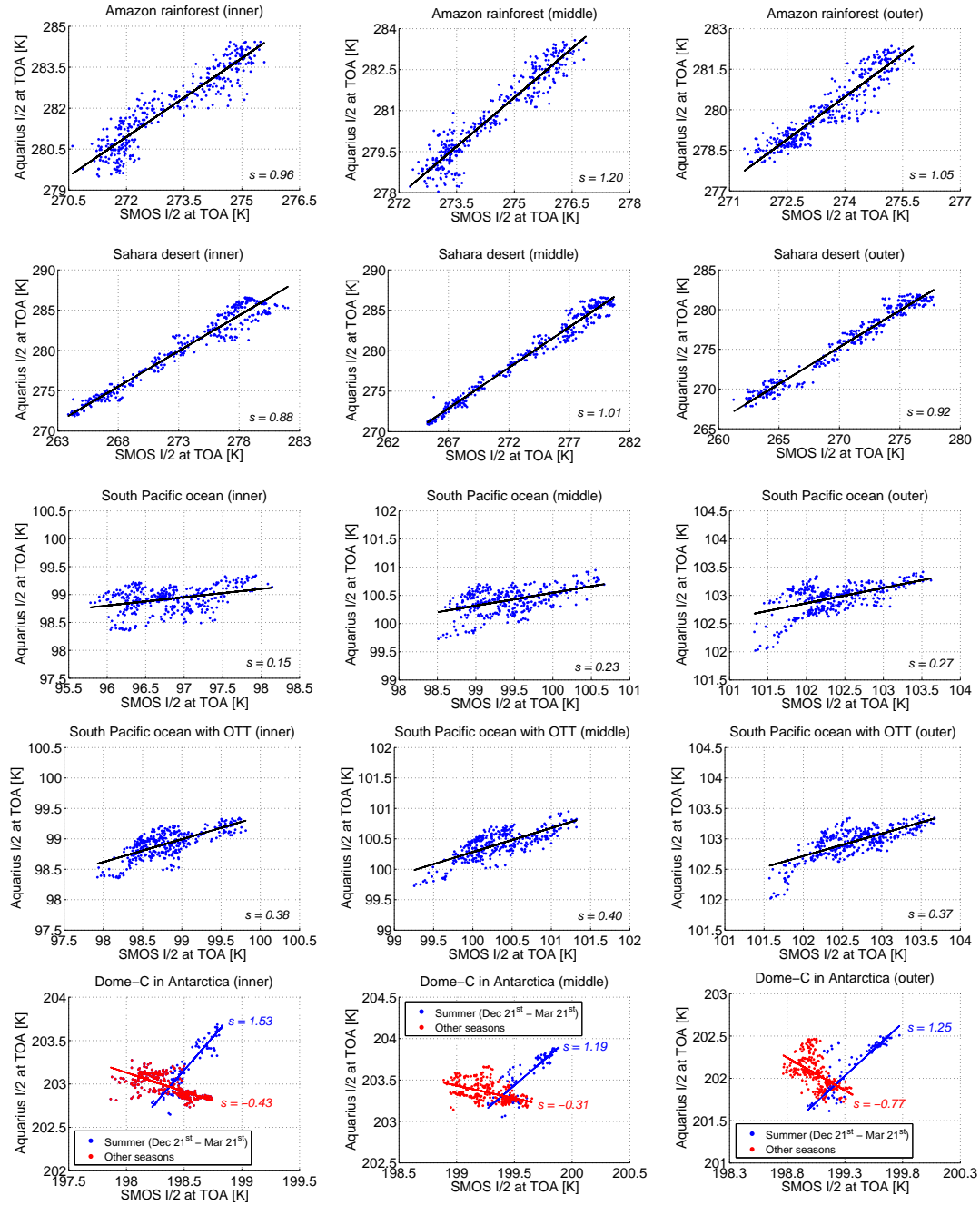
FIGURE B.1: Same as Fig. 3.4, but for half First Stokes ($I/2$).

B.2 Results using different data versions

Scatter plot of Aquarius T_{B_H} *vs.* SMOS T_{B_H} over Dome-C for the middle beam using different data versions: SMOS v.505 and Aquarius v.2 (left), SMOS v.505 and Aquarius v.3 (center), and SMOS v.620 and Aquarius v.4 (right), are displayed in Fig. B.2
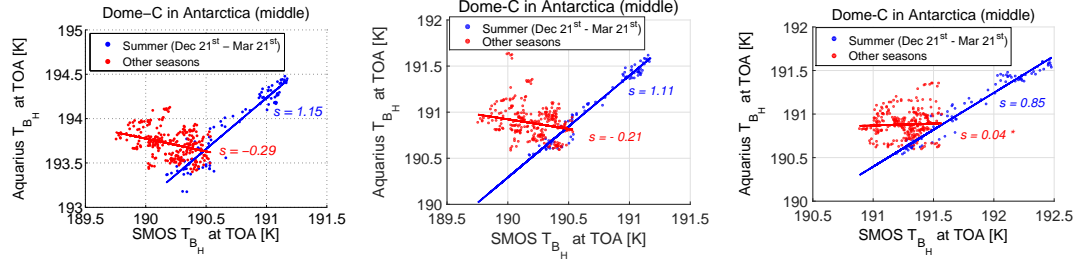
FIGURE B.2: Scatter plots of Aquarius T_{B_H} *vs.* SMOS T_{B_H} over Dome-C in Antarctica for the middle beam ($\sim$38.49°) using different data versions: SMOS v.505 and Aquarius v.2 (left), SMOS v.505 and Aquarius v.3 (center), and SMOS v.620 and Aquarius v.4 (right). Non-significant slopes ($p_{value} > 0.05$) are marked with an asterisk.

Statistical scores obtained from different data versions at H-pol and middle beam are summarized in Table B.2 .

TABLE B.2: Statistics from different data versions for horizontal polarization (T_{B_H})

Target region	Versions	Aquarius-SMOS			Slope s
		RMSD [K]	R	Difference [K]	
Dome-C	SMOS v.505 and Aquarius v.2	3.19	0.95	3.19	1.15
(Austral	SMOS v.505 and Aquarius v.3	0.37	0.98	0.37	1.11
summer)	SMOS v.620 and Aquarius v.4	0.74	0.98	-0.73	0.85
Dome-C	SMOS v.505 and Aquarius v.2	3.52	0.33	3.51	-0.29
(other	SMOS v.505 and Aquarius v.3	0.75	0.29	0.69	-0.21
seasons)	SMOS v.620 and Aquarius v.4	0.43	0.09*	-0.36	0.04*

* Non-significant values of correlations or slopes ($p_{value} > 0.05$).

Appendix C

Additional results of SMOS & Aquarius over continental ice

C.1 Results using inner beam

The mean SMOS and Aquarius T_B maps over Antarctica at inner beam are shown in Fig. C.1.
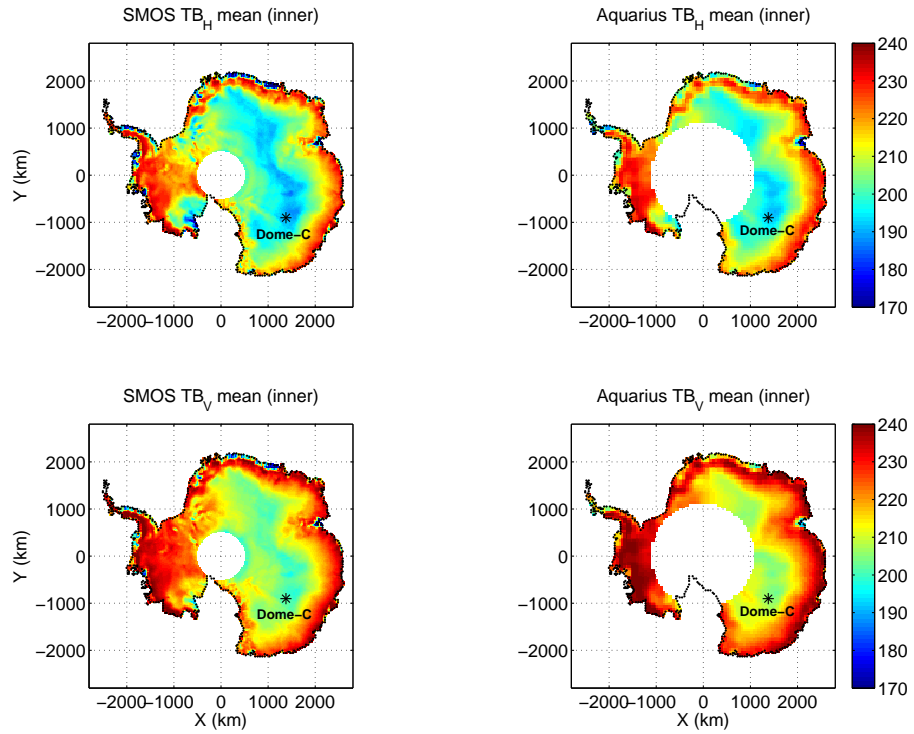
FIGURE C.1: Same as Fig. 4.5, but for inner beam.

The std SMOS and Aquarius T_B maps over Antarctica at inner beam, and the number of averaged observations are shown in Fig. C.2.
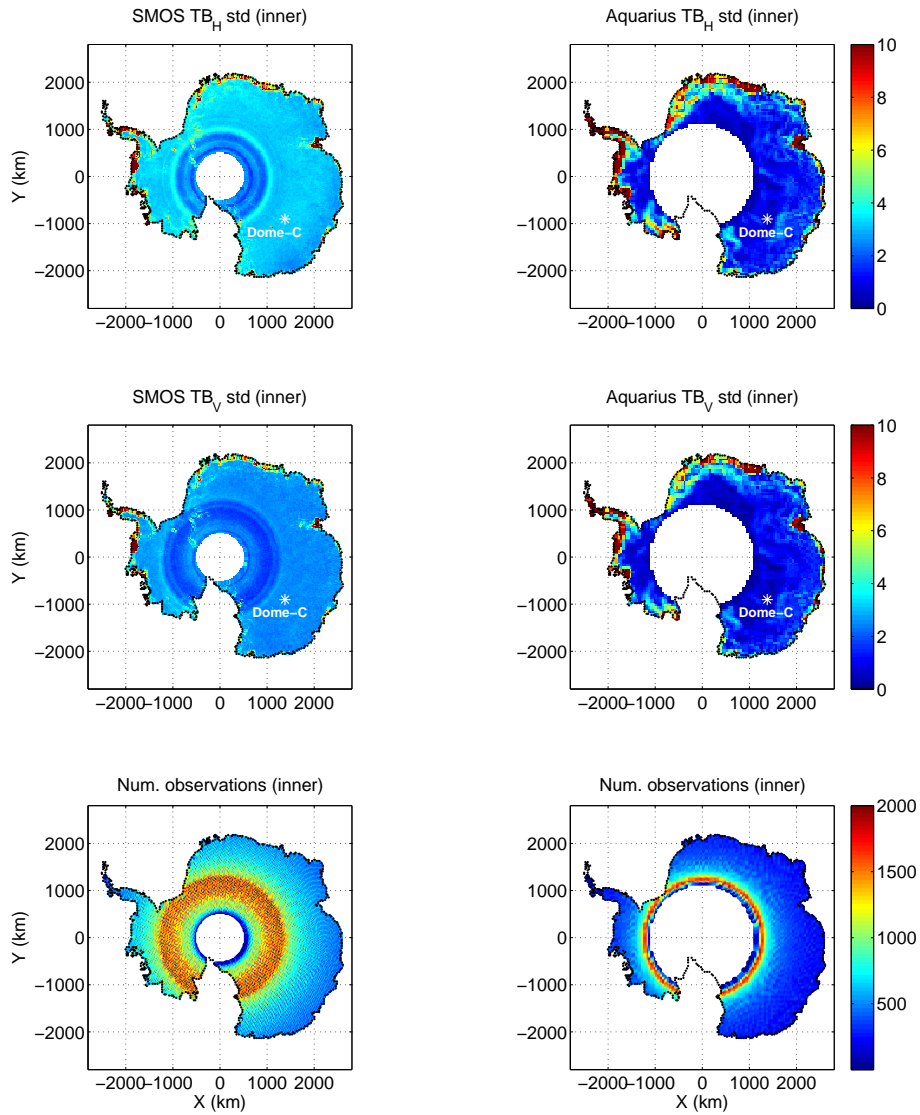
FIGURE C.2: Same as Fig. 4.6, but for inner beam

SMOS and Aquarius T_B variations at inner beam and IceTL along the four transects are shown in Fig. C.3.
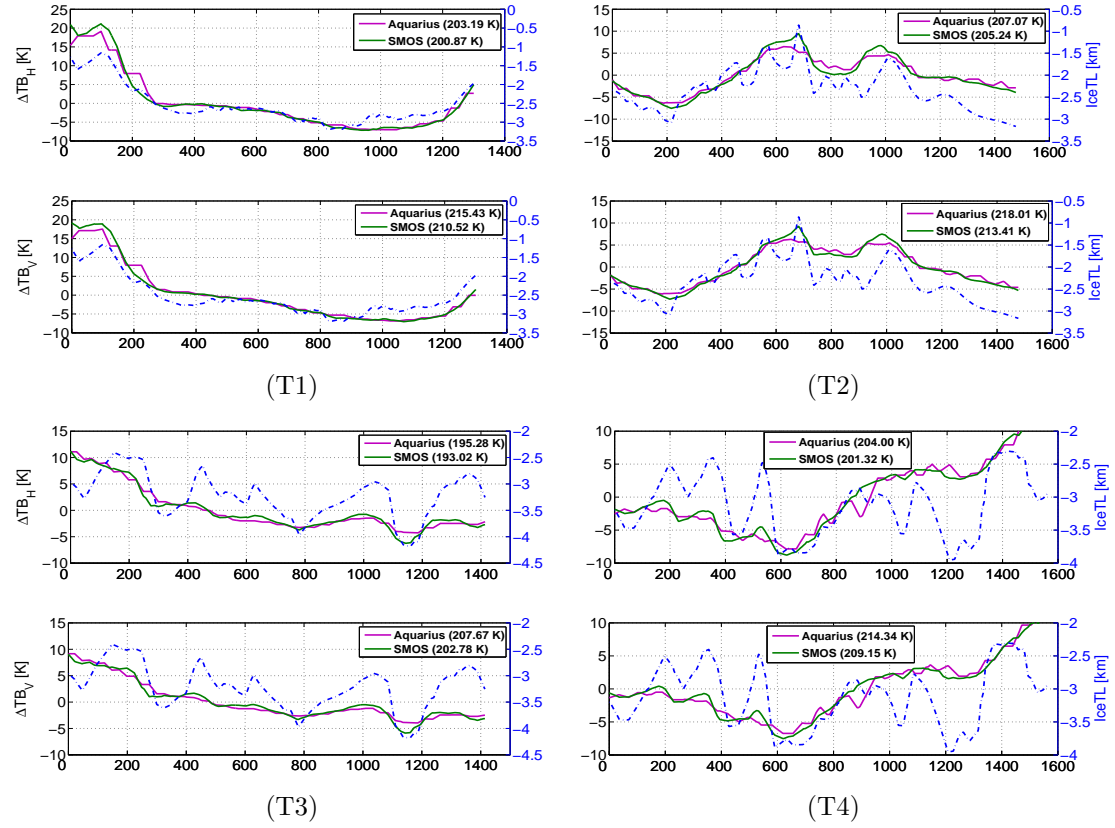
FIGURE C.3: Same as Fig. 4.7, but for inner beam.

Table C.1 summarizes the statistical scores of SMOS and Aquarius T_B at inner beam with bedrock and ice thickness.

TABLE C.1: Same as Table 4.1, but for inner beam.

Radiometer	Polarization	R_b	All pixels R_i	s_i [K/km]	Pixels with lakes R_i	s_i [K/km]	Pixels without lakes R_i	s_i [K/km]
SMOS	Horizontal	0.18	0.62	9.5±0.1	0.65	7.9±0.5	0.66	9.7±0.8
	Vertical	0.20	0.68	9.2±0.1	0.71	7.4±0.4	0.73	9.4±0.6
Aquarius	Horizontal	0.21	0.61	9.1±0.1	0.64	7.7±0.5	0.66	9.5±0.8
	Vertical	0.22	0.67	8.8±0.1	0.70	7.3±0.5	0.72	9.2±0.6

C.2   Results using outer beam

The mean SMOS and Aquarius T_B maps over Antarctica at outer beam are shown in Fig. C.4.
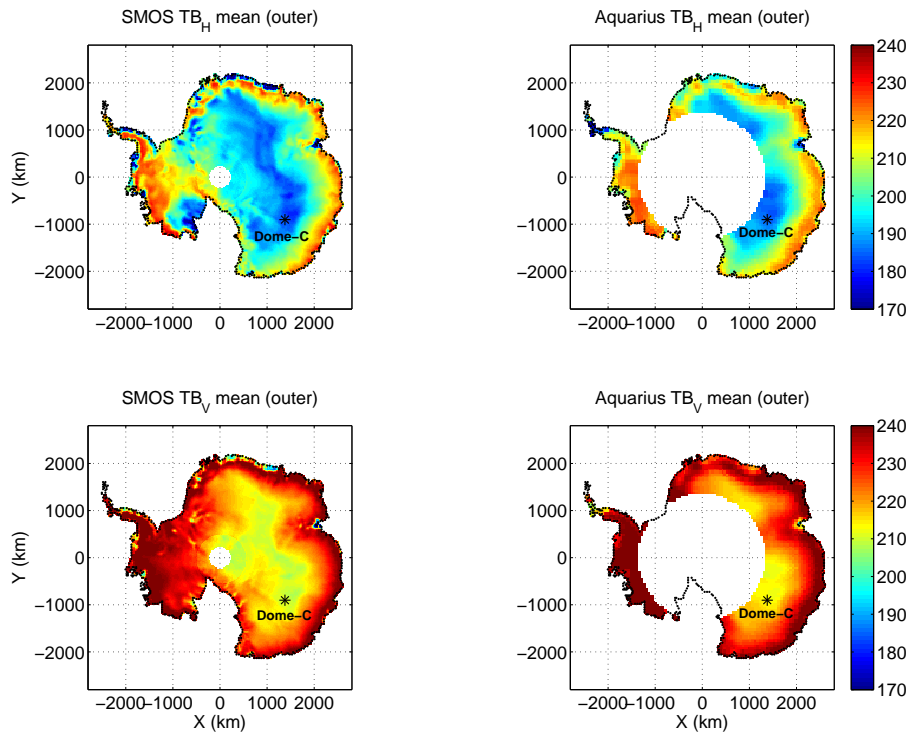
FIGURE C.4: Same as Fig. 4.5, but for outer beam.

The std SMOS and Aquarius T_B maps over Antarctica at outer beam, and the number of averaged observations within each 25-km EASE pixel are shown in Fig. C.5.
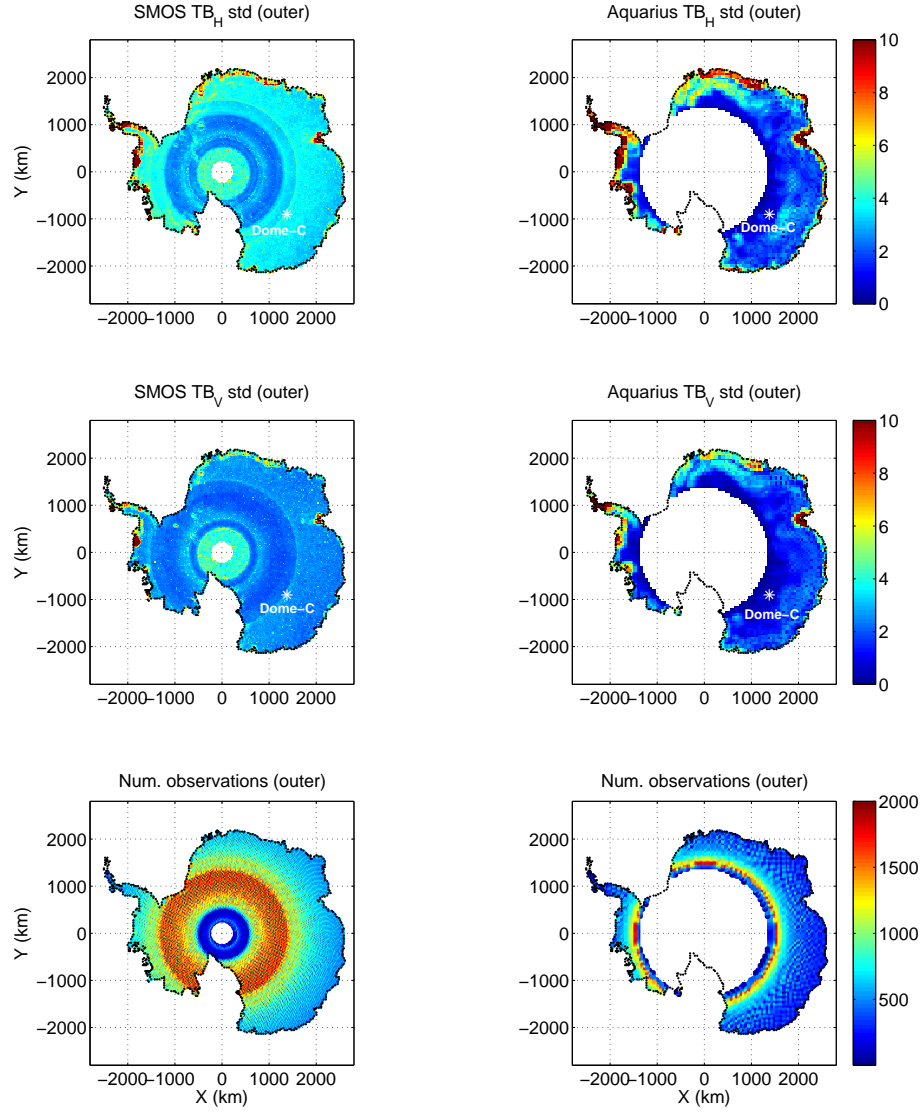
FIGURE C.5: Same as Fig. 4.6, but for inner beam.

SMOS and Aquarius T_B variations at outer beam and IceTL along the four transects are shown in Fig. C.6.
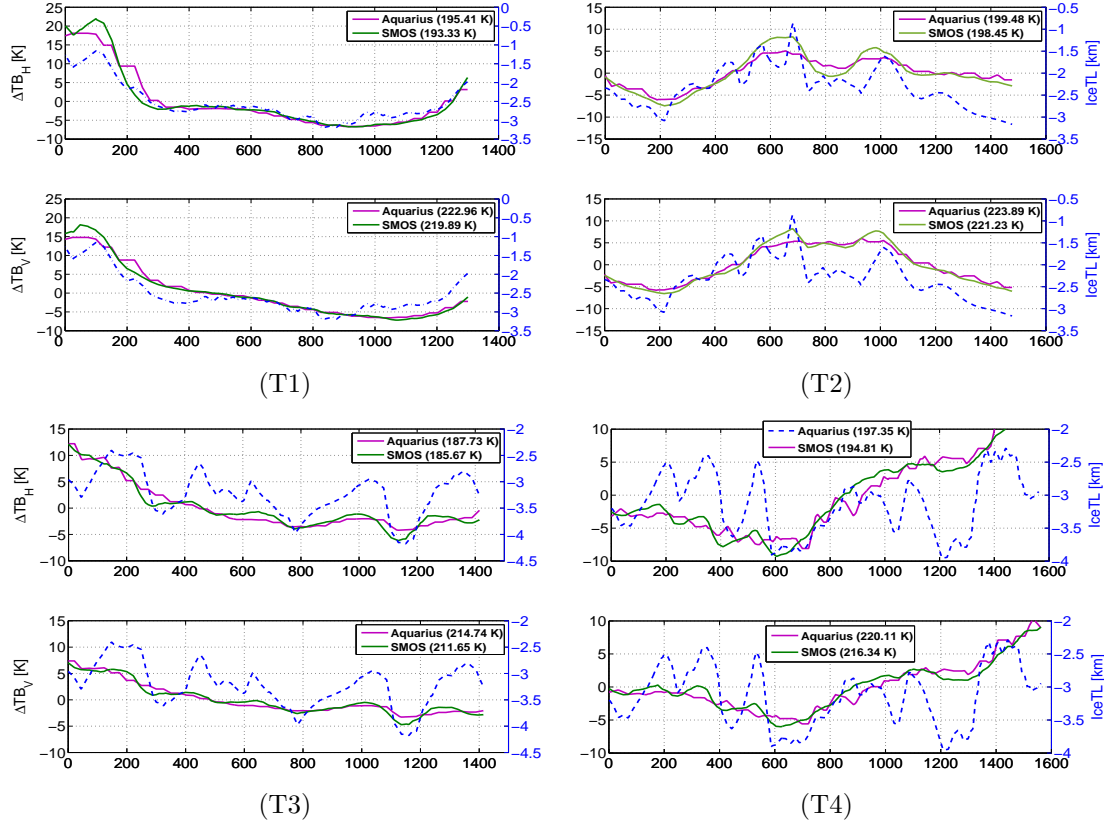
FIGURE C.6: Same as Fig. 4.7, but for outer beam.

Table C.2 summarizes the statistical scores of SMOS and Aquarius T_B at outer beam with bedrock and ice thickness.

TABLE C.2: Same as Table 4.1, but for outer beam.

Radiometer	Polarization	R_b	All pixels		Pixels with lakes		Pixels without lakes	
			R_i	s_i [K/km]	R_i	s_i [K/km]	R_i	s_i [K/km]
SMOS	Horizontal	0.08	0.65	9.8±0.1	0.66	7.5±0.6	0.70	10.6±0.8
	Vertical	0.06	0.76	8.8±0.1	0.72	5.4±0.4	0.80	9.4±0.5
Aquarius	Horizontal	0.12	0.61	8.9±0.1	0.62	6.8±0.6	0.69	10.4±0.9
	Vertical	0.10	0.71	8.2±0.1	0.68	5.2±0.5	0.77	9.2±0.6

C.3 Results using First Stokes

The SMOS and Aquarius $I/2$ variations at middle beam and IceTL along the four transects is shown in Fig. C.7.
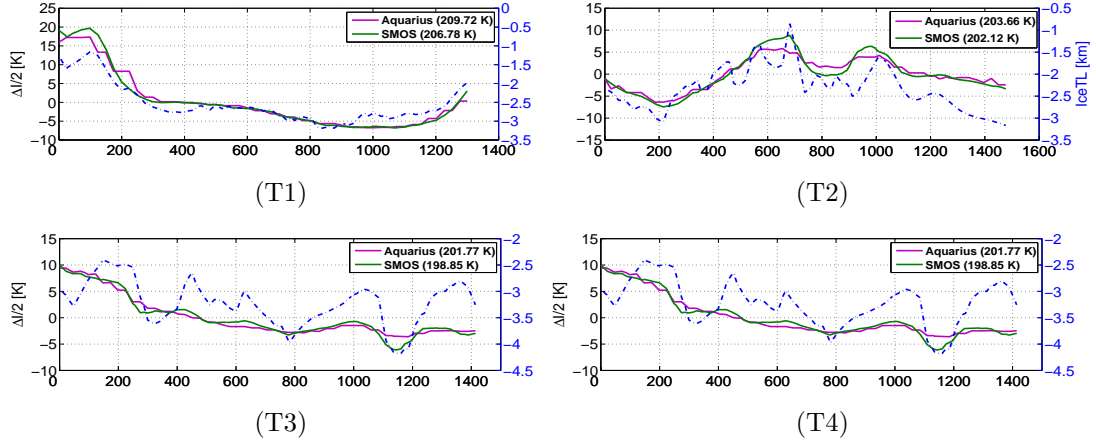
FIGURE C.7: SMOS and Aquarius $I/2$ variations ($\Delta I/2 = I/2 - \overline{I/2}$) at middle beam (pink and green solid lines, respectively) and ice thickness level (blue dashed line) along each transect. Legends display $\overline{I/2}$ values subtracted.

Table C.1 summarized statistical scores of SMOS and Aquarius $I/2$ in all beams with subglacial bedrock and ice thickness.

TABLE C.3: Correlation of SMOS and Aquarius $I/2$ at different beams with subglacial bedrock (R_b) and ice thickness (R_i), and slope respect to the ice thickness (s_i) and the error estimation for all pixels. Statistics with ice thickness are also displayed separately for pixels with known subglacial lakes and for a representative selection of a comparable number of pixels without lakes. All values are significant ($p<0.05$).

Radiometer	Beam	All pixels			Pixels with lakes		Pixels without lakes	
		R_b	R_i	s_i [K/km]	R_i	s_i [K/km]	R_i	s_i [K/km]
SMOS	inner	0.19	0.65	9.3±0.1	0.68	7.9±0.5	0.69	9.6±0.7
	middle	0.15	0.68	9.5±0.1	0.70	6.1±0.4	0.72	9.6±0.7
	outer	0.07	0.70	9.3±0.1	0.69	5.8±0.4	0.75	10.0±0.7
Aquarius	inner	0.22	0.64	8.9±0.1	0.67	7.5±0.5	0.69	9.3±0.7
	middle	0.18	0.65	9.0±0.1	0.68	6.1±0.5	0.71	9.3±0.7
	outer	0.11	0.66	8.6±0.1	0.65	6.0±0.5	0.73	9.8±0.7

Appendix D

Additional results of microwave/optical synergy

D.1   Results of SM–LST relationship using Terra

Figure D.1 shows a frequency density diagram of SMOS SM at the morning passes and MODIS LST Terra day over the REMEDHUS network.
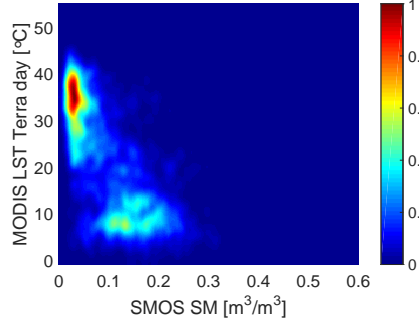
FIGURE D.1: Normalized occurrence frequency density diagram of and SMOS SM at the morning passes and MODIS LST Terra day (right) during the study period. Similar results are obtained for SMOS afternoon passes (not shown).

D.2 SM–LST relationship over the Iberian Peninsula

The correlation of SMOS SM at the morning passes and MODIS LST at different platforms and acquisition times over the Iberian Peninsula during the study period is shown in Fig. D.2.
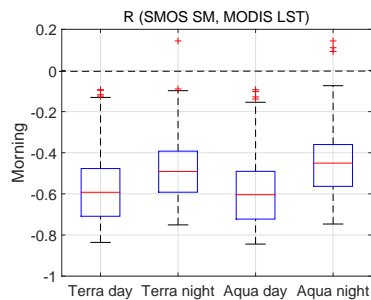
FIGURE D.2: Correlation (R) of SMOS SM at the morning passes and MODIS LST (left) over the Iberian Peninsula and their anomalies (right) for different MODIS platforms and passes: i) Terra day, ii) Terra night, ii) Aqua day, and iv) Aqua night. Similar behavior is obtained at the afternoon passes (not shown).

Figure D.3 displays correlation maps of SMOS SM at the morning passes and MODIS LST Aqua day (top left), Aqua night (top right), Terra day (bottom left), and Terra night (bottom right) over the Iberian Peninsula.
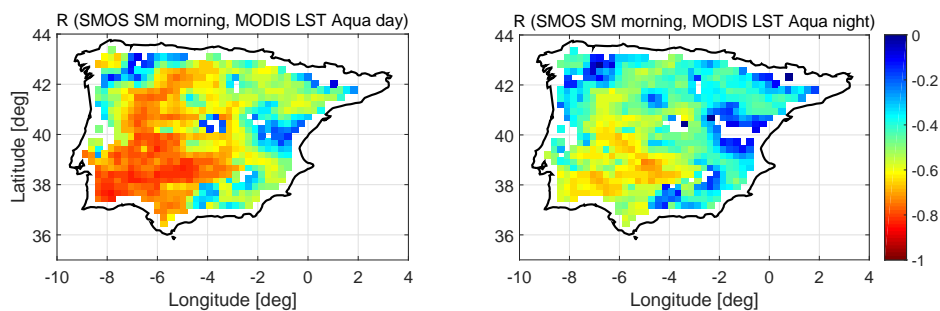
FIGURE D.3: Correlation (R) maps of SMOS SM at the morning passes over the Iberian Peninsula using MODIS LST Aqua day (left) and night (right). Similar results are obtained at the afternoon passes and/or using Terra day (not shown).

D.3 SM–LST coupling/decoupling and critical SM estimation

Figure D.4 shows the normalized time-series of *in situ* SM at the SMOS morning passes and T_{max} (top), and SMOS SM at the morning passes and MODIS LST Aqua day (bottom).
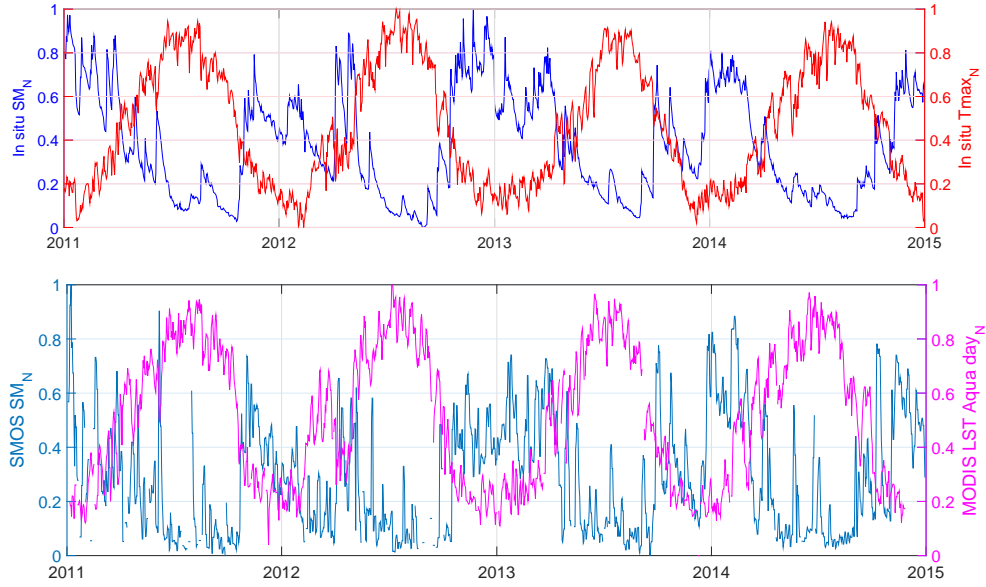
FIGURE D.4: Normalized time-series of *in situ* SM at the SMOS morning passes and T_{max} (top; blue and red lines, respectively), and SMOS SM at the morning passes and MODIS LST Aqua day (bottom; cyan and magenta lines, respectively). Similar behaviour is obtained at the afternoon passes and/or using Terra day.

D.4 Results from validation of 1-km disaggregated SM estimates

Statistical scores (R, ubRMS, bias, slope, and coverage) obtained from the validation of the 1-km disaggregated SM estimates are summarized in Tables D.1 and D.2 when using MODIS LST Aqua night, Tables D.3 and D.4 when using MODIS LST Terra day, and Tables D.5 and D.6 when using MODIS LST Terra night for SMOS morning and afternoon passes, respectively.

TABLE D.1: Same as Table 5.3, but for morning passes and MODIS LST Aqua night.

Station	R	ubRMSD [m^3/m^3]	bias [m^3/m^3]	slope s	N [days]
E10	0.73	0.05	0.07	1.50	213
F6	0.72	0.05	-0.04	0.87	216
F11	0.76	0.04	0.03	0.98	217
H7	0.21	0.06	0.07	1.08	219
H9	0.72	0.11	-0.17	0.33	207
H13	0.63	0.05	-0.01	0.77	211
I6	0.51	0.06	0.07	2.34	224
J3	0.48	0.06	0.09	1.52	218
J12	0.74	0.05	-0.15	0.87	217
J14	0.74	0.05	0.03	0.97	222
K4	0.64	0.04	0.07	2.09	223
K9	0.77	0.05	0.03	1.14	210
K10	0.78	0.04	0.06	1.35	217
K13	0.56	0.06	-0.12	0.52	226
L3	0.66	0.05	0.02	1.31	219
L7	0.73	0.06	-0.09	0.54	223
M5	0.65	0.05	0.00	1.08	219
M9	0.67	0.05	-0.08	0.63	216
M13	0.63	0.11	-0.16	0.30	234
N9	0.75	0.05	-0.06	0.66	228
O7	0.76	0.05	0.01	0.74	223
Network	0.72	0.05	0.00	1.00	292

TABLE D.2: Same as Table 5.3, but for afternoon passes and MODIS LST Aqua night.

Station	R	ubRMSD [m^3/m^3]	bias [m^3/m^3]	slope s	N [days]
E10	0.73	0.06	0.11	1.90	230
F6	0.76	0.05	-0.01	0.95	233
F11	0.83	0.05	0.07	1.24	235
H7	0.24	0.08	0.10	0.80	226
H9	0.81	0.10	-0.13	0.32	221
H13	0.60	0.05	0.02	0.80	225
I6	0.43	0.07	0.10	1.49	228
J3	0.56	0.06	0.12	1.63	231
J12	0.82	0.05	-0.12	1.07	231
J14	0.77	0.05	0.06	1.21	234
K4	0.64	0.07	0.10	2.34	235
K9	0.77	0.06	0.08	1.27	215
K10	0.82	0.06	0.09	1.69	228
K13	0.72	0.05	-0.08	0.69	236
L3	0.70	0.06	0.06	1.42	225
L7	0.79	0.05	-0.06	0.60	238
M5	0.66	0.06	0.04	1.31	226
M9	0.73	0.05	-0.04	0.73	227
M13	0.77	0.09	-0.13	0.35	245
N9	0.81	0.04	-0.02	0.72	235
O7	0.79	0.05	0.04	0.85	232
Network	0.78	0.06	0.03	1.19	314

TABLE D.3: Same as Table 5.3, but for morning passes and MODIS LST Terra day.

Station	R	ubRMSD [m³/m³]	bias [m³/m³]	slope s	N [days]
E10	0.75	0.05	0.07	1.61	187
F6	0.78	0.05	-0.04	0.87	210
F11	0.83	0.04	0.03	1.05	191
H7	0.32	0.07	0.07	1.95	190
H9	0.86	0.09	-0.16	0.38	176
H13	0.70	0.05	0.00	0.80	184
I6	0.60	0.06	0.07	2.02	179
J3	0.64	0.06	0.09	1.82	201
J12	0.82	0.04	-0.15	0.91	190
J14	0.74	0.04	0.03	0.93	181
K4	0.69	0.05	0.07	2.06	214
K9	0.76	0.04	0.03	1.11	183
K10	0.82	0.04	0.06	1.39	183
K13	0.66	0.05	-0.11	0.57	208
L3	0.73	0.05	0.02	1.29	185
L7	0.78	0.05	-0.07	0.56	207
M5	0.71	0.05	0.01	1.16	198
M9	0.73	0.05	-0.07	0.63	171
M13	0.69	0.12	-0.17	0.31	207
N9	0.78	0.05	-0.05	0.64	196
O7	0.81	0.04	0.02	0.77	179
Network	0.81	0.05	0.00	1.08	277

TABLE D.4: Same as Table 5.3, but for afternoon passes and MODIS LST Terra day.

Station	R	ubRMSD [m³/m³]	bias [m³/m³]	slope s	N [days]
E10	0.78	0.05	0.11	1.85	217
F6	0.75	0.05	-0.02	0.91	238
F11	0.85	0.04	0.07	1.20	218
H7	0.15	0.07	0.09	0.67	212
H9	0.83	0.10	-0.12	0.31	193
H13	0.60	0.05	0.02	0.78	210
I6	0.38	0.06	0.09	1.22	197
J3	0.47	0.06	0.12	1.49	230
J12	0.84	0.03	-0.12	1.01	201
J14	0.74	0.04	0.06	0.97	202
K4	0.64	0.06	0.10	2.33	238
K9	0.72	0.04	0.07	1.11	213
K10	0.85	0.04	0.09	1.54	208
K13	0.73	0.05	-0.08	0.63	226
L3	0.69	0.05	0.05	1.28	212
L7	0.80	0.05	-0.05	0.60	229
M5	0.68	0.05	0.03	1.15	210
M9	0.74	0.04	-0.04	0.65	193
M13	0.68	0.12	-0.13	0.36	232
N9	0.82	0.04	-0.03	0.70	231
O7	0.81	0.04	0.04	0.82	197
Network	0.79	0.05	0.03	1.22	315

TABLE D.5: Same as Table 5.3, but for morning passes and MODIS LST Terra night.

Station	R	ubRMSD [m^3/m^3]	bias [m^3/m^3]	slope s	N [days]
E10	0.80	0.05	0.09	1.64	224
F6	0.79	0.05	-0.03	1.02	225
F11	0.82	0.05	0.04	1.14	227
H7	0.33	0.07	0.08	1.90	225
H9	0.77	0.10	-0.15	0.36	223
H13	0.72	0.05	0.00	0.97	224
I6	0.64	0.07	0.09	2.94	225
J3	0.58	0.06	0.10	1.58	229
J12	0.79	0.04	-0.14	0.93	231
J14	0.77	0.05	0.04	1.14	227
K4	0.65	0.06	0.08	2.21	232
K9	0.70	0.05	0.04	1.11	222
K10	0.81	0.05	0.07	1.45	224
K13	0.68	0.06	-0.11	0.62	238
L3	0.69	0.05	0.03	1.27	219
L7	0.79	0.05	-0.08	0.60	236
M5	0.71	0.06	0.02	1.26	225
M9	0.75	0.05	-0.07	0.70	225
M13	0.69	0.11	-0.16	0.32	230
N9	0.81	0.05	-0.05	0.68	234
O7	0.79	0.05	0.02	0.77	240
Network	0.79	0.05	0.00	1.08	308

TABLE D.6: Same as Table 5.3, but for afternoon passes and MODIS LST Terra night.

Station	R	ubRMSD [m^3/m^3]	bias [m^3/m^3]	slope s	N [days]
E10	0.77	0.05	0.12	1.69	254
F6	0.77	0.05	-0.01	0.96	253
F11	0.82	0.05	0.07	1.24	253
H7	0.27	0.07	0.11	1.58	258
H9	0.80	0.12	-0.13	0.34	252
H13	0.70	0.06	0.03	1.13	247
I6	0.49	0.07	0.11	2.22	250
J3	0.64	0.06	0.13	2.06	252
J12	0.85	0.04	-0.11	1.11	254
J14	0.81	0.05	0.06	1.25	256
K4	0.64	0.06	0.11	2.52	259
K9	0.74	0.05	0.09	1.25	245
K10	0.86	0.05	0.10	1.65	253
K13	0.78	0.04	-0.08	0.74	263
L3	0.72	0.05	0.06	1.60	247
L7	0.81	0.05	-0.05	0.65	262
M5	0.67	0.06	0.04	1.28	246
M9	0.78	0.05	-0.04	0.79	244
M13	0.61	0.13	-0.14	0.35	261
N9	0.85	0.04	-0.02	0.78	249
O7	0.81	0.04	0.04	0.81	255
Network	0.81	0.05	0.04	1.27	329

Appendix E

Additional results of passive and active microwave vegetation parameters

E.1   Differences in MT-DCA retrievals

Figure E.1 displays the histogram and map of VOD_{MT} differences between consecutive retrievals over the same M-cell of the SMAPVEX12 domain.
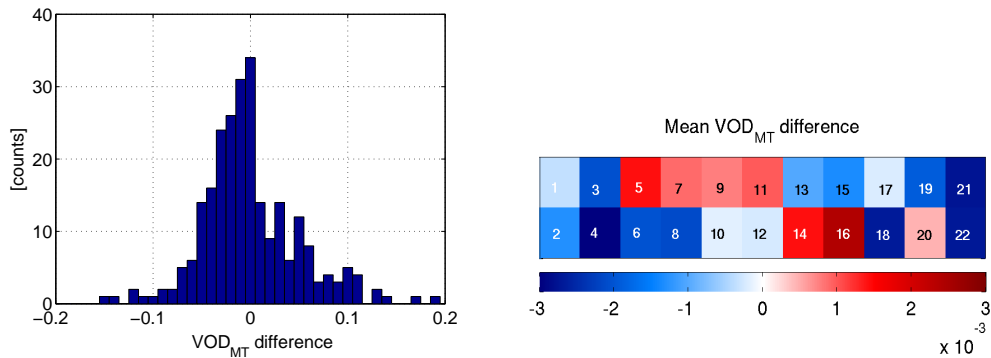
FIGURE E.1: Histogram (left) and map (right) of VOD_{MT} differences between consecutive retrievals over the same M-cell of the SMAPVEX12 domain.

Figure E.2 displays the histogram and map of SM$_{MT}$ differences between the two retrievals over the same M-cell of the SMAPVEX12 domain.
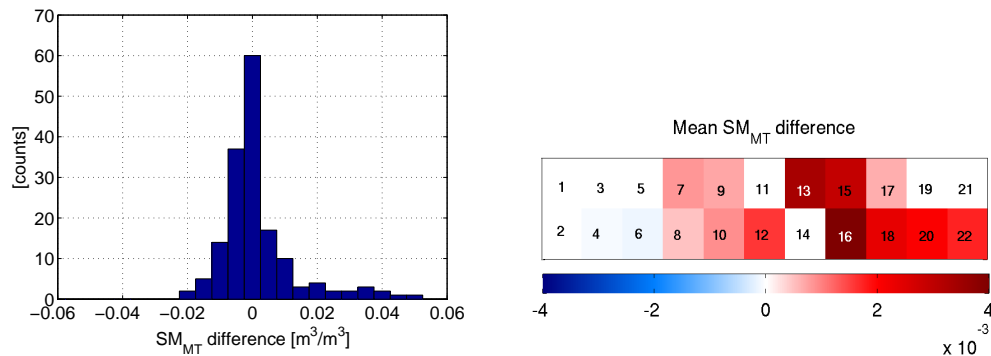
FIGURE E.2: Histogram (top) and map (bottom) of SM$_{MT}$ differences between the two retrievals over the same M-cell of the SMAPVEX12 domain.

E.2 Passive and active vegetation parameters

Figure E.3 shows time-series of σ_{HV} (top) and RVI (bottom) over the SMAPVEX12 domain along time.
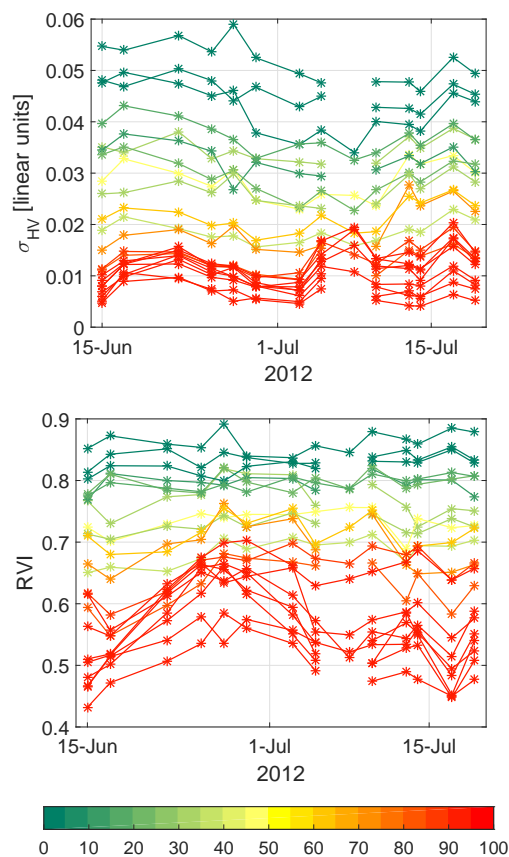
FIGURE E.3: Measured σ_{HV} (top) and RVI (bottom) over the SMAPVEX12 domain along time. The color bar indicates the agricultural fraction within each M-cell.

Maps of retrieved static ω_{MT} (top) and the temporal mean of σ_{HV} (middle) and RVI (bottom) over the SMAPVEX12 domain are shown in Fig. E.4.
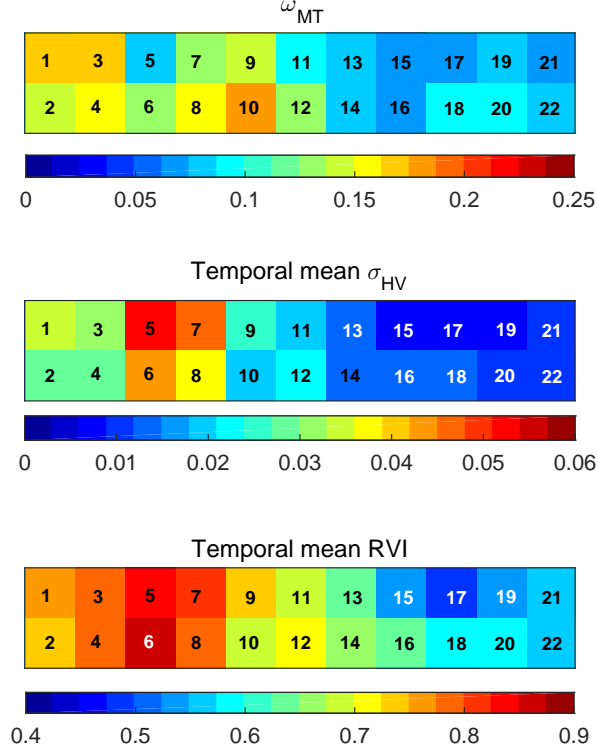
FIGURE E.4: Maps of retrieved static ω_{MT} (top) and the temporal mean of σ_{HV} (middle) and RVI (bottom) over the SMAPVEX12 domain.

Bibliography

Allen, R.G., Pereira, L.S., Raes, D., & Smith, M. 1998. Crop evapotranspiration. *Food and Agriculture Organization (FAO) Irrigation and Drainage Paper N.56.*

Aminou, D.M.A., Jacquet, B., & Pasternak, F. 1997. Characteristics of the meteosat second generation radiometer/imager: SEVIRI. *Pages 19–37 of: Proceedings of Society of Photo-optical Instrumentation Engineers*, vol. 3221.

Anderson, M.C., Norman, J.M., Diak, G.R., Kustas, W.P., & Mecikalski, J.R. 1997. A two-source time-integrated model for estimating surface fluxes using thermal infrared remote sensing. *Remote Sensing of Environment*, **60**(2), 195–216.

Anderson, M.C., Norman, J.M., Mecikalski, J.R., Otkin, J.A., & Kustas, W.P. 2007. A climatological study of evapotranspiration and moisture stress across the continental United States based on thermal remote sensing: 1. Model formulation. *Journal of Geophysical Research*, **112**(D10), 1–17.

Anterrieu, E, Y.H.Kerr, F.Cabot, G.S.E.Lagerloef, & Vine, D.M.Le. 2011. A synergy between SMOS and Aquarius: resampling SMOS maps at the resolution and incidence of Aquarius. *Pages 4142–4145 of: IEEE International Conference on Geoscience and Remote Sensing Symposium (IGARSS) 2011.*

Bará, J., Camps, A., Torres, F., & Corbella, I. 1998. Radio Science. *Angular resolution of two-dimensional, hexagonally sampled interferometric radiometers*, **33**(5), 1459–1473.

BAS. 2009. *Understanding Antarctica: Fifty years of British scientific monitoring (1959-2009).* Tech. rept. British Antarctic Survey and UK Foreign & Commonwealth Office Polar Regions Unit.

Basharinov, A.Y., & Shutko, A.M. 1975. *Simulation studies of the SHF radiation characteristics of soils under moist conditions.* Tech. rept.

BEC Team. 2015. *SMOS-BEC Ocean and Land Products Description, BEC-SMOS-0001-PD.pdf v.1.4.* Tech. rept. Barcelona Expert Centre.

BEC Team. 2016. *Quality Report: Validation of SMOS-BEC experimental Sea Surface Salinity products in the Arctic Ocean and high latitudes Oceans. Years 2011-2013.* Tech. rept. Barcelona Expert Centre: BEC-SMOS-0007-QR v1.0.

Berrisford, P, Dee, D.P., Poli, P., Brugge, R., Fielding, K., Fuentes, M., Kallberg, P.W., Kobayashi, S., Uppala, S., & Simmons, A. 2011. *The ERA-Interim archive Version 2.0.*

Bindlish, R., Jackson, T.J., Zhao, T., & Cosh, M. 2012. Use of satellite observations in SMAP cal/val. *In: Presentation at Soil Moisture Active Passive Mission 3rd SMAP Cal/Val Workshop.*

Bindlish, R., Jackson, T.J., Cosh, M., Zhao, T., & O'Neill, P.E. 2015. Global Soil Moisture From the Aquarius/SAC-D Satellite: Description and Initial Assessment. *IEEE Geoscience and Remote Sensing Letters*, **12**(5), 923–927.

Birchak, J.R., Gardner, C.G., Hipp, J.E., & Victor, J.M. 1974. High dielectric constant microwave probes for sensing soil moisture. *Proceedings of the IEEE*, **62**(1), 93–98.

Birkeland, P.W. 1974. *Pedology, weathering and geomorphological research*. New York, London and Toronto: Oxford University Press.

Blume, H.J.C., & Kendall, B.M. 1982. Passive Microwave Measurements of Temperature and Salinity in Coastal Areas. *IEEE Transactions on Geoscience and Remote Sensing*, **GE–20**(3), 394–404.

Braganza, K., Karoly, D.J., & Arblaster, J.M. 2004. Diurnal temperature range as an index of global climate change during the twentieth century. *Geophysical Research Letters*, **31**(13), L13217.

Brodzik, M.J., & Knowles, K.W. 2002. *Discrete global grids*. National Center for Geographic Information & Analysis.

Brogioni, M., Pettinato, S., Montomoli, F., & Macelloni, G. 2014. Snow layering effects on L-band passive measurements at Dome C - Antarctica. *Pages 61–64 of: 13th Specialist Meeting on Microwave Radiometry and Remote Sensing of the Environment (MicroRad), 2014*.

Brogioni, M., Macelloni, G., Montomoli, F., & Jezek, K.C. 2015. Simulating Multifrequency Ground-Based Radiometric Measurements at DOME C–Antarctica. *IEEE Journal of Selected Topics in Applied Earth Observations and Remote Sensing*, **8**(9), 4405–4417.

Brouwer, C., & Heibloem, M. 2001. *Irrigation water management: Training Manual no. 3*. Tech. rept. Food and Agriculture Organization of the United Nations, Via delle Terme di Caracalla, Rome, Italy.

Brown, M.A., Torres, F., Corbella, I., & Colliander, A. 2008. SMOS Calibration. *IEEE Transactions on Geoscience and Remote Sensing*, **46**(3), 646–658.

Brucker, L., Dinnat, E.P., & Koenig, L.S. 2013. Weekly-gridded Aquarius L-band radiometer/scatterometer observations and salinity retrievals over the polar regions: applications for cryospheric studies. *The Cryosphere Discussions*, **7**(6), 5921–5970.

Brucker, L, Dinnat, E.P., Picard, G., & Champollion, N. 2014. Effect of Snow Surface Metamorphism on Aquarius L-Band Radiometer Observations at Dome C, Antarctica. *IEEE Transactions on Geoscience and Remote Sensing*, **52**(11), 7408–7417.

Brunfeldt, D.R., & Ulaby, F. T. 1986. Microwave Emission from Row Crops. *IEEE Transactions on Geoscience and Remote Sensing*, **GE-24**(3), 353–359.

Bruscantini, C.A., Grings, F.M., Barber, M., Franco, M., Entekhabi, D., & Karszenbaum, H. 2015. A novel downscaling methodology for intermediate resolution radiometer data for SMAP. *Pages 1972–1975 of: IEEE International Geoscience and Remote Sensing Symposium (IGARSS) 2015*.

Burke, E.J., Shuttleworth, W.J., & French, A.N. 2001. Using vegetation indices for soil-moisture retrievals from passive microwave radiometry. *Hydrology and Earth System Sciences*, **5**(4), 671–678.

Burke, H.H.K., & Schmugge, T.J. 1982. Effects of Varying Soil Moisture Contents And Vegetation Canopies on Microwave Emissions. *IEEE Transactions on Geoscience and Remote Sensing*, **GE-20**(3), 268–274.

Cabot, F., Lagerloef, G.S.E., Kerr, Y., & Anterrieu, E. 2013. Intercalibration of SMOS and Aquarius over land, ice and ocean. *In: SMOS & Aquarius Science Workshop*.

Camps, A. 1996. *Application of Interferometric Radiometry to Earth Observation*. Ph.D. thesis, Universitat Politècnica de Catalunya, Barcelona.

Camps, A., Vall-llossera, M., Duffo, N., Zapata, M., Corbella, I., Torres, F., & Barrena, V. 2004. Sun effects in 2-D aperture synthesis radiometry imaging and their cancelation. *IEEE Transactions on Geoscience and Remote Sensing*, **42**(6), 1161–1167.

Camps, A., Vall-llossera, M., Corbella, I., Duffo, N., & Torres, F. 2008. Improved Image Reconstruction Algorithms for Aperture Synthesis Radiometers. *IEEE Transactions on Geoscience and Remote Sensing*, **46**(1), 146–158.

Cao, C., Uprety, S., Xiong, J., Wu, A., Jing, P., Smith, D., Chander, G., Fox, N., & Ungar, S. 2010. Establishing the Antarctic Dome C community reference standard site towards consistent measurements from Earth observation satellites. *Canadian Journal of Remote Sensing*, **36**(5), 498–513.

Carlson, T.N. 2007. An Overview of the "Triangle Method" for Estimating Surface Evapotranspiration and Soil Moisture from Satellite Imagery. *Sensors*, **7**(8), 1612–1629.

Carlson, T.N., Gillies, RR., & Perry, E.M. 1994. A method to make use of thermal infrared temperature and NDVI measurements to infer surface soil water content and fractional vegetation cover. *Remote Sensing Reviews*, **9**(1-2), 161–173.

Chan, S.K., Bindlish, R., O'Neill, P.E., Njoku, E., Jackson, T.J., Colliander, A., Chen, F., Burgin, M., Dunbar, S., Piepmeier, J., Yueh, S., Entekhabi, D., Cosh, M.H., Caldwell, T., Walker, J., Wu, X., Berg, A., Rowlandson, T., Pacheco, A., McNairn, H., Thibeault, M., Martínez-Fernández, J., González-Zamora, A., Seyfried, M., Bosch, D., Starks, P., Goodrich, D., Prueger, J., Palecki, M., Small, E.E., Zreda, M., Calvet, J.C., Crow, W.T., & Kerr, Y.H. 2016. Assessment of the SMAP Passive Soil Moisture Product. *IEEE Transactions on Geoscience and Remote Sensing*, **54**(8), 4994–5007.

Choudhury, B.J., Schmugge, T.J., Chang, A., & Newton, R.W. 1979. Effect of surface roughness on the microwave emission from soils. *Journal of Geophysical Research: Oceans*, **84**(C9), 5699–5706.

Cihlar, J., Manak, D., & D'Iorio, M. 1994. Evaluation of compositing algorithms for AVHRR data over land. *IEEE Transactions on Geoscience and Remote Sensing*, **32**(2), 427–437.

Climate Reality. 2014. *The Climate Reality Project: 2014 Annual Report*. Tech. rept.

CNAF. 2013. *Cuadro nacional de atribuciones de frecuencias*. Tech. rept. Spanish Goverment, Ministry of Industry, Energy and Tourism.

Colliander, A. 2014a. *SMAPVEX12 PALS Backscatter Data*. Tech. rept. NASA National Snow and Ice Data Center Distributed Active Archive Center (NSIDC), Boulder, Colorado, USA.

Colliander, A. 2014b. *SMAPVEX12 PALS Brightness Temperature Data*. Tech. rept. NASA National Snow and Ice Data Center Distributed Active Archive Center (NSIDC), Boulder, Colorado, USA.

Corbella, I., Torres, F., Camps, A., Duffo, N., & Vall-llossera, M. 2009. Brightness-Temperature Retrieval Methods in Synthetic Aperture Radiometers. *IEEE Transactions on Geoscience and Remote Sensing*, **47**(1), 285–294.

Corbella, .I, Torres, F., Duffo, N., González-Gambau, V., Pablos, M., Durán, I., & Martín-Neira, M. 2011. MIRAS Calibration and Performance: Results From the SMOS In-Orbit Commissioning Phase. *IEEE Transactions on Geoscience and Remote Sensing*, **49**(9), 3147–3155.

Corbella, I., Lin, Wu, Torres, F., Duffo, N., & Martin-Neira, M. 2015. Faraday Rotation Retrieval Using SMOS Radiometric Data. *IEEE Geoscience and Remote Sensing Letters*, **12**(3), 458–461.

Cosh, M. 2014. *SMAPVEX12 Vegetation Water Content Map*. Tech. rept. NASA National Snow and Ice Data Center Distributed Active Archive Center (NSIDC), Boulder, Colorado, USA.

Crane, R.K. 1971. Propagation phenomena affecting satellite communication systems operating in the centimeter and millimeter wavelength bands. *Proceedings of the IEEE*, **59**(2), 173–188.

Crow, W.T., Kustas, W.P., & Prueger, J.H. 2008. Monitoring root-zone soil moisture through the assimilation of a thermal remote sensing-based soil moisture proxy into a water balance model. *Remote Sensing of Environment*, **112**(4), 1268–1281.

Cui, Q, Shi, J., Du, J., Zhao, T., & Xiong, C. 2015a. An Approach for Monitoring Global Vegetation Based on Multiangular Observations From SMOS. *IEEE Journal of Selected Topics in Applied Earth Observations and Remote Sensing*, **8**(2), 604–616.

Cui, Q., Shi, J., Du, J., Zhao, T., & Xiong, C. 2015b. An Approach for Monitoring Global Vegetation Based on Multiangular Observations From SMOS. *IEEE Journal of Selected Topics in Applied Earth Observations and Remote Sensing*, **8**(2), 604–616.

Dai, A., Trenberth, K.E., & Karl, T.R. 1999. Effects of clouds, soil moisture, precipitation, and water vapor on diurnal temperaturerange. *Journal of Climate*, **12**, 2451–2473.

Das, N.N., Entekhabi, D., & Njoku, E.G. 2011. An Algorithm for Merging SMAP Radiometer and Radar Data for High-Resolution Soil-Moisture Retrieval. **49**(5), 1504–1512.

Das, N.N., Entekhabi, D., Njoku, E.G., Shi, J.J.C, Johnson, J.T., & Colliander, A. 2014. Tests of the SMAP Combined Radar and Radiometer Algorithm Using Airborne Field Campaign Observations and Simulated Data. *IEEE Transactions on Geoscience and Remote Sensing*, **52**(4), 2018–2028.

De Jeu, R.A.M., Wagner, W., Holmes, T.R.H., Dolman, A.J., Giesen, N.C., & Friesen, J. 2008. Global Soil Moisture Patterns Observed by Space Borne Microwave Radiometers and Scatterometers. *Surveys in Geophysics*, **29**(4), 399–420.

De Matthaeis, P., Utku, C., Vine, D.M. Le, & Moyer, A. 2014. Aquarius retrieval of sea ice thickness: Initial results. *Pages 69–71 of: 13th Specialist Meeting on Microwave Radiometry and Remote Sensing of the Environment (MicroRad) 2014*.

Del Frate, F., Ferrazzoli, P., & Schiavon, G. 2003. Retrieving soil moisture and agricultural variables by microwave radiometry using neural networks. *Remote Sensing of Environment*, **84**(2), 174–183.

Dobson, M.C., Ulaby, F.T., Hallikainen, M.T., & El-Rayes, M.A. 1985. Microwave Dielectric Behavior of Wet Soil-Part II: Dielectric Mixing Models. *IEEE Transactions on Geoscience and Remote Sensing*, **GE-23**(1), 35–46.

Dorigo, W.A., Wagner, W., Hohensinn, R., Hahn, S., Paulik, C., Xaver, A., Gruber, A., Drusch, M., Mecklenburg, S., Oevelen, P. Van, Robock, A., & Jackson, T.J. 2011. The International Soil Moisture Network: a data hosting facility for global in situ soil moisture measurements. *Hydrology and Earth System Sciences*, **15**, 1675–1698.

Dubois, P.C., Van Zyl, J., & Engman, T. 1995. Measuring soil moisture with imaging radars. *IEEE Transactions on Geoscience and Remote Sensing*, **33**(4), 915–926.

DuMouchel, W.H., & O'Brien, F.L. 1989. Integrating a Robust Option into a Multiple Regression Computing Environment. *In: Computer Science and Statistics: Proceedings of the 21st Symposium on the Interface.*

Durre, I., Wallace, J.M., & Lettenmaier, D.P. 2000. Dependence of extreme daily maximum temperatures on antecedent soil moisture in the contiguos United States during summer. *Journal of Climate*, **13**(24), 2641–2651.

England, A.W. 1990. Radiobrightness Of Diurnally Heated, Freezing Soil. *IEEE Transactions on Geoscience and Remote Sensing*, **28**(4), 464–476.

Entekhabi, D., Asrar, G.R., Betts, A.K., Beven, K.J., R.L.Bras, Duffy, C.J., Dunne, T., Koster, R.D., Lettenmaier, D.P., McLaughlin, D.B., Shuttleworth, W.J., Van Genuchten, M.T., Wei, Ming-Ying, & Wood, E.F. 1999. An agenda for land surface hydrology research and a call for the second international hydrological decade. *Bulletin of the American Meteorological Society*, **80**(10), 2043–2058.

Entekhabi, D., Reichle, R.H., Koster, R.D., & Crow, W.T. 2010a. Performance Metrics for Soil Moisture Retrievals and Application Requirements. *Journal of Hydrometeorology*, **11**(3), 832–840.

Entekhabi, D., Njoku, E.G., O'Neill, P.E., Kellogg, K.H., Crow, W.T., Edelstein, W.N., Entin, J.K., Goodman, S.D., Jackson, T.J., Johnson, J., Kimball, J., Piepmeier, J.R., Koster, R.D., Martin, N., McDonald, K.C., Moghaddam, M., Moran, S., Reichle, R., Shi, J.C., Spencer, M.W., Thurman, S.W., Tsang, Leung, & Zyl, J. Van. 2010b. The Soil Moisture Active Passive (SMAP) Mission. *Proceedings of the IEEE*, **98**(5), 704–716.

Entekhabi, D., Yueh, S., O'Neill, P., Kellogg, K., Allen, A., Bindlish, R., Brown, M., Chan, S., Colliander, A., Crow, W.T., Das, N., De Lannoy, G., Dunbar, R.S., Edelstein, W.N., Entin, J.K., Escobar, V., Goodman, S.D., Jackson, T.J., Jai, B., Johnson, J., Kim, E., Kim, S., Kimball, J., Koster, R.D., Leon, A., McDonald, K.C., Moghaddam, M., Mohamed, P., Moran, S., Njoku, E.G., Piepmeier, J.R., Reichle, R., Rogez, F., Shi, J.C., Spencer, M.W., Thurman, S.W., Tsang, L., Van Zyl, J., Weiss, B., & West, R. 2014. *SMAP Handbook*. 400-1567, Jet Propulsion Laboratory, Pasadena, California: JPL Publication.

Er-Raki, S., Chehbouni, A., Hoedjes, J., Ezzahar, J., B. Duchemin, B., & F. Jacob, F. 2008. Improvement of FAO-56 method for olive orchards through sequential assimilation of thermal infrared-based estimates of ET. *Agricultural Water Management*, 309–321.

Escorihuela, M.J., Kerr, Y.H., de Rosnay, P., Wigneron, J.P., Calvet, J.C., & Lemaitre, F. 2007. A Simple Model of the Bare Soil Microwave Emission at L-Band. *IEEE Transactions on Geoscience and Remote Sensing*, **45**(7), 1978–1987.

Fabra, F. 2013. *GNSS-R as a source opportunity for remote sensing of the cryosphere*. Ph.D. thesis, Universitat Politècnica de Catalunya, Barcelona.

Fagerlund, E, Kleman, B., Sellin, L., & Svensson, H. 1970. Physical studies of nature by thermal mapping. *Earth-Science Reviews*, **6**(3), 169–180.

Fang, B., & Lakshmi, V. 2014. Soil moisture at watershed scale: Remote sensing techniques. *Journal of Hydrology*, **516**, 258–272.

Fily, M., & Benoist, J.P. 1991. Large-scale statistical study of Scanning Multichannel Microwave Radiometer (SMMR) over Antarctica. *Journal of Glaciology*, **37**(125), 129–139.

Fisher, J.B., Tu, K.P., & Baldocchi, D.D. 2008. Global estimates of the land–atmosphere water flux based on monthly {AVHRR} and ISLSCP-II data, validated at 16 {FLUXNET} sites. *Remote Sensing of Environment*, **112**(3), 901–919.

Floury, N, Drinkwater, M., & Witasse, O. 2002. L-band brightness temperature of ice sheets in Antarctica: emission modelling, ionospheric contribution and temporal stability. *Pages 2013–2105 of: IEEE International Geoscience and Remote Sensing Symposium (IGARSS) 2002*.

Font, J., Camps, A., Borges, A., Martin-Neira, M., Boutin, J., Reul, N., Kerr, Y.H., Hahne, A., & Mecklenburg, S. 2010. SMOS: The Challenging Sea Surface Salinity Measurement From Space. *Proceedings of the IEEE*, **98**(5), 649–665.

Font, J., Boutin, J., Reul, N., Arias, M., Gabarró, C., Guimbard, S., Hernández, O., Martin, N., Martínez, J., Olmedo, E., Tenerelli, J., Vergely, J.L., Yin, X., Spurgeon, P., & Delwart, S. 2014. *SMOS L2 OS Algorithm Theoretical Baseline Document, SO-TN-ARG-GS-0007*. Tech. rept. Argans, ICM-CSIC, LOCEAN/SA/CETP and IFREMER.

Freedman, A., McWatters, D., & Spencer, M. 2006. The Aquarius Scatterometer: An Active System for Measuring Surface Roughness for Sea-Surface Brightness Temperature Correction. *Pages 1685–1688 of: IEEE International Conference on Geoscience and Remote Sensing Symposium (IGARSS) 2006.*

Fretwell, P., Pritchard, H.D., Vaughan, D.G., Bamber, J.L., Barrand, N.E., Bell, R., Bianchi, C., Bingham, R.G., Blankenship, D.D., Casassa, G., Catania, G., Callens, D., Conway, H., Cook, A.J., Corr, H.F.J., Damaske, D., Damm, V., Ferraccioli, F., Forsberg, R., Fujita, S., Gim, Y., Gogineni, P., Griggs, J.A., Hindmarsh, R.C.A., Holmlund, P., Holt, J.W., Jacobel, R.W., Jenkins, A., Jokat, W., Jordan, T., King, E.C., Kohler, J., Krabill, W., Riger-Kusk, M., Langley, K.A., Leitchenkov, G., Leuschen, C., Luyendyk, B.P., Matsuoka, K., Mouginot, J., Nitsche, F.O., Nogi, Y., Nost, O.A., Popov, S.V., Rignot, E., Rippin, D.M., Rivera, A., Roberts, J., Ross, N., Siegert, M.J., Smith, A.M., Steinhage, D., Studinger, M., Sun, B., B.K.Tinto, Welch, B.C., Wilson, D., Young, D.A., Xiangbin, C., & Zirizzotti, A. 2013. Bedmap 2: improved ice bed, surface and thickness datasets for Antarctica. *The Cryosphere*, **7**, 375–393.

GCOS. 2010. *Implementation Plan for the Global Observing System for Climate in support of the UNFCCC, GCOS-138 (GOOS-184, GTOS-76, WMO-TD/No. 1523)*. Tech. rept. Global Climate Observing System.

Gillies, R.R., & Carlson, T.N. 1995. Thermal Remote Sensing of Surface Soil Water Content with Partial Vegetation Cover for Incorporation into Climate Models. *Journal of Applied Meteorology*, **34**(4), 745–756.

Glarner. 2006. *Length of day and twilight.*

González-Gambau, V. 2012. *Contribution to the characterization of interferometric radiometers devoted to Earth observation: application to the MIRAS/SMOS payload.* Ph.D. thesis, Universitat Politècnica de Catalunya, Barcelona.

González-Zamora, A., Sánchez, N., Martínez-Fernández, J., Gumuzzio, A., Piles, M., & Olmedo, E. 2015. Long-term SMOS soil moisture products: A comprehensive evaluation across scales and methods in the Duero Basin (Spain). *Physics and Chemistry of the Earth, Parts A/B/C*, **83-84**, 123–136.

Gourrion, J., Guimbard, S., Portabella, M., & Sabia, R. 2014. Toward an Optimal Estimation of the SMOS Antenna-Frame Systematic Errors. *IEEE Transactions on Geoscience and Remote Sensing*, **51**(9), 4752–4760.

Guo, P., Shi, J., & Zhao, T. 2013. A downscaling algorithm for combining radar and radiometer observations for SMAP soil moisture retrieval. *Pages 731–734 of: IEEE International Geoscience and Remote Sensing Symposium (IGARSS) 2013.*

Hain, C.R., Crow, W.T., Mecikalski, J.R., Anderson, M.C., & Holmes, T. 2011. An intercomparison of available soil moisture estimates from thermal infrared and passive microwave remote sensing and land surface modeling. *Journal of Geophysical Research: Atmospheres*, **116**(D15), 1–18.

Hallikainen, M.T., Ulaby, F.T., Dobson, M.C., & El-Rayes, M.A. 1984. Dielectric measurements of soils in the 3-37 GHz band between -50°C and 23°C. *Pages 163–168 of: IEEE International Geoscience and Remote Sensing Symposium (IGARSS) 1984.*

Hallikainen, M.T., Ulaby, F.T., Dobson, M.C., El-Rayes, M.A., & Wu, L.k. 1985. Microwave Dielectric Behavior of Wet Soil-Part I: Empirical Models and Experimental Observations. *IEEE Transactions on Geoscience and Remote Sensing*, **GE-23**(1), 25–34.

Hasted, J.B. 1974. *Aqueous Dielectrics.* Studies in Chemical Physics. London: Chapman and Hall; New York: Distributed in the U.S.A. by Halsted Press.

Hollinger, J.P., Pierce, J.L., & Poe, G.A. 1990. SSM/I instrument evaluation. *IEEE Transactions on Geoscience and Remote Sensing*, **28**(5), 781–790.

Hornbuckle, B.K., & England, A.W. 2005. Diurnal variation of vertical temperature gradients within a field of maize: implications for Satellite microwave radiometry. *IEEE Geoscience and Remote Sensing Letters*, **2**(1), 74–77.

Hornbuckle, B.K., England, A.W., De Roo, R.D., Fischman, M.A., & Boprie, D.L. 2003. Vegetation canopy anisotropy at 1.4 GHz. *IEEE Transactions on Geoscience and Remote Sensing*, **41**(10), 2211–2223.

Huang, Y., Walker, J.P., Gao, Y., Wu, X., & Monerris, A. 2016. Estimation of Vegetation Water Content From the Radar Vegetation Index at L-Band. *IEEE Transactions on Geoscience and Remote Sensing*, **54**(2), 981–989.

Hufford, G. 1991. A model for the complex permittivity of ice at frequencies below 1 Thz. *International Journal of Infrared and Millimeter Waves*, **12**(7), 677–682.

Hydra Probe. 2008. *The Hydra Probe Soil Sensor: Comprehensive Stevens Hydra Probe Users Manual.* Tech. rept.

IPCC. 2013. *Climate Change 2013: The Physical Science Basis. Contribution of Working Group I to the Fifth Assessment Report of the Intergovernmental Panel on Climate Change.* Tech. rept. Cambridge University Press [Stocker, T.F., Qin, D., Plattner, G.K., Tignor, M., Allen, S.K., Boschung, J., Nauels, A., Xia, Y., Bex, V., & Midgley, P.M. (eds.)], Cambridge, U.K. and New York, USA.

IPCC. 2014. *Climate Change 2014: Synthesis Report. Contribution of Working Groups I, II and III to the Fifth Assessment Report of the Intergovernmental Panel on Climate Change.* Tech. rept. [Core Writing Team, Pachauri, R.K., & Meyer, L.A. (eds.)], Geneva, Switzerland.

Ishimaru, A. 1991. *Electromagnetic Wave Propagation, Radiation, and Scattering.* 910 Sylvan Avenue, Englewood Cliffs, NJ 07632, United States of America: Prentice Hall.

ITU-RP.531-12. 2013. *Ionospheric propagation data and prediction methods required for the design of satellite services and systems.* Tech. rept. International Telecommunication Union.

Jackson, T.J. 1993. Measuring surface soil moisture using passive microwave remote sensing. *Hydrological Processes*, **7**(2), 139–152.

Jackson, T.J., & Schmugge, T.J. 1991. Vegetation effects on the microwave emission of soils. *Remote Sensing of Environment*, **36**(3), 203–212.

Jackson, T.J., Schmugge, T.J., & Wang, J.R. 1982. Passive Microwave Sensing of Soil Moisture Under Vegetation Canopies. *Water Resources Research*, **18**(4), 1137–1142.

Jackson, T.J., Hsu, A.Y., & O'Neill, P.E. 2002. Surface Soil Moisture Retrieval and Mapping Using High-Frequency Microwave Satellite Observations in the Southern Great Plains. *Journal of Hydrometeorology*, **3**(6), 688–699.

Jackson, T.J., Bindlish, R., Cosh, M.H., Zhao, Tianjie, Starks, P.J., Bosch, D.D., Seyfried, M., Moran, M.S., Goodrich, D.C., Kerr, Y.H., & Leroux, D.J. 2012. Validation of Soil Moisture and Ocean Salinity (SMOS) Soil Moisture Over Watershed Networks in the U.S. *IEEE Transactions on Geoscience and Remote Sensing*, **50**(5), 1530–1543.

Jezek, K.C. 2012. *Encyclopedia of Sustainability Science and Technology.* Vol. 1. New York, USA: Springer-Verlag. Chap. Airborne and spaceborne remote sensing of cryosphere, pages 280–298.

Jezek, K.C., Merry, C., Cavalieri, D., Grace, S., Bedner, J., Wilson, D., & Lampkin, D. 1991. *Comparison between SMMR and SSM/I passive microwave data collected over the Antarctic ice sheet.* Tech. rept. 91-03. US National Aeronautics and Space Administration.

Jezek, K.C., Johnson, J.T., Drinkwater, M.R., Macelloni, G., Tsang, Leung, Aksoy, M., & Durand, M. 2015. Radiometric Approach for Estimating Relative Changes in Intraglacier Average Temperature. *IEEE Transactions on Geoscience and Remote Sensing*, **53**(1), 134–143.

Jones, M.O., Jones, L.A., Kimball, J.S., & McDonald, K.C. 2011. Satellite passive microwave remote sensing for monitoring global land surface phenology. *Remote Sensing of Environment*, **115**(4), 1102–1114.

Kaleschke, L., Tian-Kunze, X., MaaB, N., Makynen, M., & Drusch, M. 2012. Sea ice thickness retrieval from SMOS brightness temperatures during the Arctic freeze-up period. *Geophysical Research Letter*, **39**(L05501).

Kerr, Y.H., Waldteufel, P., Wigneron, J.P., Delwart, S., Cabot, F., Boutin, J., Escorihuela, M.J., Font, J., Reul, N., Gruhier, C., Juglea, S.E., Drinkwater, M.R., Hahne, A., Martin-Neira, M., & Mecklenburg, S. 2010. The SMOS Mission: New Tool for Monitoring Key Elements ofthe Global Water Cycle. *Proceedings of the IEEE*, **98**(5), 666–687.

Kerr, Y.H., Waldteufel, P., Richaume, P., Wigneron, J.P., Ferrazzoli, P., Mahmoodi, A., Al Bitar, A., Cabot, F., Gruhier, C., Juglea, S., Leroux, D., Mialon, A., & Delwart, S. 2012. The SMOS soil moisture retrieval algorithm. *IEEE Transactions on Geoscience and Remote Sensing*, **50**(5), 1384–1403.

Kerr, Y.H., Al-Yaari, A., Rodríguez-Fernández, N., Parrens, M., Molero, B., Leroux, D.J., Bircher, S., Mahmoodi, A., Mialon, A., Richaume, P., Delwart, S., Al Bitar, A., Pellarin, T., Bindlish, R., Jackson, T.J., Rudiger, C., Waldteufel, P., Mecklenburg, S., & Wigneron, J.P. 2016. Overview of SMOS performance in terms of global soil moisture monitoring after six years in operation. *Remote Sensing of Environment*, **180**, 40–63.

Kim, E., Piepmeier, J., Mohammed, P., Peng, J., De Amici, G., Hudson, D., & Dawson, D. 2013. L1 radiometer TB. *In: Presentation at Soil Moisture Active Passive Mission 4th SMAP Cal/Val Workshop.*

Kim, Y, & Van Zyl, J. 2009. A Time Series Approach to Estimate Soil Moisture Using Polarimetric Radar Data. *IEEE Transactions on Geoscience and Remote Sensing*, **47**(8), 2519–1527.

Kim, Y., Jackson, T.J., Bindlish, R., Lee, H., & Hong, S. 2012. Radar Vegetation Index for Estimating the Vegetation Water Content of Rice and Soybean. *IEEE Geoscience and Remote Sensing Letters*, **9**(4), 564–568.

Kirdiashev, K., Chukhantsev, A., & Shutko, A. 1979. Microwave radiation of the Earth's surface in presence of vegetation cover. *Radio Engineering Electronics Physics*, **24**, 256–264.

Klein, L., & Swift, C. 1977. An improved model for the dielectric constant of sea water at microwave frequencies. *IEEE Transactions on Antennas and Propagation*, **25**(1), 104–111.

Konings, A.G., McColl, K. A., Piles, M., & Entekhabi, D. 2015. How Many Parameters Can Be Maximally Estimated From a Set of Measurements? *IEEE Geoscience and Remote Sensing Letters*, **12**(5), 1081–1085.

Konings, A.G., Piles, M., Rotzer, K., McColl, K.A., Chan, S.K., & Entekhabi, D. 2016. Vegetation optical depth and scattering albedo retrieval using time series of dual-polarized L-band radiometer observations. *Remote Sensing of Environment*, **172**, 178–189.

Kristensen, S., Sobjaerg, S., Balling, J., & Sko, N. 2013. *EMIRAD data: Presentation & analysis, version 1.2.* Tech. rept. DTU Space, DOMECair Campaign.

Lagerloef, G., Colomb, F.R., Le Vine, D., Wentz, F., Yueh, S., Ruf, C., Lilly, J., Gunn, J., Chao, Y., deCharon, A., Feldman, G., & Swift, C. 2008. The Aquarius/SAC-D Mission: Designed to Meet the Salinity Remote-Sensing Challenge. *Oceanography*, **21**(1), 68–81.

Lane, J.A., & Saxton, J.A. 1952. Dielectric Dispersion in Pure Polar Liquids at Very High Radio-Frequencies. I. Measurements on Water, Methyl and Ethyl Alcohols. *Proceedings of the Royal Society of London A: Mathematical, Physical and Engineering Sciences*, **213**(1114), 400–408.

Lawrence, H, Wigneron, J. P., Demontoux, F., Mialon, A., & Kerr, Y. H. 2013. Evaluating the Semiempirical H - Q Model Used to Calculate the L-Band Emissivity of a Rough Bare Soil. *IEEE Transactions on Geoscience and Remote Sensing*, **51**(7), 4075–4084.

Le Toan, T., Beaudoin, A., Riom, J., & Guyon, D. 1992. Relating forest biomass to SAR data. *IEEE Transactions on Geoscience and Remote Sensing*, **30**(2), 403–411.

Le Vine, D.M., & Good, J.C. 1983. *Aperture Synthesis for Microwave Radiometers in Space, TM85033*. Tech. rept. National Aeronautics and Space Administration (NASA), Greenbelt,Maryland 20771, USA.

Le Vine, D.M, Swift, C.T., & Haken, M. 2001. Development of the synthetic aperture microwave radiometer, ESTAR. *IEEE Transactions on Geoscience and Remote Sensing*, **39**(1), 199–202.

Le Vine, D.M., Abraham, S., Wentz, F., & Lagerloef, G.S.E. 2005. Impact of the Sun on remote sensing of sea surface salinity from space. *Pages 288–291 of: IEEE International Geoscience and Remote Sensing Symposium (IGARSS) 2015*.

Le Vine, D.M., Lagerloef, G.S.E., Colomb, F.R., Yueh, S.H., & Pellerano, F.A. 2007a. Aquarius: An Instrument to Monitor Sea Surface Salinity From Space. *IEEE Transactions on Geoscience and Remote Sensing*, **45**(7), 2040–2050.

Le Vine, D.M., Jackson, T.J., & Haken, M. 2007b. Initial Images of the Synthetic Aperture Radiometer 2D-STAR. *IEEE Transactions on Geoscience and Remote Sensing*, **45**(11), 3623–3632.

Le Vine, D.M., Lagerloef, G.S.E., & Torrusio, S.E. 2010. Aquarius and Remote Sensing of Sea Surface Salinity from Space. *Proceedings of the IEEE*, **98**(5), 688–703.

Le Vine, D.M., Abraham, S., Utku, C., & Dinnat, E.P. 2013. Aquarius Third Stokes Parameter Measurements: Initial Results. *IEEE Geoscience and Remote Sensing Letters*, **10**(3), 520–524.

Le Vine, D.M., Piepmeier, J.R., Dinnat, E.P., De Matthaeis, P., Utku, C., Abraham, S., Lagerloef, G.S.E., Meissner, T., & Wentz, F. 2014. Aquarius radiometer status. *Pages 226–227 of: 13th Specialist Meeting on Microwave Radiometry and Remote Sensing of the Environment (MicroRad), 2014*.

Le Vine, D.M., Abraham, S., & Peng, J. 2015. Faraday Rotation Correction for the SMAP Radiometer. *IEEE Transactions on Geoscience and Remote Sensing*, In press.

Leduc-Leballeur, M., Picard, G., Mialon, A., Arnaud, L., Lefebvre, E., Possenti, P., & Kerr, Y.H. 2015. Modeling L-Band Brightness Temperature at Dome C in Antarctica and Comparison With SMOS Observations. *IEEE Transactions on Geoscience and Remote Sensing*, **53**(7), 4022–4032.

Leone, D. 2015. *NASA Focused on Sentinel as Replacement for SMAP Radar. Space News.*

Leroux, D.J., Das, N.N., Entekhabi, D., Colliander, A., Njoku, E., Jackson, T.J., & Yueh, S. 2016. Active–Passive Soil Moisture Retrievals During the SMAP Validation Experiment 2012. *IEEE Geoscience and Remote Sensing Letters*, **13**(4), 475–479.

Li, Li, Gaiser, P., Albert, M.R., Long, D.G., & Twarog, E.M. 2008. WindSat Passive Microwave Polarimetric Signatures of the Greenland Ice Sheet. *IEEE Transactions on Geoscience and Remote Sensing*, **46**(9), 2622–2631.

Macelloni, G., Brogioni, M., Pampaloni, P., Cagnati, A., & Drinkwater, M.R. 2006. DOMEX 2004: An Experimental Campaign at Dome-C Antarctica for the Calibration of Spaceborne Low-Frequency Microwave Radiometers. *IEEE Transactions on Geoscience and Remote Sensing*, **44**(10), 2642–2653.

Macelloni, G., Brogioni, M., Pettinato, S., Zasso, R., Crepaz, A., Zaccaria, J., Padovan, B., & Drinkwater, M.R. 2013. Ground-Based L-Band Emission Measurements at Dome-C Antarctica: The DOMEX-2 Experiment. *IEEE Transactions on Geoscience and Remote Sensing*, **51**(9), 4718–4730.

Macelloni, G., Brogioni, M., Aksoy, M., Johnson, J.T., Jezek, K.C., & Drinkwater, M.R. 2014. Understanding SMOS data in Antarctica. *Pages 3606–3609 of: IEEE International Geoscience and Remote Sensing Symposium (IGARSS) 2014.*

Macelloni, G., Brogioni, M., Montomoli, F., Legovini, P., & Casal, T. 2015a. Analysis of L-band brightness temperature time series at DOME C–Antarctica. *Pages 4045–4048 of: IEEE International Geoscience and Remote Sensing Symposium (IGARSS) 2015.*

Macelloni, G., Brogioni, M., Pettinato, S., & Montomoli, F. 2015b. *Technical Support for the Long-Term Deployment of an L-Band Radiometer at Concordia Station.* Tech. rept. European Space Agency.

Mahmood, R., & Hubbard, K.G. 2007. Relationship between soil moisture of near surface and multiple depths of the root zone under heterogeneous land uses and varying hydroclimatic conditions. *Hydrological Processes*, **21**(25), 3449–3462.

Marquartd, D.W. 1963. An Algorithm for Least-Squares Estimation of Nonlinear Parameters. *Journal of the Society for Industrial and Applied Mathematics*, **11**(2), 431–441.

Martín-Neira, M., Cabeza, I., Pérez, C., Palacios, M.A., Guijarro, M.A., Ribó, S., Corbella, I., Blanch, S., Torres, F., Duffo, N., González-Gambau, V., Beraza, S., Camps, A., Vall-llossera, M., Tauriainen, S., Pihlflyckt, J., González, J.P., & Martin-Porqueras, F. 2008. AMIRAS–An Airborne MIRAS Demonstrator. *IEEE Transactions on Geoscience and Remote Sensing*, **46**(3), 705–716.

Martín-Neira, M., Oliva, R., Corbella, I., Torres, F., Duffo, N., Durán, I., Kainulainen, J., Closa, J., Zurita, A., Cabot, F., Khazaal, A., Anterrieu, E., Barbosa, J., Lopes, G., Tenerelli, J., Díez-García, R., Fauste, J., Martín-Porqueras, F., González-Gambau, V., Turiel, A., Delwart, S., Crapolicchio, R., & Suess, M. 2016. SMOS instrument performance and calibration after six years in orbit. *Remote Sensing of Environment*, **180**, 19–39.

Martínez-Fernández, J., & Ceballos, A. 2003. Temporal Stability of Soil Moisture in a Large-Field Experiment in Spain. *Soil Science Society of America Journal*, **67**(6), 1647–1656.

Martínez-Fernández, J., & Ceballos, A. 2005. Mean soil moisture estimation using temporal stability analysis. *Journal of Hydrology*, **312**(1–4), 28–38.

Martínez-Vázquez, A., Camps, A., López-Sánchez, J.M., Vall-llossera, M., & Monerris, A. 2009. Numerical Simulation of the Full-Polarimetric Emissivity of Vines and Comparison with Experimental Data. *Remote Sensing*, **1**(3), 300–317.

Masson, V., Champeaux, J.L., Chauvin, F., Meriguet, C., & Lacaze, R. 2003. A Global Database of Land Surface Parameters at 1-km Resolution in Meteorological and Climate Models. *Journal of Climate*, **16**(9), 1261–1282.

Matsouka, T., Fujita, S., & S.Mae. 1996. Effects of temperature on the dielectric properties of ice in the range 5-39 GHz. *J. Appl. Phys.*, **80**(10), 5884–5890.

Matzler, C., & Wegmuller, U. 1987. Dielectric properties of freshwater ice at microwave frequencies. *Journal of Physics D. Applied Physics*, **20**(12), 1623–1630.

Matzler, C., Rosenkranz, P.W., A.Battaglia, & Wigneron, J.P. 2006. *Thermal Microwave Radiation - Applications for Remote Sensing.* IET Electromagnetic Waves Series, vol. 52. Chap. Microwave dielectric properties of ice.

McColl, K.A., Entekhabi, D., & Piles, M. 2014. Uncertainty Analysis of Soil Moisture and Vegetation Indices Using Aquarius Scatterometer Observations. *IEEE Transactions on Geoscience and Remote Sensing*, **52**(7), 4259–4272.

McMullan, K.D., Brown, M.A., Martin-Neira, M., Rits, W., Ekholm, S., Marti, J., & Lemanczyk, J. 2008. SMOS: The Payload. *IEEE Transactions on Geoscience and Remote Sensing*, **46**(3), 594–605.

McNairn, H., Powers, J., & Wiseman, G. 2014. *SMAPVEX12 Land Cover Classification Map*. Tech. rept. NASA National Snow and Ice Data Center Distributed Active Archive Center (NSIDC), Boulder, Colorado, USA.

McNairn, H., Jackson, T.J., Wiseman, G., Bélair, S., Berg, A., Bullock, P., Colliander, A., Cosh, M.H., Kim, S.B., Magagi, R., Moghaddam, M., Njoku, E.G., Adams, J.R., Homayouni, S., Ojo, E.R., Rowlandson, T.L., Shang, J., Goïta, K., & Hosseini, M. 2015. The Soil Moisture Active Passive Validation Experiment 2012 (SMAPVEX12): Prelaunch Calibration and Validation of the SMAP Soil Moisture Algorithms. *IEEE Transactions on Geoscience and Remote Sensing*, **53**(5), 2784–2801.

Mecklenburg, S., Drusch, M., Kaleschke, L., Rodríguez-Fernández, N., Reul, N., Kerr, Y., Font, J., Martín-Neira, M., Oliva, R., Daganzo-Eusebio, E., Grant, J.P., Sabia, R., Macelloni, G., Rautiainen, K., Fauste, J., de Rosnay, P., Munoz-Sabater, J., Verhoest, N., Lievens, H., Delwart, S., Crapolicchio, R., de la Fuente, A., & Kornberg, M. 2016. ESA's Soil Moisture and Ocean Salinity mission: From science to operational applications. *Remote Sensing of Environment*, **180**, 3–18.

Meesters, A.G.C.A., Jeu, R.A.M. De, & Owe, M. 2005. Analytical derivation of the vegetation optical depth from the microwave polarization difference index. *IEEE Geoscience and Remote Sensing Letters*, **2**(2), 121–123.

Merlin, O., Rudiger, C., Al Bitar, A., Richaume, P., Walker, J., & Kerr, Y.H. 2012. Disaggregation of SMOS Soil Moisture in Southeastern Australia. *IEEE Transactions on Geoscience and Remote Sensing*, **50**(5), 1556–1571.

Mialon, A., Richaume, P., Leroux, D., Bircher, S., Bitar, A. A., Pellarin, T., Wigneron, J. P., & Kerr, Y. H. 2015. Comparison of Dobson and Mironov Dielectric Models in the SMOS Soil Moisture Retrieval Algorithm. *IEEE Transactions on Geoscience and Remote Sensing*, **53**(6), 3084–3094.

Miralles, D.G., Van Den Berg, M.J., Teuling, A.J., & De Jeu, R.A.M. 2012. Soil moisture-temperature coupling: A multiscale observational analysis. *Geophysical Research Letters*, **39**(31), L21707–1–6.

Mironov, V.L., Kosolapova, L.G., & Fomin, S.V. 2009. Physically and Mineralogically Based Spectroscopic Dielectric Model for Moist Soils. *IEEE Transactions on Geoscience and Remote Sensing*, **47**(7), 2059–2070.

Mo, T., & Schmugge, T.J. 1987. A Parameterization of the Effect of Surface Roughness on Microwave Emission. *IEEE Transactions on Geoscience and Remote Sensing*, **GE-25**(4), 481–486.

Mo, T., Choudhury, B.J., Schmugge, T.J., Wang, J.R., & Jackson, T.J. 1982. A model for microwave emission from vegetation-covered fields. *Journal of Geophysical Research: Oceans*, **87**(C13), 11229–11237.

Moghaddam, M., & Berg, A. 2014. *SMAPVEX12 Probe-Based In Situ Soil Moisture Data for Forest Area*. Tech. rept. NASA National Snow and Ice Data Center Distributed Active Archive Center (NSIDC), Boulder, Colorado, USA.

Moran, M.S., Clarke, T.R., Inoue, Y., & Vidal, A. 1994. Estimating crop water deficit using the relation between surface-air temperature and spectral vegetation index. *Remote Sensing of Environment*, **49**(3), 246–263.

Napier, P.J., Thompson, A.R., & Ekers, R.D. 1983. The very large array: Design and performance of a modern synthesis radio telescope. *Proceedings of the IEEE*, **71**(11), 1295–1320.

Newton, R., & Rouse, J. 1980. Microwave radiometer measurements of soil moisture content. *IEEE Transactions on Antennas and Propagation*, **28**(5), 680–686.

Njoku, E.G., & Li, Li. 1999. Retrieval of land surface parameters using passive microwave measurements at 6-18 GHz. *IEEE Transactions on Geoscience and Remote Sensing*, **37**(1), 79–93.

Ochsner, T.E., Cosh, M.H., Cuenca, R.H., Dorigo, W.A., Draper, C.S., Hagimoto, Y., Kerr, Y.H., Njoku, E.G., Small, E.E., & Zreda, M. 2013. State of the art in large-scale soil moisture monitoring. *Soil Science Society of America Journal*, **77**(6), 1888–1919.

O'Neill, P.E., Chan, S., Njoku, E., Jackson, T.J., & Bindlish, R. 2015. *SMAP Algorithm Theoretical Basis Document: L2 & L3 Radiometer Soil Moisture (Passive) Products, Rev. B*. Tech. rept. Jet Propulsion Laboratory.

Owe, M., De Jeu, R., & Walker, J. 2001. A methodology for surface soil moisture and vegetation optical depth retrieval using the microwave polarization difference index. *IEEE Transactions on Geoscience and Remote Sensing*, **39**(8), 1643–1654.

Owe, M, De Jeu, R., & Holmes, T. 2008. Multisensor historical climatology of satellite-derived global land surface moisture. *Journal of Geophysical Research*, **113**(F1).

Pablos, M., Piles, M., González-Gambau, V., Vall-llossera, M., Camps, A., & Martínez, J. 2013a. Inter-Comparison of SMOS and Aquarius Brightness Temperatures over Selected Targets. *In: SMOS & Aquarius Science Workshop*.

Pablos, M., Piles, M., González-Gambau, V., Vall-llossera, M., Camps, A., & Martínez, J. 2013b. Inter-Comparison of SMOS and Aquarius Brightness Temperatures over Selected Targets. *Pages 386–389 of: IEEE International Conference on Geoscience and Remote Sensing Symposium (IGARSS) 2013*.

Pablos, M., Piles, M., Sánchez, N., González-Gambau, V., Vall-llossera, M., Camps, A., & Martínez-Fernández, J. 2014a. A Sensitive Study of Land Surface Temperature to Soil Moisture using *in-situ* and space-borne observations. *Pages 3267–3269 of: IEEE International Conference on Geoscience and Remote Sensing Symposium (IGARSS) 2014*.

Pablos, M., Piles, M., González-Gambau, V., Vall-llossera, M., Camps, A., & Martínez, J. 2014b. SMOS and Aquarius Radiometers: Inter-Comparison Over Selected Targets. *IEEE Journal of Selected Topics in Applied Earth Observations and Remote Sensing*, **7**(9), 3833–3844.

Pablos, M., Piles, M., González-Gambau, V., Camps, A., & Vall-llossera, M. 2015a. Ice Thickness Effects on Aquarius Brightness Temperatures over Antarctica. *Journal of Geophysical Research–Oceans*, **120**(4), 2856–2868.

Pablos, M, Piles, M., González-Gambau, V., Camps, A., & Vall-llossera, M. 2015b. Influence of ice thickness on SMOS and Aquarius brightness temperatures over Antarctica. *Pages 5178–5181 of: IEEE International Conference on Geoscience and Remote Sensing Symposium (IGARSS), 2015*.

Pablos, M., Martínez-Fernández, J., Piles, M., Sánchez, N., Vall-llossera, M., & Camps, A. 2016. Multi-temporal evaluation of soil moisture and land surface temperature dynamics using in situ and satellite observations. *Remote Sensing*, **8**(7), 587.

Pablos, M., Piles, M., Sánchez, N., Vall-llossera, M., Martínez-Fernández, J., & Camps, A. In review. Impact of day/night time land surface temperature in soil moisture disaggregation algorithms. *European Journal of Remote Sensing*.

Pablos, M, Piles, M., Konings, A.G., Entekhabi, D., & Leroux, D.J. Submitted. Comparison between active and passive vegetation parameters derived from SMAPVEX12 time-series retrievals. *IEEE Transactions and Geoscience Remote Sensing*.

Pampaloni, P., & Paloscia, S. 1986. Microwave Emission and Plant Water Content: A Comparison between Field Measurements and Theory. *IEEE Transactions on Geoscience and Remote Sensing*, **GE-24**(6), 900–905.

Paolo, F.S., Fricker, H.A., & Padman, L. 2015. Volume loss from Antarctic ice shelves is accelerating. *Science*, **348**(6232), 327–331.

Patton, J., & Hornbuckle, B. 2013. Initial Validation of SMOS Vegetation Optical Thickness in Iowa. *IEEE Geoscience and Remote Sensing Letters*, **10**(4), 647–651.

Peplinski, N.R, Ulaby, F.T., & Dobson, M.C. 1995a. Corrections to "Dielectric Properties of Soils in the 0.3-1.3-GHz Range". *IEEE Transactions on Geoscience and Remote Sensing*, **33**(6), 1340.

Peplinski, N.R, Ulaby, F.T., & Dobson, M.C. 1995b. Dielectric properties of soils in the 0.3-1.3-GHz range. *IEEE Transactions on Geoscience and Remote Sensing*, **33**(3), 803–807.

Petropoulos, G.P., Carlson, T.N., Wooster, M.J., & Islam, S. 2009. A review of Ts/VI remote sensing based methods for the retrieval of land surface energy fluxes and soil moisture. *Progress in Physical Geography*, **33**(2), 224–250.

Picard, G., Brucker, L., Roy, A., Dupont, F., Fily, M., Royer, A., & Harlow, C. 2013. Simulation of the microwave emission of multi-layered snowpacks using the Dense Media Radiative transfer theory: the DMRT-ML model. *Geoscientific Model Development*, **6**(4), 1061–1078.

Piepmeier, P., .Feldman, G, Lagerloef, G.S.E., Vine, D.M. Le, & Yueh, S.H. 2013. *Aquarius Radiomter Post-Launch Calibration for Product Version 2*. Tech. rept. Aquarius Project Document: AQ-014-PS-0015 Rev.

Piles, M., & Sánchez, N. 2016. *Satellite Soil Moisture Retrieval: Techniques and Applications*. Elsevier Science. Chap. Spatial downscaling of passive microwave data with visible-to-infrared information for high-resolution soil moisture mappin.

Piles, M., Entekhabi, D., & Camps, A. 2009. A Change Detection Algorithm for Retrieving High-Resolution Soil Moisture From SMAP Radar and Radiometer Observations. *IEEE Transactions on Geoscience and Remote Sensing*, **47**(12), 4125–4131.

Piles, M., Vall-llossera, M., Camps, A., Talone, M., & Monerris, A. 2010. Analysis of a Least-Squares Soil Moisture Retrieval Algorithm from L-band Passive Observations. *Remote Sensing*, **2**(1), 352–374.

Piles, M., Camps, A., Vall-llossera, M., Corbella, I., Panciera, R., Rudiger, C., Kerr, Y.H., & Walker, J. 2011. Downscaling SMOS-Derived Soil Moisture Using MODIS Visible/Infrared Data. *IEEE Transactions on Geoscience and Remote Sensing*, **49**(9), 3156–3166.

Piles, M., Vall-llossera, M., Laguna, L., & Camps, A. 2012. A downscaling approach to combine SMOS multi-angular and full-polarimetric observations with MODIS VIS/IR data into high resolution soil moisture maps. *Pages 1247–1250 of: IEEE International Geoscience and Remote Sensing Symposium (IGARSS) 2012*.

Piles, M., Sánchez, N., Vall-llossera, M., Camps, A., Martínez-Fernández, J., Martínez, J., & González-Gambau, V. 2014. A Downscaling Approach for SMOS Land Observations: Evaluation of High-Resolution Soil Moisture Maps Over the Iberian Peninsula. *IEEE Journal of Selected Topics in Applied Earth Observations and Remote Sensing*, **7**(9), 3845–3857.

Piles, M., Entekhabi, D., Konings, A.G., McColl, K.A., N.N.Das, & Jagdhuber, T. 2016a. Multitemporal Microwave Retrievals of Soil Moisture and Vegetation Parameters from SMAP. *In: IEEE International Geoscience and Remote Sensing Symposium (IGARSS) 2016*.

Piles, M., Petropoulos, G.P., Sánchez, N., González-Zamora, A., & Ireland, G. 2016b. Towards improved spatio-temporal resolution soil moisture retrievals from the synergy of SMOS and MSG SEVIRI spaceborne observations. *Remote Sensing of Environment*, **180**, 403–417.

Pollard, D., DeConto, R.M., & Alley, R.B. 2015. Potential Antarctic Ice Sheet retreat driven by hydrofracturing and ice cliff failure. *Earth and Planetary Science Letters*, **412**, 112–121.

Price, J.C. 1980. The potential of remotely sensed thermal infrared data to infer surface soil moisture and evaporation. *Water Resources Research*, **16**(4), 787–795.

Price, P.B., Nagornov, O.V., Bay, R., Chirkin, D., He, Yudong, Miocinovic, P., Richards, A., Woschnagg, K., Koci, B., & Zagorodnov, V. 2002. Temperature profile for glacial ice at the South Pole: Implications for life in a nearby subglacial lake. *Pages 7844–7847 of: Proceeding of the National Academy of Sciences*, vol. 99.

Pulliainen, J.T., Grandell, J., & Hallikainen, M.T. 1999. HUT snow emission model and its applicability to snow water equivalent retrieval. *IEEE Transactions on Geoscience and Remote Sensing*, **37**(3), 1378–1390.

Rahmoune, R., Ferrazzoli, P., Kerr, Y.H., & Richaume, P. 2013. SMOS Level 2 Retrieval Algorithm Over Forests: Description and Generation of Global Maps. *IEEE Journal of Selected Topics in Applied Earth Observations and Remote Sensing*, **6**(3), 1430–1439.

Rawls, W.J., Brakensiek, D.L., & Saxton, K.E. 1982. Estimation of soil water properties. *Transaction of ASAE*, **25**(5), 1316–1320 and 1328.

Ribó, S. 2005. *Calibration validation and polarimetry in 2D aperture synthesis. Application to MIRAS*. Ph.D. thesis, Universitat Politècnica de Catalunya, Barcelona.

Rignot, E., Mouginot, J., & Scheuchl, B. 2011. Ice flow of the Antarctic ice sheet. *Science*, **333**(4), 1427–1430.

Rist, M.A., Sammonds, P.R., Oerter, H., & Doake, C.S.M. 2002. Fracture of Antarctic shelf ice. *Journal of Geophysical Research: Solid Earth*, **107**(B1), ECV 2–1–ECV 2–13.

Ritz, C. 1988. Interpretation of the temperature profile measured at Vostok, East Antarctica. *Annals of Glaciology*, **12**, 138–144.

Rodríguez-Fernández, N.J., Aires, F., Richaume, P., Kerr, Y.H., Prigent, C., Kolassa, J., Cabot, F., Jiménez, C., Mahmoodi, A., & Drusch, M. 2015. Soil Moisture Retrieval Using Neural Networks: Application to SMOS. *IEEE Transactions on Geoscience and Remote Sensing*, **53**(11), 5991–6007.

Roth, K., Schulin, R., Fluhler, H., & Attinger, W. 1990. Calibration of time domain reflectometry for water content measurement using a composite dielectric approach. *Water Resources Research*, **26**(10), 2267–2273.

Rötzer, K., Montzka1, C., Entekhabi, D., Konings, A.G., McColl, K., Piles, M., & Vereecken, H. In review. Relationship Between Vegetation Optical Depth and HV-backscatter from the Aquarius mission. *IEEE Transactions on Geoscience and Remote Sensing*.

Ruf, C.S., Swift, C.T., Tanner, A.B., & Le Vine, D.M. 1988. Interferometric synthetic aperture microwave radiometry for the remote sensing of the Earth. *IEEE Transactions on Geoscience and Remote Sensing*, **26**(5), 597–611.

Ryle, M. 1952. A New Radio Interferometer and Its Application to the Observation of Weak Radio Stars. *Proceedings of the Royal Society of London A: Mathematical, Physical and Engineering Sciences*, **211**(1106), 351–375.

Ryle, M., & Hewish, A. 1960. The synthesis of large radio telescopes. *Monthly Notices of the Royal Astronomical Society*, **120**, 220–230.

Sahr, K., White, D., & Kimerling, A.J. 2003. Cartography and Geographic Information Science. *Geodesic Discrete Global Grid Systems*, **30**(2), 121–134.

Saleh, K., Wigneron, J.P., de Rosnay, P., Calvet, J.C., & Kerr, Y.K. 2006. Semi-empirical regressions at L-band applied to surface soil moisture retrievals over grass. *Remote Sensing of Environment*, **101**(3), 415–426.

Sánchez, N., Martínez-Fernández, J., Calera, A., E.A., & Pérez-Gutiérrez, C. 2010. Combining remote sensing and in situ soil moisture data for the application and validation of a distributed water balance model (HidroMORE). *Agricultural Water Management*, **98**(1), 69–78.

Sánchez, N., Martínez-Fernández, J., Rodríguez-Ruiz, M., Torres, E.A., & Calera, A. 2012a. A simulation of soil water content based on remote sensing in a semi-arid Mediterranean agricultural landscape. *Spanish Journal of Agricultural Research*, **10**, 521–531.

Sánchez, N., Martínez-Fernández, J., Scaini, A., & Pérez-Gutiérrez, C. 2012b. Validation of the SMOS L2 soil moisture data in the REMEDHUS network (Spain). *IEEE Transactions on Geoscience and Remote Sensing*, **50**(5), 1602–1611.

Sánchez, N., Marínez-Fernández, J., González-Piqueras, J., González-Dugo, M.P., Baroncini-Turrichia, G., Torres, E.A., Calera, A., & Pérez-Gutiérrez, C. 2012c. Water balance at plot scale for soil moisture estimation using vegetation parameters. *Agricultural and Forest Meteorology*, **166–167**, 1–9.

Sánchez-Ruiz, S., Piles, M., Sánchez, N., Marínez-Fernández, J., Vall-llossera, M., & Camps, M. 2014. Combining SMOS with visible and near/shortwave/thermal infrared satellite data for high resolution soil moisture estimates. *Journal of Hydrology*, **49**, 3156–3166.

Sandholt, I., Rasmussen, K., & Andersen, J. 2002. A simple interpretation of the surface temperature/vegetation index space for assessment of surface moisture status. *Remote Sensing of Environment*, **79**(2–3), 213–224.

Schmugge, T., Gloersen, P., Wilheit, T., & Geiger, F. 1974. Remote sensing of soil moisture with microwave radiometers. *Journal of Geophysical Research*, **79**(2), 317–323.

Schmugge, T., O'Neill, P.E., & Wang, J.R. 1986. Passive Microwave Soil Moisture Research. *IEEE Transactions on Geoscience and Remote Sensing*, **GE–24**(1), 12–22.

Schwank, M, Matzler, C., Guglielmetti, M., & Fluhler, H. 2005. L-band radiometer measurements of soil water under growing clover grass. *IEEE Transactions on Geoscience and Remote Sensing*, **43**(10), 2225–2237.

Seneviratne, S.I., Corti, T., Davin, E.L., Hirschi, M., Jaeger, E.B., Lehner, I., Orlowsky, B., & Teuling, A.J. 2010. Investigating soil moisture-climate interactions in a changing climate: A review. *Earth-Science Reviews*, **99**, 125–161.

Shuttleworth, W.J. 1993. *Handbook of Hydrology.* New York, USA: McGraw-Hill Inc.

Sihvola, A., & Kong, J.A. 1988. Effective permittivity of dielectric mixtures. *IEEE Transactions on Geoscience and Remote Sensing*, **26**(4), 420–429.

Six, D., Fily, M., Alvain, S., Henry, P., & Benoist, J.P. 2004. Surface characterisation of the Dome Concordia area (Antarctica) as a potential satellite calibration site, using Spot 4/Vegetation instrument. *Remote Sensing of Environment*, **89**(1), 83–94.

Skou, N., Kristensen, S.S., Sobjaerg, S.S., & Balling, J.E. 2015. Airborne L-Band Radiometer Mapping of the Dome-C Area in Antarctica. *IEEE Journal of Selected Topics in Applied Earth Observations and Remote Sensing*, **8**(7), 3656–3664.

Song, C., & Jia, L. 2013. An improved method for downscaling soil moisture retrieved by SMOS with MODIS LST/NDVI. *Pages 2696–2699 of: IEEE International Geoscience and Remote Sensing Symposium (IGARSS) 2014.*

Spencer, M., Wheeler, K., White, C., West, R., Piepmeier, J., Hudson, D., & Medeiros, J. 2010. The Soil Moisture Active Passive (SMAP) mission L-Band radar/radiometer instrument. *Pages 3240–3243 of: IEEE International Geoscience and Remote Sensing Symposium (IGARSS) 2010.*

Srivastava, P.K., O'Neill, P.E., Cosh, M., Kurum, M., Lang, R., & Joseph, A. 2015a. Evaluation of Dielectric Mixing Models for Passive Microwave Soil Moisture Retrieval Using Data From ComRAD Ground-Based SMAP Simulator. *IEEE Journal of Selected Topics in Applied Earth Observations and Remote Sensing*, **8**(9), 4345–4354.

Srivastava, P.K, O'Neill, P., Cosh, M., Lang, R., & Joseph, A. 2015b. Evaluation of radar vegetation indices for vegetation water content estimation using data from a ground-based SMAP simulator. *Pages 1296–1299 of: IEEE International Geoscience and Remote Sensing Symposium (IGARSS) 2015*.

Steinhage, D. 2013. *Dome-C airborne gravity measurements and comparison to GOCE gradient data*. Tech. rept. DTU Space, DOMECair Campaign.

Stisen, S., Sandholt, I., Norgaard, A., Fensholt, R., & Jensen, K.H. 2008. Combining the triangle method with thermal inertia to estimate regional evapotranspiration — Applied to MSG-SEVIRI data in the Senegal River basin. *Remote Sensing of Environment*, **112**(3), 1242–1255.

Sun, D., & Pinker, R.T. 2004. Case study of soil moisture effect on land surface temperature retrieval. *IEEE Transactions on Geoscience and Remote Sensing*, **1**(2), 127–130.

Swift, C.T. 1980. Passive microwave remote sensing of the ocean–A review. *Boundary-Layer Meteorology*, **18**(1), 25–54.

Tenerelli, J., & Reul, N. 2010. *Analysis of L1PP Calibration Approach Impacts in SMOS TBs and 3-days SSS Retrievals over the Pacific Using an Alternative Ocean Target Transformation Applied to L1OP Data*. Tech. rept. IFREMER/CLS.

Tenerelli, J.E., Reul, N., Mouche, A.A., & Chapron, B. 2008. Earth-Viewing L-Band Radiometer Sensing of Sea Surface Scattered Celestial Sky Radiation–Part I: General Characteristics. *IEEE Transactions on Geoscience and Remote Sensing*, **46**(3), 659–674.

Tinga, W.R., Voss, W.A.G., & Blossey, D.F. 1973. Generalized approach to multiphase dielectric mixture theory. *Journal of Applied Physics*, **44**(9), 3897–3902.

Torres, F., Corbella, I., Wu, Lin, Duffo, N., Gourrion, J., Font, J., & Martin-Neira, M. 2012. Minimization of image distortion in SMOS brightness temperature maps over the ocean. *IEEE Geoscience and Remote Sensing Letters*, **9**(1), 18–22.

Tsang, L., Chen, C.-T., Chang, A.T.C., Guo, J., & Ding, K.-H. 2000. Dense media radiative transfer theory based on quasicrystalline approximation with applications to passive microwave remote sensing of snow. *Radio Science*, **35**(3), 731–749.

Ulaby, F.T., & Long, D.F. 2014. *Microwave Radar and Radiometric Remote Sensing*. 839 Greene Street Ann Arbor, MI 48104–3209, United States of America: University of Michigan Press.

Ulaby, F.T., & Wilson, E.A. 1985. Microwave Attenuation Properties of Vegetation Canopies. *IEEE Transactions on Geoscience and Remote Sensing*, **GE-23**(5), 746–753.

USGS. 2015. *The USGS Water Science School*. Tech. rept. U.S. Geological Survey.

Van de Griend, A.A, & Wigneron, J.P. 2004. The b-factor as a function of frequency and canopy type at H-polarization. *IEEE Transactions on Geoscience and Remote Sensing*, **42**(4), 786–794.

Van De Griend, A.A., Camillo, P.J., & Gurney, R.J. 1984. Discrimination of soil physical parameters, thermal inertia, and soil moisture from diurnal surface temperature fluctuations. *Water Resources Research*, **21**(7), 997–1009.

Wan, Z., & Snyder, W. 1999. *MODIS Land-Surface Temperature Algorithm Theoretical Basis Document version 3.3*. Tech. rept. Institute for Computational Earth System Science University of California.

Wang, J.R. 1983. Passive microwave sensing of soil moisture content: The effects of soil bulk density and surface roughness. *Remote Sensing of Environment*, **13**(4), 329–344.

Wang, J.R., & Choudhury, B.J. 1981. Remote sensing of soil moisture content, over bare field at 1.4 GHz frequency. *Journal of Geophysical Research: Oceans*, **86**(C6), 5277–5282.

Wang, J.R., & Schmugge, T.J. 1980. An Empirical Model for the Complex Dielectric Permittivity of Soils as a Function of Water Content. *IEEE Transactions on Geoscience and Remote Sensing*, **GE-18**(4), 288–295.

Weil, R.R, & Brady, N.C. 2016. *The Nature and Properties of Soil*. Pearson.

West, R. 2012. L1 Radar Cal/Val Status. *In: Presentation at Soil Moisture Active Passive Mission 3rd SMAP Cal/Val Workshop*.

West, R.D., Winebrenner, D.P, Tsang, L., & Rott, H. 1996. Microwave emission from density-stratified Antarctic firn at 6 cm wavelength. *Journal of glaciology*, **42**(140), 63–76.

Wiesmann, A., & Matzler, C. 1999. Microwave Emission Model of Layered Snowpacks. *Remote Sensing of Environment*, **70**(3), 307–316.

Wigneron, J.P., Chanzy, A., Calvet, J.C., & Bruguier, N. 1995. A simple algorithm to retrieve soil moisture and vegetation biomass using passive microwave measurements over crop fields. *Remote Sensing of Environment*, **51**(3), 331–341.

Wigneron, J.P., Laguerre, L., & Kerr, Y.H. 2001. A simple parameterization of the L-band microwave emission from rough agricultural soils. *IEEE Transactions on Geoscience and Remote Sensing*, **39**(8), 1697–1707.

Wigneron, J.P., Calvet, J.C., Pellarin, T., Van de Griend, A.A., Berger, M., & Ferrazzoli, P. 2003. Retrieving near-surface soil moisture from microwave radiometric observations: current status and future plans. *Remote Sensing of Environment*, **84**(4), 489–506.

Wigneron, J.P., Kerr, Y.H., Waldteufel, P., Saleh, K., Escorihuela, M.J., Richaume, P., Ferrazzoli, P., de Rosnay, P., Gurney, R., Calvet, J.C., Grant, J.P., Guglielmetti, M., Hornbuckle, B., Matzler, C., Pellarin, T., & Schwank, M. 2007. L-band Microwave Emission of the Biosphere (L-MEB) Model: Description and calibration against experimental data sets over crop fields. *Remote Sensing of Environment*, **107**(4), 639–655.

Wigneron, J.P, Chanzy, A., Kerr, Y. H., Lawrence, H., Shi, J., Escorihuela, M. J., Mironov, V., Mialon, A., Demontoux, F., de Rosnay, P., & Saleh-Contell, K. 2011. Evaluating an Improved Parameterization of the Soil Emission in L-MEB. *IEEE Transactions on Geoscience and Remote Sensing*, **49**(4), 1177–1189.

Wilson, W.J., Yueh, S.H., Dinardo, S.J., Chazanoff, S.L., Kitiyakara, A., Li, F.K., & Rahmat-Samii, Y. 2001. Passive active L- and S-band (PALS) microwave sensor for ocean salinity and soil moisture measurements. *IEEE Transactions on Geoscience and Remote Sensing*, **39**(5), 1039–1048.

Wiseman, G., Bullock, P., & Berg, A. 2014a. *SMAPVEX12 Core-Based In Situ Soil Moisture Data for Agricultural Area*. Tech. rept. NASA National Snow and Ice Data Center Distributed Active Archive Center (NSIDC), Boulder, Colorado, USA.

Wiseman, G., Bullock, P., & Berg, A. 2014b. *SMAPVEX12 Probe-Based In Situ Soil Moisture Data for Agricultural Area*. Tech. rept. NASA National Snow and Ice Data Center Distributed Active Archive Center (NSIDC), Boulder, Colorado, USA.

Wright, A, & Siegert, M. 2012. A fourth inventory of Antarctic subglacial lakes. *Antarctic Science*, **24**(6), 659–664.

Yueh, S.H. 2000. Estimates of Faraday rotation with passive microwave polarimetry for microwave remote sensing of Earth surfaces. *IEEE Transactions on Geoscience and Remote Sensing*, **38**(5), 2434–2438.

Yueh, S.H., Wilson, W.J., LiFuk, K., Nghiem, S., & Ricketts, W.B. 1995. Polarimetric measurements of sea surface brightness temperatures using an aircraft K-band radiometer. *IEEE Transactions on Geoscience and Remote Sensing*, **33**(1), 85–92.

Yueh, S.H., Dinardo, S.J., Chan, S.K., Njoku, E., Jackson, T.J., & Bindlish, R. 2008. Passive and Active L-band System observations during the 2007 CLASIC Campaign. *In: IEEE International Conference on Geoscience and Remote Sensing Symposium (IGARSS) 2008*.

Zwally, H.J. 1977. Microwave emissivity and accumulation rate of polar firn. *Journal of Glaciology*, **18**(79), 195–215.